

THESIS FOR THE DEGREE OF DOCTOR OF PHILOSOPHY

**Time-domain modelling of curve squeal: a fast  
model for one- and two-point wheel/rail contact**

Ivan Zenzerovic

Department of Architecture and Civil Engineering  
Division of Applied Acoustics, Vibroacoustic Group  
Chalmers University of Technology  
Gothenburg, Sweden, 2017

**Time-domain modelling of curve squeal: a fast model for one- and two-point wheel/rail contact**

Ivan Zenzerovic

ISBN 978-91-7597-647-1

© Ivan Zenzerovic, 2017

Doktorsavhandlingar vid Chalmers tekniska högskola

Ny serie nr. 4328

ISSN 0346-718X

Department of Architecture and Civil Engineering

Division of Applied Acoustics, Vibroacoustic Group

Chalmers University of Technology

SE-412 96 Gothenburg, Sweden

Telephone: +46 (0)31-772 2200

Printed by

Chalmers Reproservice

Gothenburg, Sweden, 2017

# Time-domain modelling of curve squeal: a fast model for one- and two-point wheel/rail contact

Ivan Zenzerovic

Department of Architecture and Civil Engineering  
Division of Applied Acoustics, Vibroacoustic Group  
Chalmers University of Technology

## Abstract

Curve squeal is a type of railway noise that may arise when a railway vehicle negotiates a relatively tight curve. A single frequency, corresponding to a wheel mode, dominates the radiated sound, which makes squeal a very tonal noise. The high number of tight curves in cities and urban areas, its tonal nature and high noise levels make squeal a significant source of noise pollution. The rising awareness of the impact of noise on public health increases the need to address the squeal problem. Consequently, there is an increased need for practical simulation tools. In this thesis, a computationally fast squeal model formulated in the time domain is proposed. The computational efficiency is achieved by modelling the tangential contact with a point-contact model, which considers the contact variables globally. The friction model and the contact compliance are defined in a rigorous manner using Kalker's variational theory. Validation results show that the contact model is valid up to at least 5 kHz. The proposed model is further extended to include the effects of spin creepage, contact angle and two-point wheel/rail contact. Spin creepage is treated as a contact property with its influence included in the friction model. Additionally, the model is also extended with an existing model for sound radiation from the railway wheel. Parameter studies show a strong influence of parameters that influence the dynamics coupling responsible for squeal: the contact angle, friction and the wheel/rail contact position. These parameters influence both squeal occurrence, amplitudes and frequency. Spin, however, influences only squeal amplitudes. With the wheel being a significant factor in curve squeal, the influence of the wheel modal damping is also investigated. To mitigate squeal in a specific case, all modes that are susceptible to squeal in that case have to be damped. Otherwise, squeal may shift to another mode and develop even higher amplitudes. The amount of modal damping required to prevent squeal is relatively low. Finally, a two-point wheel/rail contact case is analysed. Results show that squeal can occur on curve-outer wheels. The two-point-contact case is relatively complicated: squeal is the result of a combination of the dynamic interplay of the two contact points and the presence of two closely spaced wheel modes.

**Keywords:** *Curve squeal, dynamics coupling, rolling contact, time domain, frictional instability, non-Hertzian contact, tangential point-contact model, two-point contact*



*In memoriam*

MARIJA BULIĆ

★16.3.1928. +19.6.2017.



# List of Publications

This thesis is written as a self-contained monograph. The presented work is also contained in the following four papers appended to this thesis.

## **Paper I**

Towards an Engineering Model for Curve Squeal

I. Zenzerovic, A. Pieringer and W. Kropp

In J. C. O. Nielsen, D. Anderson, P.-E. Gautier, M. Iida, J. T. Nelson, D. J. Thompson, T. Tielkes, D. A. Towers and P. de Vos, editors, *Noise and Vibration Mitigation for Rail Transportation Systems: Proceedings of the 11th International Workshop on Railway Noise*, volume 126, pp. 433-440. Springer, Berlin, Heidelberg, 2015

## **Paper II**

An engineering time-domain model for curve squeal: Tangential point-contact model and Green's functions approach

I. Zenzerovic, W. Kropp and A. Pieringer

In *Journal of Sound and Vibration*, Volume 376, pp. 149-165, 2016.

## **Paper III**

Influence of spin creepage and contact angle on curve squeal: a numerical approach

I. Zenzerovic, W. Kropp and A. Pieringer

*Manuscript submitted for publication*, 2017.

## **Paper IV**

Time-domain investigation of curve squeal in the presence of two wheel/rail contact points

I. Zenzerovic, W. Kropp and A. Pieringer

*Manuscript submitted for publication*, 2017.



## Acknowledgements

The research presented in this thesis was performed under the project “Abatement of curve squeal noise from trains” (VB11) within the Centre of Excellence CHARMEC (CHAlmers Railway MEChanics). The financial support from CHARMEC and its supporting companies, in particular, Bombardier Transportation, Trafikverket, SL and Interfleet Technology is highly acknowledged. I would also like to thank SNC-Lavalin Rail & Transport in Sweden for the provided data.

Even with all the financing and data, this thesis would not be possible without the support of people around me. First and foremost, I gratefully thank my supervisor, Prof. Wolfgang Kropp for his guidance and patience. I am also very thankful to my assistant supervisor, Astrid Pieringer, PhD, for all the discussions, advice and, in particular, the help with all the small details. I would also like to acknowledge all members of CHARMEC and members of the project reference group: the courses, seminars and meetings were an excellent source of knowledge, ideas and insights.

A sincere thank you goes to all fellow PhD students, researchers and staff at the Department of Applied Acoustics. In particular, I am deeply grateful to Börje Wijk, Gunilla Skog and Camilla Gäverström for their support with all the technical and bureaucratic matters.

I would also like to thank all colleagues at CEVT for creating a friendly and engaging work environment during my time with the company.

Naturally, there were hard times. Thanks to my friends in Croatia and Sweden, these were balanced with lots of fun. Occasional dinners, coffees, long walks, and even a gym session, were always a welcome distraction. Thank you, guys and girls!

My most profound gratitude goes to my family. This thesis would be impossible without the continuous support and encouragement from the side of my parents and brother.

Last but not least, thank you Vlatka for your love and support during this final and critical stage of my PhD journey.



# Contents

<b>Abstract</b>	<b>i</b>
<b>List of Publications</b>	<b>v</b>
<b>Acknowledgements</b>	<b>vii</b>
<b>List of Figures</b>	<b>xiii</b>
<b>List of Tables</b>	<b>xvii</b>
<b>1 Introduction</b>	<b>1</b>
1.1 Background . . . . .	1
1.2 Aim and scope of the thesis . . . . .	3
1.3 Outline . . . . .	4
<b>2 On curve squeal</b>	<b>7</b>
2.1 The phenomenon of curve squeal . . . . .	7
2.2 Mechanisms responsible for curve squeal . . . . .	12
2.2.1 Falling friction law . . . . .	12
2.2.2 Geometric coupling of wheel modes . . . . .	13
2.3 Mitigation measures . . . . .	15
2.3.1 Infrastructure measures . . . . .	15
2.3.2 Rolling stock measures . . . . .	17
<b>3 Review of existing models</b>	<b>19</b>
3.1 Models for curve squeal . . . . .	19
3.1.1 Frequency-domain models . . . . .	20
3.1.2 Time-domain models . . . . .	23
3.2 Models for the rolling contact . . . . .	26
3.2.1 Contact conditions during squeal . . . . .	29
3.2.2 Structure of a contact model . . . . .	34
3.2.3 Review of contact models used in squeal modelling . . . . .	35

<b>4</b>	<b>Formulation of the engineering model for curve squeal</b>	<b>41</b>
4.1	Coordinate systems . . . . .	43
4.1.1	The contact angle and the coordinate transformation . . . . .	45
4.1.2	Wheel/rail nominal contact positions: one-point contact . . . . .	47
4.1.3	Wheel/rail nominal contact position: two-point contact . . . . .	48
4.2	System dynamics . . . . .	49
4.2.1	Extension to two-point wheel/rail contact . . . . .	51
4.2.2	Wheel dynamics . . . . .	52
4.2.3	Rail dynamics . . . . .	58
4.3	The rolling contact model . . . . .	62
4.3.1	The normal contact model . . . . .	62
4.3.2	Normal contact: extension to two-point wheel/rail contact . . . . .	65
4.3.3	The tangential contact model . . . . .	65
4.3.4	Determination of the contact compliances . . . . .	67
4.3.5	Determination of the friction model . . . . .	70
4.3.6	Regularised friction: extension to non-zero spin creepage . . . . .	71
4.4	Sound radiation from a railway wheel . . . . .	75
4.4.1	Radiation efficiencies . . . . .	76
4.4.2	Sound radiation surfaces . . . . .	78
4.4.3	Wheel velocity field . . . . .	78
4.4.4	The boundary element model . . . . .	80
<b>5</b>	<b>Numerical validation</b>	<b>81</b>
5.1	Validation of the sound-radiation-model implementation . . . . .	81
5.1.1	Validation with unit-force excitation . . . . .	82
5.1.2	Validation for a curve squeal case . . . . .	83
5.2	Validation of the contact model . . . . .	85
5.2.1	Validation with imposed motion . . . . .	85
5.2.2	Validation in dynamic conditions . . . . .	88
5.2.3	Validation of the spin-creepage extension . . . . .	93
5.2.4	Conclusion . . . . .	95
<b>6</b>	<b>Parameter studies</b>	<b>97</b>
6.1	Lateral creepage/friction study . . . . .	97
6.1.1	Contact case $\Delta y^{WR} = -5$ mm . . . . .	99
6.1.2	Contact case $\Delta y^{WR} = -10$ mm . . . . .	100
6.1.3	Contact case $\Delta y^{WR} = -15$ mm . . . . .	102
6.1.4	Discussion . . . . .	102
6.2	Wheel modal damping study . . . . .	105
6.3	Influence of spin creepage . . . . .	111
6.4	Influence of the contact angle . . . . .	114
6.4.1	Combined influence of the contact angle and spin creepage . . . . .	116

---

<b>7</b>	<b>Two-point wheel/rail contact results</b>	<b>121</b>
7.1	Two-point wheel/rail contact case parameters . . . . .	121
7.2	Results of the two-point wheel/rail contact case . . . . .	123
7.3	Comparison to one-point wheel/rail contact results . . . . .	127
7.4	Discussion . . . . .	128
<b>8</b>	<b>Conclusions and future work</b>	<b>131</b>
8.1	Conclusions . . . . .	131
8.2	Future work . . . . .	134
	<b>References</b>	<b>137</b>



# List of Figures

1.1	Generation of rolling noise. . . . .	2
2.1	Relative velocities between wheel and rail. . . . .	9
2.2	Wheelset angle of attack and two-point contact. . . . .	10
2.3	The wheel/rail angle of attack, detail. . . . .	10
2.4	Slip-velocity dependent friction. . . . .	12
2.5	Minimal models describing the squeal excitation mechanisms. . . . .	14
2.6	Characteristics of different friction modifiers. . . . .	16
2.7	Examples of wheel damping treatments. . . . .	18
3.1	Typical structure of a model for curve squeal . . . . .	19
3.2	Conformal and non-conformal contact of wheel and rail. . . . .	27
3.3	Stick and slip in the contact area: displacements and tractions. . . . .	29
3.4	Wheel/rail contact-force time history during squeal. . . . .	31
3.5	Variation of contact variables in the contact area. . . . .	33
3.6	Typical structure of a rolling contact model. . . . .	34
3.7	Creepage-force relationship: Carter and linear Kalker. . . . .	37
4.1	Structure of the engineering model for squeal. . . . .	41
4.2	Schematic of the model extension to two-point wheel/rail contact. . . . .	42
4.3	Coordinate systems and wheel/rail contact-forces definition. . . . .	44
4.4	Coordinate systems for non-zero contact angle. . . . .	45
4.5	Coordinate transformation in the curve squeal model. . . . .	45
4.6	Contact force components in the global coordinate system. . . . .	46
4.7	Cross-section of the wheel and rail: one-point contact. . . . .	47
4.8	Cross-section of the wheel and rail: two-point contact. . . . .	48
4.9	S1002 wheel and UIC60 rail profiles in two-point contact. . . . .	49
4.10	Cross-section of the C20 wheel with the FE model mesh. . . . .	53
4.11	Receptances of the C20 wheel: one-point wheel/rail contact. . . . .	55
4.12	Receptances of the C20 wheel: two-point wheel/rail contact. . . . .	56
4.13	Cross-section of the BV50 rail with the FE model mesh. . . . .	58
4.14	Receptances of the BV50 rail: one-point wheel/rail contact. . . . .	59
4.15	Receptances of the BV50 rail: two-point wheel/rail contact. . . . .	60
4.16	Kinematics of two non-conformal surfaces in contact. . . . .	62
4.17	Discretisation of the potential contact area. . . . .	64

4.18	Contact area: discretisation and global-contact consideration. . . . .	66
4.19	Influence of tangential contact compliance on the lateral force. . . . .	69
4.20	Local and global friction models. . . . .	70
4.21	Examples of regularised friction curves. . . . .	71
4.22	Regularised friction curves for different spin creepage values. . . . .	72
4.23	Stick/slip distribution: $\Delta y^{WR} = -15$ mm, $\gamma_\omega = 0.5$ rad/m. . . . .	73
4.24	Contact area shapes of the one-point-contact cases. . . . .	74
4.25	Railway wheel cross-section: motions and dimensions. . . . .	75
4.26	Cross-section nodes and axial surfaces of the C20 wheel. . . . .	78
4.27	Boundary element model of the C20 wheel. . . . .	80
5.1	Lateral surface-velocity fields for selected C20 wheel modes. . . . .	82
5.2	Sound-radiation model validation: $\Delta L_W$ , lateral unit force. . . . .	83
5.3	Sound-radiation model validation: $\Delta L_W$ , radial unit force. . . . .	83
5.4	Squeal case: contact force amplitude spectra. . . . .	84
5.5	Sound radiation model validation: squeal-case results. . . . .	84
5.6	Contact-model validation procedure: imposed creepage. . . . .	86
5.7	Contact-model validation results: imposed creepage. . . . .	87
5.8	Wheel-receptance examples with a single mode included. . . . .	88
5.9	Contact-model dynamic-validation results: lateral force. . . . .	89
5.10	Contact-model dynamic-validation results: sound power. . . . .	90
5.11	Contact-model dynamic-validation results: $F_y$ spectrum detail. . . . .	91
5.12	Contact-model dynamic-validation: additional case. . . . .	92
5.13	Spin-extension validation: $\Delta y^{WR} = -5$ mm contact case. . . . .	94
5.14	Spin-extension validation: $\Delta y^{WR} = -10$ mm contact case. . . . .	94
5.15	Spin-extension validation: $\Delta y^{WR} = -15$ mm contact case. . . . .	95
6.1	Creepage/friction study results: $\Delta y^{WR} = -5$ mm. . . . .	99
6.2	Creepage/friction study results: $\Delta y^{WR} = -10$ mm. . . . .	100
6.3	Creepage/friction study: force-amplitude spectrum detail. . . . .	101
6.4	Creepage/friction study results: $\Delta y^{WR} = -15$ mm. . . . .	102
6.5	Creepage/friction study: simulation case detail. . . . .	103
6.6	Stick/slip distribution: $\Delta y^{WR} = -15$ mm, $\mu = [0.3 \ 0.6]$ . . . . .	104
6.7	Procedure of the wheel modal damping study. . . . .	105
6.8	Modal damping study results: case $\mu = 0.25$ , $\gamma_y = -0.012$ . . . . .	107
6.9	Modal damping study results: case $\mu = 0.25$ , $\gamma_y = -0.04$ . . . . .	107
6.10	Modal damping study results: case $\mu = 0.4$ , $\gamma_y = -0.012$ . . . . .	108
6.11	Modal damping study results: case $\mu = 0.4$ , $\gamma_y = -0.04$ . . . . .	108
6.12	Modal damping study results: case $\mu = 0.6$ , $\gamma_y = -0.012$ . . . . .	109
6.13	Modal damping study results: case $\mu = 0.6$ , $\gamma_y = -0.04$ . . . . .	109
6.14	Spin study results for the $\Delta y^{WR} = -5$ mm contact case. . . . .	112
6.15	Spin study results for the $\Delta y^{WR} = -10$ mm contact case. . . . .	112
6.16	Spin study results for the $\Delta y^{WR} = -15$ mm contact case. . . . .	113
6.17	Regularised friction curves for different spin creepage values. . . . .	113

---

6.18	Contact angle study results: $\Delta y^{\text{WR}} = -5$ mm, $\Delta y^{\text{WR}} = -15$ mm. . .	115
6.19	Contact angle study results: $\Delta y^{\text{WR}} = -10$ mm. . . . .	115
6.20	Combined angle-spin study results: $\Delta y^{\text{WR}} = -5$ mm. . . . .	118
6.21	Combined angle-spin study results: $\Delta y^{\text{WR}} = -10$ mm. . . . .	118
6.22	Combined angle-spin study results: $\Delta y^{\text{WR}} = -15$ mm. . . . .	119
6.23	Lateral contact force time-history detail. . . . .	119
7.1	Shape and size of contacts <i>cp1</i> and <i>cp2</i> . . . . .	123
7.2	Two-point-contact case: lateral force time-history. . . . .	124
7.3	Two-point-contact case: lateral force time-history, a detail. . . . .	125
7.4	Radiated sound power spectrum of the two-point-contact case. . . . .	126
7.5	Lateral contact force in one-point-contact cases. . . . .	127



# List of Tables

4.1	Eigenfrequencies and modes of the C20 wheel. . . . .	54
5.1	Wheel modes used in the sound-radiation-model validation. . . . .	82
5.2	Contact-model dynamic-validation results: numeric values. . . . .	89
5.3	Contact-model dynamic-validation results: additional case. . . . .	92
6.1	Squeal cases used in the wheel modal damping study. . . . .	106
6.2	Modal damping study results: succession of excited modes. . . . .	110
6.3	Spin creepage values for different values of the contact angle. . . . .	117
7.1	Two-point wheel/rail contact: squeal-case parameters. . . . .	122
7.2	Numerical results of the two-point-contact case. . . . .	126



# Chapter 1

## Introduction

---

### 1.1 Background

Railways are nowadays considered as one of the most efficient means of transportation of both people and material. They are also regarded as an environmentally friendly means of transportation because of their low CO<sub>2</sub> emission levels. Railways are responsible for 0.1% of greenhouse gas emissions (year 2015 levels) in the 28 European Union member states and Iceland (EU-28+ISL) [3], while accounting for 11.7% of transported goods (year 2014) [32]. Moreover, CO<sub>2</sub> emission levels from railways have decreased by 54% between the years 1990 and 2015 [3]. In comparison, road transport accounts for 21% of greenhouse gas emissions [3] and 49% of freight transport volume [32]. Approximately five times more goods are transported via road than via rail. At the same time, emissions from railways are negligible compared to road transport since railway emissions are roughly 200 times lower. Railways can therefore indeed be considered as environmentally friendly.

Compared to the emission of greenhouse gases, noise pollution is not often publicly discussed. However, the concern of noise impact on public health is rising, and noise pollution is being considered more often [1, 77]. Tram lines, suburban railways and metro systems all regularly traffic in highly populated urban areas. They result in high noise pollution that affects a significant portion of the urban population. With the increase of urban population and rail transport, awareness of railway noise has significantly increased. This higher awareness influences the operation of existing railway systems and development of new ones.

Awareness has been on the rise since the 1960s, along with the amount of conducted research [100]. Research provided many insights into the mechanisms behind railway noise and measures used to mitigate it. Still, treatment of specific railway noise issues is complaint-driven and case-specific [2].

The overall operating costs of railways increase with the addition of noise mitigation measures. This increase is driven further by the fact that different noise sources

require different measures. The most important sources of railway noise caused by forces from the wheel/rail contact are rolling noise, curve squeal and impact noise. They are usually referred to as wheel/rail noise and are significant noise sources in a broad range of vehicle speeds. Other sources of railway noise include aerodynamic noise (high speeds), power unit noise (low speeds) and ground-borne noise. Despite the fact that different wheel/rail noise types originate from the same area, their nature is very different. There is no universal solution for the mitigation of wheel/rail noise, and each source has to be approached differently.

In curve squeal and rolling noise, contact forces excite the wheel and rail, which are the main sound radiators. Rolling noise is the most common type of wheel/rail noise. The vertical force oscillation develops due to wheel and rail roughness. This force then excites the wheel and track into vibration, which results in sound radiation, see Figure 1.1. This source of railway noise is well investigated, and effective mitigation measures exist. Rail grinding, wheel re-profiling and rail and wheel dampers are all effective mitigation measures for rolling noise [2, 100].

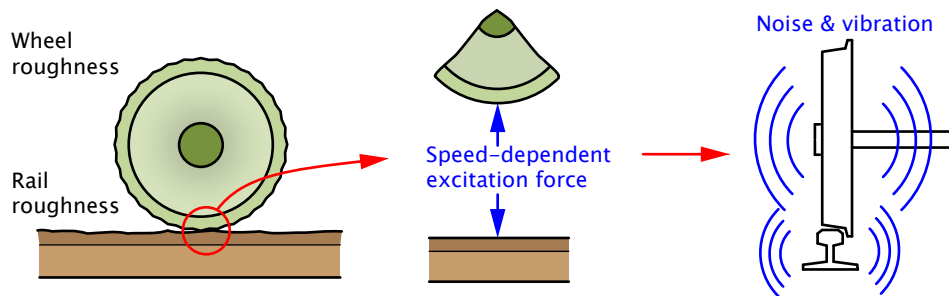


Figure 1.1: Generation of rolling noise from wheel and rail roughness [2].

Compared to rolling noise, which is present as long as the vehicle is moving, curve squeal noise originates at discrete locations along the track. Curve squeal is the consequence of a combination of tangential wheel/rail contact phenomena, wheel/rail dynamics and the vehicle behaviour during curve negotiation. Significant research has been conducted on this topic, although many questions regarding the excitation mechanisms and conditions leading to squeal are still open. Mitigation measures like track lubrication, friction-modifier application, wheel dampers and special bogie designs were used with mixed results [2]. The application of friction modifiers is a common and often efficient means of squeal mitigation. However, it is related to relatively high costs of implementation and requires regular maintenance. Additionally, the use of friction modifiers may also have a negative environmental impact (ground pollution) and impair braking performance.

Mitigation of railway noise is becoming increasingly important for railway vehicle and component manufacturers, infrastructure administrators and traffic operators. When devising and implementing mitigation measures, the sustainability aspect should be considered as well. This is something neither simply nor often done. Mitigation measures should be implemented in the design phase of new vehicles and tracks, instead of being implemented on a complaint-driven case-specific base. For

this purpose, manufacturers have to be provided with simulation tools to verify their designs. Such tools will also give the manufacturers opportunity to develop a better understanding of railway noise.

TWINS [102, 103] is a commercial tool used for prediction of radiated sound from railways. The tool is suitable for rolling noise computations with limited applicability to curve squeal. Despite the existence of several models for curve squeal, commercial tools for its prediction are virtually non-existent. Three main reasons for this can be identified. Firstly, many uncertainties related to the curve squeal phenomenon still exist. Questions are present about the exact mechanism responsible for squeal, conditions leading to its development and influencing parameters. Secondly, the target group for such a tool is rather limited. Finally, current legislation is not concerned with the tonality of railway noise. In the case of curve squeal, its tonal nature is what makes it very disturbing.

Once the legislative policymakers start imposing limits on squeal noise levels and its tonal content, simulation tools for curve squeal will become a necessity. It is, therefore, worthwhile to work towards a prediction tool for curve squeal, which can be used in engineering practice and is applicable to a broad range of cases. The same is true for the development of a better understanding of squeal, its generation mechanisms and influencing parameters. Also, squeal amplitudes are especially interesting since they enable the judgement of squeal severity. Only simulation tools formulated in the time domain can determine squeal amplitudes.

## 1.2 Aim and scope of the thesis

This thesis aims at developing a computationally fast time-domain model for curve squeal, which is suitable for practical engineering use. The model aims at covering a broad range of real-case scenarios with the ability to determine squeal amplitudes. Particular interest lies in the wheel/rail rolling-contact model and the required level of modelling detail. Apart from the model formulation, efforts are put into the investigation of parameters that influence curve squeal.

The engineering model for squeal is based on the time-domain wheel/rail interaction model developed by Pieringer [80, 81]. An efficient tangential contact model is formulated and implemented in the interaction model. The squeal model is then extended with an existing model for sound radiation from the railway wheel developed by Thompson and Jones [102, 104]. These form the core of the engineering model for curve squeal.

Contact models differ in their level of modelling detail, intended use, properties and computational costs. Particular emphasis is put on the contact modelling approach, including the definition of contact variables. The friction model and the contact stiffness are rigorously defined in the proposed contact model. This is of highest importance if different contact models are used to describe the same phenomenon. Different models have to describe the same physical properties of the contact. However, the formulation of properties can differ between models. In that

case, the different formulations must have a rigorous relationship in order to describe the same physical property.

In the engineering model, the friction model is formulated so that it includes the effects of spin creepage. Two extensions were made to both the engineering model developed in this thesis and the detailed model developed by Pieringer [81]. Firstly, the influence of the contact angle is included in the models. Secondly, and more importantly, the models are extended to cases with two-point wheel/rail contact. To the knowledge of the author, no other complete time-domain model for curve squeal that can consider two-point wheel/rail contact exists.

Curve squeal is a complex phenomenon and, owing to its high nonlinearity, small variations in kinematic, dynamic or material parameters can lead to significantly different results. This is investigated in several parameter studies. Finally, a two-point wheel/rail contact case is analysed with the aim to show how the interaction of the two contact points can lead to squeal. All performed studies and analyses indicate that curve squeal is a complex phenomenon with many influencing parameters.

Several simplifications and assumptions limit the proposed model. Firstly, the wheel and the rail surface roughness are not considered in the model. Secondly, curving is considered to be steady-state, meaning that the kinematic variables of the wheelset do not change throughout the curve. Friction properties are constant along the track as well. Thirdly, the wheel and rail models are linear. In the contact model, the wheel and rail are also linear and are locally represented with elastic half-spaces. Finally, the model includes only one suspended wheel and one continuously supported rail.

### 1.3 Outline

The thesis is divided into seven parts as follows.

*Chapter 2* introduces the problem of curve squeal. A general characterisation of the problem is given, along with a discussion of the conditions leading to squeal. The mechanisms considered to be responsible for squeal are discussed as well. Finally, the commonly used mitigation measures for curve squeal are described. The aim of this chapter to point out the still incomplete understanding of curve squeal and give the motivation for further research. In general, *Chapter 2* introduces basic concepts and the terminology used in later chapters.

*Chapter 3* gives a review of existing models for curve squeal. Particular attention is given to the classification of squeal models into time-domain and frequency-domain models, with a greater emphasis on time-domain models. Models for the rolling contact are also reviewed because of their importance in the squeal model. Additionally, the conditions present in the contact area during squeal are discussed.

The engineering model for curve squeal is elaborated in *Chapter 4*. The model covers the complete chain from source to radiated sound power. Individual parts of the model are explained in detail, with emphasis on the contact model formulation. Of special interest are the formulation of the friction model and the extension to

two-point wheel/rail contact.

Validations of the sound-radiation-model implementation and the rolling-contact model are presented in *Chapter 5*. The validation is numerical, i.e. the implemented and proposed models are validated against reference models. The implementation of the simple model for sound radiation is validated first, followed by the detailed validation of the contact model. A two-fold approach is proposed for validating the contact model. This approach gives more relevant information about the applicability of a contact model for simulations of curve squeal. A separate section covers the validation of the engineering model extended to non-zero spin creepage.

*Chapter 6* presents the application of the engineering model to parameter studies. The investigated parameters are lateral creepage, wheel/rail contact position, wheel/rail friction, wheel modal damping, contact angle and spin creepage. Besides being a showcase for the engineering model, these studies provide an insight into the influencing parameters of curve squeal.

*Chapter 7* presents the results of a two-point wheel/rail contact case. The case was analysed using the extended models for curve squeal. This chapter aims at pointing out the importance of considering two-point wheel/rail contact in the models. Two-point-contact results are compared to corresponding one-point wheel/rail contact results. Possibilities of simplifying two-point-contact cases to one-point contact are discussed, as is the dynamic interaction between the two contact points.

Finally, *Chapter 8* summarises the conclusions and suggests directions for future work.



# Chapter 2

## On curve squeal

---

### 2.1 The phenomenon of curve squeal

Curve squeal is a strong tonal noise that may occur when a railway vehicle negotiates a relatively tight curve. The definition of a tight curve depends on the vehicle bogie wheelbase. According to Rudd [90] and Remington [89], the curve radius/bogie wheelbase ratio  $R/W$  is a good indicator whether squeal can be expected. If  $R/W < 100$ , the likelihood of squeal is high. However, this rule is not universal, and squeal can be encountered even for  $R/W$  ratios higher than 100. Thompson [100] gives a practical guideline for the expectancy of squeal based on the curve radius:

$R \geq 500$ m,	mostly no squeal;
$200 \text{ m} < R < 500$ m,	sporadic occurrence;
$R \leq 200$ m,	common occurrence.

The guidelines above are rather rough and approximate. Squeal occurrence depends on a large number of parameters, and in particular on the vehicle curving performance. Consequently, the definition of a tight and squeal-prone curve depends on both the vehicle and the curve.

During squeal events, a single frequency (tone) dominates the radiated sound. Main tones of curve squeal are found in the frequency range 250 Hz - 5 kHz [37, 77, 100, 105], sometimes even higher [6, 35] and up to 10 kHz [110]. The combination of the tonal nature and sound pressure levels of up to 130 dB at 0.9 m from the wheel [90] make squeal one of the loudest and most disturbing types of railway noise. Additionally, the high number of tight curves in cities and urban areas leads to a significant portion of the urban population being exposed to curve squeal. Squeal can, therefore, be considered a potential hazard to public health.

The tonal nature of squeal is related to the dynamics of the railway wheel. Frequencies observed during squeal events mainly correspond to eigenfrequencies of axial wheel modes with zero nodal circles [60, 105, 110]. In certain cases even radial

and circumferential modes were observed excited into squeal [35, 105]. However, these observations may be related to phenomena other than curve squeal, e.g. flange squeal. Besides the excited wheel mode eigenfrequency, frequencies corresponding to higher harmonics of the excited mode are often observed. These observations point to the nonlinear nature of squeal [37]. Moreover, the close match between squeal frequencies and wheel eigenfrequencies points to the importance of the wheel dynamics. The higher vibration response of the wheel compared to that of the rail [110], together with its high sound radiation efficiency [100, 104] make the wheel a critical factor in curve squeal.

To develop and sustain self-excited vibrations responsible for curve squeal the wheel/rail vibrating system needs an energy input. It is recognised that this comes from the relative motion between the wheel and rail during curving. Rudd [90] distinguished between three different energy sources, calling them “*models for the mechanism of wheel squeal*”:

1. Flange rubbing;
2. Differential longitudinal slip;
3. Lateral creepage.

Remington [89] also referred to these energy sources as mechanisms. In the present work, they are referred to exclusively as energy sources since they primarily provide the input energy to the vibrating system. The case of flange rubbing should be considered separately because, besides being a separate energy source, it can also result in a phenomenon different than curve squeal. Mechanisms responsible for the development of squeal are discussed in Section 2.2.

Energy inputs by flange rubbing and differential longitudinal slip were discredited as causes of curve squeal by field observations and laboratory measurements [60, 89]. Experiments on a twin-disc rig, performed by Monk-Steel et al. [72] have even shown that the presence of longitudinal creepage reduces squeal. However, recent field measurements performed by Fourie et al. [34, 35] indicate that squeal in large radius curves ( $R \approx 1000$  m) can be caused by longitudinal creepage. In their measurements, Fourie et al. found that the squealing curve-inner wheel of the trailing wheelset of a freight wagon developed only longitudinal creepage. They argue that the combination of high longitudinal creepage, leading to contact-force saturation, and its unsteady behaviour led to squeal. This finding relates to a specific curving case and points out that squeal can arise under seemingly very different conditions. In the case of tight curves, lateral creepage is still considered as the primary energy source during squeal.

Creepage is defined as the relative velocity between the wheel and the rail at the contact point normalised with the rolling (vehicle) velocity  $v$ . Three types of creepage are observed in the wheel/rail contact area: longitudinal ( $\gamma_x$ ), lateral ( $\gamma_y$ )

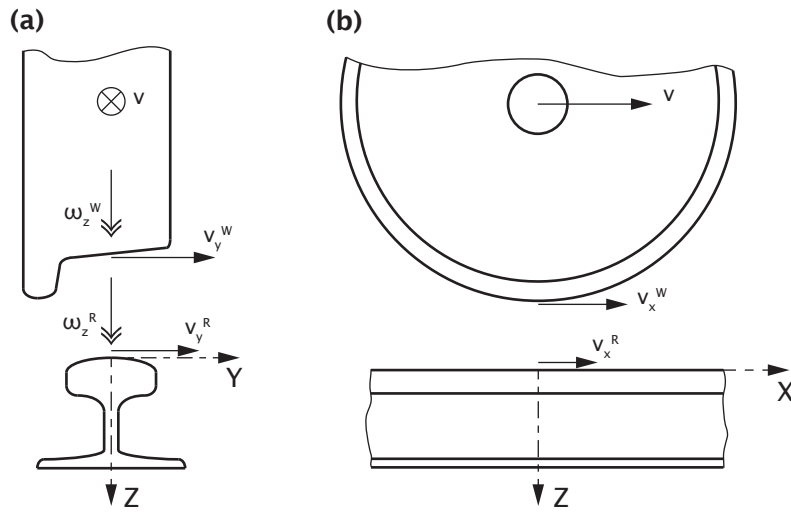


Figure 2.1: Relative velocities between the wheel and the rail: (a) lateral velocities; (b) longitudinal velocities.

and spin creepage ( $\gamma_\omega$ ). They are defined as:

$$\gamma_x = \frac{v_x^W - v_x^R}{v}, \quad (2.1)$$

$$\gamma_y = \frac{v_y^W - v_y^R}{v}, \quad (2.2)$$

$$\gamma_\omega = \frac{\omega_z^W - \omega_z^R}{v}. \quad (2.3)$$

The relative rail (superscript index  $R$ ) and wheel (superscript index  $W$ ) velocities are defined in Figure 2.1. Creepages are defined in the local coordinate system  $xyz$  of the contact, which generally differs from the global coordinate system  $XYZ$ . In Figure 2.1 the two coordinate systems are coincident. A detailed discussion of the coordinate systems is given in Section 4.1.

Longitudinal creepage arises in cases of braking, acceleration and due to differential slip during curve negotiation of rigid wheelsets (rigid connection between the left and the right wheel). Spin creepage is a consequence of a non-zero wheel/rail contact angle and vehicle yaw velocity during curving [9]. Finally, lateral creepage arises mainly during curve negotiation when the wheel forms an angle of attack (yaw angle) relative to the rail in the travel direction, see Figures 2.2 (a) and 2.3. Both the lateral and the longitudinal creepage are directly related to the contact forces required for acceleration, braking and curving.

In contrast to longitudinal and lateral creepage, spin creepage can be looked upon as a side effect of wheel/rail geometry and vehicle curving performance. In the context of curve squeal, spin creepage is not considered an energy input that sustains curve squeal. Still, spin influences squeal amplitudes by influencing the process in the contact area [122] and is, therefore, considered as a parameter influencing curve squeal.

Common to both real and simulated squeal cases is that a creepage is high enough for the tangential contact force to be near or at saturation. This is what the general guidelines for squeal expectancy from the beginning of this section predict: under which conditions does enough creepage develop for the contact to reach saturation. When the force is near or at saturation, the contact area is near or in the full slip condition. As will be discussed in Section 3.2.1, this constitutes a starting point for the development of self-excited vibrations [19, 88].

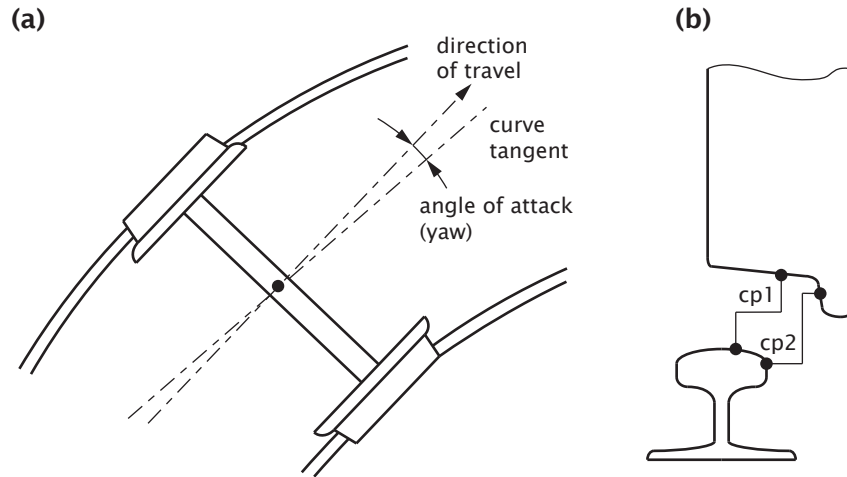


Figure 2.2: Wheelset angle of attack (a) and two-point wheel/rail contact (b).

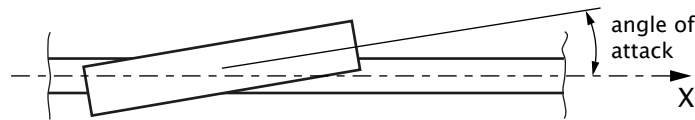


Figure 2.3: The wheel/rail angle of attack, detail.

The discussion above shows that the vehicle curving performance has a high influence on the energy input to the wheel/rail system. During the negotiation of a tight curve, the front wheelset of the leading vehicle bogie develops the largest angle of attack towards the rail. The angle of attack and, consequently, the value of lateral creepage depend on the vehicle curving performance, speed and curve radius. In a tight curve, the front wheelset tends to run under-radially, as shown in Figure 2.2 (a). The outer wheel tends towards flange contact, while the inner wheel contact occurs between the wheel tread and the rail head. At higher speed, the wheelset is pushed further outwards by centrifugal forces. High lateral creepage and the location of the contact make the inner wheel particularly susceptible to squeal [100].

Squeal was occasionally observed on the curve-outer wheel as well [26, 37, 97]. As explained above, the curve-outer wheel tends to be in contact close to or at the flange. Depending on the wheel and rail profiles, two-point contact between wheel and rail may exist. The typical situation in two-point contact is the presence of one contact

point between the wheel tread and the rail head and the other between the wheel flange and the rail gauge corner. This situation is shown in Figure 2.2 (b). Squeal in the presence of two-point wheel/rail contact was observed in [26, 97]. Recent field observations from Australia [50], show that the occurrence of squeal increased after rail grinding. Grinding restored the rail profile and caused the occurrence of two-point contact. Flange contact and two-point contact may contribute to squeal, but conclusive evidence and detailed investigations are lacking.

Besides the described kinematic parameters, curve squeal was found to be strongly influenced by wheel/rail friction properties [89]. The root of this influence comes from the contact, which couples the wheel and rail dynamics. In this coupling, the friction law influences the relationship between vertical and tangential forces. Moreover, it can also introduce negative damping in the wheel/rail system [90].

The contact angle is another parameter that influences the relation between vertical and lateral excitation forces. The contact angle is a function of the wheel and rail profiles at the contact location, and as such can be treated as constant during steady-state curving. Since it influences the relationship between vertical and lateral forces, the contact angle may have a significant influence on squeal [122]. The contact angle was usually neglected in squeal simulations with contact between the wheel tread and the rail head [81, 121]. In that case, the angle is very small, but for contact near or at the wheel flange, the contact angle is significant and cannot be neglected.

The contact angle and spin creepage are kinematically related, and both become significant in value at the curve-outer wheel/rail contact. This further complicates the simulations and root-cause analyses of curve squeal cases occurring on curve-outer wheels. The complexity of two-point wheel/rail contact and the much larger parameter space may explain why this phenomenon remains largely uninvestigated.

The parameters influencing squeal can be classified into three groups [110]:

1. Local kinematic parameters of the wheel/rail contact;
2. Contact-friction law;
3. Wheel modal parameters.

Each group is related to a specific rail vehicle property or environmental factor. As discussed, local kinematic parameters are related to the vehicle curving performance, track geometry and wheel/rail profiles. The friction law is influenced by the material and surface conditions of the wheel and rail, weather conditions, track pollutants and possible lubrication. Finally, wheel modal parameters depend on the wheel design, material, degree of wear and, if implemented, damping treatments/solutions.

Due to the large number of factors influencing curve squeal [2], many researchers found squeal to be an erratic phenomenon strongly influenced by small variations of operating and weather conditions [37, 89, 110]. Repeatability of measurements can also be an issue and a significant scatter of measured data is observed [89, 105]. Sometimes, squeal seems to be related to specific trains [37]. Even trains of the

same type can show different squeal behaviour, possibly due to different curving performance and different wheel profiles in the worn state. The possibility of varying conditions along the curve complicates matters further.

The discussion given above shows the presence of a high level of uncertainty around the squeal phenomenon. Despite the fact that significant research has been performed on curve squeal, no conclusive evidence exists about the exact conditions and excitation mechanisms behind squeal. As will be seen from the results presented in this thesis, curve squeal is a nonlinear phenomenon. Each parameter influences both the occurrence and amplitudes of squeal, with sometimes unexpected results. The following section discusses the excitation mechanisms held responsible for squeal development in more detail. This creates a foundation for a further discussion of existing squeal models and mitigation measures.

## 2.2 Mechanisms responsible for curve squeal

As discussed in Section 2.1, curve squeal is a phenomenon in which the wheel and rail dynamics, wheel/rail contact mechanics and friction law interplay and result in unstable vibrations. These self-induced vibrations with lateral creepage as the energy source are the result of nonlinearities present in the wheel/rail system. Non-linearities are present in the wheel/rail contact, but the contact itself is not enough for the development of self-induced vibrations. For squeal to develop and persist, an additional mechanism is needed. The two most discussed excitation mechanisms are the falling friction law and the geometric coupling.

### 2.2.1 Falling friction law

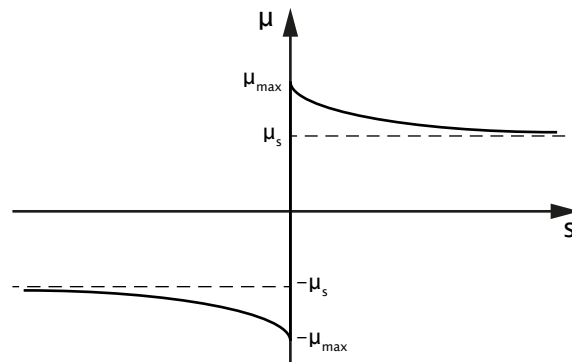


Figure 2.4: Example of a slip-velocity dependent friction law with decreasing friction value for increasing slip velocity.

The wheel/rail friction coefficient is, generally, a function of slip velocity. Slip is a contact variable defined as the relative velocity between the contact surfaces at the contact point. It includes contributions from creepage and the wheel/rail dynamic

response. In falling friction, the friction curve has a negative slope for increasing slip. This was identified by Rudd [90] as the mechanism responsible for curve squeal. Figure 2.4 shows the typical shape of a falling friction curve. Similar curves were observed from wheel/rail friction measurements [61, 87, 89].

A minimal model able to describe the falling-friction excitation mechanism is shown in Figure 2.5 (a). Since the source of instability comes from the frictional contact between two bodies, a simple mass-spring system is sufficient to describe the phenomenon. The mass is in contact with a slider, and the excitation force is related to the sliding velocity via the falling friction curve  $\mu(s)$ . The restorative force is provided by the spring.

The decrease in friction has a direct consequence on the development of stick-slip. Sliding between wheel and rail occurs when the tangential force reaches the friction limit  $\mu_{max}F_3$ , where  $F_3$  is the normal contact force and  $\mu_{max}$  is the maximum friction value, see in Figure 2.4. The friction coefficient value decreases with increasing slip velocity, causing a reduction in the tangential contact force. Sliding continues until the sum of elastic and inertial forces of the wheel/rail system in the contact drops below the instantaneous friction force value. Stick between wheel and rail is then re-established and the force builds up until again reaching its limit value. This process repeats with a frequency mainly determined by the wheel dynamics.

The falling friction law was mathematically interpreted by Rudd [90] as negative damping. The negative slope of the friction curve is responsible for feeding energy into the system during each period of vibration. This results in self-induced and self-sustained vibrations of the wheel and rail, which persist as long as there is an external source of energy, i.e. lateral creepage during curve negotiation.

A detailed description and discussion of the falling-friction excitation mechanism are out of the scope of this thesis. A more detailed overview of the falling-friction mechanism can be found in [90, 100, 105].

## 2.2.2 Geometric coupling of wheel modes

Geometric coupling between the degrees of freedom of the system is another mechanism that can lead to the development of stick-slip motion. In geometric coupling, compared to the falling-friction mechanism, the wheel deformation pattern and mode shapes are responsible for the instability development. Geometric coupling is also known as dynamics coupling or modes coupling and is well investigated in the context of automotive disc-brake squeal [44, 95, 96].

Figure 2.5 shows the schematics of minimal models used to illustrate the mechanisms responsible for the stick-slip instability. The model layout depends on the excitation mechanism. In case of the falling-friction mechanism, Figure 2.5 (a), a single stiffness element and one degree of freedom are enough. The friction law between the mass and the sliding surface is responsible for the development of stick-slip, as discussed in Section 2.2.1.

In geometric coupling, Figure 2.5 (b), two stiffness elements and two degrees of freedom are needed to describe the coupling between the directions. Due to the

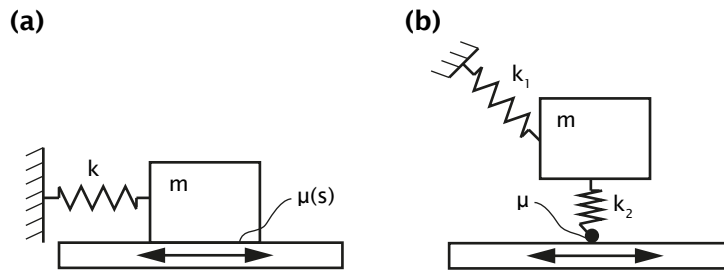


Figure 2.5: Schematics of minimal models used to illustrate the squeal excitation mechanisms [49]: (a) falling friction; (b) geometric coupling.

coupling, a vertical force causes both vertical and lateral displacement of the mass. The same can be stated for a lateral force. Additionally, friction couples the lateral and vertical forces, thereby further influencing the coupling. The friction coefficient influences the coupling strength and instability is expected to occur if friction is above a certain threshold value [49]. The geometric-coupling mechanism implies that stick-slip can also develop in cases with constant friction. This is supported by simulation results from Brunel [16], Glocker [37], Pieringer [81], Ding [29] and Fourie [34], and experimental evidence presented by Koch [60].

Regarding the railway wheel, sufficient vertical-lateral dynamics coupling may be present in a single mode shape. Sometimes coupling is the result of multiple modes with closely spaced eigenfrequencies. When combined, the mode shapes provide sufficient coupling for curve squeal development. The squeal frequency, in that case, usually lies between the mode eigenfrequencies. Glocker et al. [37] analysed a case where the combination of three modes with close eigenfrequencies was responsible for squeal development. Similarly, Ding et al. [29] found that at specific frequencies squeal would be the result of two closely spaced modes. By field measurements and experimental modal analyses of wheels, Fourie et al. [35] observed that the squeal case they investigated is most probably the result of two closely spaced wheel modes. This was confirmed in their subsequent work [34]. The exact number of required modes may depend on the wheel properties, friction and the wheel/rail contact position, which all influence the dynamics coupling strength.

While falling friction results in negative damping in the system equations, geometric coupling results in the asymmetry of the system stiffness matrix [75, 81]. Both terms, when appearing in system equations, can be used to mathematically explain the development of unstable behaviour.

Results and observations from Chiello [20], Glocker [37], Pieringer [81] and Ding [29] indicate the possibility that both excitation mechanisms may coexist in reality. Moreover, laboratory tests on a curve squeal rig performed by Liu and Meehan [67] show that squeal in some cases persists even though the falling friction curve was altered to a positive one. Liu and Meehan [67] raise the question whether the reason for the persistence of squeal lies within the instantaneous friction curve slope or the geometric-coupling mechanism. They argue that the instantaneous friction curve slope, as opposed to the average curve, can be negative due to transient processes

and temperature effects caused by high velocity and angle of attack values.

A general conclusion from the reviewed literature and, in particular, newer findings is that squeal is more often being considered as a result of both the falling friction and the geometric coupling. Typical examples are Liu and Meehan [67] and Ding et al. [29]. They both conclude, the former from laboratory test and the latter from simulations, that even if squeal does not occur due to falling friction, it may still arise due to geometric coupling. In practical terms, this means that a certain design or curving case should be evaluated for squeal against both excitation mechanisms.

## 2.3 Mitigation measures

Two groups of mitigation measures can be identified with respect to their working principle. The first group mitigates squeal by influencing the excitation mechanism responsible for squeal development. The second group reduces the input energy in the wheel/rail system. In practice, mitigation measures influence both the excitation mechanism and the input energy at the same time but to various degrees.

In the following section, mitigation measures are classified according to the location where the measure is implemented. Accordingly, infrastructure and rolling stock measures are identified.

### 2.3.1 Infrastructure measures

Infrastructure measures found in practice mainly aim at controlling friction, either by reducing it or changing the friction curve shape. Lubricants are used to reduce the friction value, which should not be too low and thus affect traction and braking performance [2]. Lubricants are, therefore, mainly applicable on the rail gauge corner and the wheel flange.

Control of the friction curve is carried out by application of friction modifiers. Their primary aim is to change the shape of the friction curve without reducing the friction coefficient. Figure 2.6 presents the general friction characteristics achievable by friction-modifier application. The negative slope of the friction curve is altered into either a neutral or a positive curve. Friction modifiers that do not impair braking performance are suitable for application on the rail head and wheel tread [2]. Modifiers are usually applied to reduce wheel/rail wear and rail corrugation in curves [2, 65]. They may also be an effective squeal mitigation measure in cases where squeal develops due to the falling-friction mechanism.

Field observations show mixed results in the case of friction modifier applications. Observations vary from squeal events of significantly shorter duration but similar overall noise levels, to events with significant attenuation of tonal components and overall noise levels [2]. Some field tests suggest a potential of friction modifiers to mitigate squeal and flanging noise [30, 31]. Other measurements, like the ones by Curley et al. [26] on Australian railway lines, show limited benefits. Laboratory tests

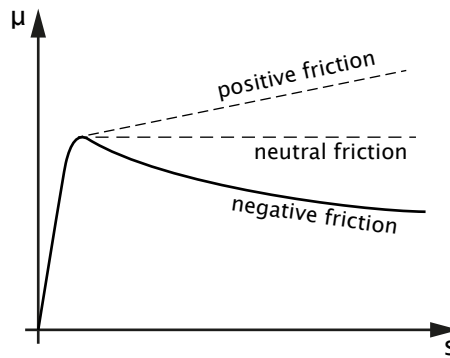


Figure 2.6: Characteristics of different friction modifiers. Adapted from [65].

on a curve squeal rig have also shown mixed results. Squeal was not eliminated in all cases, and in the case of an oil-based friction modifier, squeal became even more tonal [67].

In general, the use of friction modifiers does not guarantee complete mitigation of curve squeal. Besides their effectiveness, the environmental impact of friction modifiers is also questionable but rarely considered. With the approach to squeal on a complaint-driven basis [2], friction modifiers are often tested as a first solution. In cases where modifiers provide significant benefits, their application is followed by implementation and maintenance costs. Controlled field tests are essential when applying such a system to determine its effectiveness and optimal dosage under various weather conditions [2].

The discussion on friction modifiers is concluded with a note on the application of water as a modifier. Curve squeal was observed to occur less frequently during wet weather [100]. Application of water as a friction modifier was investigated in [76] and by Corradi et al. [23]. Promising results were observed, indicating that water may be an effective friction modifier that is both financially feasible and environmentally acceptable.

Rail gauge corner and wheel flange lubrication show promising results in cases where flange contact is present. Squeal on the Australian railway lines [26] was successfully mitigated by lubrication of the outer rail gauge face and gauge corner. However, the mechanism responsible for squeal in the Australian case is not completely clear. The possible presence of two-point wheel/rail contact at the curve-outer wheel may also be contributing to the development of squeal. Two-point contact significantly complicates analyses and may influence the excitation mechanism, i.e. the instability development.

Of other infrastructure measures, asymmetric rail profiles (used initially for reducing wear) and gauge narrowing can produce beneficial results [2, 100]. Tests with asymmetric rail profiles gave mixed results. In cases where improvements were observed, lower noise levels were measured, but the number of squeal events remained the same [2]. Tests with narrower track gauges have also shown some promising results [2, 100].

By implementing asymmetric rail profiles, the position of the contact on the wheel and the rail can be controlled. According to observations by de Beer et al. [27], the contact position influences the occurrence of squeal. Similarly, changes in the track gauge influence the contact position, but also the amount of lateral creepage, i.e. input energy. Whether a gauge narrowing or widening is preferable depends on the wheel design [105]. Asymmetric profiles and gauge changes can be used in combination to achieve a more favourable contact position and improve the curving behaviour. A change in contact position can be beneficial in cases of squeal caused by geometric coupling since the strength of the coupling depends on the contact location on the wheel tread. A reduction in input energy is beneficial for squeal caused by both excitation mechanisms.

Finally, another infrastructure measure is the installation of noise barriers for curve squeal, discussed in [92]. This is not a mitigation measure per se, as it does not mitigate squeal at the source. Noise barriers aim at obstructing the propagation of the noise radiated from a nearby source. They may even provide some sound absorption. In the case of squeal, the dominant source is the railway wheel. Setsobhonkul et al. [92] argue that noise barriers are financially feasible and efficient on short curves, but not feasible on long curves.

### 2.3.2 Rolling stock measures

Rolling stock measures include vehicle-mounted lubrication and/or friction modifier application systems, wheel dampers and special bogie designs. Lubrication and friction modifiers were already discussed in Section 2.3.1.

Special bogie designs are primarily used for improving the vehicle curving behaviour. As a consequence, lateral creepage is reduced, and a potentially more favourable wheel/rail contact position is achieved. A bogie allowing for greater yaw angles was found to reduce the likelihood of curve squeal [107]. Designs with steerable axles, independent wheel axles and active steering control are some of the available options [2, 100]. A limiting factor in the improvement of a vehicle curving performance is the requirement for high-speed stability. The two are in contradiction [9], meaning that compromises have to be made most of the time.

Wheel damping solutions were shown to be effective in reducing rolling noise, but are also useful in mitigating squeal [100]. Common wheel damping treatments include resilient wheels, constrained layer damping solutions, tuned absorbers, ring dampers and multi-material wheels [100, 105]. Figure 2.7 shows some examples of wheel damping treatments.

Damping reduces the wheel response amplitudes at resonances, which may have multiple effects on curve squeal. Damping reduces the response amplitudes, therefore, reducing the strength of the geometric coupling. In case of the falling-friction mechanism, the higher positive damping may overcome the negative damping induced by falling friction. Finally, even if the stick-slip instability is not mitigated, sound radiation from the wheel is reduced. Namely, the additional damping reduces amplitudes of the velocity field on the wheel surface.

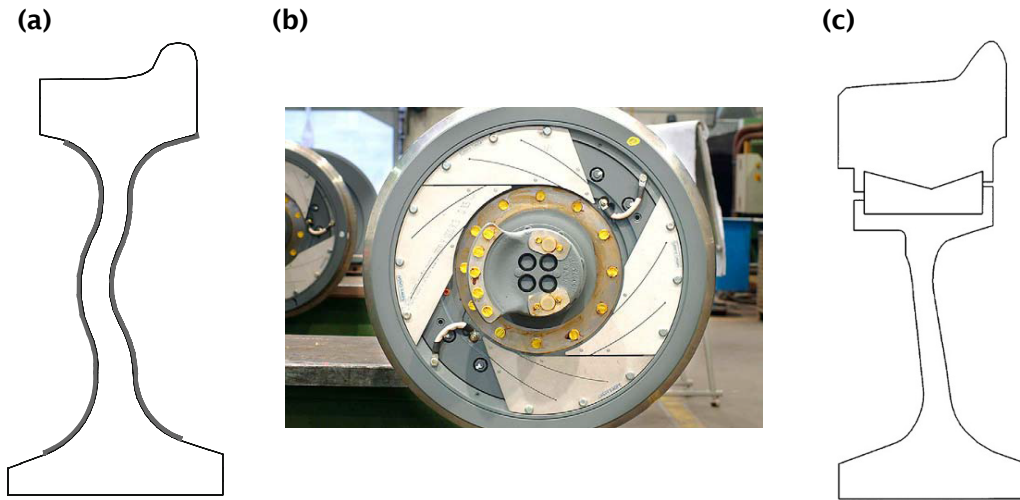


Figure 2.7: Examples of wheel damping treatments [100]: (a) constrained layer damping; (b) tuned absorber; (c) resilient wheel.

According to Thompson [100], small increases in wheel damping may be enough to eliminate squeal. Still, Squicciarini et al. [97] observed squeal on vehicles equipped with resilient wheels. This kind of wheels is supposed to be highly damped. However, two-point wheel/rail contact was present, which may be responsible for squeal development. Moreover, various practical cases were observed where wheel damping did not prevent squeal [2]. Cigada et al. [21] concluded that the use of resilient wheels to combat curve squeal is not expected to provide benefits. This conclusion is based on the vibroacoustic characterisation of a resilient wheel. Modes excited in squeal were not found to be sufficiently damped to eliminate squeal. This conclusion may hold for squeal caused by the falling-friction mechanism, but resilient wheels may still be beneficial in squeal caused by geometric coupling. Namely, Cigada et al. [21] found that they show a significantly weaker vertical-lateral dynamics coupling.

When damping is low, small variations in damping lead to high variations of the radiated sound, as shown by Merideño et al. [70] and in line with the earlier statement from Thompson [100]. When damping is high, variations in it do not affect the radiated sound significantly. An accurate determination of wheel damping values is, therefore, crucial for accurate predictions of squeal amplitudes.

In the discussion above, two different critical wheel damping values can be deduced. The first relates to the squeal generation mechanism and is the damping value at which squeal does not develop. The second relates to the attenuation of sound radiation from the wheel. Critical damping in the latter case should be defined in relation to a satisfactory attenuation of noise levels. Both damping values could be important in practice.

This section is concluded with a reference to Remington [89], who early identified the principal means for mitigating squeal. He recognised the importance of all parameters discussed above: wheel/rail friction, curving performance and wheel damping.

# Chapter 3

## Review of existing models

---

This chapter presents the review of models from the available literature. Firstly, the existing models for curve squeal are reviewed. The models are categorised according to the domain in which they operate: frequency or time domain.

Secondly, a review of wheel/rail rolling contact models is given. Types of contact occurring between wheel and rail are discussed, along with typical solution approaches. Specific contact conditions present during squeal are discussed as well. The general structure of a contact model is then presented, followed by the review of selected contact models.

### 3.1 Models for curve squeal

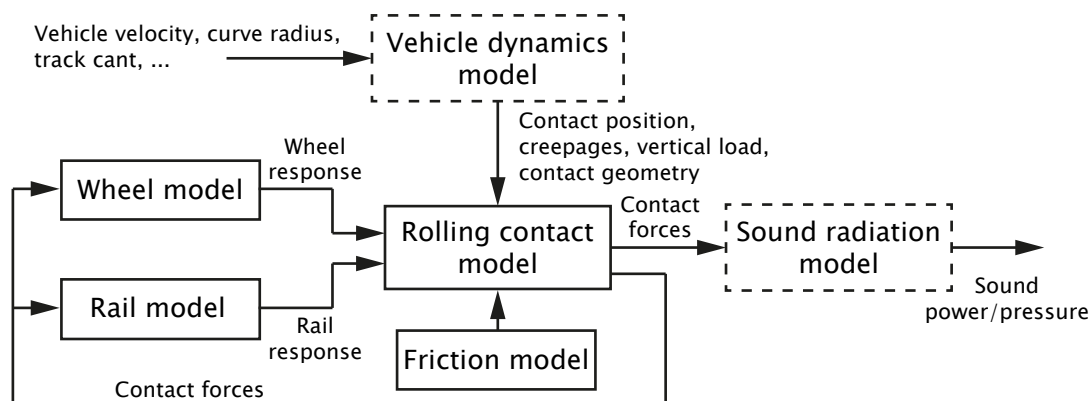


Figure 3.1: Typical structure of a model for curve squeal

The general structure of models for curve squeal is identified in Figure 3.1. The structure of the closed loop (formed by the wheel, rail and rolling contact) is independent of whether the model operates in the frequency or the time domain. Models typi-

cally consist of three or more sub-models where the most important are the wheel, the rail, and the rolling contact sub-models. Usually, the contact model includes the friction law. Some models are extended with the sound radiation sub-model, while others even include simulations of the vehicle curving behaviour.

A more in-depth insight into the state-of-the-art of curve squeal modelling can be found in the recent paper by Thompson et al. [105]. Thompson et al. review squeal models considering their level of modelling detail. They also discuss the excitation mechanisms, different squeal phenomena, measurements and mitigation measures.

### 3.1.1 Frequency-domain models

Frequency-domain models are obtained either from simple linear models of the wheel/rail system or by linearisation of nonlinear equations that describe more complex models. The formulation of the system governing equations depends on the level of modelling detail. The model formulation varies among the reviewed models. It is influenced by the wheel and rail models, contact modelling and the applied friction law.

With frequency-domain models, the system response is evaluated in the frequency range relevant for curve squeal. Potential squeal frequencies are obtained. They correspond to unstable wheel modes (falling-friction mechanism), or to a single frequency after modes couple and become unstable (geometric-coupling mechanism). Frequency-domain models are fast but unable to determine squeal amplitudes. They are, therefore, suitable for the systematic investigation of a wide range of parameters on the potential occurrence of squeal. In the reviewed literature, they are used to:

- determine the stability of wheels in the vehicle bogie, i.e. which wheels are prone to squeal [37, 71, 118];
- determine the stability of wheel modes, i.e. which modes are prone to squeal [6, 20, 41];
- determine the wheel damping required to eliminate or reduce squeal [90, 108];
- investigate the influence of kinematic parameters like rolling velocity [108], lateral contact position [27, 71], curve radius [90], longitudinal creepage [34] and presence of two wheel/rail contact points [97];
- investigate the relation between friction properties and squeal [45, 84].

One of the first models for curve squeal was developed by Rudd [90], further elaborating on the work of Stappenbeck [98]. Rudd considered the wheel as a single-degree-of-freedom system, which was described by its impedance at the contact point. The impedance was experimentally measured, and the dynamics in the lateral direction were considered. The rail dynamics were not included, which can be interpreted as if the rail was rigid.

Rudd considered a point contact on the wheel. At the contact point, the vertical and lateral forces are coupled by the falling friction law. This law adds a term in the governing equations, which Rudd [90] mathematically interpreted as negative damping. The negative damping term is the source of instability and, therefore, squeal, as discussed in Section 2.2.1.

A significant number of subsequent models were based on Rudd's approach. For example, van Ruiten [108] used Rudd's model to investigate the influence of rolling velocity and wheel damping on curve squeal. Van Ruiten's central question was how the occurrence of squeal can be controlled. To answer this question, he compared simulation results with measurements and, thus, validated Rudd's model [90].

Later frequency-domain models were inspired by Fingberg's time-domain model [33], see Section 3.1.2. Fingberg used three sub-models: the wheel, the rail and the contact. Following suit, de Beer et al. [27] developed a frequency-domain model containing the three sub-models. De Beer included the wheel and rail dynamics with mobilities obtained from the TWINS software [103, 102], along with the contact spring mobility. The falling-friction model was described using the friction law by Kraft [61], which is an analytical formulation of measured falling friction characteristics. The vertical, lateral and vertical-lateral coupling dynamics were considered. The inclusion of the coupling dynamics is a significant extension of the model. This coupling was included to investigate the influence of the normal force variation on squeal. The coupling dynamics were seen to have a significant influence on squeal frequencies. A particular importance of the lateral wheel/rail contact position was observed. Namely, the contact position influences the coupling dynamics. Nonetheless, de Beer et al. [27] concluded that falling friction is the main cause of squeal. Conclusions were based on stability analyses: the friction law was linearised, and stability was evaluated using the Nyquist criterion.

Monk-Steel et al. [71] took a similar approach to de Beer et al. [27]. The model by de Beer was extended to all three creepages to make it more general. The friction curve consists of two parts. The initial linear part was modelled with the model by Vermeulen and Johnson [109], while the falling friction part comes from Kraft's model [61]. The wheel and rail were included with mobilities obtained from their modal parameters. A finite element (FE) model of the wheel was used, while the rail was described using two models: one for the vertical dynamics and another for the lateral and torsional dynamics. Stability was determined using the Nyquist criterion.

Xie et al. [118] extended de Beer's model to include simulations of the vehicle curving behaviour in Simpack [5]. Kalker's FASTSIM [54] and the falling friction model from Gimenez et al. [36] were used for curving behaviour simulations. The friction model by Gimenez et al. is an adaptation of the model by Kraft [61] developed specifically for use within FASTSIM. This friction model stabilises the FASTSIM algorithm, which otherwise shows high instability when used in conjunction with a variable friction model [36]. The development of curve squeal for different curving cases and vehicles was then investigated using the model by de Beer et al. [27].

Huang [46] developed a model that includes the evaluation of the vehicle dynam-

ics during curving and implemented the frequency model by Monk-Steel et al. [71]. Additionally, Huang also developed a time-domain model discussed later on. Hsu et al. [45] used a variant of Huang's model. They simplified Huang's model by removing the variation of the normal contact force, and results were compared to test-rig measurements. Because the model was simplified, this can be considered only as a partial validation of Huang's model [46].

Heckl [41] developed a frequency-domain model from the time-domain model [42] described in Section 3.1.2. She developed the model to identify wheel modes susceptible to squeal. Unstable modes were identified from the analysis of complex eigenfrequencies obtained from the integro-differential equation of the linear system.

A more recent squeal model was developed by Fourie et al. [34] with the aim of investigating curve squeal in large radius curves caused by longitudinal creepage. The model consists of the wheel and rail FE models brought into contact. Contact is modelled with different normal and tangential contact springs. The tangential contact spring is used to represent the frictional work, where each spring-stiffness value corresponds to a particular wheel/rail friction value. The model considers squeal caused by the geometric-coupling mechanism and can determine unstable wheel modes. Squeal frequencies after mode-coupling are determined with the complex eigenvalue analysis carried out in a commercial FE analysis tool.

Wang et al. [117] also took a similar direction and developed a frequency-domain model in a commercial FE analysis tool. The stability of the wheel/rail system was evaluated using the complex eigenvalue analysis. Wang et al. investigated the influence of different parameters (friction, wheel rim thickness, lateral offset, lateral and longitudinal creepage) on curve squeal in the presence of constant friction.

The models by Fourie [34] and Wang [117] may not be reliable since a finite-length rail with free undamped ends is modelled. Without damping at the free ends and a with a relatively short rail, waves travelling along the rail are reflected from the ends and influence the response at the contact point. These reflections ultimately show as rail eigenmodes that do not exist in reality. In reality, the rail behaves like an infinitely long waveguide, and wave reflections do not occur.

Finally, a significant model for squeal was developed by Squicciarini et al. [97]. The frequency-domain model by Huang [46] was extended to account for two-point wheel/rail contact. This is a significant extension, as squeal was observed in conjunction with flange contact. Squicciarini included the wheel using its mobilities with wheel parameters tuned to match measurements. A resilient wheel was considered. The rail was modelled using the same approach as in Monk-Steel et al. [71]. Kalker's FASTSIM [54] was implemented to couple the wheel and rail, along with Kraft's falling friction model [61]. The system was then linearised and unstable frequencies determined for a defined parameter space. The same squeal model, but applied to one-point wheel/rail contact was used by Alfi [6].

### 3.1.2 Time-domain models

Time-domain models are capable of considering nonlinearities present in the wheel/rail system. Higher harmonic components in the system response can, therefore, also be determined. Moreover, time-domain models can determine the amplitudes of squeal, which are crucial for evaluating squeal severity.

Schneider and Popp's model [91] for curve squeal is among the first squeal models formulated in the time domain. The system response was determined from nonlinear differential equations that describe the system dynamics using a Runge-Kutta integration routine. While the rail was considered rigid, the wheel FE model was based on ring elements used to obtain the modal parameters. Modal transformation techniques were used in the determination of the wheel displacement response. The wheel/rail contact was treated as a point contact with friction described by Kraft's falling friction model [61]. Additionally, the radiated sound was evaluated using the Rayleigh integral for a baffled plate.

A subsequent model by Fingberg [33] included more elaborate wheel and rail models, a semi-transient rolling-contact model and evaluation of the radiated sound. The more elaborate wheel FE model included half of the wheelset. The rail was described using two models: one for the lateral dynamics and the other for the longitudinal dynamics. Modal expansion techniques were used to determine both the wheel and rail receptances. For the contact model, Fingberg [33] used Kalker's linear theory [53] extended with the first-order system of Knothe and Groß-Thebing [57]. The use of this semi-transient model was an attempt to take into account transient contact conditions present during squeal<sup>1</sup>. Kraft's friction law [61] was implemented.

Fingberg combined the boundary element method and modal expansion techniques to determine the radiated sound from the wheel. The contribution of each wheel mode to the radiated sound was evaluated separately. The partial contributions of wheel modes were then summed to obtain the overall radiated sound.

Periard [79] further extended Fingberg's model. The wheelset model was mainly retained, but a discretely supported rail was included. The rail dynamics were obtained from an FE model. Separate models were used for the sleepers and slabs, which were then assembled with the rail in a single track model. The track was, like the wheel, included with its system matrices. Moreover, two contact models with falling friction characteristics were used: Kalker's FASTSIM [54] and the theory from Vermeulen and Johnson [109]. To extend the model further, Periard included the evaluation of the vehicle curving behaviour in the same time-stepping loop. The radiated sound was evaluated using the Rayleigh integral. In the sound radiation model, the contribution of each mode to the overall sound was evaluated separately. This is a combination of Schneider's [91] and Fingberg's [33] approach to the evaluation of the radiated sound.

Sound radiation was also addressed in the squeal model by Huang et al. [46, 47]. He implemented the sound radiation model developed by Thompson and Jones [104],

---

<sup>1</sup>The mentioned contact model is not a fully transient model, see Section 3.2.3.

which uses an approach similar to Fingberg's [33]. Huang's model considered both wheel and rail with their mobilities in the lateral, vertical and longitudinal directions. The wheel/rail contact was solved using Kalker's FASTSIM [54]. Several falling friction models were used to account for the influence of different creepages on the lateral force. Huang's frequency-domain model [46] was discussed in Section 3.1.1.

Ding et al. [29] used the model by Huang [46] to investigate the influence of rail dynamics. The model [29] includes a frequency-domain stability analysis with a subsequent time-domain analysis of the unstable cases. The effect of having constant or falling friction was investigated as well.

In their model, Heckl and Abrahams [42] used convolution instead of a classical integration scheme to determine the system response. They modelled the wheel as a circular disc and obtained the Green's function (impulse response) from the superposition of the disc modes. Only the dynamics in the lateral direction were considered, and the rail was not included in the model. A point contact on the wheel, with a piecewise-linear falling friction characteristic, was implemented. The wheel response was then obtained by convolution of the contact force and the Green's function. From their time-domain model, Heckl also developed a frequency-domain model [41] described in Section 3.1.1.

Another analytical model for curve squeal was developed by Liu and Meehan [66, 69]. The model considers only the lateral dynamics and the falling-friction excitation mechanism. The wheel/rail system was modelled as a single-degree-of-freedom system. Liu and Meehan investigated the influences of rolling velocity, the angle of attack and the falling friction curve on squeal amplitudes. The squeal model was also validated against laboratory tests on a two-disc test rig.

Chiello et al. [20] used a combination of frequency and time-domain models. The stability analysis was carried out using the frequency-domain model, and the unstable cases were simulated in the time domain. The wheel was described with its modal parameters, while the rail was considered as rigid. The contact problem was modelled with a nonlinear exponential creep model [20]. A linearly falling friction model was implemented.

The governing equations in Chiello's model have an asymmetric stiffness matrix due to the coupling of the vertical and lateral dynamics. The coupling is, however, only present in the time-domain model. The frequency-domain model, on the other hand, only considers the falling-friction mechanism. Consequently, the model predicts squeal caused by the falling-friction mechanism but includes the dynamics coupling in time-domain computations of squeal cases. The authors argue that geometric coupling could be another possible source of instability, but in their case, they attribute squeal to the falling-friction mechanism.

Measurements in [60, 110] correlated well with the theoretical model of Chiello et al. [20]. However, the falling friction characteristic was not observed in measurements. This brought about the question of the friction model formulation. Chiello et al. argued that an instantaneous friction model (valid for high-frequency phenomena) may have a falling characteristic. With measurements only able to measure the average friction, which was constant, instantaneous friction cannot be obtained.

Transient phenomena in the contact area were held responsible for influencing the friction law. As a side note, Collette [22] has shown that squeal can occur with constant friction. He attributed the development of squeal to the variation in the normal force caused by the geometric coupling.

In contrast to Chiello's model, Brunel et al. [16] obtained squeal in cases with constant and falling friction. Brunel et al. developed an axi-symmetric FE model of the wheel. The excitation and displacements were defined as a Fourier series with harmonics associated with the number of nodal diameters of wheel modes. In the transient analysis, the final displacement field is obtained by summation of the Fourier series. The rail was not considered. Results have shown that squeal occurrence may be insensitive to the exact shape of the friction model. Even a positive friction curve could result in unstable behaviour. However, most severe squeal was associated with the falling friction curve.

The work of Glocker et al. [37] focused on squeal being the result of geometric coupling alone. They also argued that squeal is rather insensitive to the exact shape of the friction curve, as properties can change along the curve due to wear, surface irregularities and contamination. Moreover, Glocker et al. questioned whether the common understanding of stick-slip makes sense in the case of small displacements. Namely, the displacements of particles during stick-slip are in the order of the size of asperities, which in their opinion reduces the importance of the friction model. Instead, they focused on the wheel dynamics.

Similarly to Chiello et al. [20], Glocker et al. [37] also used a combination of frequency and time-domain models. The frequency-domain model was used to study the stability of wheels in a bogie, while the time-domain model was used to study the development of squeal in the time domain. The wheel was included with its mass and stiffness matrices obtained from an FE model. The rail was not considered. A point contact was assumed and modelled as a hard unilateral constraint with constant friction (Coulomb model). A suitable time-integration scheme was also developed.

Glocker et al. found that three wheel modes with closely spaced eigenfrequencies had to be present for curve squeal to develop. When combined, these modes show a strong coupling between the vertical and tangential degrees of freedom.

The time-domain models presented above assume steady-state conditions in the rolling contact or use certain approximations to include transient phenomena (for example Fingberg [33]). In contrast, by implementing Kalker's variational contact theory [55], Pieringer [80, 81] included the ability to consider transient contact phenomena in her model. Kalker's variational contact theory [55] is a three-dimensional, nonlinear and transient rolling contact model.

Pieringer used an approach by Manfred Heckl [40] which enables the rail response in a moving point to be represented with Green's functions. The wheel and rail were included with Green's functions for the lateral, vertical and vertical-lateral coupling dynamics. Convolution was used to obtain the wheel/rail displacements from the contact forces and Green's functions. As earlier mentioned, Heckl and Abrahams [42] also used the convolution approach. The friction coefficient was kept constant (Coulomb model), thus considering squeal caused by geometric coupling.

The circumvention of explicit numerical integration, implementation of an elaborate contact model and inclusion of the rail dynamics are significant improvements over other models. The computational cost of the detailed contact model is high, resulting in long computation times. Still, the model is significantly faster than a comparable FE model with the same level of accuracy.

Pieringer et al. [84] recently compared the time-domain model [81] with the frequency-domain model developed by Torstensson et al. [106]. Torstensson's model was used to investigate the linear stability of the wheel/rail system via the complex eigenvalue analysis. To properly compare the two models, the wheel/rail system was linearised and evaluated in the time domain. Good agreement between results of the two models with the linear wheel/rail system was found. The nonlinear time-domain model predicted the same unstable frequencies but has also shown the presence of higher harmonics. The higher harmonics, which can be of significant amplitude, are the result of nonlinearities that are present in the system.

This section is concluded with a note about two-point wheel/rail contact. To the knowledge of the author, no complete time-domain model for curve squeal exists in the available literature that can consider two-point wheel/rail contact. Yang et al. [120] made a step towards such a model by building an FE model of the wheel and the rail and coupling the two. The model is meant to contribute to flange squeal modelling but is currently only able to describe the transition from one-point to two-point wheel/rail contact. Yang et al. [120] still have to extend the model to a full flange squeal simulation model. Moreover, the model by Yang has two main drawbacks. Firstly, it is completely based on an FE method approach and explicit time integration making it computationally very expensive and impractical. Secondly, a finite-length rail with free ends is considered. Such a rail model may influence the model accuracy, as discussed in relation to the models by Fourie [34] and Wang [117] in Section 3.1.1.

## 3.2 Models for the rolling contact

Wheel/rail contact models are used to determine contact variables: forces in the vertical<sup>2</sup>, lateral and longitudinal direction, normal pressure and tangential traction<sup>3</sup> distributions, along with the contact area shape and size. Knowledge of the contact forces is usually sufficient for simulations of vehicle dynamics, rolling noise and even curve squeal. However, for certain purposes, the normal pressure and tangential traction distributions are important, along with displacements in the contact area. Determination of wear is one example where this detailed information is required. The interest in details of the stick-slip process during squeal is another example.

<sup>2</sup>Normal contact forces are, in this thesis, sometimes called “vertical”. This statement is only true for zero contact-angle value and is used only in that context. The normal contact force acts along the direction normal to the wheel/rail contact patch.

<sup>3</sup>The surface stress in the normal direction is referred to as “pressure”. Despite having the same unit, the surface stress acting along a tangential direction (lying in the contact plane) is referred to as “traction”.

Contact variables are dependent on a number of parameters: wheel and rail material parameters, kinematic and geometric parameters that determine the wheel/rail relative motion (creepages, see Section 2.1), the geometry of the contacting surfaces and loading of the contact. Additionally, environmental parameters play a significant role in the tangential contact by influencing friction. The mentioned parameters form the input to the contact model.

Material parameters and the material behaviour are necessary for the computation of displacements and stresses in the contact. Wheels and rails are virtually always made of the same material, steel, which is usually considered a linear-elastic material in contact models used in squeal modelling. Therefore, all contact models encountered in squeal models assume linear elasticity of the material.

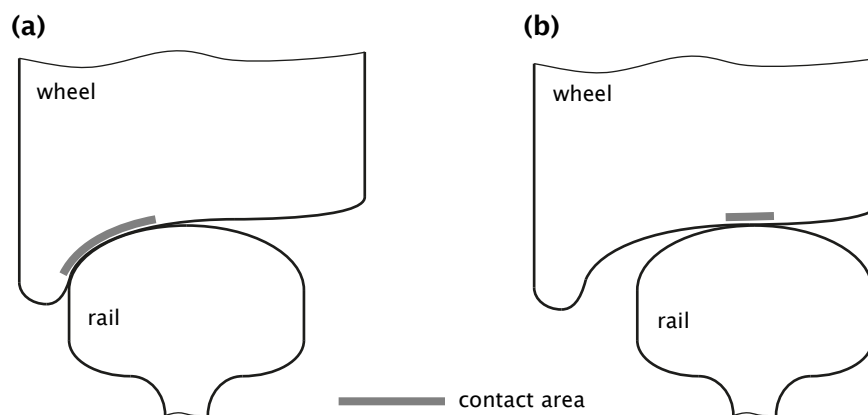


Figure 3.2: Wheel/rail contact: (a) conformal flange root/rail gauge corner contact; (b) non-conformal wheel tread/rail head contact.

The geometry of the contacting surfaces is an important factor in contact modelling. The shape of the contact bodies at and around the contact area has a significant impact on the distribution of stresses in the bodies. Conformal and non-conformal contact is distinguished. Figure 3.2 shows examples of both conformal and non-conformal contact surfaces. In the context of wheel/rail contact, non-conformal contact occurs in wheel tread/rail head contact (Figure 3.2 (b)). Conformal contact, on the other hand, may occur when the wheel flange root and the rail gauge corner are in contact (Figure 3.2 (a)).

A contact is considered to be conformal when the dimensions of the contact area are of the order of the characteristic dimensions of the bodies in contact [51]. In flange contact, the radii of curvature of the wheel and rail surfaces at the contact point are comparable to the contact size [80]. Additionally, the wheel flange thickness may also be comparable to the contact size. The stress distribution over the complete body has to be considered in that case.

Approaches to the solution of the conformal contact problem in the general case require numerical methods [51]. Finite-element and boundary-element approaches, like the one by Paul and Hashemi [78], can be used to solve the conformal problem.

Non-conformal contact is simpler to model compared to the conformal one. The

contact stresses are concentrated close to the contact region and do not affect the stress distribution in the complete body [51]. Contact stresses can then be computed as if the bodies were semi-infinite, bounded by a plane surface [51]. This corresponds to the so-called elastic half-space, which is one of the few geometries in three-dimensional elasticity for which influence functions are explicitly known [80]. Influence functions describe the elastic deformation of the elastic half-space due to a unit load acting in a point on the half-space.

Finally, the distinction between Hertzian and non-Hertzian contact is made. Hertzian contact comprises contact of surfaces that can be described with second-order polynomials in the vicinity of the contact area [68, 80]. This description is characteristic of the so-called Hertzian surfaces. In that case, the function describing the distance between the undeformed surfaces is also a second-order polynomial. Besides, for a contact to be Hertzian, surfaces must be smooth, frictionless, the material linear elastic and the half-space assumption must be valid [51]. Hertzian contact leads to an elliptical contact area and an ellipsoidal distribution of the normal contact pressure.

The definition of the Hertzian contact excludes conformal contact per se. Still, under certain conditions, conformal contact can be analysed as non-conformal without significant loss of accuracy. Yan and Fischer [119] analysed a contact case when the contact-body radius of curvature is smaller than the size of the contact area. Because stresses are no longer localised around the contact area, the elastic half-space assumption is not valid. Since the Hertz theory relies on the elastic half-space assumption [51], this would be a case where this theory is expected to be inaccurate. However, Yan and Fischer show that the pressure distribution obtained with the Hertz contact theory agrees well with results of the finite element method. The agreement is good as long as elastic contact is considered, i.e. no plastic deformation occurs in the contact. Therefore, in some cases, it is safe to consider conformal contact as non-conformal. However, it is necessary to be aware of the additional limitations introduced by this assumption.

While conformal contact is non-Hertzian by definition, non-conformal contact can be both Hertzian and non-Hertzian. Non-Hertzian contact of the wheel and rail is, in the first place, a consequence of the contact surfaces that cannot be described with second-order polynomials. A non-elliptical contact area is then obtained. Moreover, the radii of curvature may change significantly for small changes in the lateral position on the wheel tread [119]. This change in curvature is even more pronounced for worn wheel and rail profiles [80]. Such discontinuities in the curvature may also lead to multiple contact patches.

Surface roughness may also lead to non-Hertzian contact [80, 83]. In reality, all surfaces have a degree of roughness and contact occurs at distinct locations within the contact area. At these locations, asperities of the two surfaces touch, leading to local pressures several times higher than the maximum predicted by the Hertz theory [59]. However, asperities in contact show plastic deformations due to high contact pressures, which in turn lower the contact pressure by increasing the real contact area. If one is not interested in asperity-level phenomena, elastic models can

be used with acceptable accuracy [48].

The review of models used in squeal modelling given in Section 3.2.3 is limited to models for non-conformal contact. Both Hertzian and non-Hertzian models are considered. This is motivated by observations that curve squeal is usually expected on the curve inner wheel (see Section 2.1). At the inner wheel, contact is usually located on the wheel tread and rail head, and is non-conformal, but can still be non-Hertzian. For the case of contact near or at the wheel flange and rail gauge corner, it may still be safe to assume non-conformal contact, especially since linear elasticity is assumed in squeal models.

### 3.2.1 Contact conditions during squeal

This section presents a discussion of contact-level processes observed in rolling contact. The main focus of the discussion is the process of stick-slip related to squeal. The understanding of contact processes is important in making an educated choice of contact model for the specific purpose.

The overall relative motion between wheel and rail is defined by the three creepages, see Equations (2.1) to (2.3) in Section 2.1. In the finite-sized contact area, this overall (gross) relative motion manifests itself in two ways<sup>4</sup>. One way is the local elastic deformation of wheel and rail particles that travel through the contact area [51, 80]. The other is the relative motion (sliding, slip) between particles in contact.

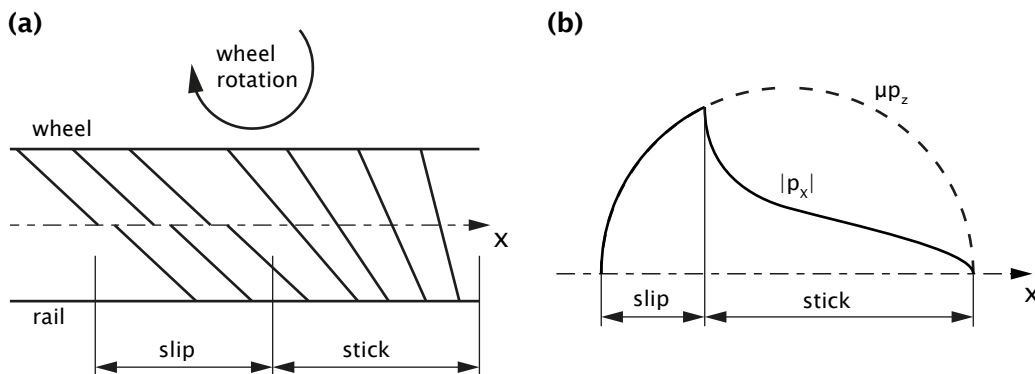


Figure 3.3: Division of the contact area into stick and slip regions: (a) displacement of the contacting particles; (b) tangential traction distribution according to Carter [17].

Figure 3.3 (a) shows the displacement of the wheel and rail particles as they travel through the contact area. This example assumes pure longitudinal creepage. As the particles travel through the contact, they deform more, and the load on them increases. The displacement and loading depend on the creepage, friction, material and vertical wheel load. The contact region where the relative motion manifests only

<sup>4</sup>The two manifestations of the gross relative motion on the contact level are a consequence of the nature of rolling contact and the contact elasticity.

as elastic contact deformation is called the stick region. However, there is a friction-defined limit of how much load a particle can take. When the particle load reaches this limit, relative motion (slip) between contact particles occurs. This region is called the slip region.

Figure 3.3 (b) shows the corresponding distribution of the longitudinal traction, which was obtained by Carter [17]. In the stick region, wheel and rail particles do not move relative to each other because the tangential traction limit defined by the friction coefficient and normal pressure is not reached. From the leading edge of the contact towards the trailing edge, the traction  $p_x$  builds up, leading to the build-up of displacements. However, at one point the longitudinal traction reaches the friction limit. The contacting particles cannot stick any longer, and relative motion occurs. The rest of the contact area is in slip.

Whenever creepage is present between wheel and rail, slip will occur in the contact area. The amount of slip, i.e. the size of the slip region, depends on the amount of creepage. The relative motion between wheel and rail gives also rise to the tangential contact forces. In the case of longitudinal creepage, these are longitudinal forces involved in acceleration or braking and forces caused by the differential longitudinal slip in curves.

Local slip between particles in contact is defined for each tangential direction  $\tau = x, y$  as [55]:

$$s_\tau = w_\tau - v \frac{\partial u_\tau}{\partial x} + \frac{\partial u_\tau}{\partial t}, \quad \tau = x, y, \quad (3.1)$$

where  $v$  is the rolling velocity,  $u_\tau$  the displacement difference between wheel and rail,  $x$  is the longitudinal and  $y$  the lateral direction. The term  $w_\tau$  is the contribution of creepage to the slip velocity. This contribution depends on the creepages and, only with non-zero spin creepage, on the particle location in the contact area. Kalker [55] refers to  $w_\tau$  as rigid slip, which is defined as:

$$w_x = (\gamma_x - \gamma_\omega y) v, \quad w_y = (\gamma_y + \gamma_\omega x) v. \quad (3.2)$$

The last two terms in Equation (3.1) denote the material derivative of the particle displacement. This, in the general case, depends on both space and time, and Equation (3.1) describes the general case of transient rolling. In the steady-state problem, the time-dependency vanishes:  $\partial u_\tau / \partial t = 0$ . Equation (3.1) is valid for both the stick and the slip region, where, in the stick region, slip is zero, i.e.  $s_x = s_y = 0$ . The solution of this equation gives the distribution of stick and slip regions and tangential tractions. To solve Equation (3.1), the displacements of contact particles have to be known. Contact displacements are most often determined from the elastic half-space [17, 51, 55].

As early as 1926, Carter [17] investigated the steady-state tractive rolling of a cylinder. He carried out a two-dimensional analysis of the problem and was the first to solve the tractive rolling-contact problem. The resulting traction distribution is shown in Figure 3.3 (b). However, the steady-state assumption may not be valid during squeal due to its high frequency, as discussed later on.

During squeal, the distribution of stick and slip areas in the contact changes with time, following the stick-slip instability. The distinction between global (contact-area level) and local (contact-particle level) motion is important for understanding the stick-slip process. This understanding will also prove useful in Section 4.3.3 where the point-contact model is formulated.

On the local level, stick-slip manifests as an interchange of periods with full slip and periods with partial slip in the contact. In the slip period, all contact particles are in sliding, while in the stick period only a portion slides. Full slip and partial slip are shown in Figures 3.4 (b) and (c), respectively. On this level, processes between contact particles are in focus. The exact transition from full slip to partial slip can be studied, along with displacements and stresses over the contact area. While this is of high importance in the fields of contact mechanics and wear, this may not be as important for squeal modelling. The resulting contact forces have a higher importance in curve squeal.

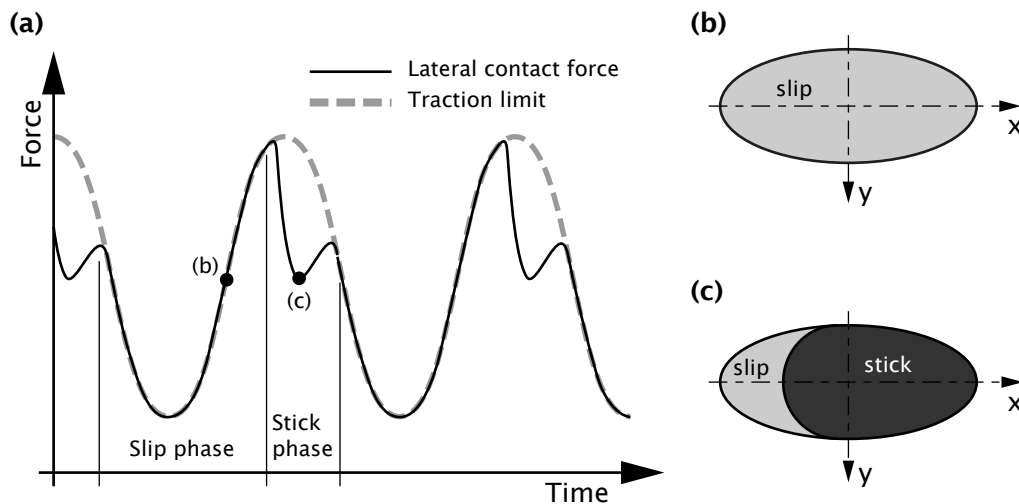


Figure 3.4: Detail of wheel/rail contact-force time history during stick-slip characteristic to squeal (a). Contact conditions during the slip phase (b), and the stick phase (c) are depicted.

On the global level, stick-slip motion is noticed from periods with tangential force on the traction limit, and periods with force under the traction limit. This is illustrated in Figure 3.4 (a), where the presence of higher harmonics in squeal can be noticed. The traction limit, proportional to the normal force and friction coefficient, does not change in shape throughout stick and slip phases. In contrast, the lateral force shows a sharp decline as the stick phase occurs, thus introducing higher harmonics. In terms of global slip<sup>5</sup>, periods with higher relative motion and periods with lower relative motion can be observed. During the stick phase, global

<sup>5</sup>Global slip is defined as the velocity difference between the wheel and the rail at the contact point. It includes contributions from creepage and the wheel/rail dynamic response. Global slip is also referred to as gross sliding.

slip between wheel and rail is lower than during the slip phase. This is a natural consequence since the lateral force is directly related to the relative wheel/rail motion. In conclusion, on the global level, the wheel and rail always slide one relative to the other due to non-zero creepage. Stick-slip is, therefore, associated with global-slip-velocity oscillations about a mean value determined by the creepages.

At this point, it is worth mentioning that the tangential forces have to be near or at saturation for stick-slip to develop. Chen et al. [19] and Qian et al. [88] discussed force-saturation as a probable cause for the stick-slip instability. Per definition, stick-slip involves the interchange of periods with full slip and periods of partial slip in the contact area. Since the frequency of stick-slip is usually close to a specific wheel eigenfrequency, the interchange can be looked upon as caused by small and fast variations of the wheel/rail displacement response. This is a simplistic view since the contact itself develops forces that cause the wheel/rail displacements. The important fact here is that stick-slip involves small variations about an equilibrium position. This equilibrium or mean position is most adequately expressed with the tangential force. For stick-slip, this force needs to be near or at the saturation limit, which is defined by friction. When this condition is met, small variations in the displacement can cause the contact to alternate between full and partial slip, i.e. stick-slip may develop.

If considered from the energy aspect, stick-slip instability can be looked upon as an interchange of potential and kinetic energy. During the phase with lower relative motion, the force builds up and stores potential (elastic) energy into the system. The potential energy is stored as elastic deformation in the wheel and the rail<sup>6</sup>. When the friction limit is reached, relative motion between the wheel and rail increases. The stored potential energy is released and transforms into kinetic energy. Due to higher sliding, more energy is now dissipated through damping, while the rest is transformed back to potential energy. The motion decreases until the tangential force drops below the friction limit. The process then repeats.

The explanation above is somewhat vague. The exact process of stick-slip is influenced by the wheel and rail dynamics, friction characteristic and value and creepages. What can be seen though, is that the stick-slip instability occurs under conditions where the potential, kinetic, input and dissipated energies are in a particular balance during each period. Moreover, squeal occurs at wheel modes since they can store large amounts of potential and kinetic energy. This relates to high vibration amplitudes that develop when a mode is excited.

The high frequency of curve squeal leads to fast changes in contact conditions, which are expressed with contact variables defined on the contact particle level. In this case, a particle will go through significant changes in variable values during the time it travels through the contact area. Additionally, at high frequencies, the contact particle dynamics may become influential. With increasing frequency, the vibration velocities increase for the same displacement amplitude. Inertial effects may then influence the behaviour of contact particles. Such conditions are called

---

<sup>6</sup>Some potential energy is even stored as elastic deformation in the contact.

transient contact conditions, and contact models able to describe such processes, transient contact models.

Figure 3.5 illustrates the change of variables in the contact area. Two cases are presented: a low-frequency motion and a high-frequency motion, each characterised by its characteristic wavelength  $L$  used to describe the rate of change of a contact variable. In low-frequency motion, the rate of change is rather low. The change of contact variables along the contact area can be neglected without introducing a significant error. However, in the high-frequency case of Figure 3.5, the rate of change is significant. In theory, this should not be neglected [57, 58].

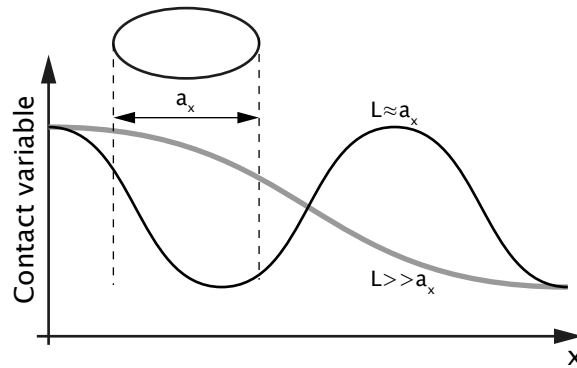


Figure 3.5: Variation of the contact variable along the contact length for case of a high-frequency motion ( $L \approx a_x$ ) and a low-frequency motion ( $L \gg a_x$ ) [58].

Knothe and Groß-Thebing [57, 58] used the ratio  $L/a_x$  of the characteristic motion wavelength  $L$  and the contact length in the rolling direction  $a_x$  to characterise contact conditions. A ratio lower than ten characterises transient conditions [58]. Although they considered rail corrugation, the same approach can be used to determine conditions during squeal. A case of squeal with  $f = 2$  kHz,  $v = 50$  km/h rolling velocity and  $a_x = 12$  mm contact length gives the characteristic motion wavelength of  $L = v/f = 0.007$  m and an  $L/a_x$  ratio of 0.58. The contact conditions during squeal are, thus, transient.

Whether a transient contact model is required for squeal modelling is still not clear. Guidelines from Knothe and Groß-Thebing [57, 58] indicate the need for a transient model. However, in response to [57], Kalker [55] compared results of steady-state and transient analyses of a rail corrugation case. The steady-state approach resulted in a slight overestimation of the frictional work compared to results from the transient model. Kalker found that the effect of transient contact conditions is not pronounced, questioning conclusions of Knothe and Groß-Thebing [57]. He finally concludes that transient contact processes can be described as a succession of steady-states.

Baeza et al. [12] investigated the influence of transient processes on contact variables. A harmonically varying force was imposed on the contact, and the resulting creepages were observed. In cases with rapid force variations, steady-state models did not give satisfactory results. Differences between results of steady-state and

transient models were found to depend on the  $L/a_x$  ratio. Specific values that would define the validity limit of steady-state models were not given.

Uncertainties related to the influence of transient contact conditions on contact variables and contact-model results are still high. It may even be so that the exact influence of transient conditions is specific to the case at hand.

### 3.2.2 Structure of a contact model

In this section, the general structure of a rolling contact model is described. The discussion focuses on peculiarities of the wheel/rail contact that influence the model formulation.

A contact model relates contact forces, pressure and tractions to the wheel/rail relative motion and imposed load. Information flow and sub-models in a contact model are presented in Figure 3.6. Three main sub-models are distinguished: the normal contact, the tangential contact and the friction model.

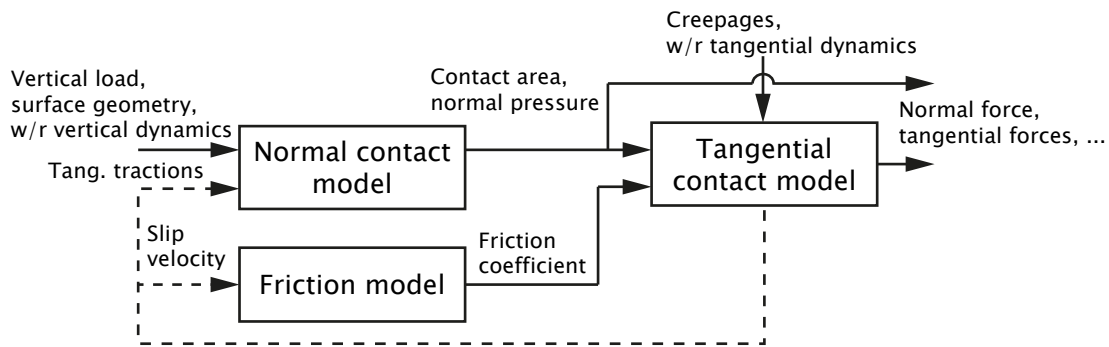


Figure 3.6: Typical structure of a rolling contact model.

The first step in solving the complete contact problem is the determination of the contact area shape and size, along with the normal contact pressure distribution. These quantities are obtained by solving the normal contact problem. For that, the vertical load, wheel and rail contact-surface geometries and, if considered, the wheel/rail vertical response are required. Also, material properties have to be known. The results of the normal problem form the input to the tangential contact model.

An additional input to the normal contact model can come in the form of tangential tractions. Tangential tractions are fed back from the tangential contact solution, as shown in Figure 3.6. In the general case, the solution of the normal problem is influenced by the tangential tractions. The reason behind this lies in the behaviour of the elastic half-space, where tangential loading causes displacements in both the normal and the tangential direction [51, 55]. The converse is also true: normal loading of the elastic half-space causes both normal and tangential displacements. The magnitude of the contact-area-displacement direction-coupling depends on the materials of the bodies in contact. Kalker [55] describes the difference between materials with the difference parameter  $K$ . Generally, the materials can differ, giving

$K \neq 0$ . The normal and the tangential contact problems are then coupled and have to be solved simultaneously.

In practice, however, the wheel and rail are virtually always made of steel. The difference parameter for identical materials is  $K = 0$ , which defines a case Kalker refers to as quasiidentity [55]. Displacements of elastic half-space, which locally describes the wheel and rail, are then equal in magnitude and opposite in direction. This equality eliminates the feedback loop, the normal and tangential problems are uncoupled and solved independently. Normal contact is solved first, followed by the tangential problem solution. Results of tangential contact problem consist of tangential tractions and slip velocities between wheel and rail particles. More information and mathematical details can be found in Kalker [55] and Johnson [51].

Another feedback loop runs between the tangential model and the friction model. This loop depends on the formulation of the friction law. A slip-velocity-dependent friction model requires a slip velocity value to determine the actual value of the friction coefficient. Slip is determined in the tangential contact, and a feedback loop is required in this situation. In the case of Coulomb friction, the friction coefficient is constant and independent of slip velocity. Constant friction eliminates the need for the feedback loop and simplifies the contact model.

### 3.2.3 Review of contact models used in squeal modelling

In this section, contact models implemented in different squeal models are reviewed. The review includes but is not limited to contact models used in the squeal models reviewed in Section 3.1. Various combinations of normal and tangential contact models can be used within the same squeal model. Moreover, different tangential models can be used within the same frequency-domain squeal-model to define the force-creepage relationship. Tangential contact models are described in more detail due to their importance for modelling curve squeal.

Point-contact models are simple models that describe contact processes on the global level. Both the normal and the tangential problem can be modelled as point contacts. This modelling approach leads to fast algorithms, especially when used for the tangential problem. There are many possibilities how a point-contact model can be formulated. They are mainly based on analytical or empirical formulas used to represent the force-creepage relationship.

Hertz's theory of normal contact [43] is a relatively simple and widely used analytical contact model. It is suitable for the wheel tread/rail head contact case which often fulfils requirements for Hertzian contact (see Section 3.2). Hertz's theory can be considered as a point-contact since contact variables, and their distributions, are determined from analytical expressions. Details about the Hertz theory of contact can be found in [51, 68], along with a comprehensive description of the model.

A large number of contact models use Hertz's theory for normal contact. Moreover, many squeal models [27, 45, 47, 97, 118] model the normal contact with a nonlinear spring characteristic, which is, in turn, obtained from the Hertz theory.

The formulation of the tangential point contact varies between models. A com-

mon approach to the one-dimensional problem is based on the relationship between normal and tangential forces:

$$F_\tau = \mu(s) F_z, \quad \tau = x \text{ or } y. \quad (3.3)$$

Nota bene, Equation (3.3) is valid for one tangential direction only, either  $\tau = x$  or  $\tau = y$ . A tangential force is proportional to the normal contact force. The factor of proportionality is the friction coefficient  $\mu(s)$ .

The complexity of the tangential point-contact model depends on whether the friction model is slip-velocity dependent or not, and whether both tangential directions are considered. If, for example, both directions are considered, the slip velocity is determined as  $s = \sqrt{s_x^2 + s_y^2}$ , and the right-hand side of Equation 3.3 should be multiplied by  $s_\tau/s$ . The latter term guarantees that the vectorial sum of tangential forces is less or equal to the friction limit. This term, thereby, enforces compliance with the physics of the problem. A nonlinear system of two equations then describes the problem. However, if a single tangential direction is considered, the model is simple, with a single linear equation to be solved.

While they are simple and computationally efficient, point-contact models cannot properly describe processes on the contact particle level. This inability is caused by the global consideration of the contact and especially concerns transient contact processes. Point-contact models may have a limited ability to evaluate transient cases with acceptable accuracy. Improvements in accuracy can, however, be achieved by including some contact-process information in the friction model.

More elaborate models can include the influence of local contact processes without the need to alter or extend the friction model. They may, however, still be similar to point-contact models in nature. A typical example is Kalker's linear theory [56].

The linear theory was developed by linearising Carter's solution [17], which is exact for the case of a cylinder rolling on a plane. This contact case is a two-dimensional problem. Carter's creepage-force relationship is nonlinear [56]:

$$\frac{F_x}{\mu F_z} = \begin{cases} -k\gamma_x + \frac{1}{4}k^2\gamma_x|\gamma_x| & \text{for } k|\gamma_x| \leq 2, \\ -\text{sign}(\gamma_x) & \text{for } k|\gamma_x| > 2, \end{cases} \quad (3.4)$$

where  $k = 4R_W/(\mu a)$  is Carter's creepage coefficient,  $R_W$  is the cylinder radius, and  $a$  is half of the contact length in the rolling direction. This nonlinear equation describes the transition from the no-slip (full stick) contact case towards the full slip (gross sliding) case. The solid line in Figure 3.7 shows Carter's solution given in Equation (3.4).

Kalker's linear theory gives the exact solution of the tangential-contact problem for the limiting case of no slip in the contact area. Moreover, Kalker generalised Carter's theory to all three creepages, thus extending it to three-dimensional contact. The quadratic term in Equation (3.4) is disregarded for small creepage, and a linear relationship between creepage and force is established [56]:

$$F_x = -c^2 G C_{11} \gamma_x, \quad (3.5)$$

$$F_y = -c^2 G C_{22} \gamma_y - c^3 G C_{23} \gamma_\omega. \quad (3.6)$$

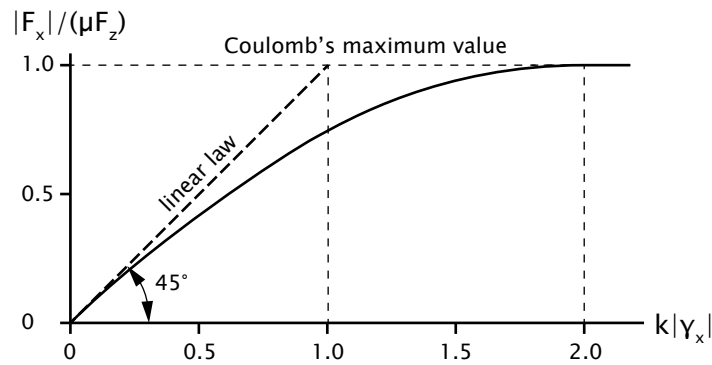


Figure 3.7: Creepage-force relationship according to Carter's theory (solid line) and Kalker's linear theory (dashed line). Adapted from [56].

The normal problem is solved using the Hertz theory. The quantity  $c = \sqrt{ab}$  is determined from the contact ellipse semi-axes  $a$  and  $b$ . Kalker's creepage coefficients  $C_{11}$ ,  $C_{22}$  and  $C_{23}$  depend only on the contact-ellipse semi-axes ratio  $a/b$  and Poisson's ratio of the material. Creepage coefficients can be found tabulated in [56]. The shear modulus of the material is denoted with  $G$ .

The linear theory does not consider any interaction between longitudinal and lateral forces, but the contributions of the two directions can be superposed [51].

Knothe and Groß-Thebing [38, 57] extended the linear theory to transient problems. They calculated frequency-dependent creepage coefficients valid for small harmonic variation of creepages. In [57], Kalker's assumption of vanishing creepages (no-slip condition) was kept. However, in [38] the model was extended to a more general case of contact conditions with finite creepages. In his squeal model, Fingberg [33] implemented Kalker's linear theory [56] with the frequency-dependent creepage coefficients from Knothe and Groß-Thebing [57]. As this model is not fully transient but rather an extension of Kalker's linear theory, it was referred to as semi-transient in Section 3.1.2.

The tangential contact model by Vermeulen and Johnson [109] is an approximate nonlinear model. The model is valid for elliptical contact areas, making it a suitable addition to Hertz's normal contact theory. The stick region is also assumed to be elliptical, which introduces a certain error in the model [51]. Still, a good correlation between measurements and model results was found [109]. The model is steady-state and unable to account for spin creepage.

To include the effects of spin, Shen, Hedrick and Elkins [93] extended the model of Vermeulen and Johnson. Shen et al. [93] noted that, with increasing spin creepage, the differences between their method, Kalker's FASTSIM and Kalker's variational theory increase. Moreover, Kalker [56] commented that this theory is suitable only for small-spin calculations. The models by Kalker, which were mentioned above, are discussed later on in this section.

Polach [87] developed a tangential contact model for the case of large creepages. Under these circumstances, the contact is dominantly in slip and the resulting tan-

gential force close to the traction limit (saturation). Polach applied Kalker's linear theory to determine the contact shear stiffness and to approximate the effects of spin. The effects of running on the traction limit were included by different reduction factors. These factors were determined by comparison of measurements and simulation results [87]. The model is limited to cases with elliptical contact areas and steady-state contact conditions.

All models above are limited to Hertzian contact. As mentioned in the introduction of Section 3.2, non-Hertzian contact is commonly encountered in wheel/rail interaction. Significant work has been performed on non-Hertzian contact models, which are discussed next.

Piotrowski and Chollet [85] addressed cases with multiple contact patches. They developed two approximate solutions: one based on a multi-Hertzian method and another based on a virtual penetration method. Other models that use similar approaches to multiple patches include those by Piotrowski and Kik [86] and Ayasse and Chollet [11]. These models, however, consider only the normal contact problem. The finite element method (FEM) provides the most accurate solution to such contact problems. However, FEM is inevitably accompanied with high computational cost.

Theories developed by Kalker prevail in the topics of tangential and non-Hertzian contact. The most detailed, transient and nonlinear theory is Kalker's variational contact theory [55], which he calls the "exact" theory. This theory was initially implemented in Kalker's CONTACT program [55] with computational improvements made by Vollebregt [111, 114]. Nowadays, the package is a commercial tool with the same name [112] and is being further developed by Vollebregt [113]. Details about the formulation and implementation of Kalker's variational theory can be found in [55, 80].

Kalker's variational method is based on the principle of maximum complementary energy. The model consists of two algorithms: NORM for the normal and TANG for the tangential problem. Both algorithms use an iterative solution procedure, which Kalker calls active-set algorithm [55]. The potential contact area is discretised into rectangular elements on which pressure, tractions and displacements are constant. The NORM algorithm solves the normal contact problem and determines the contact shape and size, along with the normal pressure distribution. The contact displacements are obtained from the elastic half-space equations. Kalker calls this theory "exact" since he used the exact Boussinesq-Cerruti equations [14, 18, 55] to determine the elastic half-space influence coefficients.

The TANG algorithm solves the kinematic Equation (3.1) for the transient rolling contact for each discretisation element in contact. The division of the contact area in stick and slip regions is determined, along with the distribution of tangential tractions. The model can handle both vanishing and large creepages, making it very versatile for many practical problems.

To sum up, Kalker's variational theory, in its general formulation, is applicable to [59, 80]:

- steady-state and transient processes;

- Hertzian and non-Hertzian contacts;
- considerations with any combination of the three creepages;
- contact of bodies made of different materials;
- cases with variable normal force, creepages and contact geometry.

However, Kalker’s model is limited by the elastic half-space assumption. The conformal contact problem cannot, therefore, be properly considered. Additionally, this detailed and capable rolling contact model is computationally expensive [59].

Initially, Kalker developed the model for the case of constant friction, but a slip-velocity dependent friction law can be implemented as well. This was done by Croft [25] and Pieringer [80], who implemented the friction model from Kraft [61]. They, however, had issues with multiple solutions of the tangential contact problem and numerical instabilities. Vollebregt [113] also implemented a falling friction law but introduced what he calls “*friction memory*” to reduce the irregularity of results. This topic is a subject of on-going research.

Kalker made an effort to reduce the computational cost of the variational method while retaining acceptable accuracy. This effort resulted in the simplified theory [54, 56], better known under the name FASTSIM, which is the name of the solution algorithm. While the model includes both normal and tangential contact, the normal contact solution is not reliable [116]. Kalker [56] states that best results are achieved in the case of Hertzian contact.

In the simplified theory, the elastic half-space was abandoned in favour of a bedding of independent springs<sup>7</sup>. The displacement of a point in the contact area, according to the simplified theory, is proportional only to the traction at that point. Kalker determined the flexibility of the springs in the bedding from his linear theory. The implementation of independent springs leads to a simple algorithm. Tangential tractions are evaluated within strips of elements along the rolling direction. A gradual build-up of displacement and tractions is obtained within a strip. According to Kalker [55], this approach is about 400 times faster than his CONTACT program. The simplified theory is considered to have the best precision-to-computational cost ratio [8] but is suited only to steady-state problems.

A significant amount of research focused on extending the simplified theory to include transient effects and falling friction. The inclusion of falling friction is rather common in curve squeal modelling. For example, Periard [79], Xie et al. [118], Huang et al. [47] and Squicciarini et al. [97] implemented a falling friction law in FASTSIM for squeal modelling purposes. Xie applied it in simulations of the vehicle curving behaviour to determine input creepages for the squeal model. Vollebregt and Schuttelaars [115] and Giménez et al. [36] also implemented the slip-velocity dependent friction law into FASTSIM.

Significant work in extending Kalker’s simplified theory to transient processes has been performed by Shen and Li [94], Alonso and Giménez [8] and Guiral et al. [39].

---

<sup>7</sup>This is also known as the Winkler bedding.

Shen and Li [94] considered the case with moderate longitudinal creepage and small spin in the transient case. They included transient effects by including the term  $\partial u_\tau / \partial t$  in the kinematic equation of the simplified theory. Good correlation with the results of the variational theory was found, except for the case with significant spin.

To better describe transient effects, Alonso and Giménez [8] introduced an additional flexibility coefficient in FASTSIM. This dynamic flexibility coefficient relates to the transient term, while Kalker's flexibility coefficient was retained next to the steady-state term. In comparison, Shen and Li [94] used Kalker's flexibility coefficient for both steady-state and transient terms. The contact area was assumed to be elliptical, and only one creepage was considered to be time dependent. Alonso and Giménez pointed out that the model can be easily extended to include non-Hertzian contacts [7, 8].

Guiral et al. [39] extended the model by Alonso and Giménez [8] to address the general case with all creepages. An arbitrary combination of creepages was considered, along with a variable normal contact force. Good agreement with Kalker's variational theory results was found in the case of large harmonic variation of the creepages.

The more elaborate and transient contact models were seldom used for squeal modelling. Uncertainties whether a transient contact model is really needed (see Section 3.2.1) form part of the explanation. Additionally, the contact model behaviour may depend on the formulation of the squeal model. For example, Zenzerovic et al. [124] observed numerical instabilities when FASTSIM was implemented in Pieringer's squeal model [81], which is formulated in the time domain. In contrast, a number of other squeal models [46, 79, 97] successfully implemented FASTSIM or a FASTSIM-derived model.

This section is concluded with a comment about the transient rolling contact. In Section 3.2.1, a transient rolling contact model was defined as having two characteristics. One is the ability to describe the change of contact variables in the contact area. The other is the ability to consider inertial effects of contact particles. According to this description, the transient models discussed above fulfil only the first criterion. To the knowledge of the author, no transient contact model that fulfils both conditions exists in the available literature. With the current state-of-the-art, the fully transient contact case could be solved with the finite-element-method approach. Still, according to Knothe et al. [59] and Pieringer [80], the FE solution of the complete transient contact problem (normal and tangential) is not yet available.

# Chapter 4

## Formulation of the engineering model for curve squeal

The squeal model is formulated in the time domain since the ability to predict squeal amplitudes is considered central to the engineering model. Time-domain models can determine amplitudes alongside the actual squeal frequency and the higher harmonic components caused by nonlinearities.

The engineering model for squeal is based upon the squeal model developed by Pieringer [80, 81]. The structure of the proposed model is presented in Figure 4.1. The main differences to Pieringer’s model are (1) the implementation of a fast tangential point-contact model; (2) the extension to two-point wheel/rail contact (Figure 4.2) and; (3) the implementation of a sound radiation model.

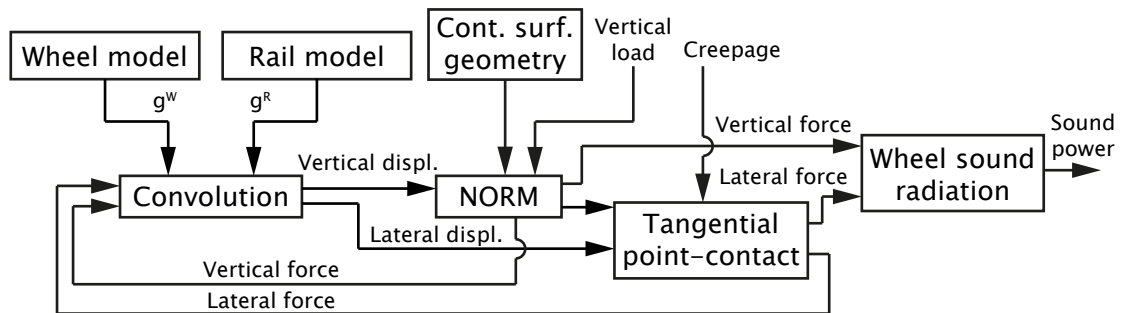


Figure 4.1: Structure of the time-domain engineering model for curve squeal.

The premise of an engineering model is that it is versatile, fast and adequately accurate. The versatility of a model for curve squeal means that different wheel and rail combinations, curving and contact cases can be readily investigated. In an engineering model, this is very important and allows the fast execution of a large number of studies. The representation of wheel and rail dynamics by Green's functions makes the original model [81] quite versatile. Green's functions ( $g^W$  and  $g^R$

in Figure 4.1) are predetermined before running squeal simulations as they depend only on the wheel and rail geometry, material data and wheel suspension. Since Green's functions are used, only linear wheel and rail models, presented in Section 4.2, can be considered. Real geometries of contacting surfaces can be easily included, which adds to the model versatility. Even surface roughness can be included, as was done by Pieringer [83].

Versatility is further improved with the proposed extension to two-point wheel/rail contact. The same model can be used for both one-point and two-point contact cases, meaning that a wide range of cases can be analysed with the model. In particular, practical cases with two-point contact that develop severe squeal [26, 97] can now be analysed in the time domain. The interaction between contact points, the instability development and possible mitigation measures can all be studied. Hopefully, this tool will allow for in-depth investigations of curve squeal excitation mechanisms and conditions that lead to squeal.

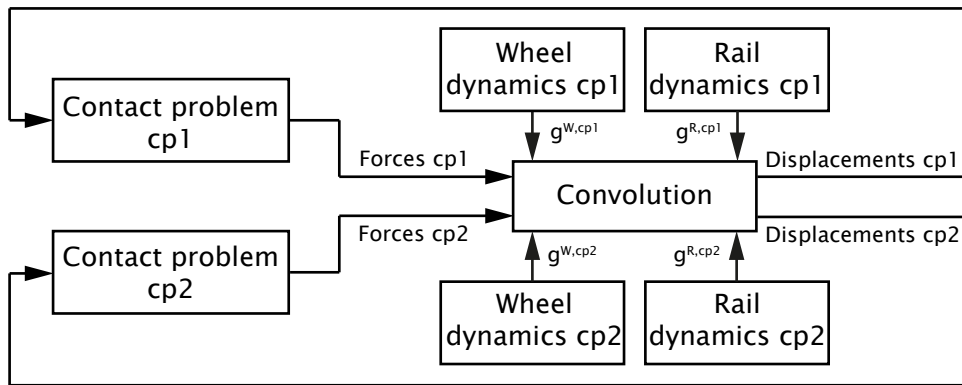


Figure 4.2: Schematic of the model extension to two-point wheel/rail contact.

Figure 4.2 presents the extension of the squeal models to two-point contact. The general structure of the squeal model presented in Figure 4.1 remains largely the same. The second contact point requires one additional contact problem to be solved in each time step. Wheel and rail dynamic terms that describe the displacement at the second contact and the coupling between the contacts have to be included. The dynamics of the two contact points get coupled in the convolution step, as explained Section 4.2.1.

Computation time is important in engineering practice where tight deadlines are often encountered. Therefore, an engineering model should run fast. The use of Green's functions and convolution, described in Section 4.2, gives a significant advantage in computation time over classical numerical integration methods. This approach was used by Heckl [40], Heckl and Abrahams [42] and Pieringer [81]. Further speed-ups of Pieringer's model [81] are achieved with an efficient contact model [124]. Kalker's variational theory [55] is kept for the normal contact problem to retain the ability to evaluate non-Hertzian contacts. As the tangential contact model is the most computationally expensive sub-model, a fast tangential point-contact model is proposed.

The global contact consideration of the point-contact model requires a suitable definition of the friction model, as discussed in Section 3.2.3. The full-stick to full-slip transition and the effects of spin creepage are included in the friction model [122]. Particularly significant is the inclusion of spin, which enables the engineering model to consider cases with non-zero spin creepage. The proposed friction model is determined using Kalker's variational theory, which on the local level assumes Coulomb friction. In contrast to Kalker's transient model, the point-contact model is a steady-state model. The contact model is presented in Section 4.3.

Ideally, an engineering model for curve squeal should address the complete source-to-receiver chain. A simple model for sound radiation from the railway wheel is implemented to cover at least part of this chain. The model computes the radiated sound power and was originally developed by Thompson and Jones [102, 103, 104]. The model is outlined in Section 4.4.

The squeal model [80, 81] was developed with the assumption that creepages and the wheel/rail contact position do not change during the time the vehicle negotiates a curve. Additionally, the creepages and contact position are assumed to be known in advance, either precomputed using a vehicle dynamics software or estimated.

## 4.1 Coordinate systems

Three Cartesian coordinate systems and one cylindrical coordinate system, shown in Figure 4.3, are used. The wheel model is defined in the cylindrical  $(y^W, z^W, \varphi^W)$  coordinate system, while the rail model is defined in the Cartesian  $(x^R, y^R, z^R)$  system. The  $(x^k, y^k, z^k)$  system is the contact coordinate system<sup>1</sup> in which the contact problem is solved. The index  $k = 1, 2$  denotes the contact point to which the coordinate system refers. In the case of one-point contact, the index  $k$  is omitted. Finally, the last coordinate system to be defined is the global  $(X, Y, Z)$  coordinate system in which the displacement response of the wheel and rail is determined.

The wheel and rail coordinate systems are fixed to the wheel and rail, respectively. The rail  $x^R$ -axis is oriented opposite to the rolling (longitudinal) direction and the lateral  $y^R$ -axis towards the field side of the track. The wheel  $y^W$ -axis is oriented towards the centre of the track, while the  $z^W$ - and  $z^R$ -axes are vertical axes. The wheel azimuth angle  $\varphi^W$  describes the wheel circumferential direction. These coordinate systems are only relevant when considering the wheel and rail models.

All contact variables are defined in the contact coordinate system. Its position is defined by the nominal contact point location. This is the point at which the wheel and rail make contact for a given lateral displacement of the wheelset (see Section 4.1.2). In the two-point-contact case, there are two nominal contact points and, consequently, two contact coordinate systems (see Section 4.1.3). The longitudinal axis  $x^k$  lies in the contact plane and is positive in the direction of travel. Axis  $y^k$  also lies in the contact plane, perpendicular to axis  $x^k$  and positive towards the field side of the wheel and rail. Finally, axis  $z^k$  is the normal axis positive towards the

<sup>1</sup>This coordinate system is sometimes referred to as the (1, 2, 3) system.

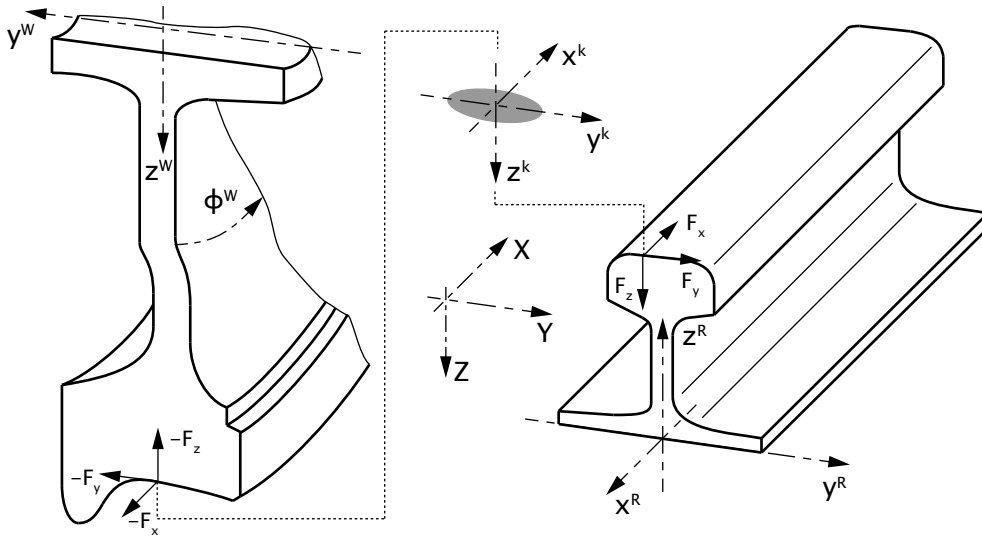


Figure 4.3: Coordinate systems and contact forces on the curve-inner wheel/rail system. The index  $k$  is omitted from the force notations.

ground (rail). This coordinate system travels with the contact point along the rail with rolling velocity  $v$ . Its absolute position along the rail at a time  $t$  is  $x_{ccs}^R = vt$ .

The contact forces  $F_x^k$ ,  $F_y^k$  and  $F_z^k$  are defined in the contact coordinate system belonging to contact  $k$ . Positive contact forces act on the rail, while forces on the wheel are reactive and, therefore, act in the opposite direction. Figure 4.3 shows the directions of contact forces acting on the wheel and the rail.

The global  $(X, Y, Z)$  coordinate system differs from the contact coordinate systems  $(x^k, y^k, z^k)$  by the rotation around the  $X$ -axis. The contact coordinate system is rotated relative to the global system by the value of the contact angle  $\alpha_c^k$ , see Section 4.1.1. The longitudinal axes of the two systems remain coincident, i.e.  $x^k \equiv X$ . Like the contact coordinate system, the  $(X, Y, Z)$  systems travels along the rail. The exact location of the origin of the global coordinate system is not important and does not influence the modelling. What is of importance, is the orientation of the axes and their relation to the contact-coordinate-system axes.

A note regarding the coordinate systems in the two-point wheel/rail contact case. As discussed in Section 2.1, two-point contact usually occurs between outer wheel and rail in a curve. The coordinate systems described above are defined in the same manner on both the inner and the outer wheel/rail system. As a consequence, the coordinate systems on the inner and the outer wheel/rail system are not identical. They differ in the orientation of the  $Y$ - and  $y^k$ -axes. As the squeal model considers a single wheel and rail in contact, no changes in it are required. However, care has to be taken when determining the lateral creepage sign on the inner and outer wheel/rail system.

### 4.1.1 The contact angle and the coordinate transformation

In this thesis, the contact angle  $\alpha_c^k$  is defined as the angle between the global  $Y$ -axis and the local  $y^k$ -axis of contact point  $k$ . The angle is determined by the wheel and rail profiles and the location of the contact point on the profiles.

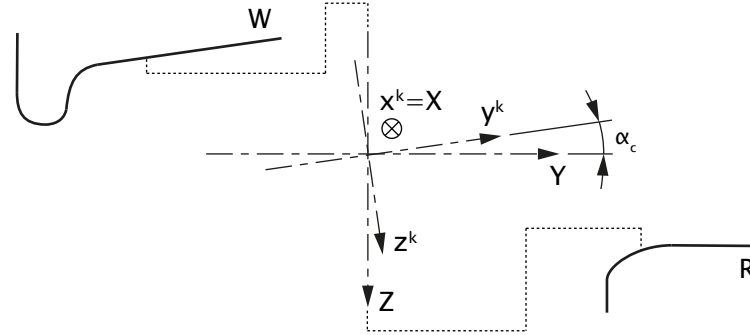


Figure 4.4: Coordinate systems in the presence of a non-zero contact angle.

For the case of zero contact angle, the contact and the global coordinate systems are identical. In that case, there is no need for differentiating the two systems, and the contact problem and displacement response are defined in one system. For a non-zero contact angle, the  $(x^k, y^k, z^k)$  system rotates so that the contact area lies in the  $x^k - y^k$  plane. This rotation is illustrated in Figure 4.4. Each of the two systems is then required, and each has its role, as explained next.

Each coordinate system has a specific role in the contact problem solution and displacement response determination. The contact problem is solved in the contact coordinate system  $(x^k, y^k, z^k)$  in which the forces  $F_x^k$ ,  $F_y^k$  and  $F_z^k$  are defined. Since the global coordinate system  $(X, Y, Z)$  does not rotate, its axes remain parallel to the wheel  $(x^W, y^W, z^R)$  and rail  $(x^R, y^R, z^R)$  coordinate system axes. This makes the global coordinate system suitable for the definition of the wheel and rail displacement response. The excitation forces  $F_X^k$ ,  $F_Y^k$  and  $F_Z^k$ , which excite the wheel and rail, are defined in the global system together with the wheel and rail dynamics. Then, using convolution, the wheel and rail combined displacements<sup>2</sup>  $\xi_Y^k$  and  $\xi_Z^k$  are obtained.

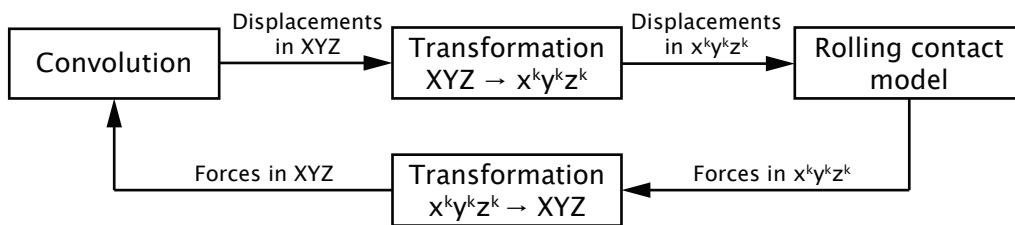


Figure 4.5: Schematic of coordinate transformations in the curve squeal model.

<sup>2</sup>The wheel and rail combined displacement is the difference between the wheel and the rail displacements at the contact point, see Section 4.3.

The influence of the contact angle is included in the squeal model by considering force and displacement transformations between the  $(x^k, y^k, z^k)$  and  $(X, Y, Z)$  systems. Figure 4.5 shows the schematic of the coordinate transformations in the squeal model. Contact forces, as outputted from the rolling contact model, are defined in the contact coordinate system. They have to be transformed to forces in the global system before convolving them with Green's functions to obtain displacements. The displacement response is then inputted in the contact model and influences the following time-step contact forces. However, contact-point displacements are in the global system, so they have to be transformed to the contact coordinate system. From Figure 4.5 and the description above, the coordinate transformations can be understood as interfaces between the contact model and the convolution.

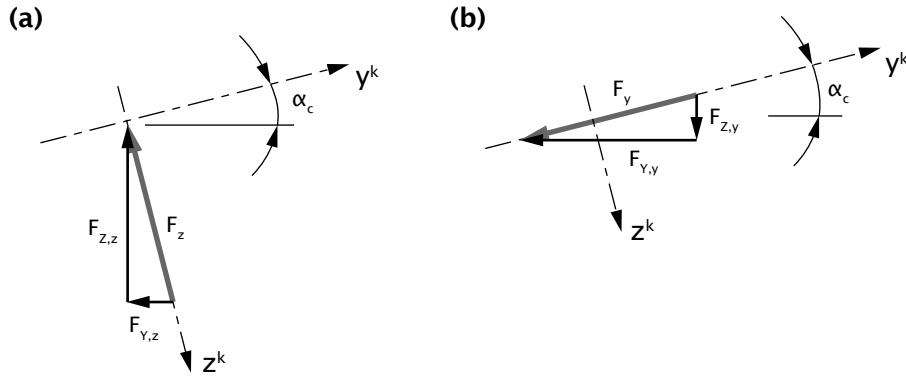


Figure 4.6: Contact force components: (a) normal contact force; (b) lateral contact force.

Components of the normal  $F_z^k$  and the lateral  $F_y^k$  contact forces in the  $(X, Y, Z)$  coordinate system are shown in Figure 4.6 (a) and (b), respectively. The normal force  $F_z^k$  has components  $F_{Y,z}^k$  in direction  $Y$  and  $F_{Z,z}^k$  in direction  $Z$ . Similarly, the lateral force  $F_y^k$  has components  $F_{Y,y}^k$  and  $F_{Z,y}^k$  along  $Y$  and  $Z$ , respectively. Mathematically, the coordinate transformation of forces is expressed as:

$$\begin{bmatrix} F_X^k \\ F_Y^k \\ F_Z^k \end{bmatrix} = \begin{bmatrix} 1 & 0 & 0 \\ 0 & \cos \alpha_c^k & \sin \alpha_c^k \\ 0 & -\sin \alpha_c^k & \cos \alpha_c^k \end{bmatrix} \begin{bmatrix} F_x^k \\ F_y^k \\ F_z^k \end{bmatrix}. \quad (4.1)$$

In the coordinate transformation above, the longitudinal contact force does not transform, i.e.  $F_X^k = F_x^k$ . This is due to collinearity of  $x^k$  and  $X$  ( $x^k \equiv X$ ). Displacements are transformed from the  $(X, Y, Z)$  system to the  $(x^k, y^k, z^k)$  system according to:

$$\begin{bmatrix} \xi_x^k \\ \xi_y^k \\ \xi_z^k \end{bmatrix} = \begin{bmatrix} 1 & 0 & 0 \\ 0 & \cos \alpha_c^k & -\sin \alpha_c^k \\ 0 & \sin \alpha_c^k & \cos \alpha_c^k \end{bmatrix} \begin{bmatrix} \xi_X^k \\ \xi_Y^k \\ \xi_Z^k \end{bmatrix}. \quad (4.2)$$

In analogy with the forces transformation, the longitudinal displacements do not transform, i.e.  $\xi_x^k = \xi_X^k$ .

### 4.1.2 Wheel/rail nominal contact positions: one-point contact

Three different one-point wheel/rail contact cases are analysed in this thesis. The contact cases were determined from measured wheel and rail profiles in [81]. The wheel profile corresponds to a worn S1002 profile, while the rail profile is a worn BV50 rail profile with 1:40 inclination. Contact between the inner wheel and rail in a curve is considered. Each contact case is defined with a lateral displacement (offset)  $\Delta y^{WR}$  of the wheelset on the rail. To each offset  $\Delta y^{WR}$  corresponds a lateral coordinate on the wheel tread  $y^W$  and a lateral coordinate on the rail head  $y^R$ :

$$\Delta y^{WR} = \begin{cases} -5 \text{ mm}, & \text{where } y^W = 5 \text{ mm}, y^R = -16 \text{ mm}, \\ -10 \text{ mm}, & \text{where } y^W = -4 \text{ mm}, y^R = -12 \text{ mm}, \\ -15 \text{ mm}, & \text{where } y^W = -32 \text{ mm}, y^R = 12 \text{ mm}. \end{cases} \quad (4.3)$$

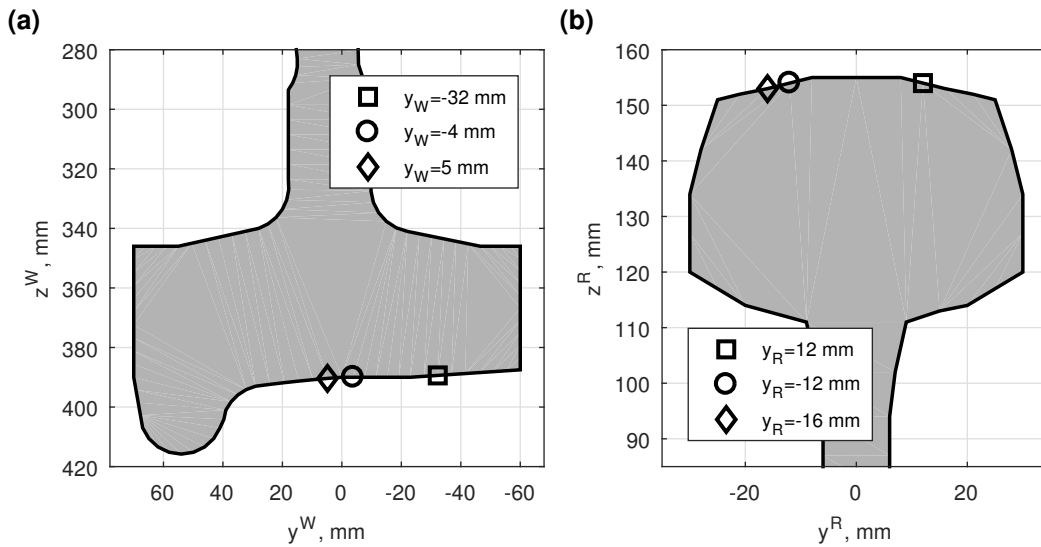


Figure 4.7: Cross-section of the wheel (a) and the rail (b) model. Markers denote the nominal contact points of the three one-point-contact cases.

Figure 4.7 shows cross-sections of the wheel and rail models. Wheel tread and rail head points coming into contact are represented with the same markers on the wheel and the rail model. For each contact position, the measured wheel and rail surface profiles around the nominal-contact point were considered. The surface profiles form part of the input to the normal contact problem.

The contact angle for contact between the wheel tread and rail head is usually very small and can be safely ignored. In the analyses of the defined one-point contact cases, the contact angle is, therefore, assumed to be zero ( $\alpha_c = 0$ ). One exception to this assumption are the theoretical studies on the influence of the contact angle presented in Section 6.4 and 6.4.1.

### 4.1.3 Wheel/rail nominal contact position: two-point contact

A two-point wheel/rail contact case is obtained by considering a new (nominal) S1002 wheel profile (with 30.5 mm flange thickness) and a worn UIC60 rail profile. The rail profile was obtained from measurement, courtesy of SNC-Lavalin Rail & Transit, Sweden. Contact between the wheel and rail was analysed using the GENSYS software [28]. As expected, two-point contact is obtained between the outer wheel and rail when the wheelset displaces outwards, further away from the curve centre.

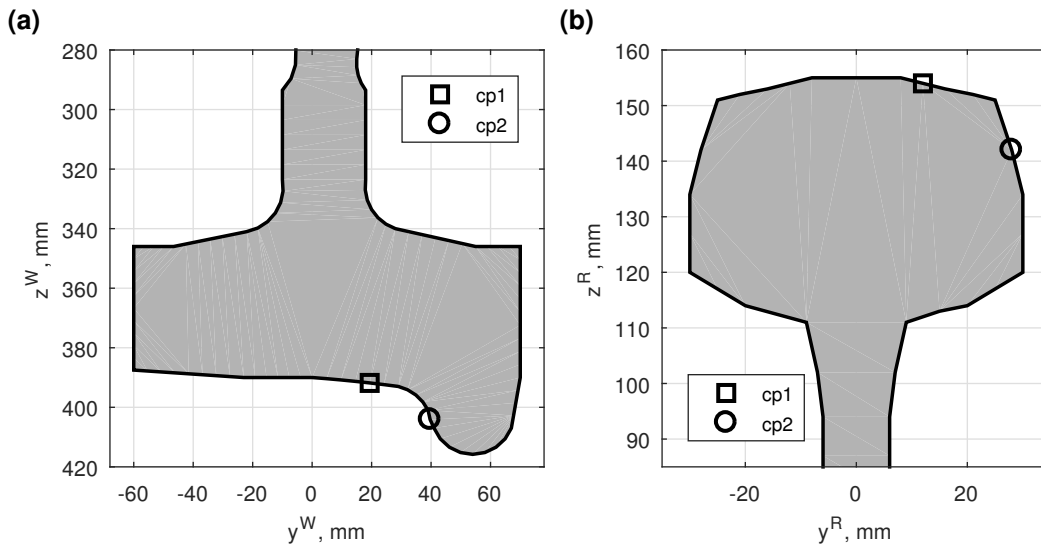


Figure 4.8: Cross-section of the wheel (a) and the rail (b) model. Markers denote nominal contact points of the two-point-contact case.

Two-point contact is obtained for a lateral offset value of  $\Delta y^{WR} = -8$  mm. The two contact points are referred to as contact point 1 ( $cp1$ ) and contact point 2 ( $cp2$ ). Contact point 1 occurs between the wheel tread and rail head, while contact point 2 occurs between the wheel flange and rail gauge corner. This is the typical two-point-contact situation, as discussed in Section 2.1.

Initial contact between wheel and rail is assumed at  $cp1$ . Contact at  $cp2$  occurs after sufficient approach of the wheel and the rail at the  $cp2$  location. The required approach is expressed with the term  $\delta_z$ , which is referred to as the normal distance between  $cp1$  and  $cp2$ . In this thesis, this distance is determined from the undeformed wheel and rail profiles by considering the normal distance between the profiles at the  $cp2$  position with the profiles touching at  $cp1$ . The normal distance is defined along the  $z^2$ -axis of the  $cp2$  contact coordinate system.

As can be anticipated, the normal distance  $\delta_z$  influences the distribution of the vertical load between the contact points. The normal distance can, therefore, also be determined from the knowledge of the static vertical-load distribution between the two contact points. In that case, the determination of the normal distance is more

complicated. An iterative procedure that determines the wheel/rail displacement at  $cp2$  to obtain the known vertical load distribution has to be performed.

As mentioned above, contact at  $cp2$  occurs after the wheel and rail have approached each other by at least  $\delta_z$  at the  $cp2$  location. The approach is equal to the combined displacement of the wheel and rail at  $cp2$ . This is accounted for in the normal-contact problem of  $cp2$ , where the distance  $\delta_z$  is included as a kinematic parameter. In Section 4.3.2, the mathematical formulation of the normal contact problem for  $cp2$  is presented. From the analysis of wheel/rail profiles in contact at  $cp1$ , the normal distance value is obtained and is equal to  $\delta_z = 2 \cdot 10^{-5}$  m.

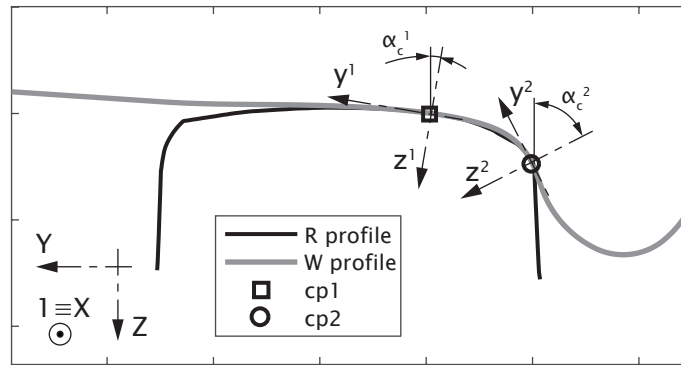


Figure 4.9: New S1002 wheel profile and worn UIC60 rail profile in contact for  $\Delta y^{WR} = -8$  mm.

In addition to the location of the contact points, the contact angle  $\alpha_c^k$  is also determined from the GENSYNS analysis. The contact angles at the two contact points are  $\alpha_c^1 = 8^\circ$  and  $\alpha_c^2 = 66.5^\circ$ . Figure 4.9 shows the wheel and rail profiles in two-point contact. The contact coordinate system at each point are also shown. High influence of the contact angles is expected due to their high values. Therefore, the angles have to be considered in the model.

## 4.2 System dynamics

As mentioned, the wheel and rail dynamics are included in the model through Green's functions. Green's functions are commonly used in mathematics for solving non-homogeneous differential equations subject to specific initial or boundary conditions. The non-homogeneity is considered concentrated in a point, meaning that it can be described by the Dirac delta ( $\delta$ ) function. The response of a system described by a differential equation and excited by the  $\delta$  function is the Green's function of the problem [24]. Because the Dirac  $\delta$  function describes a unit impulse, Green's functions are often called impulse response functions.

In the case of mechanical systems, the Green's function  $g(X, Y, t)$  is seen as the time response of the system at point  $X$  due to a unit-impulse excitation at point  $Y$  and time  $t$  (usually  $t = 0$ ) [13, 24]. Green's functions for the wheel and the rail can

be easily obtained from receptances defined in the frequency domain. Receptance is defined as the ratio between displacement and force at a frequency  $f$ . For the case when the excitation acts at the same point in which the displacement response is evaluated, the receptance is called point receptance:

$$G_{ij}(f) = \frac{\xi_i(f)}{F_j(f)}, \quad i, j = X, Y, Z. \quad (4.4)$$

The term  $\xi_i(f)$  is the displacement response in the coordinate direction  $i$  due to the excitation force  $F_j(f)$  acting in the direction  $j$ .

The method used for obtaining the Green's functions (time domain) from the receptances (frequency domain) was proposed by Kropp [62] and is described in [10]. This method is used within the Vibroacoustic Group of the Division of Applied Acoustics, Chalmers University of Technology. The advantages of the method, which is described below, are that the obtained Green's function is causal and that the Gibbs phenomenon is avoided [10].

The method assumes that the system is sufficiently damped so that the system response decays to zero after a finite time. Firstly, a frequency spectrum is constructed by taking the real part of the receptances and doubling it:

$$S_{G,ij}(f_d) = 2\Re\{G_{ij}(f_d)\}, \quad i, j = X, Y, Z, \quad (4.5)$$

where  $f_d$  is the discrete frequency. Secondly, the inverse Fourier transform is performed to obtain  $s_{G,ij}(n\Delta t)$ :

$$s_{G,ij}(n\Delta t) = \mathcal{F}^{-1}\{S_{G,ij}(f_d)\}, \quad i, j = X, Y, Z, \quad (4.6)$$

which gives a time signal with the period  $n = 0, \dots, (N_t - 1)$ , where  $N_t$  is the number of samples. The discrete time-step length is  $\Delta t$ . The time-domain signal  $s_{G,ij}(n\Delta t)$  contains the Green's function  $g_{ij}(n\Delta t)$ , which is finally extracted as:

$$g_{ij}(n\Delta t) = \begin{cases} 0.5\Delta t s_{G,ij}(n\Delta t) & \text{for } n = 0, \\ \Delta t s_{G,ij}(n\Delta t) & \text{for } n = 1, \dots, N_t/2. \end{cases} \quad (4.7)$$

By the time  $(N_t/2)\Delta t$ , the Green's function is assumed to have decayed to zero.

Green's functions can be used to determine the response of a system subjected to arbitrary excitation. The solution of a non-homogeneous differential equation is the superposition of elementary solutions (Green's functions) weighted by the excitation function [24]. This superposition can be looked upon as a discretisation of the excitation function into impulses. Green's functions for each discrete impulse are then superposed to obtain the final system response. This approach is known as convolution. The limitation of the approach is that the superposition principle is valid only for linear systems.

Mathematically, the displacement response at time  $t$  is defined by the convolution integral of the excitation  $F$  and Green's function  $g$ :

$$\xi(t) = F \otimes g = \int_0^t F(\tau) g(t - \tau) d\tau. \quad (4.8)$$

In the case of discrete Green's functions and excitation forces acting in multiple directions, the convolution of Equation (4.8) takes the discrete form:

$$\xi_i(t_d) = \mathbf{F} \otimes \mathbf{g}_i = \sum_{\tau=0}^{t_d} \sum_{j=X}^Z F_j(\tau) g_{ij}(t_d - \tau), \quad i = X, Y, Z, \quad (4.9)$$

where  $t_d$  is the current discrete time-point. As will be discussed later, under certain circumstances the first value of Green's functions,  $g_{ij}(0)$  corresponding to  $\tau = t_d$ , can be neglected. It is therefore convenient to separate the convolution defined in Equation (4.9) into two parts:

$$\xi_i(t_d) = \sum_{j=X}^Z F_j(t_d) g_{ij}(0) + \sum_{\tau=0}^{t_d - \Delta t} \sum_{j=X}^Z F_j(\tau) g_{ij}(t_d - \tau), \quad i = X, Y, Z. \quad (4.10)$$

The first sum in Equation (4.10) defines the instantaneous response  $\xi_i(t_d)$  due to the force acting at that same time  $t_d$ . This term may present difficulties since the current time-step force  $F_j(t_d)$  is not always known and can depend on the current displacement. The first value of a Green's function gives the instantaneous local displacement of the body due to a contemporaneous unit-excitation force. This value can be treated as a dynamic flexibility coefficient, which takes into account the effects of the system dynamics [10].

The second, double sum in Equation (4.10) depends only on forces from the past. However, this term is not a convolution per definition any more. For it to regain the convolution form, the substitution  $t'_d = t_d - \Delta t$  is introduced in Equation (4.10):

$$\xi_i(t_d) = \sum_{j=X}^Z F_j(t_d) g_{ij}(0) + \sum_{\tau=0}^{t'_d} \sum_{j=X}^Z F_j(\tau) g_{ij}(t'_d - \tau + \Delta t), \quad i = X, Y, Z. \quad (4.11)$$

The method discussed above is presented for one excitation and one (coincident) response point. In the case of the wheel/rail system, this is sufficient to model one-point contact. However, the case of two-point wheel/rail contact requires the extension of the convolution to two excitations and two response points. This extension is presented in the following section.

### 4.2.1 Extension to two-point wheel/rail contact

In the case of two-point wheel/rail contact, displacements at both contact points have to be obtained. Forces at both contacts excite the same body (wheel and rail) and influence displacements in both points. Equation (4.11) is, therefore, extended

to account for the coupling dynamics between the two points:

$$\begin{aligned} \xi_i^k(t_d) = & \sum_{j=X}^Z \sum_{l=1}^2 F_j^l(t_d) g_{ij}^{kl}(0) \\ & + \sum_{\tau=0}^{t'_d} \sum_{j=X}^Z \sum_{l=1}^2 F_j^l(\tau) g_{ij}^{kl}(t'_d - \tau + \Delta t), \quad i = X, Y, Z; \quad k = 1, 2. \end{aligned} \quad (4.12)$$

Equation (4.12) describes the response at point  $k$  in direction  $i$ . Compared to Equation (4.11), this equation contains the additional summation over the index  $l$  for the two excitation points. This summation shows that the response at point  $k$  depends upon forces in both excitation points and all Green's functions describing the response at point  $k$ . The convolution defined in Equation (4.12) is central to the extension of the squeal model to two-point contact, as seen in Figure 4.2. This convolution step couples the two contact points and enforces the excitation of the same body at both contacts. Correct coupling of the two points is then achieved.

The system dynamics in the two-point case are described by 36 Green's functions  $g_{ij}^{kl}$  (three directions per index  $i$  and  $j$ , and two points  $k$ ). In comparison, the dynamics of the one-point case are described by nine Green's functions  $g_{ij}$ . This illustrates the significantly higher complexity of the two-point-contact case.

In the following sections, a description of the wheel and the rail model is given. The wheel and rail models are taken from Pieringer [80, 81].

## 4.2.2 Wheel dynamics

The wheel analysed in this thesis is a C20-type wheel with a nominal rolling diameter of 780 mm. This wheel type can be, for example, found on vehicles in the Stockholm metro system.

The wheel was modelled using finite elements. The axial symmetry of the wheel enabled the use of axi-symmetric elements, which require only the wheel cross-section to be modelled [80, 81]. Figure 4.10 shows the FE mesh of the wheel cross-section. The model also includes the primary suspension of the wheelset [80].

A harmonic solution is assumed along the wheel circumference, which results in a complete three-dimensional wheel model. The harmonic variation along the circumference is described with  $\hat{a} \cos(n\varphi)$  and  $\hat{a} \sin(n\varphi)$  terms. The amplitude  $\hat{a}$  varies with the contact position on the wheel cross-section. Which harmonic term describes the axial, radial<sup>3</sup> and circumferential displacement depends on the direction of the excitation force. In case of radial or axial excitation, the radial and axial displacements are described with cosine terms, while the circumferential displacement comes with the sine term. On the other hand, when excitation is

<sup>3</sup>When considering the wheel outside of the wheel/rail-interaction context, the lateral and vertical directions can be referred to as axial and radial, respectively. This nomenclature comes from the directions of the cylindrical coordinate-system axes.

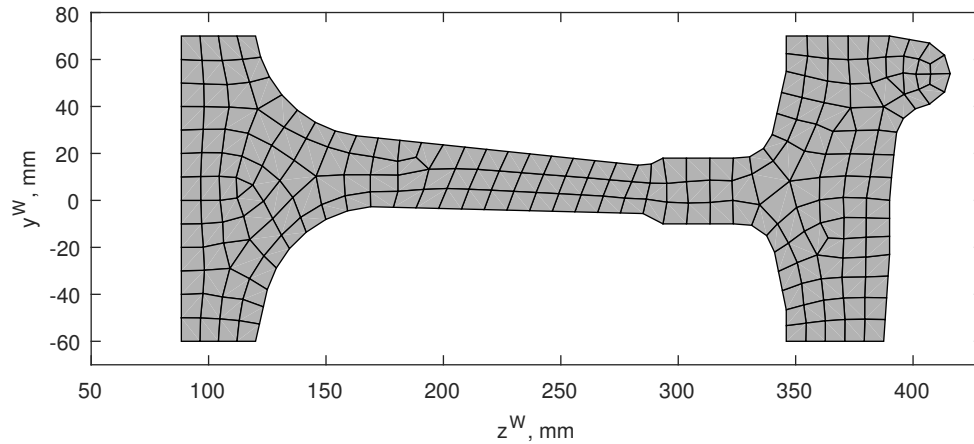


Figure 4.10: Cross-section of the C20 wheel with the FE model mesh.

circumferential, the radial and axial displacements are described with the sine and the circumferential with the cosine term.

The wheel eigenfrequencies and eigenmodes were determined in [80] for frequencies up to 7 kHz using the ANSYS commercial FE analysis software [4]. Table 4.1 lists wheel eigenfrequencies and eigenmodes classification. Wheel modes are classified according to  $(n, m, \text{Class})$ , where  $n$  is the number of nodal diameters, and  $m$  is the number of nodal circles. The term *Class* describes the dominant motion of the wheel, which can be axial (*a*), radial (*r*) or circumferential (*c*). More information about the classification of wheel modes and wheel vibration characteristics can be found in [80, 99, 100].

Modal superposition is used to determine wheel receptances  $G_{ij}^{W,kl}(\Omega)$  from wheel mode shapes  $\Phi_r$ , eigenfrequencies  $\omega_r$  ( $\omega_r = 2\pi f_r$ ) and modal damping factors  $\zeta_r$ :

$$G_{ij}^{W,kl}(\Omega) = \sum_r \frac{\Phi_{ri}^{kl} \Phi_{rj}^{kl}}{m_r (\omega_r^2 - \Omega^2 + i2\zeta_r \omega_r \Omega)}. \quad (4.13)$$

The receptance  $G_{ij}^{W,kl}$  gives the response in the degree of freedom  $i$  at point  $k$  due to excitation in the degree of freedom  $j$  of point  $l$ . The term  $m_r$  is the modal mass of mode  $r$  and  $\Omega$  ( $\Omega = 2\pi f$ ) is the angular frequency of the harmonic excitation force.

Indices  $k$  and  $l$  depend on whether a one- or two-point wheel/rail contact is considered. In the case of one-point contact, the excitation and response are evaluated at the same point ( $k = l = 1$ ), and the indices are omitted. In the case of two-point contact, the indices are not omitted and take values  $k, l = 1, 2$ .

Modal damping factors are a common source of uncertainty in wheel models. Damping factors cannot be measured with high precision that is required for accurate predictions of curve squeal. Therefore, the determination of modal damping usually involves estimation. Approximate values of wheel modal-damping factors, used in

$f_r$ , Hz	(n, m, Class)	$f_r$ , Hz	(n, m, Class)
243.2	(1, 0, a)	3886.2	(1, 0, c)
332.8	(0, 0, a)	4131.1	(6, 0, a)
429.9	(2, 0, a)	4176.8	(0, 2, a)
721.9	(0, 0, c)	4236.6	(1, 2, a)
1143.2	(3, 0, a)	4349.6	(5, 0, r)
1586.4	(1, 0, r)	4417.2	(2, 2, a)
1923.9	(0, 1, a)	4635.2	(5, 1, a)
2058.3	(4, 0, a)	4871.7	(3, 2, a)
2089.4	(1, 1, a)	5215.9	(7, 0, a)
2242.5	(2, 0, r)	5227.5	(2, 0, c)
2584.8	(2, 1, a)	5267.8	(6, 0, r)
2834.1	(3, 0, r)	5454.1	(6, 1, a)
3070.8	(5, 0, a)	5546.6	(4, 2, a)
3193	(3, 1, a)	6268.7	(7, 0, r)
3535.8	(4, 0, r)	6315.6	(8, 0, a)
3625.1	(0, 0, r)	6343	(7, 1, a)
3880.8	(4, 1, a)	6405.5	(5, 2, a)

Table 4.1: The C20 wheel eigenfrequencies and classification of modes below 7 kHz [80, 81].

[80], were proposed by Thompson [100, 101]:

$$\zeta_r = \begin{cases} 10^{-3} & \text{for modes with } n = 0, \\ 10^{-2} & \text{for modes with } n = 1, \\ 10^{-4} & \text{for modes with } n \geq 2. \end{cases} \quad (4.14)$$

A correction has to be made when the wheel is coupled with the axle. The radial (1, 0, r) mode shows a high resonance peak in the wheel model, but is not observed in receptance measurements [52]. To account for the axle influence, the damping factor for the (1, 0, r) mode is set to one [52, 100]. According to Thompson [100], this corrections leads to more accurate noise predictions.

Figure 4.11 shows the vertical and lateral point-receptances and the vertical-lateral cross-receptance. Receptances at the three contact points of the analysed one-point contact cases are presented. Locations of the three contact points are marked on Figure 4.7 (a). Largest differences in receptances at the three points are observed in the vertical point-receptance and vertical-lateral cross-receptance. The lateral point receptance of Figure 4.11 (b) is virtually identical at all three points.

Figure 4.12 shows receptances for the two contact points of the two-point-contact case presented in Section 4.1.3 and Figure 4.8 (a). Receptances  $G_{ij}^{W,11}$  and  $G_{ij}^{W,22}$  for  $i, j = Y, Z$  are presented to show the difference in the wheel response at the two contact points. Again, largest differences are observed in the vertical point-receptances and the vertical-lateral cross-receptances, Figure 4.12 (a) and (c).

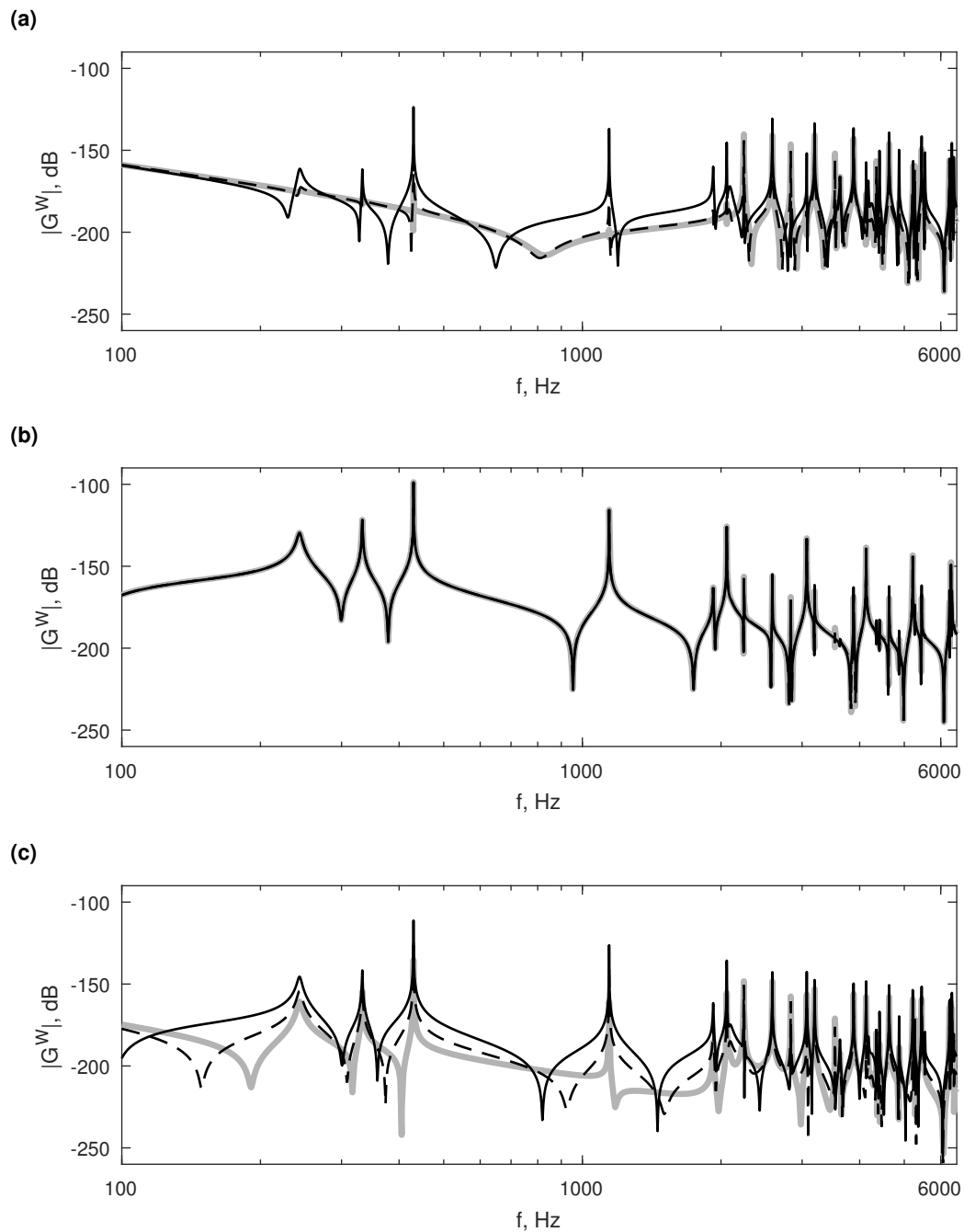


Figure 4.11: Receptances of the C20 wheel for the one-point-contact cases: (a) vertical point-receptance, (b) lateral point-receptance and (c) vertical-lateral cross-receptance. Receptances are evaluated at the three contact points marked in Figure 4.7 (a): (— black)  $y^W = -32$  mm; (- - black)  $y^W = -4$  mm; (— grey)  $y^W = 5$  mm. Magnitudes are given in levels (dB rel. 1 m/N) for the frequency range of 100 Hz to 6.5 kHz.

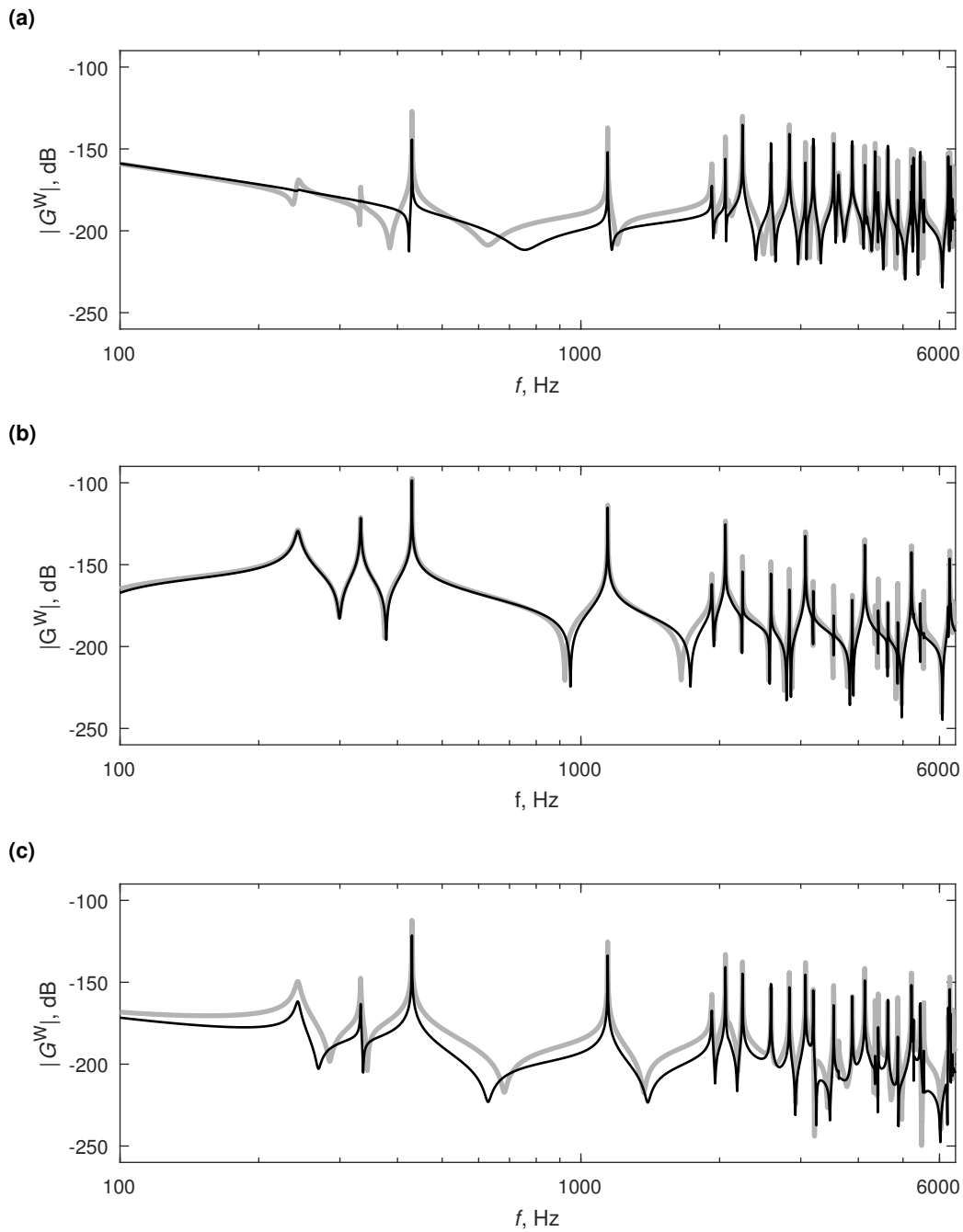


Figure 4.12: Receptances of the C20 wheel for the two-point-contact case: (a) vertical point-receptance, (b) lateral point-receptance and (c) vertical-lateral cross-receptance. Receptances are evaluated at the two contact points marked in Figure 4.8 (a): (— black) contact point 1; (— grey) contact point 2. Magnitudes are given in levels (dB rel. 1 m/N) for the frequency range of 100 Hz to 6.5 kHz.

Receptances presented in Figures 4.11 and 4.12 show that the lateral point-receptance is fairly insensitive to the contact position. This is expected since the lateral dynamics of the wheel are mostly determined by the vertical position  $z^W$  on the wheel. The lateral receptance of point *cp2* in Figure 4.12 (b) shows this dependence. Since the  $z^W$  coordinate of contacts *cp1* and *cp2* differ, their lateral receptances also differ. The other receptances mainly differ in the response amplitudes, but some anti-resonances move in frequency as well. Vertical receptances differ between points, and in some cases, new lower-frequency resonance peaks appear, but with low amplitudes. Finally, the vertical-lateral cross-receptance shows a large spread for different contact points. The cross-receptances are comparable in amplitude to the point-receptances, which points to a strong vertical-lateral coupling dynamics of the wheel. This coupling is the consequence of the wheel asymmetry and is responsible for squeal caused by the geometric-coupling mechanism.

The effects of wheel rotation can be neglected, as shown in a study by Pieringer et al. [82]. In this study, the inclusion of wheel rotation effects did not significantly influence results of the squeal model. Contact forces during squeal development and steady-state squeal were evaluated, and only minor differences were observed. However, effects of wheel rotation on the radiated sound were not evaluated.

As described in Section 4.2, the wheel Green's functions  $g_{ij}^{W,kl}$  are obtained from the receptances  $G_{ij}^{W,kl}$  by means of an inverse Fourier transform, Equation (4.6). The wheel displacement response is then obtained from the discrete convolution, analogous to Equation (4.11) for the case of one-point wheel/rail contact:

$$\xi_i^W(t_d) = - \sum_{j=X}^Z F_j(t_d) g_{ij}^W(0) - \sum_{\tau=0}^{t'_d} \sum_{j=X}^Z F_j(\tau) g_{ij}^W(t'_d - \tau + \Delta t), \quad i = X, Y, Z, \quad (4.15)$$

The negative signs in Equation (4.15) come from the direction of the contact forces acting on the wheel, see Figure 4.3.

In the squeal model by Pieringer [80, 81], two simplifications were made: (1) only the lateral and vertical dynamics of the wheel and rail are considered; (2) the first values of the wheel and rail Green's functions are omitted.

Longitudinal wheel/rail dynamics are not considered to play an important role during squeal. Rudd [90] and Remington [89] found that longitudinal creepage is not a cause of curve squeal (see Section 2.1). Recent findings by Fourie et al. [35] indicate that, in certain cases, longitudinal creepage might lead to squeal, see Section 2.1. However, this is a still insufficiently researched topic, and lateral dynamics are still considered to have the highest importance.

As discussed in Section 4.2, the first value of a Green's function describes the instantaneous local displacement. For this value to be realistic, the wheel and rail models have to be very detailed around the contact point. However, the present wheel FE model is inappropriate and cannot provide an accurate value [80]. The first value of the wheel Green's functions is, therefore, set to zero ( $g_{ij}^{W,kl}(0) = 0$ ). Instead, the instantaneous local displacement is, at least partly, accounted for in the

contact model. Equation (4.15) simplifies to:

$$\xi_i^W(t_d) = - \sum_{\tau=0}^{t'_d} \sum_{j=Y}^Z F_j(\tau) g_{ij}^W(t'_d - \tau + \Delta t), \quad i = Y, Z. \quad (4.16)$$

Equation (4.16) is valid for one-point wheel/rail contact. The same equation for two-point contact is obtained by simplifying Equation (4.12):

$$\xi_i^{W,k}(t_d) = - \sum_{\tau=0}^{t'_d} \sum_{j=Y}^Z \sum_{l=1}^2 F_j^l(\tau) g_{ij}^{W,kl}(t'_d - \tau + \Delta t), \quad i = Y, Z; \quad k = 1, 2. \quad (4.17)$$

The displacement response of the wheel given by Equations (4.16) and (4.17) is dependent only on previous time-step forces. This leads to a simpler solution algorithm in which the current wheel/rail displacement response does not depend on the current time-step forces [80].

### 4.2.3 Rail dynamics

The analysed rail is a BV50-type rail, a common Swedish rail type. The rail was modelled in [80] as a continuously supported rail with the rail pad included in the model.

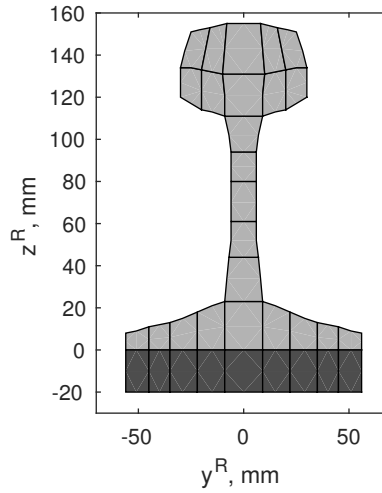


Figure 4.13: Cross-section of the BV50 rail with the FE model mesh.

The two-dimensional cross-section of the rail with the rail pad was modelled using finite elements. The FE mesh is shown in Figure 4.13 where the rail mesh is shown in light grey and the rail pad in dark grey. An analytical wave-type solution was assumed in the longitudinal direction to extend the model in the third dimension. This takes advantage of the constant two-dimensional rail cross-section. The resulting model is referred to as waveguide finite element (WFE) model [73].

The rail receptances were obtained by Pieringer [80, 81] using the WANDS software [73]. Figure 4.14 shows the vertical and lateral point receptances and the vertical-lateral cross receptance for the three rail-head points of the one-point contact cases marked in Figure 4.7 (b). Receptances  $G_{ij}^{R,11}$  and  $G_{ij}^{R,22}$  at contact points *cp1* and *cp2* of the two-point-contact case marked in Figure 4.8 are presented in Figure 4.15.

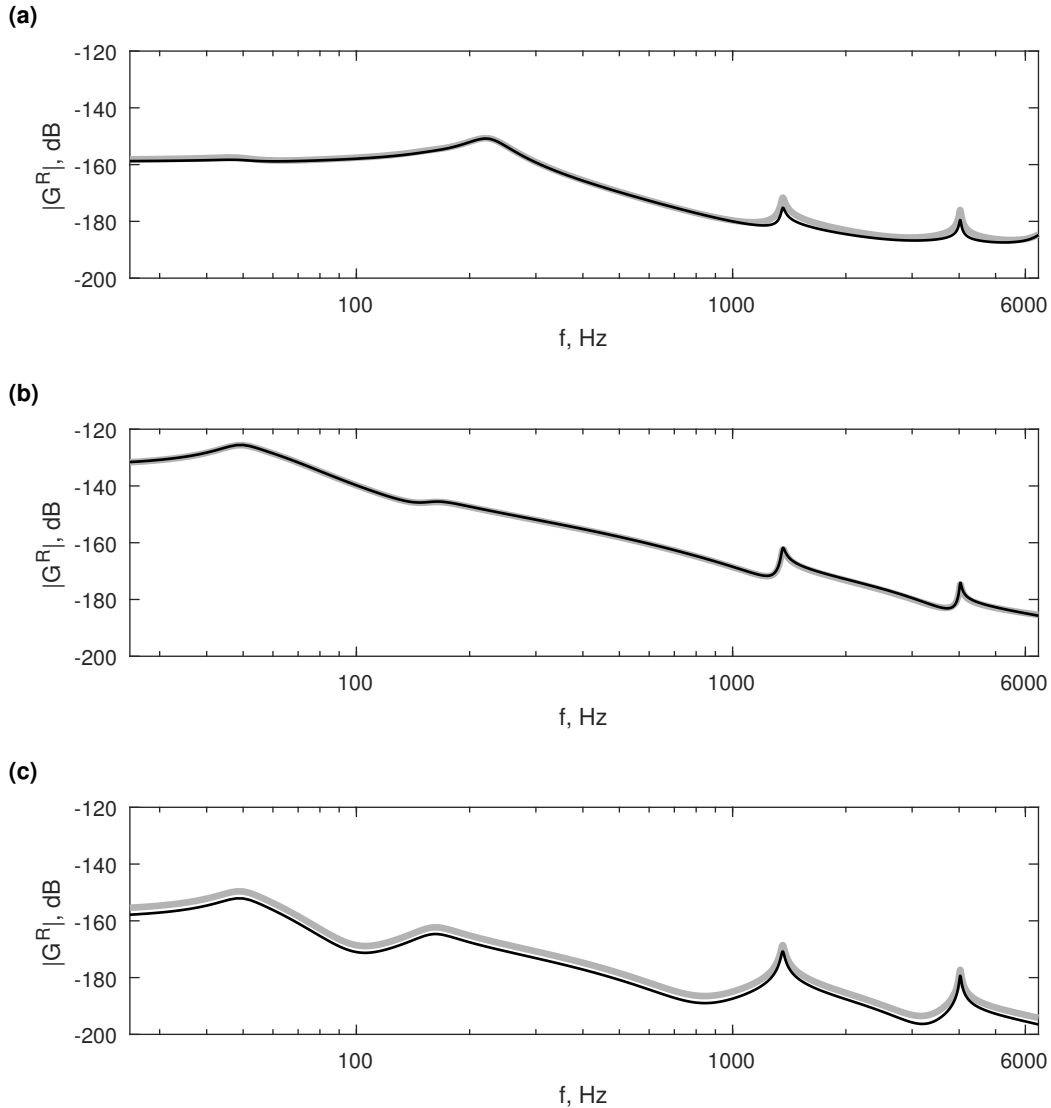


Figure 4.14: Receptances of the BV50 rail for the one-point-contact cases: (a) vertical point-receptance, (b) lateral point-receptance and (c) vertical-lateral cross-receptance. Receptances are evaluated at the three contact points marked in Figure 4.7 (b): (— black)  $y^R = \pm 12$  mm; (— gray)  $y^R = -16$  mm. Magnitudes are given in levels (dB rel. 1 m/N) for the frequency range of 25 Hz to 6.5 kHz.

The rail has considerably fewer resonances than the wheel. Also, the rail vertical-lateral coupling dynamics are not so strongly influenced by the lateral contact po-

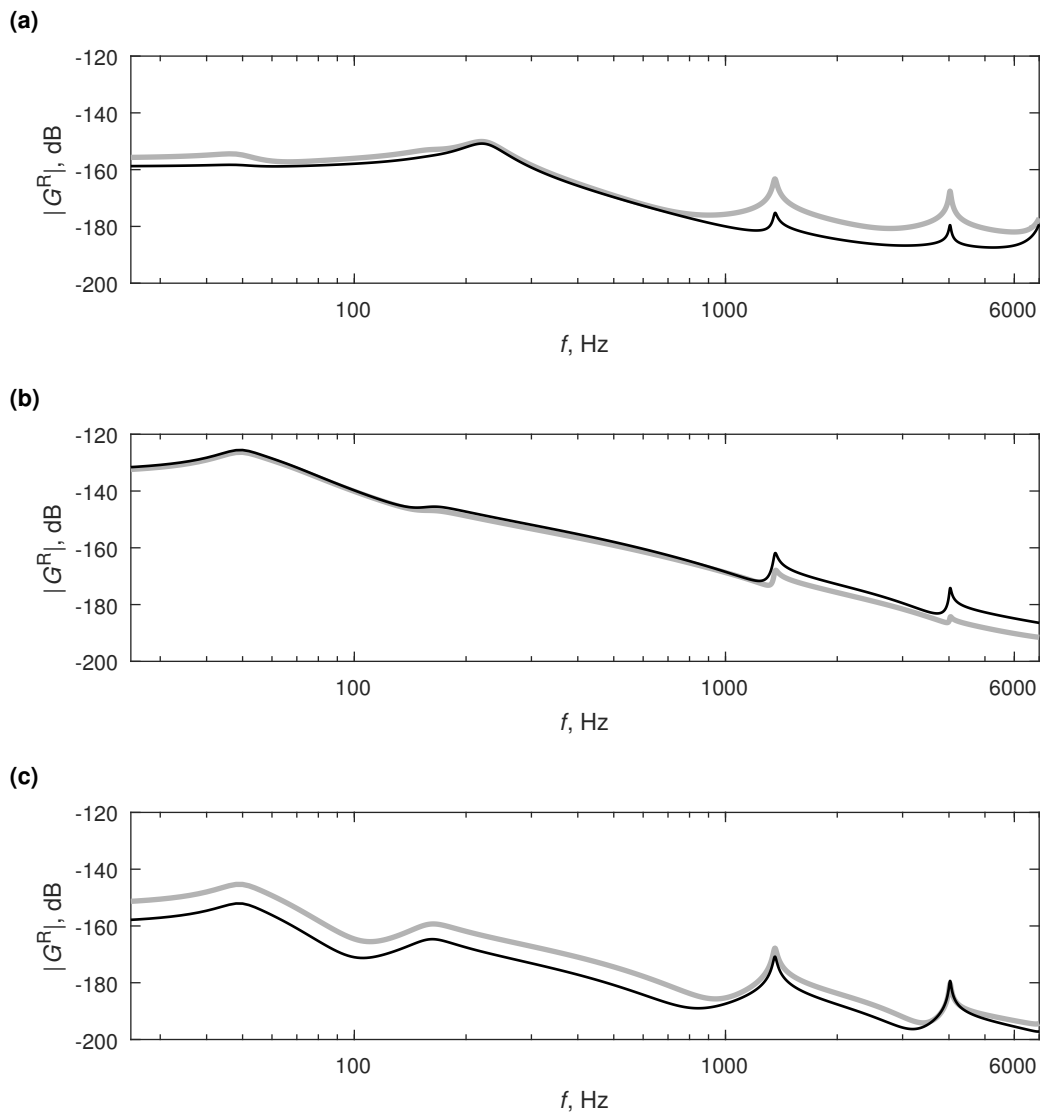


Figure 4.15: Receptances of the BV50 rail for two-point-contact case: (a) vertical point-receptance, (b) lateral point-receptance and (c) vertical-lateral cross-receptance. Receptances are evaluated at the two contact points marked in Figure 4.8 (b): (— black) contact point 1; (— gray) contact point 2. Magnitudes are given in levels (dB rel. 1 m/N) for the frequency range of 25 Hz to 6.5 kHz.

sition on the rail head. This is seen from Figure 4.14 (c) showing the rail vertical-lateral cross-receptance. Figure 4.15 shows higher differences between receptances at contact points of the two-point wheel/rail contact case. The two points are located in significantly different locations on the rail, as shown in Figure 4.9 (b), leading to a different dynamic response. Receptances differ in amplitudes, but all peaks are coincident. In conclusion, the rail may be of lesser importance for curve squeal in the one-point contact case. However, in two-point contact, the rail behaves differently at the two points. This may result in a higher influence of the rail in the

two-point-contact squeal case.

As for the wheel, the rail Green's functions  $g_{ij}^{R,kl,x_0^R+v\tau}$  are obtained from the rail receptances  $G_{ij}^{R,kl}$  utilizing the inverse Fourier transform, Equation (4.6). However, there is a crucial difference between wheel and rail Green's functions. Because the wheel rotation is neglected and the lateral contact position is assumed constant in time, the excitation is fixed to one wheel point. On the rail, however, the excitation travels along the rail with the rolling velocity  $v$ . This effect cannot be neglected. A special kind of Green's functions, called moving Green's functions [40, 74], are, therefore, defined for the rail.

Moving Green's functions describe the displacement response at a point with coordinates  $x_0^R + v\tau$  moving along the rail with velocity  $v$ , away from the excitation at  $x_0^R$ . The moving contact point case can be looked upon as a case where the observer moves along the rail. Both time and spatial information have to be included in the moving Green's functions to describe the rail response accurately. The spatial information, which describes the location of the contact in previous time-steps, does not explicitly appear in the functions. Instead, this information is included in the functions during their construction. Details about the construction of moving Green's functions can be found in [80]. Moving Green's functions were also used by Pieringer et al. [82] to include the effects of wheel rotation. In the case of the rotating wheel, the excitation travels along the wheel circumference.

In analogy to the determination of the wheel response, the convolution for the rail displacement response in the one-point-contact case is given with:

$$\begin{aligned} \xi_i^R(t_d) = & \sum_{j=X}^Z F_j(t_d) g_{ij}^{R,x_0^R+vt_d}(0) \\ & + \sum_{\tau=0}^{t'_d} \sum_{j=X}^Z F_j(\tau) g_{ij}^{R,x_0^R+v\tau}(t'_d - \tau + \Delta t), \quad i = X, Y, Z. \end{aligned} \quad (4.18)$$

Excitation forces are defined positive on the rail (see Figure 4.3) so all terms in Equation (4.18) are positive. As discussed in Section 4.2.2, only the vertical and lateral dynamics are considered and first values in the rail Green's functions are omitted ( $g_{ij}^{R,kl,x_0^R+vt_d}(0) = 0$ ). Equation (4.18) simplifies to:

$$\xi_i^R(t_d) = \sum_{\tau=0}^{t'_d} \sum_{j=Y}^Z F_j(\tau) g_{ij}^{R,x_0^R+v\tau}(t'_d - \tau + \Delta t), \quad i = Y, Z. \quad (4.19)$$

Equation (4.19) is valid for one-point wheel/rail contact. The same equation for two-point contact is obtained by simplifying Equation (4.12):

$$\xi_i^{R,k}(t_d) = \sum_{\tau=0}^{t'_d} \sum_{j=Y}^Z \sum_{l=1}^2 F_j^l(\tau) g_{ij}^{R,kl,x_0^R+v\tau}(t'_d - \tau + \Delta t), \quad i = Y, Z; \quad k = 1, 2. \quad (4.20)$$

### 4.3 The rolling contact model

The general structure of a rolling contact model was discussed in Section 3.2.2. In this section, each sub-model is presented and discussed. Emphasis is on the proposed novelties: the tangential point-contact model, extension to two-point wheel/rail contact, friction model formulation and its extension to non-zero spin creepage.

As was mentioned in Section 4.1.1, the contact problem is solved in the contact coordinate system  $(x^k, y^k, z^k)$  of each contact  $k = 1, 2$ . The formulation of the contact model is presented for the case of one-point wheel/rail contact. The index  $k$  is, therefore, omitted from the equations. The inclusion of two-point contact requires only changes in the normal contact model. These are explicitly mentioned, and the index  $k$  is reintroduced where required.

#### 4.3.1 The normal contact model

The consideration of the normal contact problem starts with the definition of the normal-contact kinematics. Figure 4.16 shows the contact kinematics for the case of two non-conformal surfaces. Not shown in the figure is the  $y^k$ -axis, which points towards the reader. Surfaces in contact are denoted with indices W and R indicating the wheel and the rail, respectively.

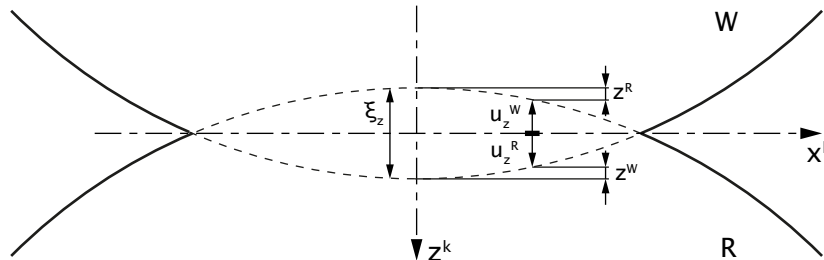


Figure 4.16: Kinematics of two non-conformal surfaces in contact.

The term  $\xi_z = \xi_z^R - \xi_z^W$  is the displacement-response difference between the wheel and the rail at the contact point<sup>4</sup>. Equations (4.16) and (4.19) give the vertical displacements in the one-point wheel/rail contact case. Displacements in the two-point-contact case are given in Equations (4.17) and (4.20). The computed displacements are then transformed from the global to the contact coordinate system using Equation (4.2). In this way, the wheel/rail displacement in the normal contact direction is obtained. The combined normal displacement  $\xi_z$  is constant over the contact area and is evaluated at the point of initial contact.

Undeformed wheel and rail profiles are described with the  $z^W(x, y)$  and  $z^R(x, y)$  terms. Measured wheel and rail profiles, analysed in Sections 4.1.2 and 4.1.3, are

<sup>4</sup>This is also referred to as the combined wheel/rail normal displacement.

considered. Finally, the wheel/rail contact area displacements<sup>5</sup> are denoted with  $u_z^W(x, y)$  and  $u_z^R(x, y)$ . The combined contact area displacement is defined with  $u_z(x, y) = u_z^R(x, y) - u_z^W(x, y)$ .

The distance between points on the wheel and rail surfaces in the vicinity of the initial contact point is provided by the distance function  $d(x, y)$ :

$$d(x, y) = \xi_z + z^R(x, y) - z^W(x, y) + u_z(x, y). \quad (4.21)$$

The value of the distance function defines whether particles of the wheel and rail are in contact. Only positive and zero values are admissible. Negative values signify penetration of the bodies, which is not physical, while positive values indicate that the particles are not in contact.

The distance function for particles with established contact is zero. Equation (4.21) then transforms to:

$$u_z(x, y) = -\xi_z - z^R(x, y) + z^W(x, y), \quad (4.22)$$

which is called the displacement function. The displacement function is valid only for particles at coordinates  $(x, y)$  which are in contact. The solution of Equations (4.21) and (4.22) reveals the contact area shape and size. However, the displacement difference  $u_z(x, y)$  is still unknown, as it depends on the normal contact pressure  $p_z(x, y)$ . To solve the problem, the relationship between pressure and displacement in the contact area has to be defined. Kalker's solution approach [55] is used.

In Kalker's variational contact model [55], the wheel and rail are locally represented with elastic half-spaces. The analytical relationship between pressure and displacement is, therefore, known. Kalker discretised the potential contact area into a finite number of rectangular elements. Displacements and pressure are constant on each element. Figure 4.17 shows the discretisation of the potential contact area  $P$  into  $N_P = n_x \times n_y$  rectangular elements of size  $\Delta x \times \Delta y$ . In simulations of rolling, the longitudinal dimension of the elements has to satisfy the kinematic relation  $\Delta x = v\Delta t$ . This relation ensures that in each time-step of the simulation the contact area moves by one element length.

The kinematic equations are solved for each element  $I \in P$ . The location of element  $I$  is defined by its centre-coordinates  $(x_I, y_I)$ . From the elastic half-space solution, the contact-area displacement difference on element  $I$  is:

$$u_{Iz} = \sum_{J=1}^{N_P} A_{Iz, Jz} p_{Jz}. \quad (4.23)$$

The elastic half-space influence coefficient  $A_{Iz, Jz}$  gives the normal displacement at the centre of element  $I$  due to a unit normal pressure acting on element  $J$ . Pressures

---

<sup>5</sup>Contact-area displacements  $u_z$  are not to be mistaken with the  $\xi_z$  displacement of the wheel and rail. The former are local displacements in the contact area, while the latter are global displacements due to the flexibility of the wheel and the rail.

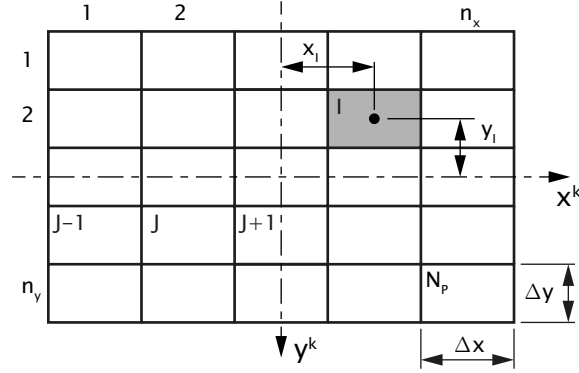


Figure 4.17: Discretisation of the potential contact area  $P$  into  $N_P$  rectangular elements.

on all elements  $J \in P$  influence the displacement of element  $I$ . Due to quasiidentity of the wheel and rail materials discussed in Section 3.2.2, influence coefficients coupling the normal and tangential directions ( $A_{Ix,Jz}$ ,  $A_{Iz,Jx}$ ,  $A_{Iy,Jz}$  and  $A_{Iz,Jy}$ ) are zero. Expressions for the influence coefficients can be found in [55] and [80].

The distance function, Equation (4.21), and the displacement function, Equation (4.22), are written in the discrete form for each element  $I \in P$ :

$$d_I = \xi_z + z_I^R - z_I^W + u_{Iz}, \quad (4.24)$$

$$u_{Iz} = -\xi_z - z_I^R + z_I^W. \quad (4.25)$$

The contact conditions for each element are formulated in terms of the distance function and normal contact pressure [55]:

$$d_I \geq 0, \quad (4.26)$$

$$p_{Iz} \geq 0, \quad (4.27)$$

$$d_I p_{Iz} = 0. \quad (4.28)$$

Equation (4.26) excludes penetration ( $d_I < 0$ ), while Equation (4.27) excludes adhesion ( $p_{Iz} < 0$ ) between the surfaces. Finally, Equation (4.28) tells that pressure and distance cannot both be non-zero at the same time. The contact conditions can be summarised as follows: if element  $I$  is in contact, the distance function is zero, but pressure is non-zero and positive. The opposite is also true: if there is no contact, the distance function is positive, and pressure is zero. To solve the problem defined by Equations (4.23) to (4.28), Kalker developed an iterative procedure named “active set algorithm”, which was implemented in the NORM algorithm [55]. The algorithm iteratively sorts out elements that are in contact and determines the pressure on them. As a result, the contact area shape and size and normal pressure distribution are obtained. The normal contact force is computed from the normal pressure and element dimensions:

$$F_z(t_d) = \sum_{I=1}^{N_P} p_{Iz} \Delta x \Delta y, \quad (4.29)$$

which is a sum of element forces. A detailed description of the algorithm can be found in [55, 80].

### 4.3.2 Normal contact: extension to two-point wheel/rail contact

As discussed in the introduction of Chapter 4, the inclusion of a second contact point requires the definition of an additional contact problem. Contact at the second point occurs only after sufficient approach of the wheel and the rail, as explained in Section 4.1.3. To model this occurrence, the formulation of the contact problem for contact point 2 has to be modified.

The normal contact formulation for contact point 1 remains unchanged since this is the initial contact point. However, the formulation of the normal problem for contact point 2 is extended with the normal distance term  $\delta_z$ . This term, discussed in Section 4.1.3, defines the required approach of the wheel and the rail for contact to occur at *cp2*. The normal distance is introduced in the distance and displacement functions defined in Equations (4.24) and (4.25). The kinematic equations for contact point 2 are then:

$$d_I^2 = \xi_z^2 + z_I^{R,2} - z_I^{W,2} + u_{Iz}^2 + \delta_z, \quad (4.30)$$

$$u_{Iz}^2 = -\xi_z^2 - z_I^{R,2} + z_I^{W,2} - \delta_z. \quad (4.31)$$

Contact point 2 is denoted with the superscript 2. The rest of the normal contact problem formulation for *cp2* remains the same and no changes in contact conditions are needed.

As the combined wheel/rail displacement  $\xi_z^2$ , the normal distance  $\delta_z$  describes the displacement on the global contact level. The same distance value  $\delta_z$  is present on all elements belonging to *cp2*. Equation (4.30) mathematically expresses the fact that the combined wheel/rail displacement  $\xi_z^2$  has to be opposite in sign and at least equal to the normal distance  $\delta_z$  for contact to occur at *cp2*.

### 4.3.3 The tangential contact model

The proposed tangential contact model is a point-contact model, where the contact is treated globally and contact variables are defined for the complete contact. General properties of point-contact models were discussed in Section 3.2.3.

The difference between the tangential point-contact model and Kalker's variational contact model [55] is shown graphically in Figure 4.18. The different nature of the two contact models is readily noticed. Kalker's theory relies on the discretisation of the contact area to model processes on the local contact level, see Figure 4.18 (a). In contrast, the point-contact model considers processes on the global contact level, as shown in Figure 4.18 (b).

In the global view, the variation of contact variables throughout the contact area cannot be described. The contact area shape and size do not directly influence the

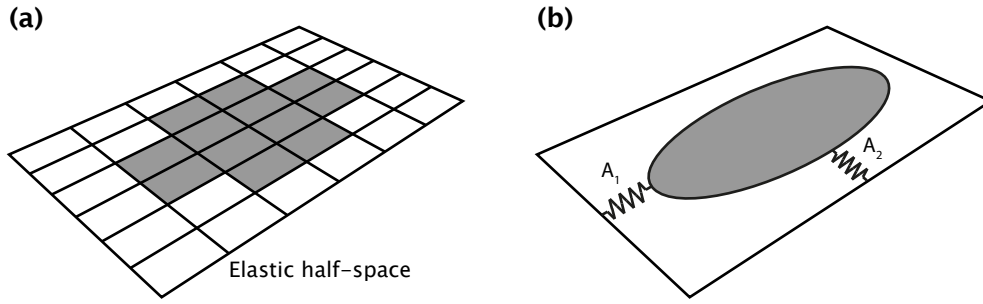


Figure 4.18: Two approaches to contact modelling: (a) discretisation and the elastic half-space assumption in Kalker [55]; (b) point-contact and the global contact elasticity [124].

tangential point-contact model. They are, however, considered in the formulation of the global friction model in Section 4.3.5. The global approach leads to significantly fewer equations that have to be solved. In Kalker's approach, equations that define the tangential problem have to be solved for each element in contact.

Equation (3.3) is the starting point for the definition of the tangential point-contact model. Both the lateral and the longitudinal directions are considered. The tangential contact forces in the current time step  $t_d$  are defined as:

$$F_\tau(t_d) = -\mu_{RF}(s) F_z(t_d) \frac{s_\tau(t_d)}{s(t_d)}, \quad \tau = x, y, \quad (4.32)$$

with the absolute slip velocity in the contact area defined as:

$$s(t_d) = \sqrt{s_x^2(t_d) + s_y^2(t_d)}. \quad (4.33)$$

The longitudinal component  $s_x$  and the lateral component  $s_y$  of the slip velocity  $s$  follow from Equation (3.1). Because the contact is considered globally, contact variables are not dependent on the location in the contact area. The spatial derivative  $\partial u_\tau / \partial x$  is then disregarded and Equation (3.1) simplifies to:

$$s_\tau = w_\tau + \frac{\partial u_\tau}{\partial t}, \quad \tau = x, y. \quad (4.34)$$

The rigid slip term  $w_\tau$  is defined in Equation (3.2), while the partial derivative of the displacement with respect to time is approximated with the finite backward difference:

$$\frac{\partial u_\tau}{\partial t} = \frac{u_\tau(t_d) - u_\tau(t_d - \Delta t)}{\Delta t}, \quad \tau = x, y. \quad (4.35)$$

The terms  $u_\tau(t_d)$  and  $u_\tau(t_d - \Delta t)$  are the current and previous time-step contact displacements, respectively. In the squeal model, the lateral and vertical wheel/rail dynamics are considered. Additional dynamic terms are, therefore, introduced in the slip equation for the lateral direction. As with the contact displacements, the difference between two adjacent time-step values matters for the slip velocity. Taking

that into account and combining Equations (4.34) and (4.35), the final expressions for the slip velocity components are:

$$s_x(t_d) = \left( \gamma_x + \frac{u_x(t_d) - u_x(t_d - \Delta t)}{\Delta x} \right) v, \quad (4.36)$$

$$s_y(t_d) = \left( \gamma_y + \frac{u_y(t_d) - u_y(t_d - \delta t)}{\Delta x} - \frac{\xi_y(t_d) - \xi_y(t_d - \Delta t)}{\Delta x} \right) v, \quad (4.37)$$

where  $\xi_y(t_d) = \xi_y^W(t_d) - \xi_y^R(t_d)$  and  $\xi_y(t_d - \Delta t) = \xi_y^W(t_d - \Delta t) - \xi_y^R(t_d - \Delta t)$  are the current and the previous time-step combined wheel/rail displacements, respectively. Displacements in the one-point wheel/rail contact case are determined from Equation (4.16) and (4.19) for the wheel and rail, respectively. In the case of two-point contact, displacements are determined from Equation (4.17) and (4.20). Equation (4.2) is used to transform the displacements from the global to the contact coordinate system.

The mathematical formulation of the tangential point-contact model consists of two nonlinear equations, given by Equation (4.32). In comparison, Kalker's variational model defines two equations (linear or nonlinear) for each element in contact. In Kalker's model, the discretisation enables for a detailed description of contact processes, but at high computational cost. The point-contact model considerably reduces the computational cost by considering the contact globally and avoiding discretisation. The mathematical formulation of the two contact models directly reflects the differences between the models.

The price for improved efficiency is the steady-state nature of the point-contact model. This may not be obvious since the transient term  $\partial u_\tau / \partial t$  is retained in Equation (4.34). However, the omission of the spatial derivative  $\partial u_\tau / \partial x$  results in the inability to describe the distribution of contact variables in the contact area. According to Knothe and Groß-Thebing [58], a model unable to describe the variation of variables on a particle travelling through the contact cannot be considered transient. Transient contact phenomena may, therefore, not be properly described by the tangential point-contact model as they are with Kalker's model [55].

To completely define the point-contact model, two quantities used in Equations (4.32), (4.36) and (4.37) have to be defined. Firstly, a method is proposed for the determination of the global contact displacements  $u_\tau$ . Secondly, the friction model  $\mu_{RF}(s)$  is defined in a rigorous manner.

#### 4.3.4 Determination of the contact compliances

Because contact is considered on the global level, contact displacements are defined in global terms as well. The contact elasticity is modelled with two springs, one for each tangential direction, as shown in Figure 4.18. Springs are defined with their compliances  $A_\tau$ , and the contact displacements are calculated as:

$$u_\tau = A_\tau F_\tau, \quad \tau = x, y. \quad (4.38)$$

If the spring compliances are known, the contact displacements can be easily obtained. A method is proposed for the determination of the contact spring compliances  $A_\tau$ . The method relies on the following assumptions:

- the wheel and rail can be locally represented with elastic half-spaces;
- the tangential contact forces do not change significantly between the two adjacent time steps  $t_d - \Delta t$  and  $t_d$ ;
- stick vanishes in the contact area;
- the contact pressure and traction distributions are ellipsoidal.

The first assumption enables the determination of displacements at different points in the contact area. The same assumption is already used in the normal contact model. The other assumptions define the load on the elastic half-space. By assuming that the contact forces do not change significantly between adjacent time steps, the compliances can be determined based on results from the previous time-step. This avoids an additional loop that would otherwise be required to determine compliances with the current time-step forces. The third assumption defines the distribution of tangential tractions. In the full-slip case, tangential tractions have the same distribution as the normal pressure. Finally, the last assumption enables for a simple computation of mean displacement in the contact.

The method starts from the normal contact problem solution and the resulting normal pressure. The following steps are performed in each simulation time-step and for each contact point to determine the current contact compliances.

1. Compute the full-slip tangential-traction distribution from the previous time-step tangential forces  $F_\tau(t_d - \Delta t)$ , the current time-step normal force  $F_z(t_d)$  and the normal pressure distribution  $p_{Iz}$ :

$$p_{I\tau}^{fs} = p_{Iz} \frac{F_\tau(t_d - \Delta t)}{F_z(t_d)}, \quad \tau = x, y. \quad (4.39)$$

2. Compute the elastic half-space deformation field (on contact elements  $I$ ) caused by the tangential tractions determined in step 1:

$$u_\tau^{fs} = A_{\tau x} p_{Ix}^{fs} + A_{\tau y} p_{Iy}^{fs}, \quad \tau = x, y, \quad (4.40)$$

where  $A_{\tau\kappa}$  ( $\tau = x, y$ ;  $\kappa = x, y$ ) are the elastic half-space influence coefficients.

3. Compute the mean displacement  $\bar{u}_\tau^{fs}$  of the contact area using Equation (4.42), see discussion below.
4. Compute the contact compliances:

$$A_\tau = \frac{\bar{u}_\tau^{fs}}{F_\tau(t_d - \Delta t)}, \quad \tau = x, y. \quad (4.41)$$

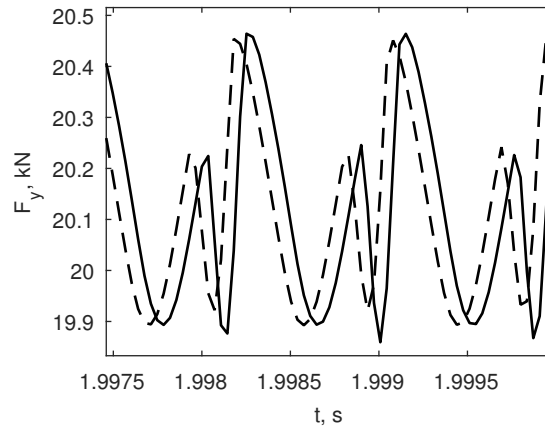


Figure 4.19: Detail of the lateral force time-history for two tangential-contact compliances: (—) Equation (4.41); (- -) double value of Equation (4.41). Squeal case:  $\Delta y^{WR} = -10$  mm,  $\gamma_y = -0.01$ ,  $\mu = 0.3$ .

To compute the mean displacement  $\bar{u}_\tau^{fs}$  of the contact area, the assumption of ellipsoidal distribution of tractions is used. It is also implicitly assumed that the contact area is elliptical or quasi-elliptical. As a result, the distribution of displacements is also elliptical. The mean displacement value is then obtained using:

$$\bar{u}_\tau^{fs} = \frac{V_{hel}}{A_{el}} = \frac{\frac{4}{6}\pi ab \cdot \max(u_\tau^{fs})}{\pi ab} = \frac{2}{3}\max(u_\tau^{fs}), \quad \tau = x, y, \quad (4.42)$$

where  $a$  and  $b$  are the contact ellipse semi-axes. In Equation (4.42), the sum of displacements is calculated as the half-ellipsoid volume  $V_{hel}$ . When this volume is divided by the contact ellipse area  $A_{el}$ , the mean displacement value is obtained.

Contact compliances determined using the proposed method depend nonlinearly on the contact forces. The scaling in step 1 takes into account that tangential forces can be well under the traction force limit. Therefore, the normal pressure is scaled with  $F_\tau/F_z$ , rather than with the friction coefficient  $\mu$ .

Assumptions used in the method introduce errors, but the squeal model seems to be insensitive to variations in the contact compliances. This is at least true for the main frequency components and overall amplitude of the contact force. In Figure 4.19, a detail of the time-history of the lateral contact force is presented. Results were obtained for two different contact-compliance values. One was obtained directly from Equation (4.41), while the other was double of the first value. Despite a two-fold difference in compliances, the amplitude and main frequency components of the contact force are not significantly affected. In conclusion, the error introduced by the assumptions can be neglected.

### 4.3.5 Determination of the friction model

The contact area gradually transitions from full-stick to full-slip contact conditions with increasing creepage. This results in a gradual build-up of tangential forces from zero to the traction bound  $\mu F_z$ . Unfortunately, the full-stick to full-slip transition cannot be directly described by the tangential point-contact model. This transition is, therefore, included in the friction curve used in the point-contact model. Due to the continuous nature of the transition, the friction model is also continuous and is referred to as regularised friction (RF).

When compared to the Coulomb friction model used in Kalker's variational theory, the regularised friction model is a global model that describes friction properties of the complete contact area. In Kalker's model, the Coulomb friction model represents a local model that defines friction properties on the contact element level, see Figure 4.20. As a consequence, slip in the Coulomb and the regularised friction model do not have the same physical meaning. In the Coulomb model, slip velocity represents micro-slip between contact elements. In contrast, slip velocity in the regularised friction model represents the slip of the complete contact area.

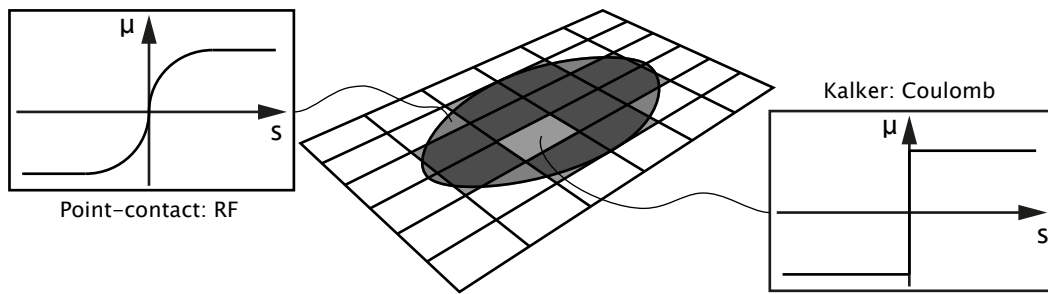


Figure 4.20: Local and global friction models and the level of discretisation.

For the local and global friction models to describe the same friction properties, the two models must have a rigorous and well-defined relation. Therefore, a method for the determination of the RF model is proposed. The method uses Kalker's variational theory and takes into account the contact area shape and size.

An RF model is determined for each value of the Coulomb friction coefficient and for each contact case that leads to a different contact area shape and size. The lateral creepage input into Kalker's variational model is defined to vary according to:

$$\gamma_y^{RF} = \gamma_y^{lim} \frac{t}{t_{end}}, \quad (4.43)$$

where the creepage limit is  $\gamma_y^{lim} = -0.05$ , and the end time is  $t_{end} = 2$  s. The wheel and rail dynamics are not considered and the wheel/rail displacement response terms are disregarded, i.e.  $\xi_z = \xi_y = 0$ . The lateral contact force  $F_y^{RF}$  is obtained from Kalker's contact model for each value of the lateral creepage. The normal contact force  $F_z^{RF}$  is constant since there are no dynamic effects.

Although Kalker's model is transient, a steady-state solution is assumed in each time step. This assumption is valid as long as the input creepage is slowly varying

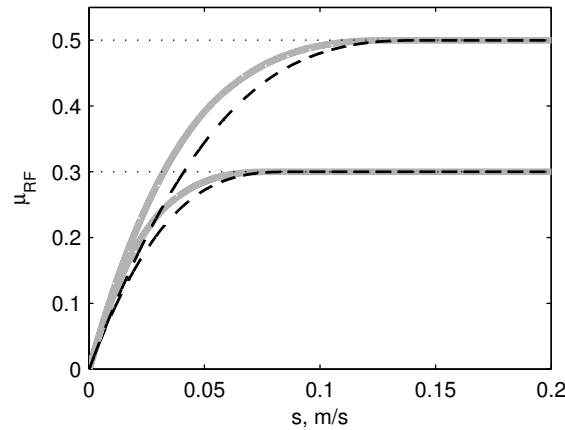


Figure 4.21: Regularised friction curves for friction coefficient values  $\mu = 0.3$  and  $\mu = 0.5$ , and two one-point-contact cases: (— grey)  $\Delta y^{WR} = -15$  mm; (- - black)  $\Delta y^{WR} = -10$  mm.

in time. Quasi-steady-state contact conditions are then achieved in every time step. The RF friction model is defined with the  $\mu_{RF}(s)$  characteristic<sup>6</sup>:

$$\mu_{RF}(s) = \frac{F_y^{RF}(s)}{F_z^{RF}}. \quad (4.44)$$

The gross slip velocity of the contact is related to the lateral creepage via the rolling velocity  $s = \gamma_y^{RF} v$ . Since the wheel and rail dynamics are not included, the slip velocity is equal to the rigid slip of Equation (3.2).

In Figure 4.21 four regularised friction curves are presented. The models are obtained for different values of the Coulomb friction coefficient and different wheel/rail contact cases. The contact case defines the exact wheel/rail profiles at the contact location, which influence the contact area shape and size. Besides a higher asymptotic value, a higher friction coefficient results in a longer transition from full-stick to full-slip contact conditions. The contact geometry mainly influences the shape of the transition region. Some influence of the contact shape on the point at which curves reach the asymptotic value is also noticed.

### 4.3.6 Regularised friction: extension to non-zero spin creepage

Due to the formulation of the tangential point-contact model and the way the regularised friction model is determined, the engineering model is not able to consider cases with non-zero spin creepage. As discussed in Section 2.1, spin creepage becomes significant in contact cases with significant contact angle values. The contact angle is especially high for contact located near or at the wheel flange, as in the

<sup>6</sup>The regularised friction model, calculated as the ratio of the lateral and vertical force is often called “traction coefficient” in the literature specific to rail vehicle dynamics.

two-point-contact case of Section 4.1.3. To be able to analyse the two-point-contact case properly, the engineering model has to be extended to non-zero spin creepage.

Non-zero spin creepage is included in the tangential point-contact by extending the regularised friction model. In the extended regularised friction model, spin creepage is included as a contact property. The friction model is then a function of slip velocity and spin creepage. Equation (4.44) takes the form:

$$\mu_{RF}(s, \gamma_\omega) = \frac{F_y^{RF}(s, \gamma_\omega)}{F_z^{RF}}. \quad (4.45)$$

The main difference between Equations (4.44) and (4.45) is how the lateral force  $F_y^{RF}$  is determined. In Equation (4.44), the transient solution is used and assumed to be equal to the steady-state solution due to the slow variation of lateral creepage. However, the transient solution results in  $\mu_{RF}(s=0, \gamma_\omega) = 0$  for any value of spin, which is incorrect. Namely, the effect of spin creepage cannot be seen in the immediate time step when spin is applied. Therefore, in Equation (4.45), the real steady-state solution for  $F_y^{RF}$  has to be obtained in order to correctly include the influence of spin.

The steady-state solution for the lateral contact force is obtained by running Kalker's transient model sufficiently long for the result variables to reach a stable solution. Kalker's model is run for each slip-velocity and spin-creepage value. A relatively small number of spin-creepage values can be used as friction curves for intermediate values can be interpolated.

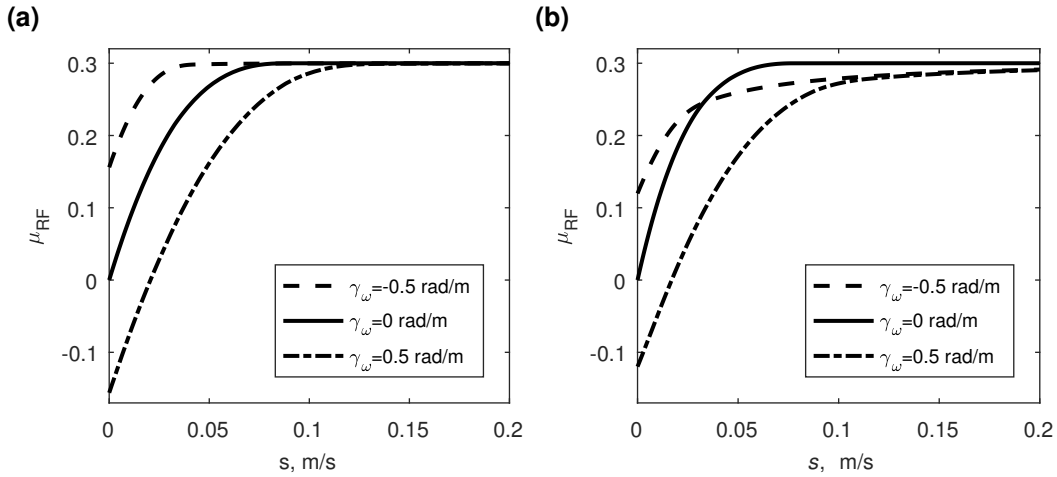


Figure 4.22: Regularised friction curves for  $\mu = 0.3$  friction coefficient, different spin creepage values and one-point wheel/rail contact cases: (a)  $\Delta y^{\text{WR}} = -5 \text{ mm}$  case; (b)  $\Delta y^{\text{WR}} = -10 \text{ mm}$  case: (- - -)  $\gamma_\omega = -0.5 \text{ rad/m}$ ; (—)  $\gamma_\omega = 0 \text{ rad/m}$ ; (-.-)  $\gamma_\omega = 0.5 \text{ rad/m}$ .

The regularised friction model defined with Equation (4.45) is a surface dependent on slip velocity in one direction and spin creepage in the other. Figure 4.22 presents regularised friction curves for different values of spin and two one-point

wheel/rail contact cases. Even though the complete model is a surface, only three curves per contact case are shown for simplicity: for  $-0.5$ ,  $0$  and  $0.5$  rad/m spin. A similar influence of spin on friction curves was also observed by Huang et al. [47].

In free straight line rolling with  $\gamma_\omega = 0$  rad/m, the complete contact area is in stick, global slip is zero and  $\mu^{RF}(s = 0, \gamma_\omega = 0) = 0$ . For non-zero spin, however, the friction model will have non-zero values at zero global slip. The explanation for this behaviour lies in the combination of the nature of rolling contact, the rotational character of spin and the shape of the contact area. All three factors are explained with the example given in Figure 4.23. This figure presents the distribution of the stick and slip regions in the contact for a case with pure spin. Contact case  $\Delta y^{WR} = -15$  mm is considered with  $\gamma_\omega = 0.5$  rad/m, zero longitudinal and lateral creepage and  $\mu = 0.3$ . The stick/slip distributions are obtained using Kalker's contact model without consideration of the wheel/rail dynamics.

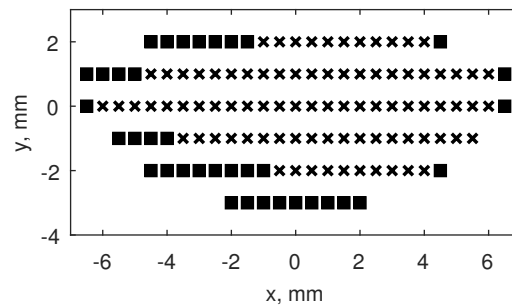


Figure 4.23: Stick and slip distribution in the contact area for the one-point-contact case  $\Delta y^{WR} = -15$  mm with pure spin creepage  $\gamma_\omega = 0.5$  rad/m: (■) slip zones; (×) stick zones.

Tangential load and displacement build-up on a particle as it travels through the contact. Particles are continually entering the contact area at the leading edge and, gradually, they take up more contact loads. Consequentially, the rear of the contact is more loaded than the front: the loading is asymmetric about the  $y$ -axis. Such is the nature of the rolling contact. As shown in Figure 4.23, even with pure spin the front of the contact is dominantly in stick (lower loads), while the rear is in slip (higher loads). The rotational character of spin causes the partial lateral forces in the front and rear of the contact to have different directions. Due to higher load in the rear, the lateral force in the rear is higher than the front one. In combination, the different signs and values of the partial forces lead to a non-zero net lateral force (i.e. non-zero friction). Finally, the exact influence also depends on the contact area shape since spin causes higher relative motion at points further away from the contact centre.

In the longitudinal direction, this behaviour is much less pronounced since the contact loading and contact area are often symmetric about the  $x$ -axis. This symmetry leads to cancellation of the spin-induced forces from different sides of the contact. However, if the contact would be asymmetric about the  $x$ -axis, spin would influence the longitudinal forces as well.

The geometry of the contact area has a significant influence on the regularised friction curves for non-zero spin. Still, small differences in the contact area do not influence the curves significantly. Only curves for contact cases  $\Delta y^{\text{WR}} = -5$  mm and  $\Delta y^{\text{WR}} = -10$  mm are presented in Figure 4.22. The -5 and -15 mm cases have almost identical regularised friction curves as these cases have a similar contact area shown in Figure 4.24 (a) and (c). In comparison, the -10 mm case friction curve differs significantly as the case shows an area consisting of three distinct patches. In general, the influence of spin on the regularised friction curves depends on the combination of asymmetry in shape and loading of the contact.

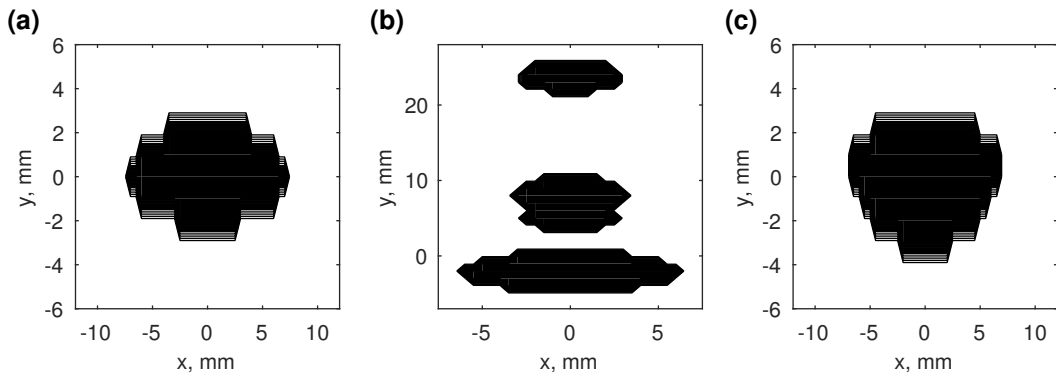


Figure 4.24: Contact area shapes for the analysed one-point wheel/rail contact cases: (a)  $\Delta y^{\text{WR}} = -5$  mm; (b)  $\Delta y^{\text{WR}} = -10$  mm; (c)  $\Delta y^{\text{WR}} = -15$  mm. Discontinuous edges of the areas are due to the resolution of the contact area discretisation.

The proposed formulation of the friction model opens new possibilities. Firstly, measured friction curves can be used in the model. Real cases can then be evaluated without the need to approximate the friction model. Secondly, spin creepage can be considered as a contact property and is, therefore, included in the friction model. These possibilities show that simpler contact models can be extended to more complex cases. Measured data contain much more contact-property information (e.g. roughness) and environmental information (e.g. contact pollution). This information is hard or even impossible to model, but it may be possible to include it in the friction model in the same manner as spin.

Finally, the tangential point-contact model does not require any changes to account for spin creepage effects. The only change happens in the model implementation, where an additional interpolation selects the appropriate regularised friction curve for a given spin creepage value. Equation (4.32) defining the point-contact model can be written in the general form, which includes spin creepage as:

$$F_{\tau}(t_d) = -\mu_{RF}(s, \gamma_{\omega}) F_z(t_d) \frac{s_{\tau}(t_d)}{s(t_d)}, \quad \tau = x, y. \quad (4.46)$$

## 4.4 Sound radiation from a railway wheel

Curve squeal is a noise disturbance and, as such, its severity is best judged from its sound levels. During squeal, the vibration level of the railway wheel is considerably higher than that of the rail [110]. Combined with its high sound-radiation efficiency [100, 104], the wheel is evidently the dominant noise source during squeal. Therefore, to predict squeal severity, only the sound radiation from the wheel is evaluated.

Evaluation of the radiated sound can be computationally expensive, as is the case with the boundary-element-method (BEM) approach. For engineering purposes, a fast and simple to use radiation model is preferred, even at some cost of accuracy. For sound radiation from the railway wheel, a suitable engineering model was developed by Thompson and Jones [102, 104]. The model is also implemented in the TWINS software [102, 103].

The model by Thompson and Jones is based on modal expansion techniques. Radiation efficiencies of different wheel modes were obtained from BEM analyses. The radiated sound field was evaluated over a spherical mesh surrounding the wheel model [104]. Radiation efficiencies of modes were computed for a defined frequency range, and analytical functions were then fitted to the computed data. These functions take into account the wheel geometry so that the model applies to different wheels. The determined analytical functions for the radiation efficiencies are the backbone of the sound radiation model.

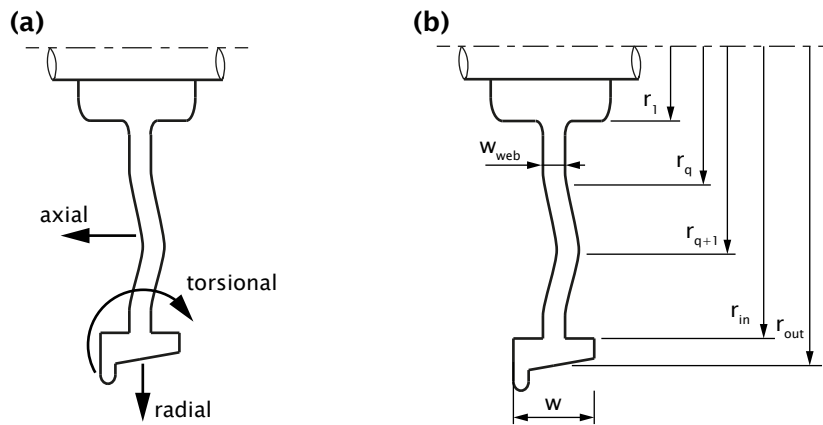


Figure 4.25: Railway wheel cross-section: (a) possible motions; (b) dimensions of the sound radiation surfaces.

Contributions to the overall radiated sound were identified for the axial, radial and torsional motion of the wheel cross-section. Wheel cross-section motions are shown in Figure 4.25 (a). Vibrations of the wheel surface in the three directions are described with velocity fields  $\tilde{v}_a^2$ ,  $\tilde{v}_r^2$  and  $\tilde{v}_t^2$ . The model groups wheel modes according to the number of nodal diameters  $n$ . The radiated sound power  $W^W$  at

frequency  $f$  is evaluated as a sum of contributions from modes with the same  $n$ :

$$W^W(f) = \rho c_0 \sum_n \left[ \sigma_a(n, f) \sum_{q=1}^{N_a} \left( S_{aq} \overline{\tilde{v}_{aq}^2}(n, f) \right) + \sigma_r(n, f) S_r \overline{\tilde{v}_r^2}(n, f) + \sigma_t(f) S_t \overline{\tilde{v}_t^2}(n, f) \right], \quad (4.47)$$

where  $c_0$  is the speed of sound in air and  $\rho$  is the air density. The axial, radial and torsional motion radiation efficiencies are  $\sigma_a$ ,  $\sigma_r$  and  $\sigma_t$ , respectively. Surface areas from which sound is radiated due to the three cross-section motions are denoted with  $S_{aq}$ ,  $S_r$  and  $S_t$ . The axial surface is divided into  $N_a$  annular surfaces  $S_{aq}$ , each defined with two radii  $r_q$  and  $r_{q+1}$ , where  $r_1 \leq r_q < r_{out}$ . Figure 4.25 (b) shows the main dimensions of the wheel cross-section from which the surface areas are determined.

Next, the analytical functions for the axial, radial and torsional radiation efficiencies are presented. Surface areas and the velocity field on the analysed C20 wheel are also defined.

#### 4.4.1 Radiation efficiencies

The radiation efficiencies are functions of frequency  $f$  and the number of nodal diameters  $n$ . The expressions for the radiation efficiencies presented here are taken from [103].

##### Axial motion

The axial motion radiation efficiency has the form of a multipole [104]:

$$\sigma_a(n, f) = \frac{1}{1 + \left( \frac{f_{ca}(n)}{f} \right)^{2n+4}}, \quad (4.48)$$

where  $f_{ca}$  is the critical (transition) frequency for the axial direction:

$$f_{ca}(n) = \frac{c_0 \kappa(n)}{2\pi r}. \quad (4.49)$$

The radius  $r$  is the nominal rolling radius of the wheel and the coefficient  $\kappa$  is defined as:

$$\kappa(n) = 1.9 + 1.015n - 0.0189n^2. \quad (4.50)$$

Both the radiation efficiency and the critical frequency are dependent on the number of nodal diameters  $n$ , i.e. the wheel mode shape.

### Radial motion

The radiation efficiency for the case of radial motion is more complex due to sound cancellation caused by the wheel geometry [104]:

$$\sigma_r(n, f) = \begin{cases} \frac{\Gamma}{1 + \left(\frac{f_{r2}(n)}{f}\right)^2}, & \text{for } n = 0, \\ \frac{\Gamma}{1 + \left(\frac{f_{r1}(n)}{f}\right)^{2n}} \cdot \frac{1}{1 + \left(\frac{f_{r2}(n)}{f}\right)^2}, & \text{for } n > 0, \end{cases} \quad (4.51)$$

where the critical frequencies  $f_{r1}$ ,  $f_{r2}$  and  $f_{r3}$  are:

$$f_{r1}(n) = \frac{120n}{\sqrt{\frac{r}{0.42}}}, \quad (4.52)$$

$$f_{r2} = \frac{800}{\sqrt{\frac{r}{0.42}}}, \quad (4.53)$$

$$f_{r3}(n) = \frac{280 + 150n}{\sqrt{\frac{r}{0.42}}}. \quad (4.54)$$

The parameter  $\Gamma$  takes into account the cancellation between the outer and the inner tyre<sup>7</sup>:

$$\Gamma = \begin{cases} \sqrt{\frac{S_{out} - S_{in}}{S_{out} + S_{in}}}, & \text{for } f < f_{r3}, \\ 1, & \text{for } f > f_{r3}, \end{cases} \quad (4.55)$$

with the outer and inner tyre surfaces calculated from:

$$S_{out} = 2\pi r w, \quad (4.56)$$

$$S_{in} = 2\pi r_{in} (w - w_{web}). \quad (4.57)$$

### Torsional motion

The radiation efficiency for the torsional motion is not dependent on the number of nodal diameters:

$$\sigma_t(f) = \frac{1}{1 + \left(\frac{f_{ct}}{f}\right)^4}, \quad (4.58)$$

where the critical frequency  $f_{ct}$  is:

$$f_{ct} = \frac{2c_0}{\pi w}. \quad (4.59)$$

The contribution of the torsional motion to the overall sound power is neglected [103]. Therefore, the term  $\sigma_t(f) S_t \tilde{v}_t^2$  in Equation (4.47) is assumed to be zero.

<sup>7</sup>The outer tyre surface is the outer cylindrical surface on which the wheel runs. The inner tyre consists of two surfaces opposite to the tyre and facing towards the wheel axis. They are split by the wheel web.

### 4.4.2 Sound radiation surfaces

Figure 4.26 shows the cross-section of the C20 wheel. Dots on the cross-section boundary represent the FE nodes of the model. Main dimensions that define the sound radiation surface-areas are specified in the figure.

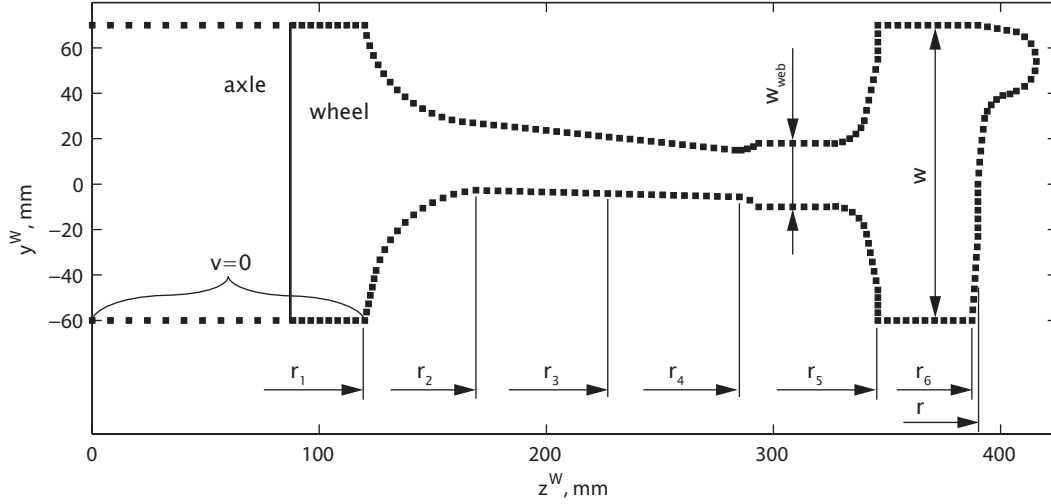


Figure 4.26: C20 wheel cross-section nodes and division into axial-surface sections.

The axial surface of the wheel is divided into five annular surfaces  $S_{aq}$  bounded by radii  $r_{q+1}$ ,  $q = 1, \dots, 5$ . The largest part of the axial surface belongs to the wheel web, and only a small portion belongs to the wheel tyre axial surface. Surface areas of the annuli are calculated from:

$$S_{aq} = 2\pi (r_{q+1} - r_q), \quad q = 1, \dots, 5. \quad (4.60)$$

The surface areas from which sound is radiated due to radial motion are the outer and inner tyre surfaces:

$$S_r = 2\pi [rw + r_5 (w - w_{web})]. \quad (4.61)$$

Even if torsional motion is not considered, the torsional motion surface-area is defined nonetheless. Torsional (angular) velocity has the dimension of rad/s. Therefore, the corresponding surface area has to be expressed in  $\text{m}^4$  to obtain volume velocity ( $\text{m}^3/\text{s}$ ). The area consists of the outer and inner wheel tyre surfaces of the two side walls of the tyre:

$$S_t = \frac{\pi}{6} [rw^3 + r_5 (w^3 - w_{web}^3) + (r + r_5) (r - r_5)^3]. \quad (4.62)$$

### 4.4.3 Wheel velocity field

Equation (4.47) weighs the surface-velocity fields with corresponding surface areas and radiation efficiencies. The velocity fields are expressed as spatially averaged,

mean-square velocities  $\overline{\tilde{v}^2}$ . They are computed from velocities on nodes of the wheel cross-section in direction  $y^W$  for axial motion, and direction  $z^W$  for radial motion.

The complex velocity in the degree of freedom  $i$  due to the complex excitation in direction  $j$  at the nominal contact point is obtained from:

$$v_i(n, f) = 2\pi i f \sum_j G_{ij}^W(n, f) \hat{F}_j(f). \quad (4.63)$$

In the receptances  $G_{ij}^W$  defined with Equation (4.13), only modes with the same number of nodal diameters  $n$  are included. The velocity field is, therefore, separately evaluated for every  $n$ . The wheel is excited by vertical and lateral forces which are described with their complex amplitude spectra  $\hat{F}_j(f)$ ,  $j = Y, Z$ . As the longitudinal wheel/rail dynamics are not considered in the squeal model, circumferential excitation is disregarded. Equation (4.63) can now be written as:

$$v_i(n, f) = 2\pi i f \left[ G_{iY}^W(n, f) \hat{F}_Y(f) + G_{iZ}^W(n, f) \hat{F}_Z(f) \right]. \quad (4.64)$$

The receptances  $G_{iY}^W$  and  $G_{iZ}^W$  give the response in the degree of freedom  $i$  due to lateral and vertical excitation at the nominal contact point. The degrees of freedom  $i$ , for which the velocity field is evaluated, depend upon the wheel surface and the motion direction under consideration.

In the case of two-point wheel/rail contact, the surface velocity field has to include the influence of excitation at the second contact point. Equation (4.64) then expands to:

$$v_i(n, f) = 2\pi i f \left[ G_{iY}^{W,1}(n, f) \hat{F}_Y^1(f) + G_{iZ}^{W,1}(n, f) \hat{F}_Z^1(f) \right. \\ \left. + G_{iY}^{W,2}(n, f) \hat{F}_Y^2(f) + G_{iZ}^{W,2}(n, f) \hat{F}_Z^2(f) \right], \quad (4.65)$$

where superscripts 1 and 2 denote the contact point.

The mean-square velocity at the degree of freedom  $i$  is determined according to:

$$\tilde{v}_i^2(n, f) = \begin{cases} |v_i(n, f)|^2, & \text{for } n = 0, \\ 0.5|v_i(n, f)|^2, & \text{for } n \neq 0. \end{cases} \quad (4.66)$$

Factors 1 and 0.5 in Equation (4.66) are the mean-square values of  $\sin(n\varphi)$  for  $n = 0$  and  $n \neq 0$ , respectively. The sine term describes the velocity field along the wheel circumference. Spatial averaging is performed over  $n_i$  degrees of freedom  $i$ :

$$\overline{\tilde{v}^2}(n, f) = \frac{\sum_i \tilde{v}_i^2(n, f)}{n_i}. \quad (4.67)$$

The wheelset axle is included in the model but is considered fixed, and its surface velocities are zero. Because of the negligible amplitudes of wheel surface velocities near the axle, the surface area  $r_1^2\pi$  is not considered in Equation (4.60).

#### 4.4.4 The boundary element model

At this point, the boundary element model of the C20 wheel is described. The boundary element (BE) model is used in Section 5.1 to validate the implementation of the simple sound-radiation model.

The C20 wheel BE model consists of 8111 elements, of which 2528 triangular and 5583 quadrangle elements. The wheel is lifted so that its tread is 0.15 m (approx. the rail height) above the hard reflecting ground. This lift accounts for the position of the wheel on the rail. The sound field is evaluated at 321 points on a half-sphere surrounding the wheel. Evaluation points are located far enough from the wheel for the far-field assumption to be valid. The wheel BE model and the evaluation half-sphere are shown in Figure 4.27 (a).

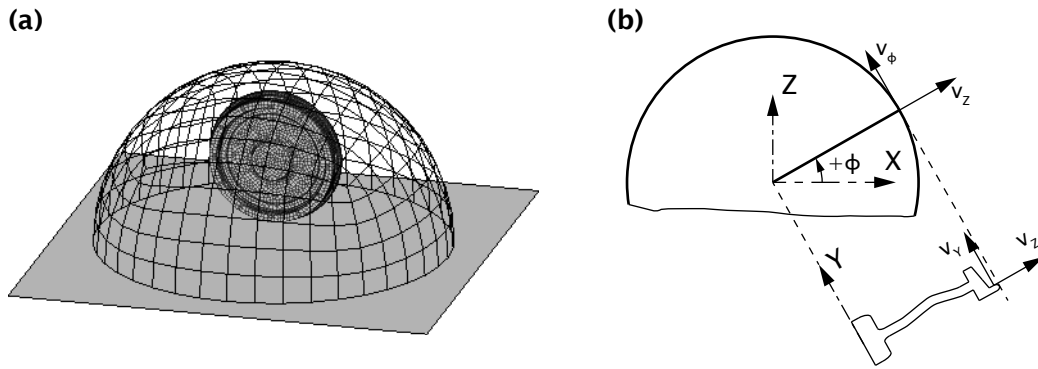


Figure 4.27: C20 wheel boundary element model: (a) BE mesh, the reflecting ground and the sound-field evaluation mesh; (b) coordinate transformation.

Velocities on nodes of the BE model are determined from the wheel FE model velocities. The FE model velocities are determined using Equation (4.64) or (4.65), and then transformed from the wheel coordinate system  $(x, y, \varphi)$ <sup>8</sup> to the BE model coordinate system  $(X, Y, Z)$ <sup>9</sup>. The BE model velocities are obtained from velocities  $v_x$ ,  $v_z$  and  $v_\varphi$  for each circumferential angle  $\varphi$  and number of nodal diameters  $n$  as:

$$v_X(n, \varphi, f) = v_x(n, f) \cos(n\varphi) \cos(\varphi) - v_\varphi(n, f) \sin(n\varphi) \sin(\varphi), \quad (4.68)$$

$$v_Y(n, \varphi, f) = v_y(n, f) \cos(n\varphi), \quad (4.69)$$

$$v_Z(n, \varphi, f) = v_x(n, f) \cos(n\varphi) \sin(\varphi) + v_\varphi(n, f) \sin(n\varphi) \cos(\varphi). \quad (4.70)$$

The terms  $\sin(n\varphi)$  and  $\cos(n\varphi)$  describe the circumferential distribution of the velocity field. They are valid for the case of radial (vertical) and axial (lateral) wheel excitation.

Sound radiation from the railway wheel was evaluated at specific frequencies with the BEM code developed by Brick [15]. Ground reflections were taken into account.

<sup>8</sup>The superscript  $W$  is omitted from the FE model axes notation, and the wheel coordinate system  $(y^W, z^W, \varphi^W)$  is denoted with  $(y, z, \varphi)$ .

<sup>9</sup>The BE model coordinate system is not to be confused with the global coordinate system defined in Section 4.1.

# Chapter 5

## Numerical validation

---

In this chapter, the numerical validation of models presented in Chapter 4 is carried out. Firstly, the implementation of the sound-radiation model is validated against BEM results in Section 5.1. The validation of the sound radiation model is presented first since the sound radiation model is afterwards used in the validation of the tangential point-contact model.

Secondly, the tangential point-contact model is validated in Section 5.2 using a detailed two-fold validation procedure. The contact model is validated against Kalker's variational theory within the squeal model, i.e. with included wheel/rail dynamics. Additionally, a traditional validation approach is carried out. A creepage variation is imposed, and the contact model is considered independently (stand-alone), without wheel/rail dynamic effects. The proposed validation procedure provides more information about the applicability of rolling contact models for squeal modelling. Finally, the extension of the tangential point-contact model to non-zero spin creepage is validated on two curve squeal cases.

All validation studies were performed on the three one-point wheel/rail contact cases defined in Section 4.1.2.

### 5.1 Validation of the sound-radiation-model implementation

Thompson and Jones [102, 104] developed their sound-radiation model on the base of BEM analyses of sound radiation from a railway wheel. It is, therefore, sensible to validate the model implementation against results of BEM analyses of the C20 wheel. The C20 wheel BE model was presented in Section 4.4.4.

Two cases are used in the validation. First, the radiated sound power is evaluated for the case of unit excitation force at frequencies around selected wheel modes. Second, the radiated sound power is evaluated for a simulated squeal case. In both

cases, the wheel is excited at the nominal contact point of the  $\Delta y^{WR} = -15$  mm one-point wheel/rail contact case.

### 5.1.1 Validation with unit-force excitation

Axial wheel modes with zero nodal circles are commonly found to be excited during squeal [60, 110]. The sound model validation is therefore performed for frequencies around modes  $(0, 0, a)$ ,  $(1, 0, a)$ ,  $(2, 0, a)$  and  $(3, 0, a)$ .

The BE model of the wheel has a typical element dimension of  $l_{elem} = 0.034$  m. Of the selected modes, mode  $(3, 0, a)$  has the highest eigenfrequency of  $f_{max} = 1144$  Hz. The number of elements per wavelength is then  $n_{elem}/\lambda = c_0/(f_{max}l_{elem}) = 8.8$ . This is well within the range of six to ten elements per acoustic wavelength recommended in the literature [70].

The frequency resolution required to describe the resonance peaks accurately is determined from wheel receptances, Figure 4.11. About five to seven frequency points should be present in the frequency region around a resonance peak. This frequency region is determined from points in the receptance-magnitude plot which are 3 dB lower than the receptance value at resonance. Table 5.1 shows the selected wheel modes, corresponding eigenfrequencies and the required frequency resolution. Figure 5.1 shows the lateral surface-velocity field on the wheel for unit lateral excitation at the wheel tread. The excitation frequency corresponds to the wheel mode eigenfrequency. Mode-shapes of the four wheel modes are readily distinguished.

Mode	$f_r$ , Hz	$\Delta f$ , Hz
$(0, 0, a)$	332.8	0.13
$(1, 0, a)$	243.2	0.8
$(2, 0, a)$	429.9	0.012
$(3, 0, a)$	1143.2	0.045

Table 5.1: Wheel modes used in the sound-radiation-model validation: eigenfrequencies and the required frequency resolution.

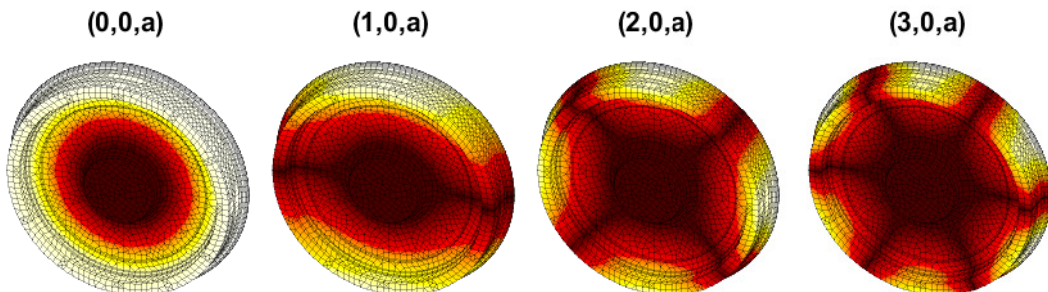


Figure 5.1: Shape of the lateral surface-velocity field  $v_Y$  for the selected wheel modes. Brighter color corresponds to higher velocity.

Pure lateral and pure radial excitations of the wheel are used in the validation. Figure 5.2 shows the difference between the BEM and the simple model results for the case of lateral wheel excitation. Results are presented with the absolute difference of the radiated sound power levels  $\Delta L_W = L_W^{BEM} - L_W^{simple}$ . Figure 5.3 shows the validation results for the case of radial wheel excitation. The absolute differences between BEM and the simple model are practically identical for both the lateral and the radial excitation. This identity shows that the differences between the two approaches (BEM and simple model) are not dependent on the wheel excitation.

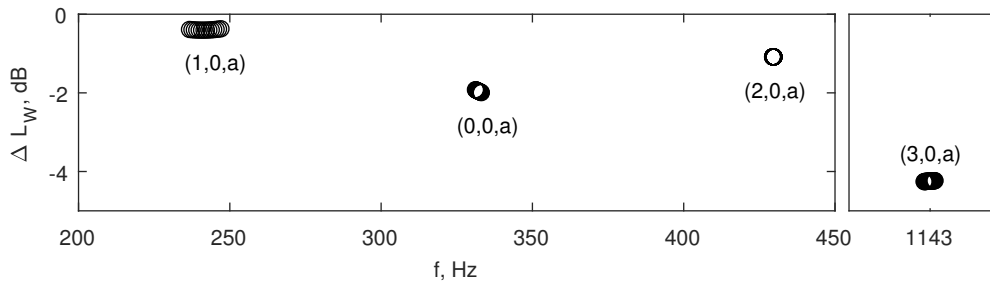


Figure 5.2: Sound power level difference  $\Delta L_W = L_W^{BEM} - L_W^{simple}$  for lateral wheel excitation for frequencies around the selected wheel modes.

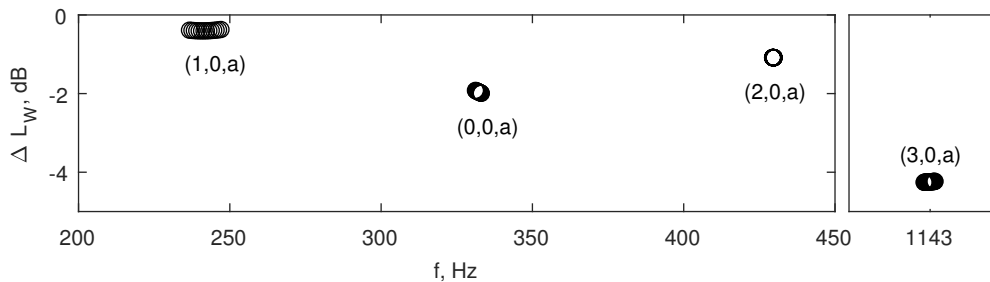


Figure 5.3: Sound power level difference  $\Delta L_W = L_W^{BEM} - L_W^{simple}$  for radial wheel excitation for frequencies around the selected wheel modes.

The differences are, however, dependent on the velocity-field shape, i.e. wheel modes. Differences are in the range of 0.5 to 4 dB, with the simple model overestimating the sound power compared to BEM results. These observations are in accordance with results from Thompson and Jones [52, 104]. They found that the simple model typically overestimates the radiated sound power by 2-3 dB.

### 5.1.2 Validation for a curve squeal case

The second part of the validation consists of evaluating the radiated sound power for a simulated curve squeal case. The contact forces were obtained using the squeal model developed in Chapter 4. The squeal case is defined on the one-point contact case  $\Delta y^{WR} = -15$  mm with a friction coefficient value of 0.35 and a lateral creepage

value of  $-0.014$ . Negative values of the lateral creepage are obtained for the case of under-radial curving of the wheelset [9]. The vehicle rolling velocity is  $50 \text{ km/h}$ , and the simulation time-step is  $36 \mu\text{s}$ . Figure 5.4 shows the lateral and vertical contact-force amplitude spectra obtained from the force time-histories. The wheel is excited simultaneously with both the lateral and the vertical force.

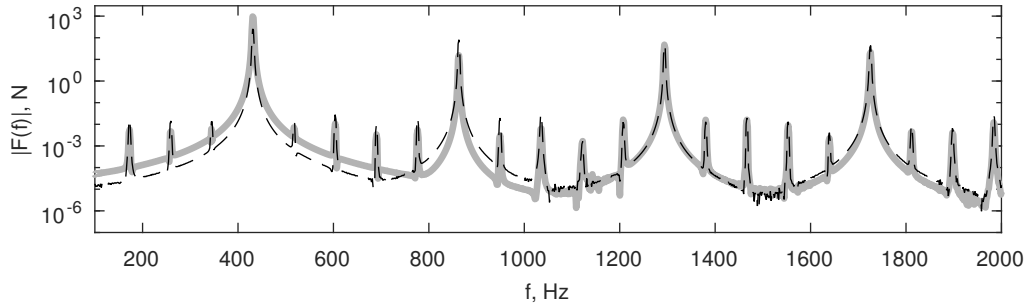


Figure 5.4: Magnitude of the contact force amplitude spectra: ( - - black) lateral contact force; ( — grey) vertical contact force.

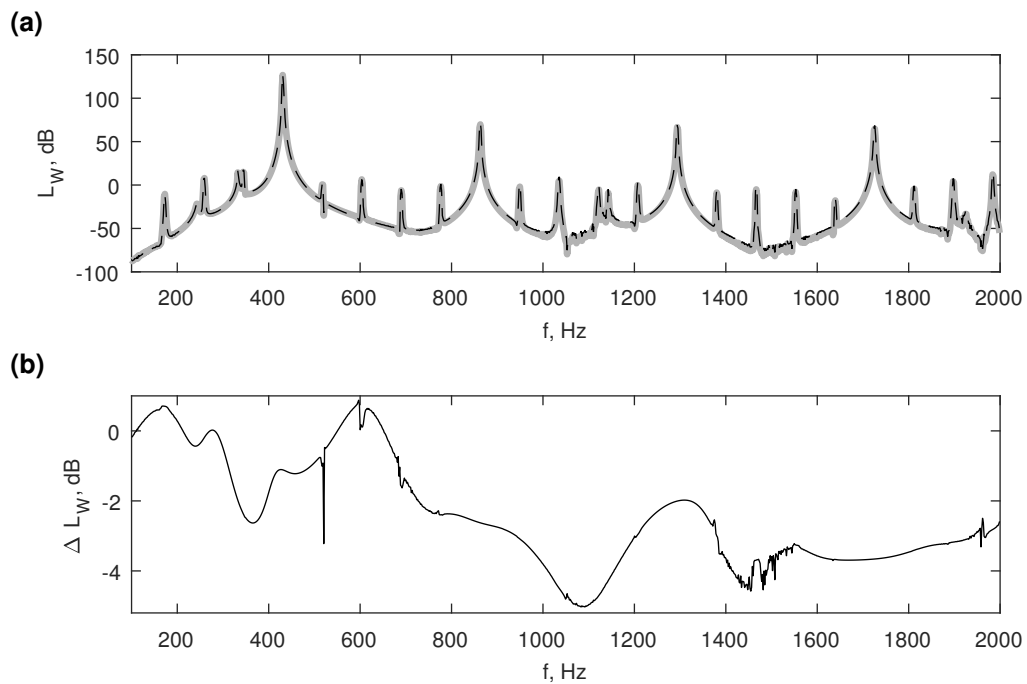


Figure 5.5: Radiated sound power for the squeal case  $\mu = 0.35$ ,  $\gamma_y = -0.014$  and  $\Delta y^{WR} = -15 \text{ mm}$ : (a) sound power spectrum: ( - - black) simple model; ( — grey) BEM; (b) difference between the BEM and simple-model results.

The BEM and the simple-model results show good agreement in Figure 5.5 (a). The difference between the results is presented in Figure 5.5 (b). Differences in the radiated sound-power levels are comparable to those found in the validation with

unit-force excitation in Section 5.1.1. Larger differences of up to 5 dB are observed at frequencies where the sound power levels are almost insignificant. The difference in the overall (total) sound-power level is considerably lower than the maximum difference. The total sound power from BEM is 127.1 dB, while the simple-model total power is 128.2 dB: this gives an acceptable difference of 1.1 dB between the two radiation models.

In conclusion, differences between results of the two approaches are well within the differences observed by Thompson and Jones [52, 104]. The implementation of the simple sound-radiation model is, therefore, found valid.

## 5.2 Validation of the contact model

In this section, the point-contact model is validated against Kalker's variational theory in a two-fold validation approach. Firstly, the contact model is validated with an imposed motion, which is a traditional validation approach. The wheel/rail dynamics are not included, and the contact model can be considered as independent from the squeal model<sup>1</sup>. Secondly, the validation within the squeal model is performed. In that case, the wheel/rail dynamics are included and define the demands on the contact model.

The case with imposed motion evaluates the contact model under very different conditions compared to the case when the wheel/rail dynamics are included. In the latter case, the contact model input is determined by the system response and the contact forces. Due to the coupling between the response and the forces, the contact model solution influences its input in the next time step. This closely replicates the real operating conditions of the contact model and gives more information about its applicability to squeal modelling.

The validation aims at determining the frequency limit up to which the tangential point-contact model provides acceptable results. Solutions obtained from Kalker's variational model are taken as reference. Particular emphasis is put on differences in amplitudes and the ability to predict squeal with the two models. Consequently, the validation also provides the validity limit of the time-domain engineering model for curve squeal.

### 5.2.1 Validation with imposed motion

The stand-alone validation is presented first. The displacement response of the wheel and the rail are not included in Equations (4.24), (4.25), (4.36) and (4.37). The case of imposed wheel/rail motion corresponds to imposed creepage between the wheel and the rail. Figure 5.6 graphically describes the procedure.

The input lateral creepage varies harmonically around the mean value  $\gamma_y^0$  with amplitude  $\gamma_y^a$  and frequency  $f$ :

$$\gamma_y(t) = \gamma_y^0 + \gamma_y^a \sin(2\pi ft). \quad (5.1)$$

---

<sup>1</sup>Therefore, this validation approach is also referred to as stand-alone validation.

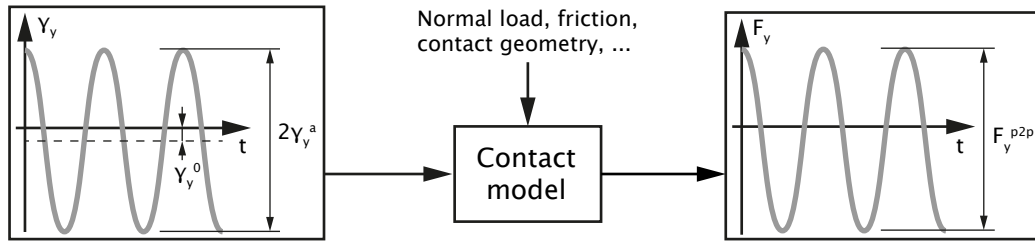


Figure 5.6: Procedure of the contact model validation with imposed lateral creepage.

Two validation cases are defined with different creepage parameters and a different one-point wheel/rail contact position. Case 1 is defined with  $\gamma_y^0 = -0.01$  and  $\gamma_y^a = 0.005$  with the nominal contact point defined with  $\Delta y^{WR} = -10$  mm. Frequencies for which the validation was performed are 240, 330, 430, 1140, 1900, 2100 and 3000 Hz.

Case 2 parameters are  $\gamma_y^0 = -0.005$  and  $\gamma_y^a = 0.005$ , and the  $\Delta y^{WR} = -15$  mm one-point wheel/rail contact case. This validation case was run for creepage variation frequencies of 240, 330, 430, 1100, 2100, 3100, 4100, 5200 and 6300 Hz. The vertical wheel pre-load  $F_{LZ} = 65$  kN, rolling velocity  $v = 50$  km/h and simulation time-step length  $\Delta t = 36$   $\mu$ s are common to both cases.

Results are expressed in terms of the lateral contact-force peak-to-peak (p2p) amplitude  $F_y^{p2p}$ , as shown in Figure 5.6. The procedure shown in Figure 5.6 is carried out with Kalker's model and with the point-contact model.

Figures 5.7 (a) and (b) present the validation results for case 1 and case 2, respectively. Relative differences between Kalker's model and the point-contact model are presented in Figure 5.7 (c). Significant differences are observed between the models. Differences are frequency dependent, with different behaviour in the two validation cases.

The relative differences between the two models are considerably larger in case 1 compared to case 2, see Figure 5.7 (c). In both cases, the point-contact model deviates substantially for frequencies above roughly 400 Hz. The  $L/a_x$  ratio, introduced in Section 3.2.1, has a value of 2.9 at 400 Hz (contact length  $a_x = 12$  mm). This is well below the  $L/a_x = 10$  ratio suggested by Knothe and Groß-Thebing [58], below which transient contact conditions should be considered. With increasing frequency, the lateral force amplitude obtained from Kalker's model steadily decreases. The same decrease is significantly less pronounced in results of the tangential point-contact model. This deviation is attributed to the steady-state nature of the point-contact model, which is unable to describe high-frequency contact processes properly. The steady-state nature of the model can, in turn, be attributed to the formulation of the regularised friction model. This discussion is continued in Section 5.2.4.

Another difference between validation cases 1 and 2 is found in the values of the lateral contact-force amplitude. Case 2 shows very high values of the force amplitude compared to case 1. This is attributed to the different creepage-variation parameters

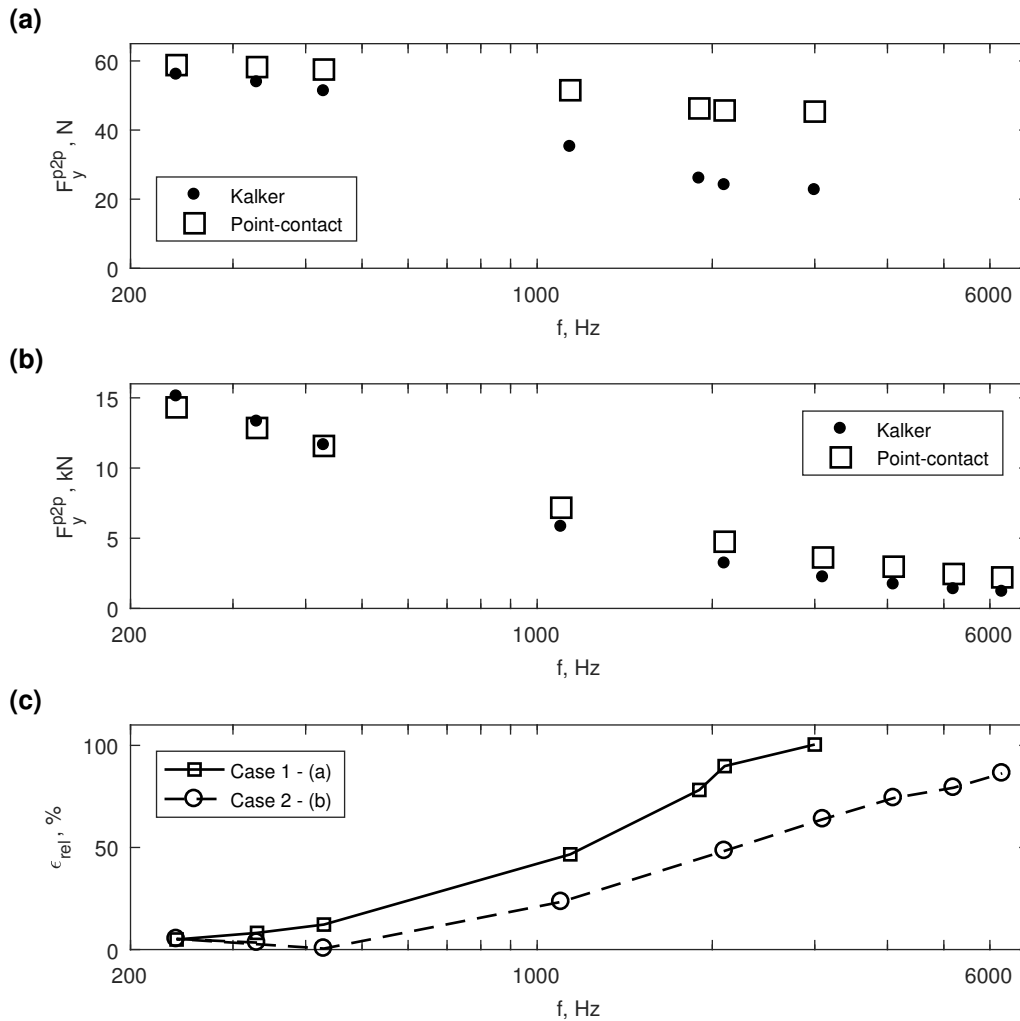


Figure 5.7: Peak-to-peak amplitudes of the lateral contact force due to harmonic creepage variation: (a) case 1; (b) case 2: (●) Kalker's variational theory; (□) point-contact model; (c) relative difference between the contact models in the validation: (□) case 1; (○) case 2.

and the different geometry of surfaces in contact. Therefore, validation results are dependent on the imposed creepage variation and contact parameters.

In conclusion, results obtained from the validation with imposed creepage are in line with observations from Knothe and Groß-Thebing [58]. To solve transient contact problems involving imposed motion or imposed force, the contact model should be chosen according to the guidelines given in [58] and discussed in Section 3.2.1. As seen from Figure 5.7, the differences between results of a transient and steady-state contact model are large for the imposed creepage case. According to these results, a transient contact model should be used in squeal models even for simulating squeal of lower frequencies (around 400 Hz). Differences between the point-contact model and Kalker's transient theory become significantly lower when

the models are compared within the squeal model. This is discussed in the following section.

## 5.2.2 Validation in dynamic conditions

In the dynamic validation approach, the wheel and rail displacement response terms are included in Equations (4.24), (4.25), (4.36) and (4.37). The contact model input is then subject to dynamic variations determined by the system itself. Under these circumstances, the wheel/rail system dynamics will determine the frequency of the response. However, without further interventions instability would be obtained only at a single frequency (and its higher harmonics).

In an attempt to obtain more response frequencies from the wheel/rail system, the wheel dynamics are altered. Only one wheel mode at a time is lightly damped, while other modes are highly damped. Figure 5.8 shows examples of the wheel vertical-lateral cross receptance obtained when all except a single mode are damped out. The lightly damped mode has its modal damping set to:

$$\zeta_{incl} = 10^{-6}, \quad (5.2)$$

while other modes are critically damped,  $\zeta_{not-incl} = 1$ . The wheel suspension was retained, along with the unchanged rail dynamics. The wheel Green's functions are obtained from the modified receptances.

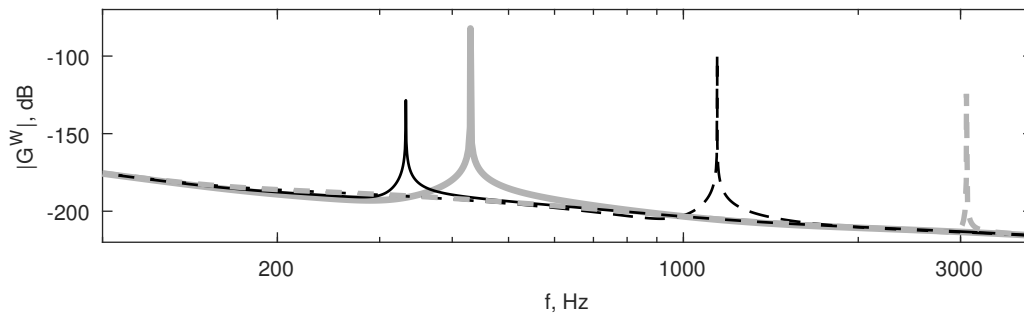


Figure 5.8: Examples of the wheel vertical-lateral cross-receptance for cases when a single mode is included and with  $y^W = -4$  mm: (— black) mode  $(0, 0, a)$ ; (— grey) mode  $(2, 0, a)$ ; (- - black) mode  $(3, 0, a)$ ; (- - grey) mode  $(5, 0, a)$ .

In the proposed validation approach, the number of simulations with each contact model is equal to the number of wheel modes (34 modes, see Table 4.1). One simulation per wheel mode and contact model is carried out. The simulation parameters are:  $\Delta y^{WR} = -15$  mm one-point wheel/rail contact case,  $\mu = 0.6$  friction coefficient,  $\gamma_y = -0.04$  lateral creepage,  $v = 50$  km/h vehicle velocity,  $F_{LZ} = 65$  kN vertical wheel pre-load and  $\Delta t = 36$   $\mu$ s simulation time-step length.

Table 5.2 presents the lateral contact-force amplitudes obtained from the validation in dynamic conditions. Only wheel modes for which the system has responded with unstable motion (squeal) are presented. Other modes did not result in curve

Mode	$f_r$ , Hz	K $F_y^{p2p}$ , N	P $F_y^{p2p}$ , N	$L/a_x$
(1, 0, a)	243.2	6609.7	5917.6	4.76
(0, 0, a)	332.8	3117.5	3000.1	3.48
(2, 0, a)	429.9	9601.3	9859.8	2.69
(3, 0, a)	1143.2	15836.2	17222.3	1.01
(4, 0, a)	1923.9	11037.6	12973.8	0.6
(5, 0, a)	3070.8	12242.2	11748.6	0.38
(6, 0, a)	4131.1	5917.8	6180.4	0.28
(7, 0, a)	5215.9	7073.2	7223.4	0.22
(8, 0, a)*	6315.6	72.8	38.1	0.18

Table 5.2: Numeric results of the validation in dynamic conditions. The mode eigenfrequency, lateral force p2p amplitudes and  $L/a_x$  ratios are given. \* = modes resulting in low amplitudes; K = Kalker's model; P = point-contact model.

squeal. The same results are presented graphically in Figure 5.9 (a). Wheel modes that resulted in squeal are axial modes with zero nodal circles, which agrees with observations from the literature [60, 100, 110].

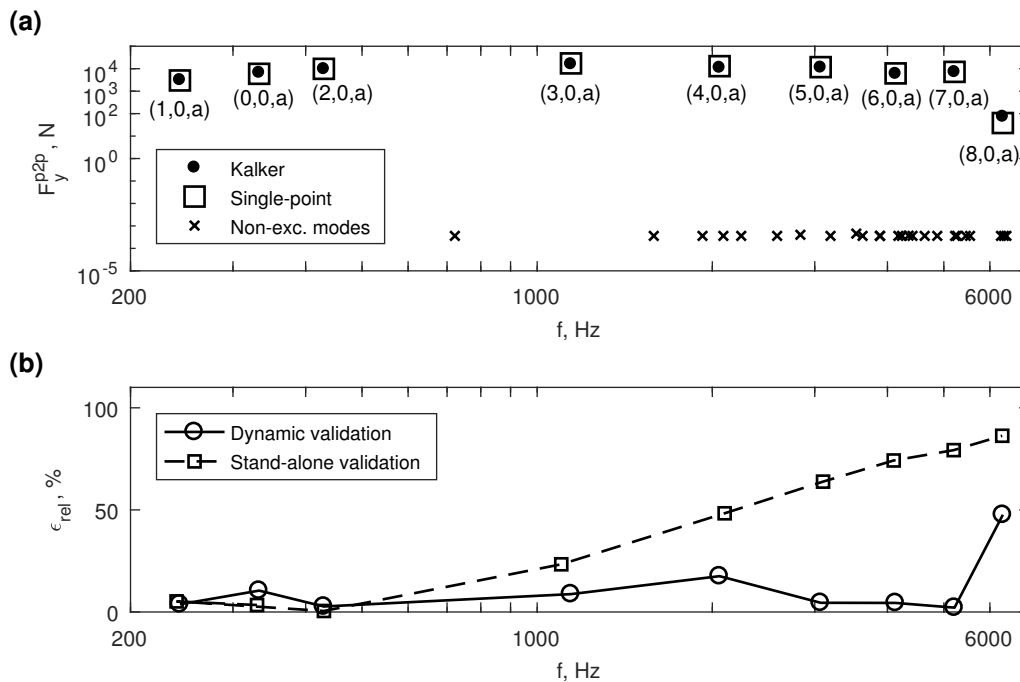


Figure 5.9: Results of the validation under dynamic conditions: (a) lateral contact force p2p amplitudes: (●) Kalker, (□) point-contact model, (×) wheel modes that were not excited; (b) relative difference between the two contact models: (-○-) dynamic validation; (-□-) stand-alone validation.

Good agreement between Kalker's model and the point-contact model results is observed especially in cases with high lateral force amplitudes. The case with mode

$(8, 0, a)$  results in low force amplitude and a high relative difference between the two contact models. Relative differences computed from results of both stand-alone and dynamic validations are presented in Figure 5.9 (b). While the relative difference is frequency-dependent in the imposed-motion validation, such a dependency is not seen in the validation within the squeal model. The steady-state point-contact model shows good results for  $L/a_x$  ratios as low as 0.22. For such a low  $L/a_x$  ratio the contact conditions are inevitably transient, yet the steady-state model returns results which are very close to Kalker's transient model results.

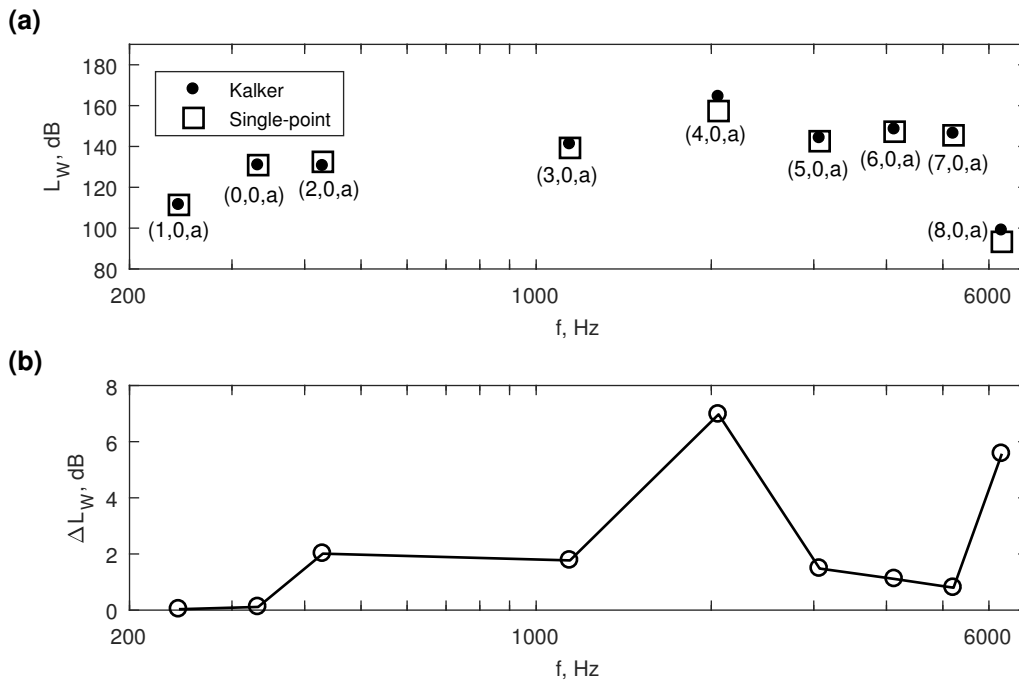


Figure 5.10: Results of the validation under dynamic conditions: (a) radiated sound power levels: (●) Kalker, (□) point-contact model; (b) relative difference between the contact models.

The point-contact and Kalker's variational theory results are presented with the radiated sound power in Figure 5.10. The sound power is evaluated with the simple model for sound radiation (Section 4.4) for each dynamic-validation case where squeal was obtained. The radiated sound was evaluated for the original wheel model with all modes included. A difference of around 2 dB between the contact models is observed in Figure 5.10 (b) for most cases. Two cases, at modes  $(4, 0, a)$  and  $(8, 0, a)$ , show large differences in the overall radiated sound power. The difference occurring at mode  $(4, 0, a)$  cannot be attributed to the force-amplitude difference, which is relatively low at that mode (see Figure 5.9). The large sound-power-level difference at mode  $(4, 0, a)$  is due to differences in the lateral force amplitude spectrum obtained from the two contact models. Figure 5.11 shows a detail of the lateral force amplitude spectra. The peak in the lateral force spectrum obtained from Kalker's model is closer to the resonance peak in the receptance. In comparison, the force

peak in the spectrum obtained from the point-contact model is further away from the resonance peak. This may point to higher numerical damping in the point-contact model compared to Kalker's model. The lateral force spectrum obtained from the squeal model with Kalker's contact model excites the wheel closer to the  $(4, 0, a)$  eigenfrequency. This leads to a stronger vibration field on the wheel and, consequently, higher sound radiation.

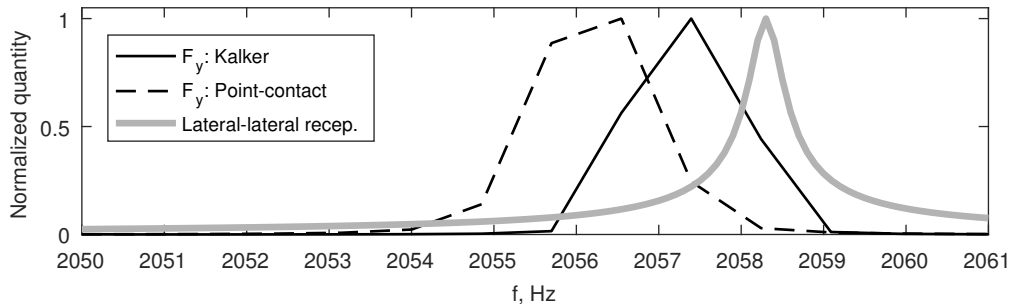


Figure 5.11: Amplitude spectra of the lateral contact force and lateral point-receptance around the wheel mode  $(4, 0, a)$ : (— black) Kalker, (- - black) point-contact model, (— grey) lateral point receptance. Quantities are normalised with their maximum values.

Regarding wheel mode  $(8, 0, a)$ , the difference in the force amplitude is high. This leads to a significant difference in the radiated sound power. However, the lateral force amplitude obtained with this mode is low, as is the radiated sound power. Because of the relatively small amplitudes, it is not possible to reliably assess the validity of the tangential point-contact model at the  $(8, 0, a)$  mode.

The presented validation results indicate that the wheel and rail dynamics put different demands on the contact model compared to the imposed-motion approach. In the imposed-motion validation, the point-contact model shows large differences above 400 Hz. When used in the squeal model, acceptable results are obtained from the point-contact model for frequencies up to at least 5 kHz. The tangential point-contact model may be valid even for frequencies above 5 kHz. Only wheel modes up to 7 kHz are included in the model, which limits the validation. However, even below 5 kHz differences may still arise at specific wheel modes, which are most noticeable in the radiated sound power.

### An additional validation case

The proposed validation method requires the definition of simulation parameters (nominal contact position, friction and creepage) for the squeal case used in the procedure. It is not known in advance whether the chosen parameter combination will result in squeal at different wheel modes. Therefore, squeal simulations with different parameter combinations may be required to obtain more information at different frequencies.

An additional dynamic validation case shows a situation where the chosen squeal case gives useful information only up to 2 kHz. The squeal case parameters are:  $\Delta y^{WR} = -10$  mm one-point wheel/rail contact case,  $\mu = 0.3$  friction coefficient,  $\gamma_y = -0.01$  lateral creepage,  $v = 50$  km/h vehicle velocity,  $F_{LZ} = 65$  kN vertical wheel pre-load and  $\Delta t = 36 \mu s$  simulation time-step length. Figure 5.12 (a) shows the p2p amplitude values of the lateral contact force. Numeric values are presented in Table 5.3.

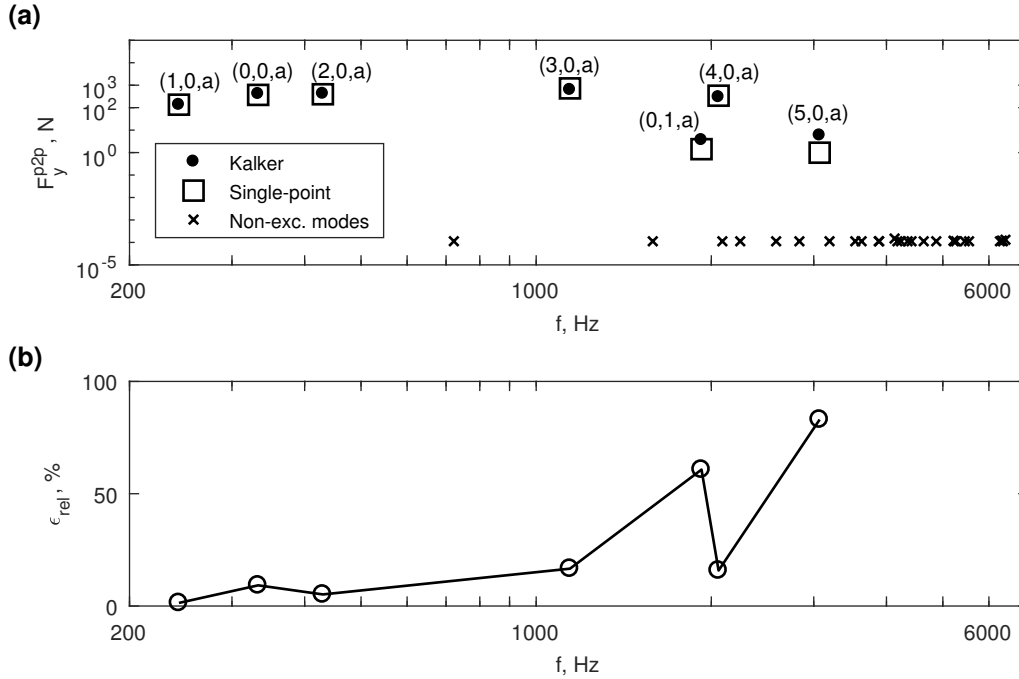


Figure 5.12: Additional dynamic validation case: (a) lateral contact force p2p amplitudes: (●) Kalker, (□) point-contact model, (×) wheel modes that were not excited; (b) relative difference between the contact models.

Mode	$f_r$ , Hz	K $F_y^{p2p}$ , N	P $F_y^{p2p}$ , N	$L/a_x$
(1, 0, a)	243.2	133.8	135.7	4.76
(0, 0, a)	332.8	407.4	369.9	3.48
(2, 0, a)	429.9	416.4	394.9	2.69
(3, 0, a)	1143.2	619	722	1.01
(0, 1, a)*	1923.9	3.6	1.4	0.6
(4, 0, a)	2058.3	294.2	340.7	0.56
(5, 0, a)*	3070.8	5.8	1	0.38

Table 5.3: Numeric results of the additional dynamic validation case. The mode eigenfrequency, force p2p amplitudes and  $L/a_x$  ratios are given. \* = modes resulting in low amplitudes; K = Kalker's model; P = point-contact model.

Significant differences are noticed when comparing the results of the additional

case to results of the dynamic validation case of Figure 5.9. Not all axial wheel modes with zero nodal circles develop squeal and, additionally, the mode  $(0, 1, a)$  is excited. Relative differences are presented in Figure 5.12 (b). Modes  $(0, 1, a)$  and  $(5, 0, a)$  show significant differences between Kalker's and point-contact model results, but their amplitudes are low. Similarly to the case of mode  $(8, 0, a)$  in Figure 5.9, low force-amplitude modes show high relative differences. Interestingly, the mode  $(4, 0, a)$ , with a frequency between the  $(0, 1, a)$  and  $(5, 0, a)$  mode frequencies, has a high force amplitude and a low relative difference. This indicates that modes leading to low force amplitudes should be approached with some caution.

The additional validation case does not give as much information as the case presented in Figure 5.9. From the additional case, the validity of the point-contact model is confirmed for frequencies up to at least 2 kHz. In the initial validation case, the model was shown to be valid for up to at least 5 kHz. It is, therefore, preferable to validate a contact model on more cases to get a clearer picture of its behaviour under dynamic conditions.

### 5.2.3 Validation of the spin-creepage extension

The extension of the tangential point-contact model to non-zero spin creepage is validated in dynamic conditions only. The dynamics of the wheel and rail are hence included in the model. As discussed in Section 5.2.2, this is a more sensible approach to validation of contact models. In contrast to the procedure in Section 5.2.2, the wheel dynamics are not altered, and all wheel modes are retained.

A total of six squeal cases is analysed: two lateral creepage values ( $\gamma_y = -0.3$  and  $\gamma_y = -0.01$ ) and the three one-point wheel/rail contact cases (Section 4.1.2) are considered. The friction coefficient value is  $\mu = 0.3$  in all cases. Other parameters, common to all simulations, are:  $\gamma_x = 0$  longitudinal creepage,  $v = 50$  km/h rolling velocity,  $F_{LZ} = 65$  kN vertical wheel pre-load and  $\Delta t = 36 \mu\text{s}$  time-step length.

The validation consists of a number of squeal simulations for each squeal case. In each squeal case, the spin creepage was varied within the range  $-0.5 \leq \gamma_\omega < 0.5$  rad/m with  $\Delta\gamma_\omega = 0.1$  rad/m. Results are obtained using the squeal models based on the point-contact model and Kalker's variational theory. Simulation results are then compared with the results of Kalker's model, which is taken as reference.

Results are expressed with the lateral contact force amplitude  $F_y^{\text{p2p}}$ , which is non-zero if squeal occurs. Figures 5.13, 5.14 and 5.15 show the validation results for the three one-point contact cases. Two plots are shown for each contact case, one for each lateral creepage value. Force amplitudes are plotted for each spin creepage value together with the relative difference between the point-contact model and Kalker's model.

Differences between the two models can reach up to 20%. Largest differences are observed in the -10 mm contact case results, see Figure 5.14. This case displays a highly non-Hertzian contact, as shown in Figure 4.24 (b). The shape of the contact, consisting of three distinct patches, may be the reason behind the large differences. As discussed in Section 4.3.6, the influence of spin creepage depends on the contact

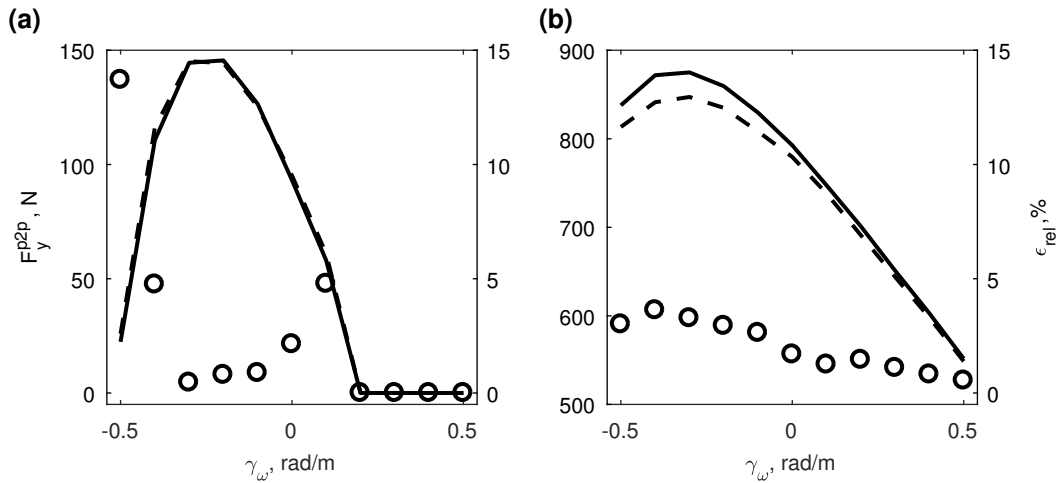


Figure 5.13: Results of the spin-extension validation for the  $\Delta y^{WR} = -5$  mm contact case: (a) sub-case  $\gamma_y = -0.01$ ; (b) sub-case  $\gamma_y = -0.03$ : (---) Kalker's model; (—) point-contact model; (o) relative difference.

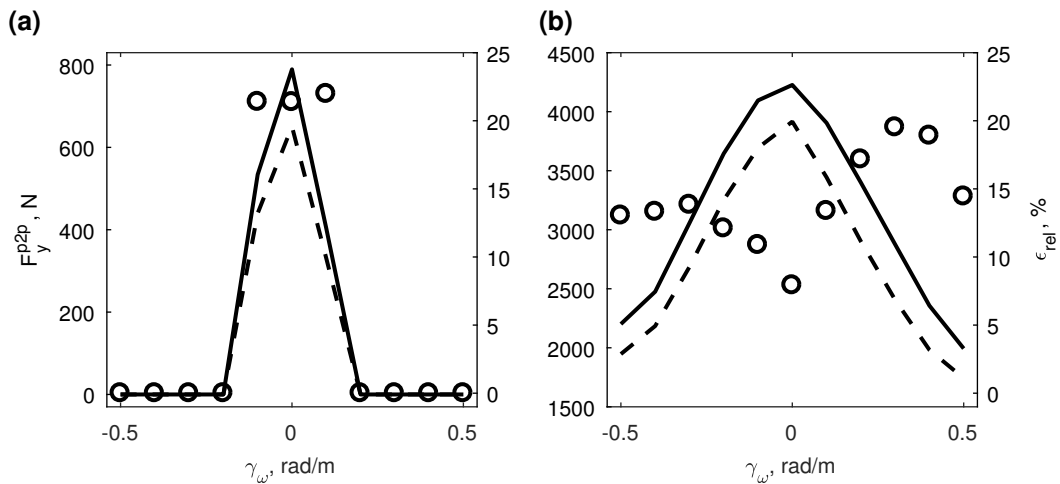


Figure 5.14: Results of the spin-extension validation for the  $\Delta y^{WR} = -10$  mm contact case: (a) sub-case  $\gamma_y = -0.01$ ; (b) sub-case  $\gamma_y = -0.03$ : (---) Kalker's model; (—) point-contact model; (o) relative difference.

area shape. However, in the case of curve squeal, the main interest lies in the radiated sound from the wheel. A difference in the lateral contact force of around 20% is expected to result in about 1.6 dB difference in the radiated sound power. This is an acceptable deviation, which is also in line with the observations in Section 5.2.2.

In the -5 and -15 mm contact cases, relative differences between the two models are below five percent. These are negligible, especially if considered in terms of the radiated sound power. An exception is noticed in the -5 mm case with  $\gamma_y = -0.01$  and -0.5 rad/m spin creepage, see Figure 5.13 (a). In that case, a larger relative

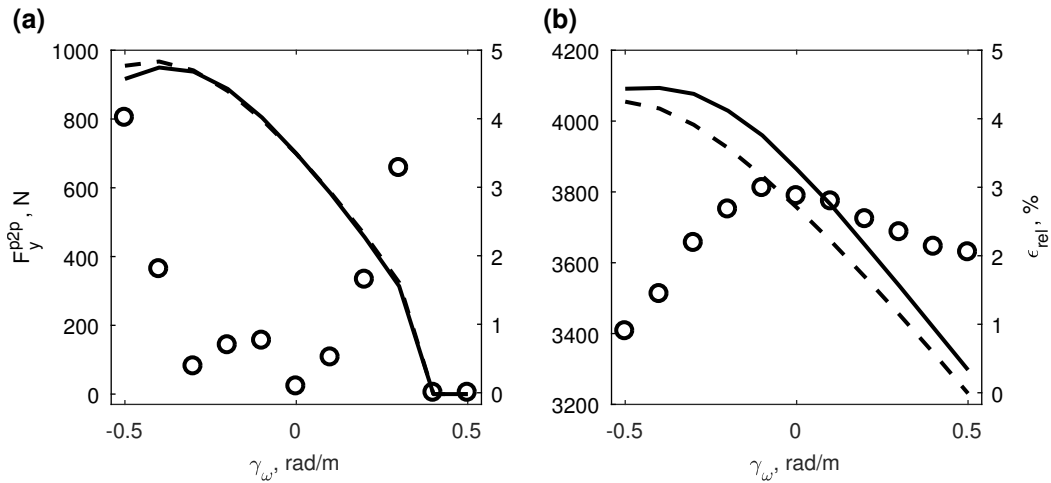


Figure 5.15: Results of the spin-extension validation for the  $\Delta y^{WR} = -15$  mm contact case: (a) sub-case  $\gamma_y = -0.01$ ; (b) sub-case  $\gamma_y = -0.03$ : (---) Kalker's model; (—) point-contact model; (o) relative difference.

difference of 14% is observed. Still, this deviation is not significant and can be disregarded as the case results in low force-amplitudes.

Two different squeal frequencies are observed in the validation. Squeal in -5 and -15 mm contact cases develops at the  $(2, 0, a)$  wheel mode with a frequency of 429.9 Hz. In the -10 mm contact case, the  $(3, 0, a)$  wheel mode at 1143.2 Hz is excited.

The two models show differences in force amplitudes that are comparable to differences found in Section 5.2.2. More importantly, the engineering model predicts squeal in the same cases as the detailed model [80, 81]. The level of accuracy of the point-contact model extended to non-zero spin is very close to the original point-contact model formulation. Therefore, the spin extension is not expected to introduce significant error in most cases. In conclusion, the method proposed in Section 4.3.6 is valid and provides acceptable results.

## 5.2.4 Conclusion

The proposed contact model (Section 4.3) is validated against Kalker's variational theory in a two-fold approach. Firstly, the contact model is validated independently of the squeal model, with an imposed creepage variation. Secondly, the model is validated within the squeal model.

Validation results indicate that the two approaches put significantly different demands on the contact model. The validation with imposed motion (Section 5.2.1) gives results which are in line with observations from the literature [12, 58]. In contrast, the results of the validation in dynamic conditions (Section 5.2.2) give a very different picture.

The squeal model with the tangential point-contact model predicts squeal occurrence equally well as the squeal model with Kalker's variational theory. This is

true even for high-frequency curve squeal where the  $L/a_x$  ratio is significantly lower than ten. In that case, transient phenomena should be considered [58]. Still, the steady-state point-contact model provides acceptable results. These findings seem to support Kalker's statement that transient contact processes can be described as a succession of steady-states [55]. Kalker's statement was discussed in Section 3.2.1.

According to the validation with imposed motion, the point-contact model is not able to accurately describe the contact processes during squeal. The source of the steady-state nature of the point-contact model can be traced back to the formulation of the regularised friction model. Every point in the regularised friction curve, introduced in Section 4.3.5, is obtained from a steady-state solution of Kalker's model. Consequently, the friction model describes the steady-state transition from full-stick to full-slip contact conditions. Since the point-contact model relies on the information included in the friction curve, it makes sense that the model has difficulties in accurately describing transient processes. This issue can be addressed with a regularised friction curve that describes the transient full-stick to full-slip transition for a specific frequency. The point-contact model is then expected to provide accurate results in the imposed motion case, but only at the frequency for which the friction curve is obtained. In the case of curve squeal, a transient friction curve cannot be devised since the squeal frequency is not known in advance.

Stand-alone validation results stand in sharp contrast to the dynamic validation results. The exact reason for the different results is not known. In conclusion, the applicability of a contact model for squeal modelling should not be judged exclusively from an imposed-motion (or imposed-force) validation. Instead, the validity of a contact model for high-frequency wheel/rail interaction modelling should be determined in conditions that replicate the real application as closely as possible.

Finally, the validation of the tangential point-contact model extended to non-zero spin creepage confirms the validity of the proposed method. Good agreement with results of the squeal model using Kalker's variational theory is found. Deviations of the extended point-contact model are, with a few exceptions, in line with deviations of the initial point-contact model. Cases resulting in higher force deviations are not expected to lead to significant differences in the radiated sound power.

# Chapter 6

## Parameter studies

---

In this chapter, the proposed engineering model for squeal is used to investigate the influence of different parameters on curve squeal occurrence and amplitudes. The influence of lateral creepage and friction coefficient is investigated in Section 6.1. The investigation is run for different contact cases to examine the influence of the vertical-lateral coupling dynamics.

The influence of wheel damping on curve squeal is investigated in Section 6.2. For each wheel mode excited in curve squeal, a modal damping value is determined for which squeal at that mode disappears. This approach gives information about the severity and persistence of squeal at different wheel modes.

Section 6.3 presents results of the spin-creepage influence study. As discussed in Section 2.1, spin is not considered to provide significant energy input and thus cause squeal. However, spin influences squeal amplitudes by influencing the processes in the contact area.

Besides the contact location, the contact angle is another parameter that influences the dynamics coupling. It is, therefore, of interest to study the influence of the contact angle on curve squeal occurrence and amplitudes. The contact angle study, presented in Section 6.4, is a purely theoretical study. In reality, the contact angle is defined by the wheel and rail profiles and the contact location. Additionally, spin creepage and contact angle are kinematically related. A combined angle-spin study investigates the simultaneous influence of spin creepage and the contact angle.

All parameter studies presented in this Chapter are performed on the three one-point wheel/rail contact cases defined in Section 4.1.2.

### 6.1 Lateral creepage/friction study

The vehicle curving behaviour has a direct influence on curve squeal by influencing the amount of lateral creepage and the wheel/rail contact position [27, 81, 100]. Friction between the wheel and the rail is another parameter that significantly influences

squeal.

The combination of lateral creepage and friction defines the amount of input energy to the wheel/rail vibrating system. It also defines the point at which the tangential contact force comes into saturation. The wheel/rail lateral contact position influences the dynamics coupling, which is held responsible for squeal development. These kinematic and friction parameters are expected to have a significant influence on squeal occurrence and amplitudes.

Both low and high values of the angle of attack, defining the amount of lateral creepage, were observed in field measurements of curve squeal [26, 27, 110]. Additionally, the wheel/rail friction coefficient is difficult to measure, which leads to uncertainties in its value. To account for the rather large spread and uncertainties in the parameter values, a relatively large parameter space is defined:

$$\begin{aligned} -0.06 \leq \gamma_y \leq -0.002, & \quad \Delta\gamma_y = 0.002, \\ 0.1 \leq \mu \leq 0.6, & \quad \Delta\mu = 0.05. \end{aligned} \quad (6.1)$$

The terms  $\Delta\gamma_y$  and  $\Delta\mu$  are the creepage and friction steps between adjacent values used in the study. In tight curves, the front wheelset of the leading bogie tends to run under-radially, as shown in Figures 2.2 (a) and 2.3. Consequently, lateral creepage is negative on wheels belonging to the front wheelset. Only negative values of lateral creepage are, therefore, used in the studies. Simulation parameters common to all cases are:  $v = 50$  km/h rolling velocity,  $\Delta t = 36 \mu\text{s}$  time-step length,  $F_{LZ} = 65$  kN vertical wheel pre-load and zero longitudinal and spin creepage ( $\gamma_x = \gamma_\omega = 0$ ).

Simulations with the engineering squeal model are run until the limit cycle is achieved. However, a limit of eight seconds was set for the simulated rolling time. If squeal does not occur or fully develop within the time limit, it is considered that squeal would not occur in practice. Results are expressed with the lateral force rms<sup>1</sup> level  $L_{F_y}$ :

$$L_{F_y} = 20 \log \left( \frac{F_y^{rms}}{1 \text{ N}} \right). \quad (6.2)$$

The rms value of the lateral contact force is determined from  $n_s$  samples of the force time history as:

$$F_y^{rms} = \sqrt{\frac{1}{n_s} \sum_{t=t_d}^{t_d+(n_s-1)\Delta t} (F_y(t) - \bar{F}_y)^2}, \quad (6.3)$$

where  $\bar{F}_y$  is the mean value of the force in the considered time interval. By subtracting the mean value  $\bar{F}_y$  from the lateral force  $F_y(t)$ , the dynamic part of the lateral force is obtained. As a result, cases that do not develop squeal have negative values of the force level. The dominant frequency of the force response is also determined.

The radiated sound power is evaluated for cases with a force rms level  $L_{F_y} \geq 10$  dB rel. 1 N. Squeal with a lateral force level below 10 dB is not considered severe and, therefore, ignored. The radiated sound power level and its frequency spectrum are computed using the simple model for sound radiation described in Section 4.4.

<sup>1</sup>The ‘‘rms’’ abbreviation stands for ‘‘root mean square’’, also known as the quadratic mean.

### 6.1.1 Contact case $\Delta y^{WR} = -5$ mm

Results of the parameter study for the  $\Delta y^{WR} = -5$  mm one-point wheel/rail contact case are presented in Figure 6.1. The figure presents the lateral force rms levels, the dominant force-response frequency, the radiated sound power levels and the dominant sound frequency for each simulated case. Squeal does not develop for low lateral creepage and/or friction values, see Figures 6.1 (a) and (c). With increasing values of creepage and friction, both lateral force and sound power levels increase considerably.

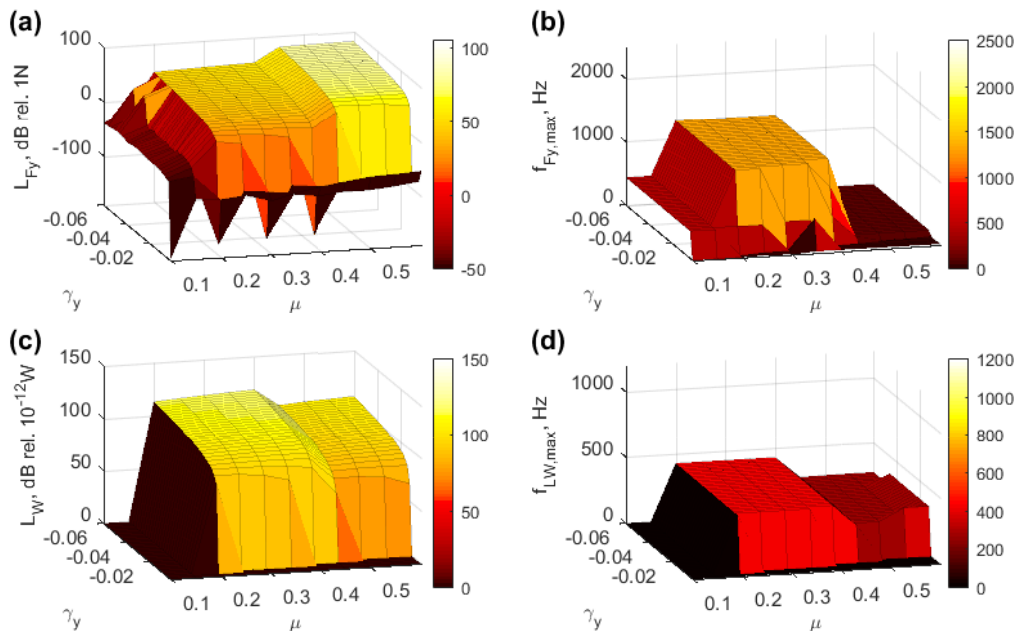


Figure 6.1: Contact case  $\Delta y^{WR} = -5$  mm: (a) lateral force amplitude rms levels; (b) dominant response frequency of the contact force; (c) radiated sound power levels; (d) dominant frequency of the radiated sound.

In Figure 6.1 (b), three different frequencies dominate in the lateral force response. The 434 and 1292 Hz frequencies correspond to the eigenfrequency and the third harmonic of the  $(2, 0, a)$  wheel mode ( $f_r = 429.9$  Hz). The presence of higher harmonics is a consequence of the nonlinear behaviour of the system [37].

Results also show the development of severe oscillations with a frequency of 90 Hz and significant force levels. This type of instability takes place for friction values above 0.45, which is seen in Figures 6.1 (a) and (b). The primary vertical suspension of the wheelset is found to be responsible for this instability. Once the vertical suspension damping is sufficiently increased, the 90 Hz instability disappears. A similar vibration phenomenon was already investigated within the context of rail corrugation by Kurzeck [63, 64]. Kurzeck explains that the instability is caused by the coupling of the vertical in-phase wheelset and track resonance (P2-resonance) and the first bending mode of the wheelset. The explanation for the behaviour

observed in the present case may be similar, although the complete wheelset is not included in the present model.

Results for the radiated sound presented in Figures 6.1 (c) and (d) show the importance of wheel modes in sound radiation. The dominant sound frequency (see Figure 6.1 (d)) is, in the investigated cases, coincident with the excited wheel mode eigenfrequency and not its higher harmonics. Axial wheel modes are especially efficient at sound radiation [104]. The excited  $(2, 0, a)$  wheel mode results in relatively high radiated sound power levels in the order of  $L_W \approx 100 \dots 120$  dB. In comparison, cases developing suspension-related vibrations radiate significantly less sound ( $L_W \approx 90 \dots 106$  dB), despite the higher excitation force. In that case, dominant sound radiation from the wheel occurs at around 270 Hz, with the closest wheel mode being the  $(1, 0, a)$  mode. However, at lower frequencies, sound radiation from the rail and sleepers may be more influential. These contributions are not included in the model.

### 6.1.2 Contact case $\Delta y^{WR} = -10$ mm

Results of the parameter study for the  $\Delta y^{WR} = -10$  mm one-point wheel/rail contact case are given in Figure 6.2. Friction does not influence the occurrence of squeal, but the influence of lateral creepage is still present.

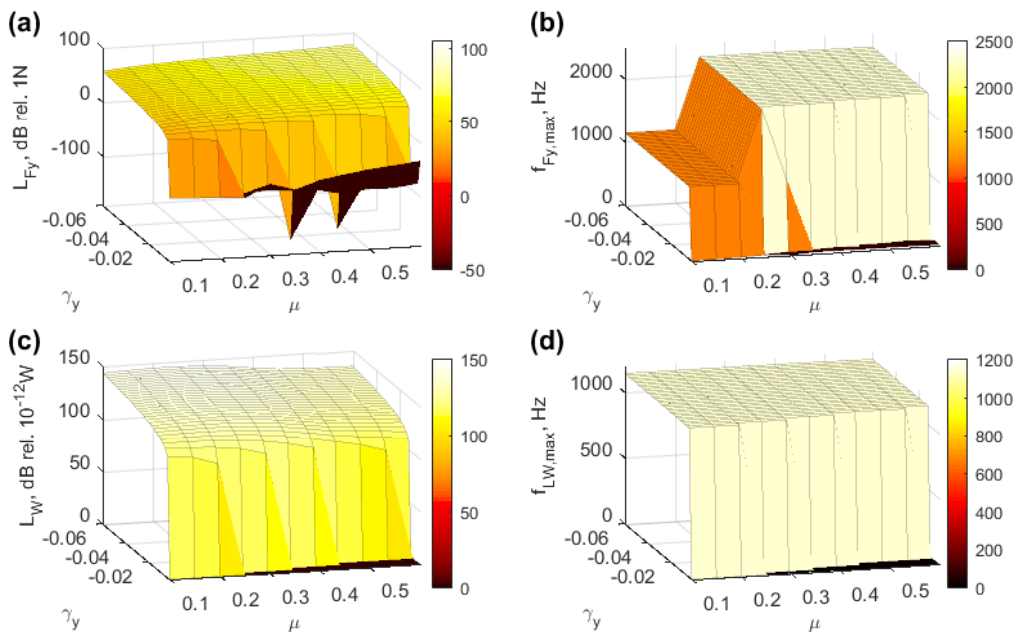


Figure 6.2: Contact case  $\Delta y^{WR} = -10$  mm: (a) lateral force amplitude rms levels; (b) dominant response frequency of the contact force; (c) radiated sound power levels; (d) dominant frequency of the radiated sound.

The different location of the contact leads to squeal at the  $(3, 0, a)$  wheel mode ( $f_r = 1143.2$  Hz). The force responds with two dominant frequencies, either 1143 Hz

or 2282 Hz, see Figure 6.2 (b). These frequencies correspond to the  $(3, 0, a)$  mode eigenfrequency and its second harmonic.

The radiated sound power levels shown in Figure 6.2 (c), are in the order of  $L_W \approx 120 \dots 140$  dB. These are significantly higher than power-levels observed in the -5 mm contact-case study. The dominant sound frequency corresponds to the squealing wheel mode eigenfrequency, see Figure 6.2 (d).

Different behaviour between the lateral force and the sound power levels is noticed when comparing Figure 6.2 (a) with Figure 6.2 (c). The force levels increase with increasing friction, while the sound power levels show a maximum around 0.25 friction coefficient value. To explain this, the forces amplitude spectra have to be considered in combination with wheel receptances. Maximum wheel excitation is obtained when a peak in the excitation force spectrum is coincident with a resonance peak. Resonance peaks in the wheel receptance are very narrow. Therefore, small shifts in the excitation-spectra peaks lead to substantial differences in the vibration levels of the wheel. A change in the wheel vibration levels directly causes a change in the radiated sound power. Figure 6.3 shows force-spectra and receptance peaks for two simulation cases.

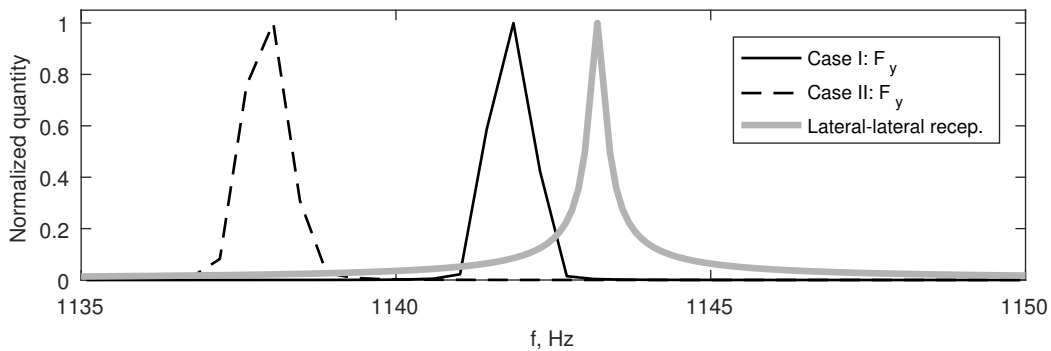


Figure 6.3: Amplitude spectra of the lateral force and lateral point-receptance near the wheel mode  $(3, 0, a)$  eigenfrequency for  $\gamma_y = -0.04$ : (— black) Case I  $\mu = 0.25$ ; (- - black) Case II  $\mu = 0.55$ ; (— grey) lateral point-receptance. Quantities are normalised with their maximum values.

Case I in Figure 6.3 has a peak in the force spectrum close to a resonance peak in the receptance. The friction value in case I is 0.25. A shift away from the resonance peak is noticed in the force spectrum of case II, which has a friction value of 0.55. Both cases have the same lateral creepage value of -0.04. Due to the shift in the force spectrum, case II results in lower sound power levels than case I. A 7 dB higher sound power level is obtained in case I, despite a 10 dB lower lateral force level than that of case II (see Figures 6.2 (a) and (c)).

Lateral creepage does not show such an influence. With increasing creepage at constant friction value, both force and sound-power levels increase.

### 6.1.3 Contact case $\Delta y^{WR} = -15$ mm

Results of the parameter study for the  $\Delta y^{WR} = -15$  mm one-point wheel/rail contact case are presented in Figure 6.4. The influence of friction and lateral creepage is similar to the influence observed in the -5 mm case results in Figure 6.1.

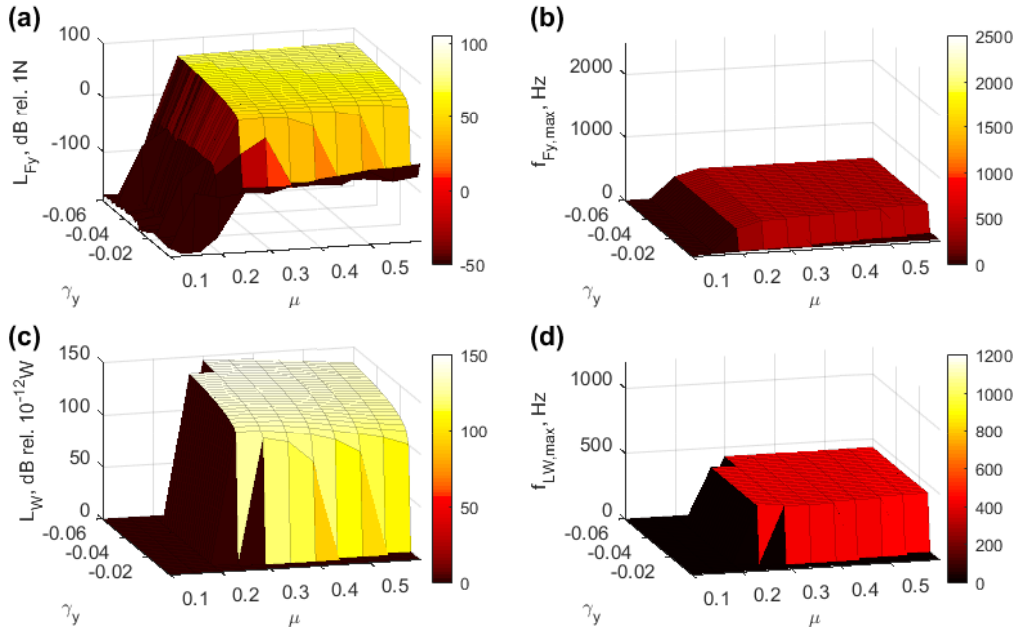


Figure 6.4: Contact case  $\Delta y^{WR} = -15$  mm: (a) lateral force amplitude rms levels; (b) dominant response frequency of the contact force; (c) radiated sound power levels; (d) dominant frequency of the radiated sound.

The dominant force-response frequencies in Figure 6.4 (b) are consistent with the  $(2, 0, a)$  wheel mode in all cases. The same observation is valid for the dominant sound frequency presented in Figure 6.4 (d). The radiated sound power is in the order of  $L_W \approx 120 \dots 140$  dB, comparable to results of the -10 mm contact case.

As in the -10 mm case, a similar maximum in the radiated sound power is observed. The sound power level maximum occurs for 0.3 friction value. Regarding squeal occurrence, the -15 mm case is similar to the -5 mm case, but with squeal starting at higher friction values.

### 6.1.4 Discussion

A strong influence of the wheel/rail contact position is seen from results of the creepage/friction study performed on the three contact cases. The contact location influences the contact area shape and size, as well as the wheel dynamics coupling. The dynamics coupling has a strong influence on which wheel mode is excited into curve squeal. As a consequence, it also influences the radiated sound power.

The maxima observed in results of the sound-power levels of the -10 and -15 mm contact cases are related to wheel/rail friction. Friction influences squeal frequencies

by slightly shifting the system response frequency, as explained in Figure 6.3. Mathematically, this increase in friction may be interpreted as additional damping in the wheel/rail system. In a single-degree-of-freedom system, an increase in damping will cause a decrease in the system response frequency. Despite the higher complexity of the wheel/rail system, the same behaviour can be expected. An increase in friction causes a shift in the wheel/rail system response towards lower frequency, as shown in Figure 6.3.

Whether friction acts as additional damping is unclear since friction can also influence the contact stiffness. Higher friction leads to higher tangential loading of the contact for the same lateral creepage. The higher loading, in turn, influences the contact stiffness which is determined from the elastic half-space (see Section 4.3.4). Changes in the contact stiffness may, therefore, cause a slight shift in the response frequency, like the one observed in Figure 6.3.

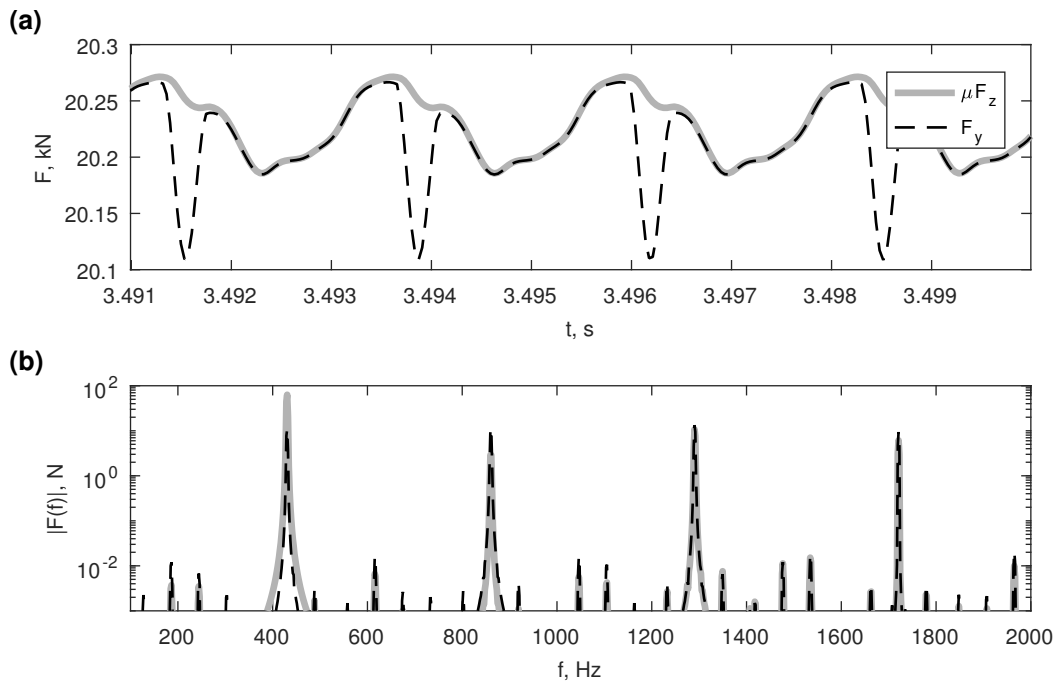


Figure 6.5: Simulation case  $\Delta y^{WR} = -5$  mm,  $\gamma_y = -0.012$ ,  $\mu = 0.3$ : (a) detail of the contact-forces time-history: (- - black) lateral force  $F_y$ ; (— grey) vertical force multiplied by the friction coefficient,  $\mu F_z$ ; (b) amplitude spectra of the contact forces: (- - black) lateral force; (— grey) vertical force.

In the investigated cases, the dominant sound frequency is coincident with the excited mode eigenfrequency. This is a result of the high vertical-force amplitude with a dominant frequency coincident with the excited mode eigenfrequency. Figure 6.5 presents an example of the contact forces time-history and their amplitude spectra. In Figure 6.5 (b), the vertical force shows a significantly higher response at 430 Hz, corresponding to the  $(2, 0, a)$  wheel mode. The higher harmonics of the vertical force are significantly lower than the fundamental. In comparison, the lat-

eral force has a maximum at the third harmonic. This maximum is not significantly higher than the response at other harmonics. It is, however, much lower in amplitude than the vertical-force fundamental harmonic. As a consequence, the wheel is most strongly excited at the  $(2, 0, a)$  mode eigenfrequency. The dominant sound frequency is, therefore, coincident with the excited mode eigenfrequency.

As can be seen from Figure 6.5 (a), stick-slip is best observed in the lateral force response. The force suddenly drops when stick takes place. The interchange of stick and slip causes the force variation. As a consequence, higher harmonics are present in the force spectra. The vertical force shows a lower deviation from the pure sinusoidal shape. Deviations in the vertical force response are caused by the coupling between the vertical and the lateral direction.

Additionally, results of the -10 and -15 mm one-point contact cases share similarities regarding the lateral force and sound power levels. Compared to those cases, the -5 mm case shows significantly lower levels. Differences of up to 20 dB in the sound power levels are noticed for the same simulation parameters.

Amongst the studied contact cases, the -10 mm case is the most critical one. Squeal occurs even for low wheel/rail friction values. The application of friction modifiers in real situations with this contact case may not lead to abatement of curve squeal. This partly explains the findings from the literature [2, 26], where squeal was not eliminated despite the application of friction modifiers. However, a change in wheel/rail friction may influence the vehicle dynamics and result in a more favourable contact position. With so many different parameters and interconnections, it is not surprising that mixed findings are encountered in both literature and practice.

The contact position has a high influence on squeal levels and its occurrence at low friction values. It does not, however, significantly influence the value of the lateral creepage threshold. The creepage threshold is the minimum lateral creepage value above which squeal occurs. This threshold is dependent on the friction value and increases with increasing friction.

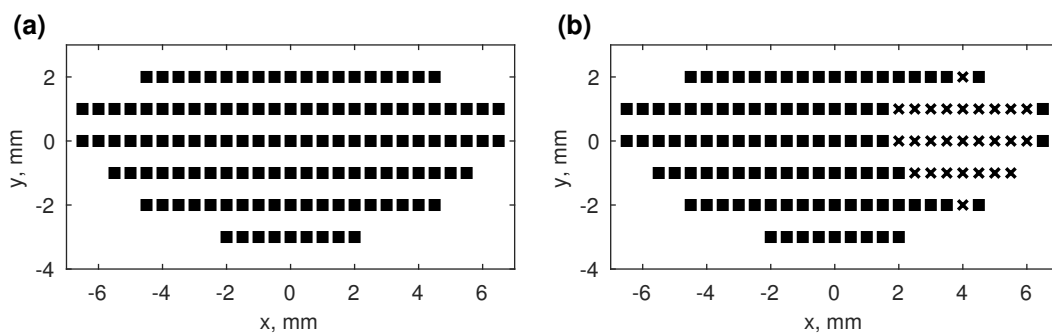


Figure 6.6: Stick and slip distribution in the contact area for the contact case  $\Delta y^{WR} = -15$  mm with  $\gamma_y = -0.008$  and two friction values: (a)  $\mu = 0.3$ ; (b)  $\mu = 0.6$ : (■) slip zones; (×) stick zones.

Figure 6.6 explains why the creepage-threshold depends on friction. The figure shows the distribution of the contact area into stick and slip regions for the -15

mm contact case and two different friction values. Lateral creepage is identical in both cases and equals to  $-0.008$ . The stick/slip distributions are obtained using Kalker's contact model without consideration of the wheel/rail dynamics. For a constant  $-0.008$  creepage value, the results in Figure 6.4 show that squeal develops in the case with 0.3 friction, but not in the 0.6 friction case. In the 0.3 friction case, the tangential contact force is saturated, and the contact is in full slip, as visible in Figure 6.6 (a). In contrast, the case with 0.6 friction is further away from force-saturation and, visible in Figure 6.6 (b), part of the contact is in stick. The presented findings support observations from Chen et al. [19] and Quian et al. [88] discussed in Section 3.2.1: stick-slip, and consequently curve squeal, can develop when the tangential force is saturated<sup>2</sup>. In conclusion, the lateral creepage threshold is related to the onset of force saturation (or near-saturation). Friction influences the creepage value at which saturation occurs. Higher friction results in higher tangential contact loading. The latter allows for better compensation of the wheel/rail relative motion in the contact via higher contact deformations.

The creepage/friction parameter study demonstrated that wheel/rail kinematic and friction parameters strongly influence the occurrence and, especially, amplitudes of squeal. Finally, only axial modes with zero nodal circles are excited into curve squeal. This is in accordance with findings presented in the contact model validation, Section 5.2.2, and observations from the available literature [60, 100, 110].

## 6.2 Wheel modal damping study

As discussed in Section 2.3.2, wheel damping treatments are a common mitigation measure for curve squeal and rolling noise. The wheel is the main sound radiator during squeal and a significant contributor to higher-frequency ( $> 1$  kHz) rolling noise [100]. Wheel damping is, therefore, expected to provide benefits. This section aims at investigating the relation between wheel modal damping and the occurrence, amplitude and frequency of squeal. To the author's knowledge, no studies exist in the available literature about the direct influence of wheel damping on curve squeal.

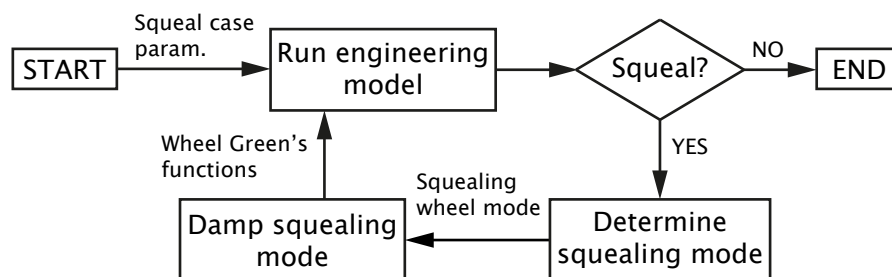


Figure 6.7: Procedure of the wheel modal damping study.

<sup>2</sup>However, it may also be enough to be near saturation for stick-slip to develop. This was already discussed in Section 3.2.1, but without a definite conclusion. More research on this topic is needed to determine the exact conditions required for the development of curve squeal.

Figure 6.7 presents the procedure of the modal damping study. The starting point is the definition of a curve squeal case, which is then simulated using the engineering model. The lateral contact force time-history is analysed to determine whether squeal develops or not. If squeal develops, the wheel mode responsible for squeal is identified. The damping factor value  $\zeta_{sq}$  for which squeal disappears at that mode is determined in a separate analysis. This damping factor value is referred to as the “squeal-critical” modal damping factor.

Next, the wheel model is updated so that the previously-squealing mode(s) are squeal-critically damped. The damping of other modes is unchanged and follows from Equation (4.14). New wheel Green’s functions are obtained, the squeal case is analysed again, and results checked for squeal. If squeal persists, the next wheel mode excited into squeal is considered and its squeal-critical damping determined. The described procedure is repeated as long as squeal moves to another mode after the previously-squealing mode is damped.

The squeal-critical modal damping factor  $\zeta_{sq}$  is determined in a procedure similar to the damping-study procedure in Figure 6.7. The main difference is that the wheel response is significantly modified to determine the critical damping. Only the squealing wheel mode and the wheel suspension effects are included in the dynamic response. Squeal simulations are then run with this altered wheel model. Modal damping of the included mode is gradually increased until squeal disappears in the analysed case. The squeal-critical damping of the considered mode is then used to obtain new wheel Green’s functions, as described above.

$\Delta y^{WR}$ , mm	$\mu$	$\gamma_y$	Results
-15	0.25	-0.012	Figure 6.8
-15	0.25	-0.04	Figure 6.9
-15	0.4	-0.012	Figure 6.10
-15	0.4	-0.04	Figure 6.11
-15	0.6	-0.012	Figure 6.12
-15	0.6	-0.04	Figure 6.13

Table 6.1: Squeal cases used in the wheel modal damping study.

The presented procedure is performed on squeal cases defined in Table 6.1. A combination of cases with moderate and high values of friction and lateral creepage is chosen. The  $\Delta y^{WR} = -15$  mm one-point wheel/rail contact case was considered.

Results of the study are presented for each squeal case with the lateral force rms-level  $L_{F_y}$  and the squeal-critical modal damping factor  $\zeta_{sq}$ . The first result point of each case corresponds to the initial squeal simulation with the original wheel dynamics. The next result point gives results of the simulation with altered wheel dynamics, where the previously squealing mode is squeal-critically damped. This progression of results (and squeal) is indicated by arrows in the force rms-level plots. Figures 6.8 to 6.13 present results of the damping study. Numerical values of the squeal-critical damping factor and the mode eigenfrequency are also given.

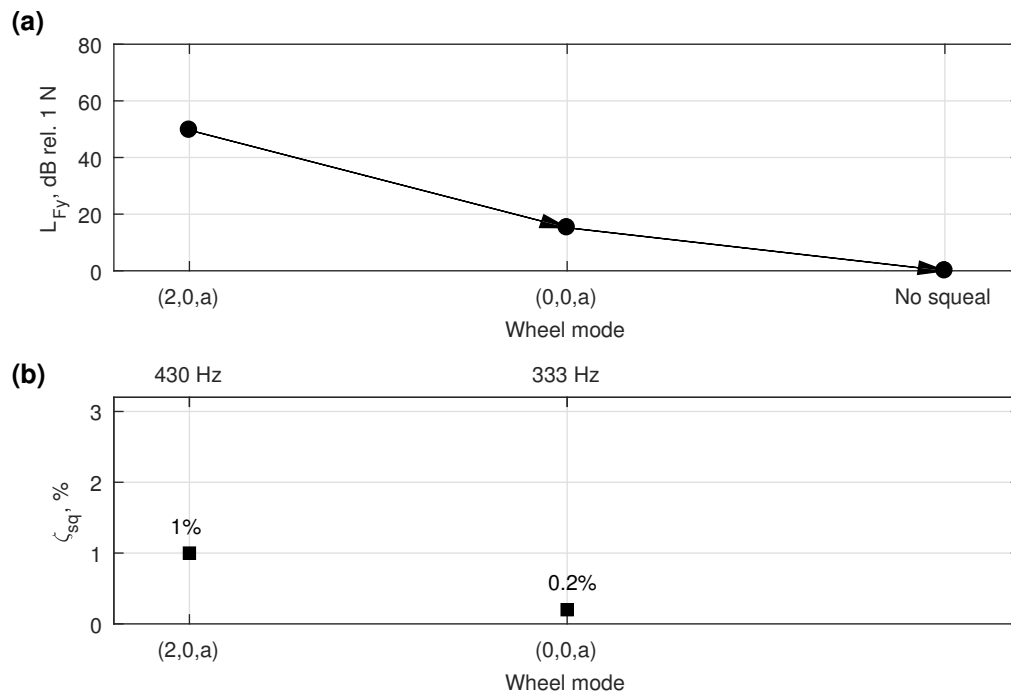


Figure 6.8: Squeal case  $\mu = 0.25$ ,  $\gamma_y = -0.012$  damping study results: (a) lateral contact force levels at squealing modes; (b) squeal-critical modal damping factors.

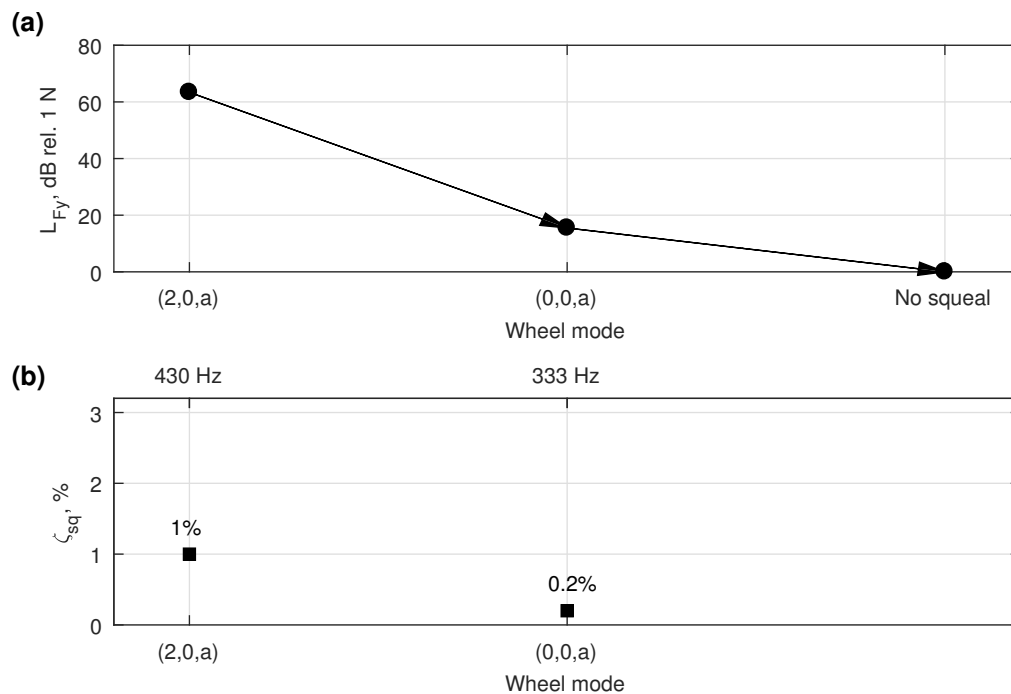


Figure 6.9: Squeal case  $\mu = 0.25$ ,  $\gamma_y = -0.04$  damping study results: (a) lateral contact force levels at squealing modes; (b) squeal-critical modal damping factors.

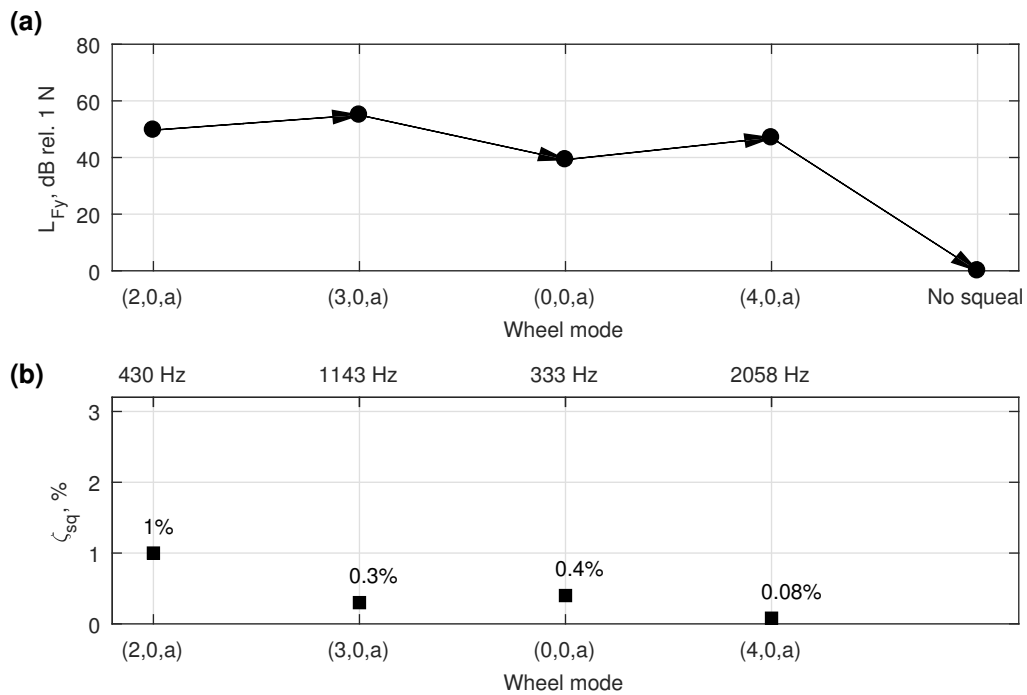


Figure 6.10: Squeal case  $\mu = 0.4$ ,  $\gamma_y = -0.012$  damping study results: (a) lateral contact force levels at squealing modes; (b) squeal-critical modal damping factors.

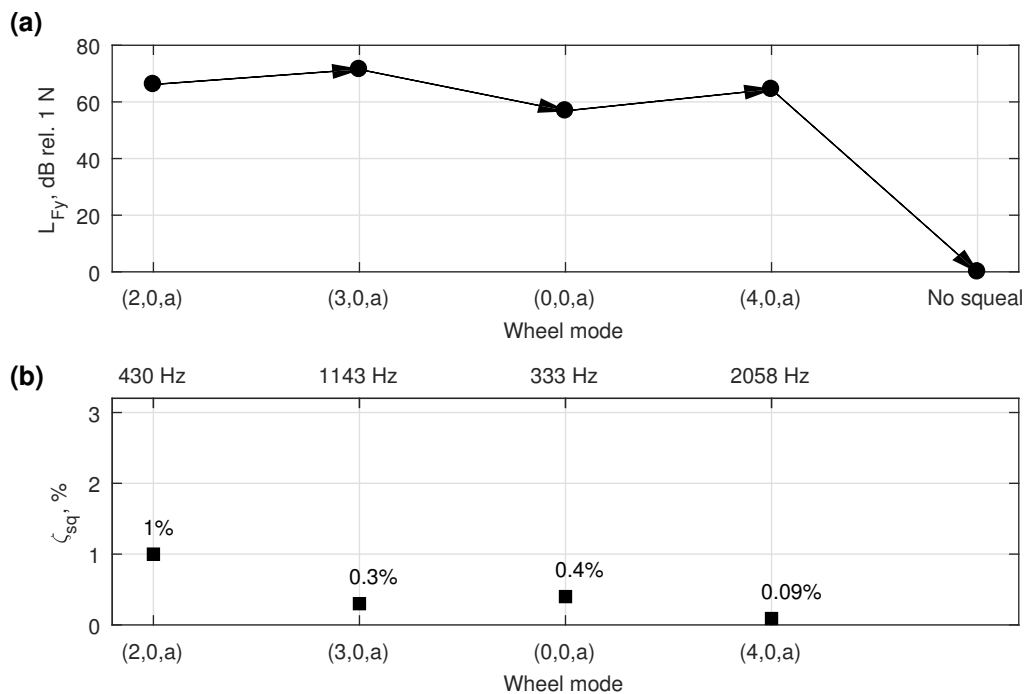


Figure 6.11: Squeal case  $\mu = 0.4$ ,  $\gamma_y = -0.04$  damping study results: (a) lateral contact force levels at squealing modes; (b) squeal-critical modal damping factors.

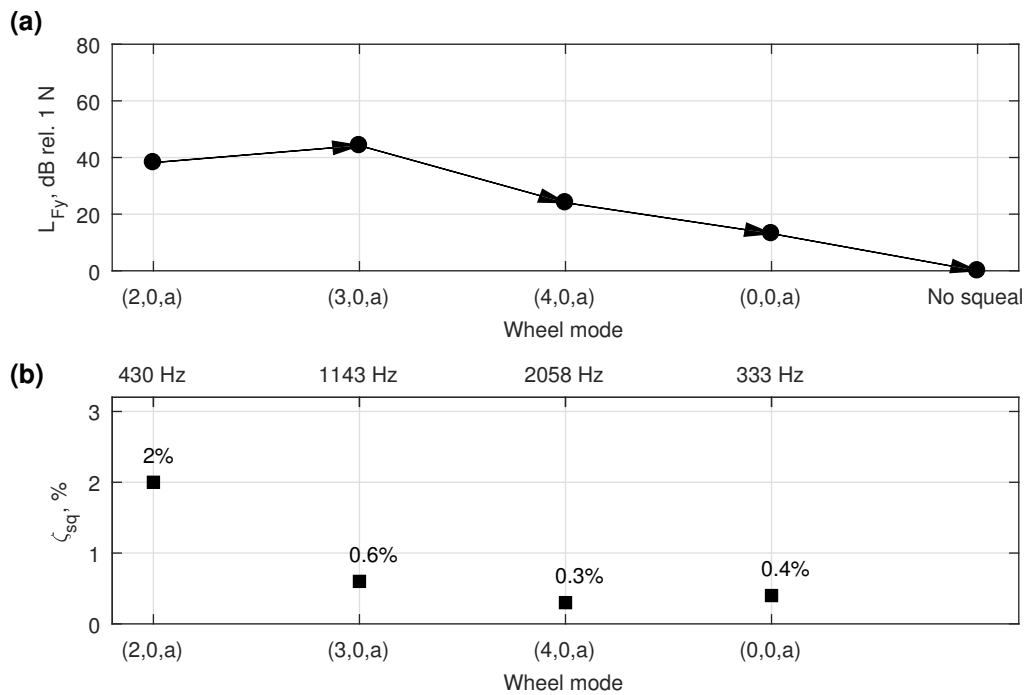


Figure 6.12: Squeal case  $\mu = 0.6$ ,  $\gamma_y = -0.012$  damping study results: (a) lateral contact force levels at squealing modes; (b) squeal-critical modal damping factors.

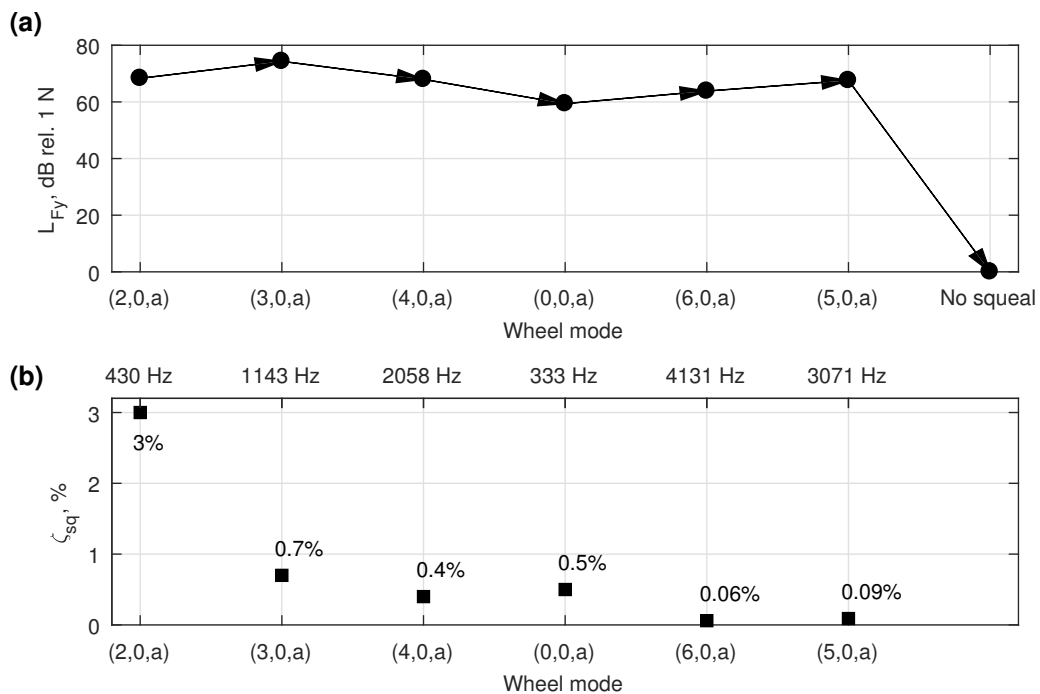


Figure 6.13: Squeal case  $\mu = 0.6$ ,  $\gamma_y = -0.04$  damping study results: (a) lateral contact force levels at squealing modes; (b) squeal-critical modal damping factors.

The friction coefficient has a strong influence on the number of wheel modes that are successively excited into curve squeal. The cases with  $\mu = 0.25$  friction, presented in Figures 6.8 and 6.9, show a relatively simple behaviour. Squeal moves only once, from wheel mode  $(2, 0, a)$  to mode  $(0, 0, a)$  with a significant reduction in force levels. After the  $(0, 0, a)$  mode is critically damped, squeal is completely eliminated. In contrast, cases with friction values  $\mu = 0.4$  (Figures 6.10 and 6.11) and  $\mu = 0.6$  (Figures 6.12 and 6.13) show a more complex behaviour. The rather extreme squeal case with  $\mu = 0.6$  and  $\gamma_y = -0.04$  shows six modes being successively excited into squeal, see Figure 6.13. Table 6.2 presents the succession of wheel modes that are excited into squeal at each squeal case. Squeal successively moves from one axial mode with zero nodal circles to another. Interestingly, the lateral force level does not necessarily decrease as squeal moves to another wheel mode.

$\mu$	$\gamma_y$	Wheel-modes succession
0.25	-0.012	$(2, 0, a) \rightarrow (0, 0, a)$
0.25	-0.04	$(2, 0, a) \rightarrow (0, 0, a)$
0.4	-0.012	$(2, 0, a) \rightarrow (3, 0, a) \rightarrow (0, 0, a) \rightarrow (4, 0, a)$
0.4	-0.04	$(2, 0, a) \rightarrow (3, 0, a) \rightarrow (0, 0, a) \rightarrow (4, 0, a)$
0.6	-0.012	$(2, 0, a) \rightarrow (3, 0, a) \rightarrow (4, 0, a) \rightarrow (0, 0, a)$
0.6	-0.04	$(2, 0, a) \rightarrow (3, 0, a) \rightarrow (4, 0, a) \rightarrow (0, 0, a) \rightarrow (6, 0, a) \rightarrow (5, 0, a)$

Table 6.2: Succession of squealing modes in the wheel modal damping study.

The influence of lateral creepage is only secondary to the influence of friction. Higher lateral creepage leads to higher lateral force levels during squeal, but it mainly does not influence which modes are excited. Only in the high-friction case ( $\mu = 0.6$ ) does a high creepage value lead to more modes being excited into squeal.

The squeal-critical damping factor is relatively low for the  $\mu = 0.4$  and  $\mu = 0.25$  squeal cases, but increases for cases with  $\mu = 0.6$  friction. This increase is much higher at the initially squealing  $(2, 0, a)$  mode than at following modes. Friction influences the vertical-lateral coupling, energy input, force-saturation point and perhaps even the damping in the system. Input energy and the dynamics coupling are directly influenced by friction since it defines the relation between the tangential and the normal contact force. Due to the broad influence of friction, it is impossible to fully explain its influence on the squeal-critical damping.

The presented results indicate that squeal is easier to mitigate in cases with low to moderate friction. While this is an expected finding, the behaviour observed in high-friction cases is rather interesting. In high-friction cases, the damping treatment has to increase the modal damping of a significant number of modes. Ideally, all wheel modes susceptible to squeal (here, all axial modes with zero nodal circles) should be damped. A favourable finding is that the amount of wheel damping required to eliminate squeal is relatively low, which supports Thompson's observation [100].

In the investigated cases, the critical damping of the initially squealing mode is much higher than the damping of subsequently squealing modes. However, practical

damping treatments do not increase the damping of a single mode without introducing damping at other modes<sup>3</sup>. Therefore, practical damping treatments that critically damp the initially squealing mode may also sufficiently damp other wheel modes and completely mitigate squeal. Unfortunately, this is not always achieved, and squeal was also observed on vehicles with resilient wheels [2, 97]. The conclusion based on the findings of this study and practical observations is that damped wheels have a potential to mitigate curve squeal. This potential is highly dependent on the squeal case at hand (curve, vehicle, friction value) and how effectively the wheel is damped. Moreover, different phenomena might also cause squeal despite high wheel damping. An example is curve squeal in the presence of two-point wheel/rail contact [97].

When squeal moves to another wheel mode, amplitudes do not necessarily decrease. Simulation cases where amplitudes increase after squeal moved to another mode are often encountered. However, the present study was performed on a small number of cases, and general conclusions should not be drawn. A more extensive study should be conducted on different wheel/rail contact cases, a larger sample of squeal cases and different wheel/rail combinations. Only then can general conclusions be made with higher certainty. Still, the performed study gave engaging insights into the behaviour of curve squeal.

### 6.3 Influence of spin creepage

In this section, the influence of spin creepage on curve squeal is studied in six squeal cases. The three one-point wheel/rail contact cases and two lateral creepage values are considered. The analysed squeal cases are the same cases used in the validation of the spin-creepage extension presented in Section 5.2.3. The present study is theoretical. In reality, the amount of spin creepage depends on the contact angle and vehicle yaw velocity during curve negotiation. It is, however, of interest to identify the individual influence of spin on squeal occurrence and amplitudes.

Figures 6.14 to 6.16 present results of the spin-influence study on the three one-point contact cases. They are identical to Figures 5.13, 5.14 and 5.15 of the spin-extension validation, but the present figures show only results of the engineering model. Spin mainly influences the lateral contact-force  $F_y^{p2p}$  amplitude. Because spin does not influence squeal frequencies (i.e. the excited wheel mode), frequencies are not presented in the result plots. In the  $\Delta y^{\text{WR}} = -5$  mm and  $\Delta y^{\text{WR}} = -15$  mm contact cases, squeal occurs at the  $(2, 0, a)$  wheel mode at 429.9 Hz. Squeal in the  $\Delta y^{\text{WR}} = -10$  mm contact case corresponds to wheel mode  $(3, 0, a)$  at 1143.2 Hz.

The influence of spin on squeal amplitudes strongly depends on the contact case, i.e. the contact area shape and size. The same observation was already made in the spin-extension validation, Section 5.2.3. Results of contact cases -5 and -15 mm, presented in Figures 6.14 and 6.16, show a similar influence of spin. For increasing

<sup>3</sup>Tuned mass dampers (tuned absorbers) may be an exception to this rule. They do, however, probably influence wheel modes in other ways (e.g. stiffness or mass influence).

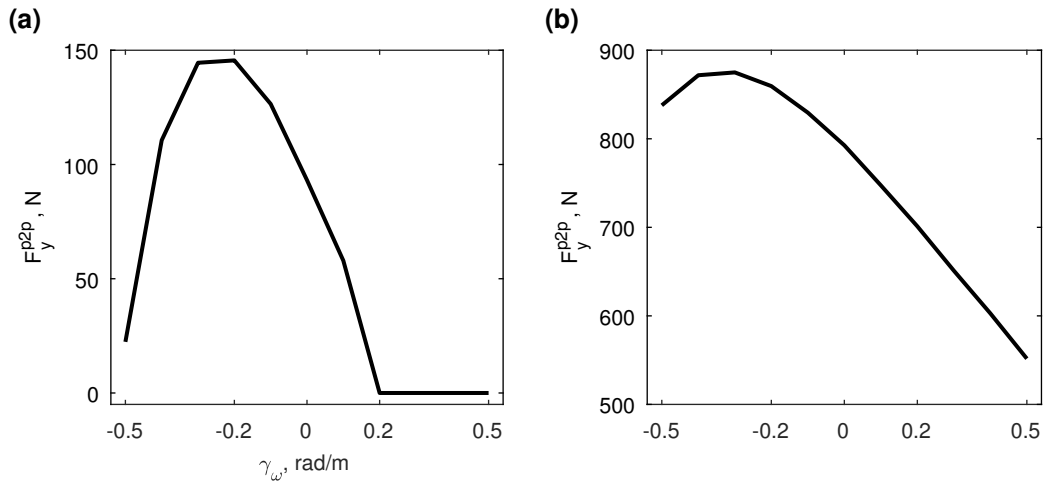


Figure 6.14: Results of the spin-influence study for the  $\Delta y^{\text{WR}} = -5$  mm contact case: (a) sub-case  $\gamma_y = -0.01$ ; (b) sub-case  $\gamma_y = -0.03$ .

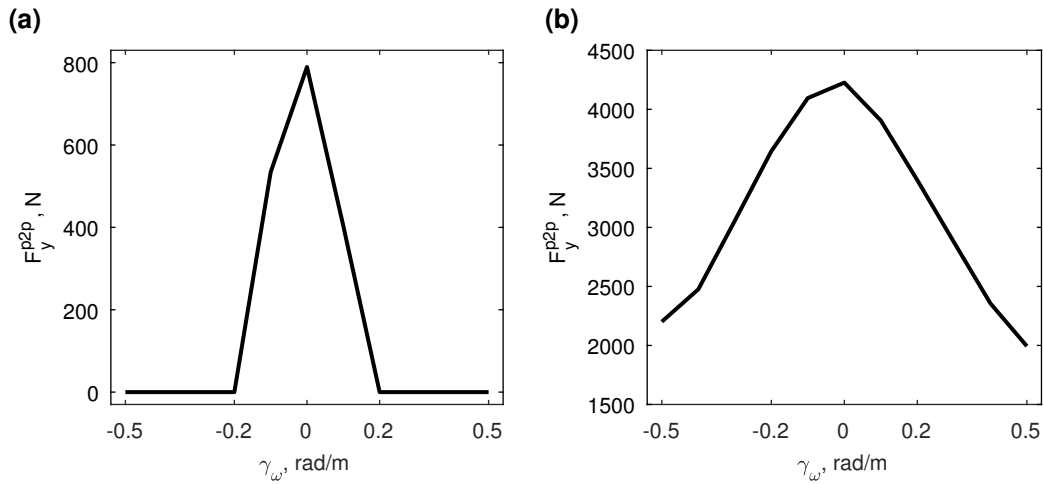


Figure 6.15: Results of the spin-influence study for the  $\Delta y^{\text{WR}} = -10$  mm contact case: (a) sub-case  $\gamma_y = -0.01$ ; (b) sub-case  $\gamma_y = -0.03$ .

negative spin the lateral-force amplitude increases until reaching a maximum. For a further decrease in spin, amplitudes start to decrease. With increasing positive spin, the force amplitudes decrease until, depending on the case, squeal disappears. The reason for similar result behaviour of the two contact cases is the shape-similarity of the contact areas, see Figures 4.24 (a) and (c).

The  $\Delta y^{\text{WR}} = -10$  mm contact case behaves significantly different, as can be seen from Figure 6.15. For both positive and negative spin, force-amplitudes decrease with increasing absolute spin values. The curves in Figure 6.15 are almost symmetric with respect to zero spin. In comparison to the other two contact cases, the -10 mm case has a significantly different contact area shape shown in Figure 4.24 (b). The contact area consists of three distinct patches, which may be the reason for the

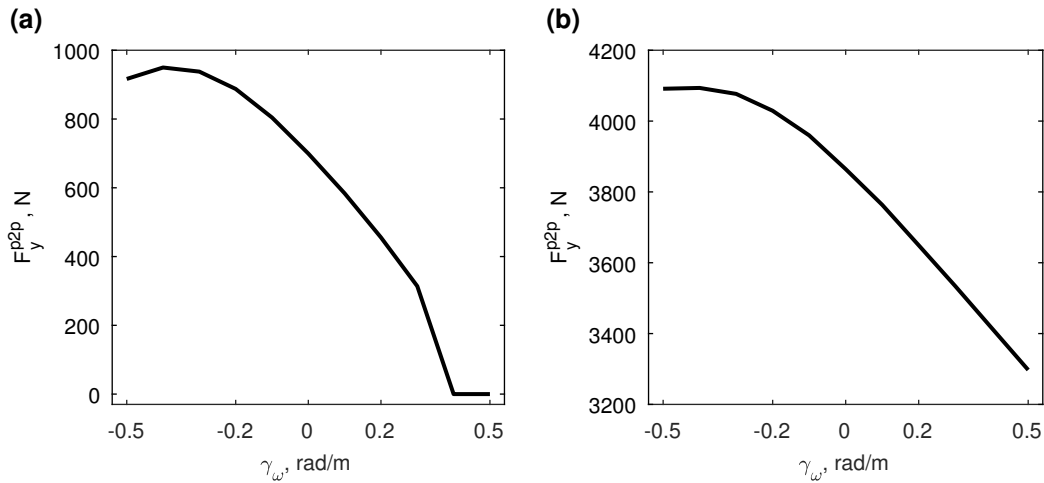


Figure 6.16: Results of the spin-influence study for the  $\Delta y^{\text{WR}} = -15$  mm contact case: (a) sub-case  $\gamma_y = -0.01$ ; (b) sub-case  $\gamma_y = -0.03$ .

observed behaviour.

Part of the explanation for the observed results behaviour lies in the shape of the friction curves. Figure 4.22, showing friction curves for non-zero spin, is repeated in Figure 6.17 for explanatory purposes. The relation between the force amplitude and the friction curve is rather complex. The exact position of the working point on the friction curve depends on the slip velocity. Slip velocity, in turn, depends upon the wheel/rail dynamics and the contact forces. This dependence forms a closed excitation loop. Nevertheless, a relationship between the friction curves and the results of the present study is observed.

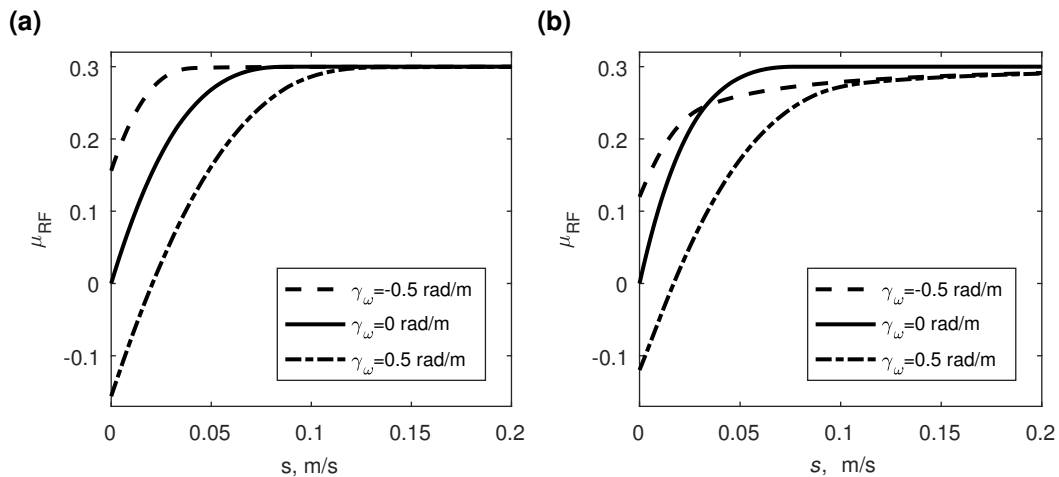


Figure 6.17: Regularised friction curves for  $\mu = 0.3$  friction coefficient, different spin creepage values and one-point wheel/rail contact cases: (a)  $\Delta y^{\text{WR}} = -5$  mm case; (b)  $\Delta y^{\text{WR}} = -10$  mm case: (- - -)  $\gamma_\omega = -0.5$  rad/m; (—)  $\gamma_\omega = 0$  rad/m; (-.-)  $\gamma_\omega = 0.5$  rad/m.

In the -5 and -15 mm contact cases, regularised friction curves for positive, negative and zero spin significantly differ in their approach to the asymptote. For negative spin, they reach the asymptotic value at lower slip than the zero-spin curve. The asymptotic value for positive spin is reached at higher slip-velocity values. This is seen from Figure 6.17 (a). As discussed in Sections 4.3.5 and 4.3.6, regularised friction curves describe the transition from full-stick to full-slip contact conditions. Therefore, the full-stick to full-slip transition is very different for different spin-creepage values.

The friction curves of the -10 mm contact case reach the asymptote at higher slip for both positive and negative spin compared to the zero spin case. As seen from Figure 6.17 (b), friction curves for positive and negative spin have a similar approach to the asymptote. Therefore, the full-stick to full-slip transition for positive and negative spin-creepage values is quite similar in the -10 mm case.

The quasi-symmetry of results in the -10 mm case (Figure 6.15) is mainly attributed to the explained similarity of friction curves with respect to zero spin. Other one-point contact cases do not show such similarity, leading to asymmetric results with respect to zero spin, see Figures 6.14 and 6.16. Besides the friction curve influence, the behaviour of the results also depends on the wheel and rail dynamics at each contact location.

In conclusion, spin creepage is seen to only influence amplitudes of the lateral contact force. This directly translates to an influence on amplitudes of curve squeal. High spin-creepage values may even completely disrupt the stick-slip process in the contact area. This disruption occurs most probably due to the rotational nature of spin. Therefore, the influence is also very dependent on the direction of spin. Due to its nature, spin influences the distribution of stick and slip regions in the contact area and the saturation point of the tangential force.

## 6.4 Influence of the contact angle

The contact-angle influence study presented in this section is a purely theoretical study. In reality, the contact angle is defined by the wheel and rail profiles and the location of the contact point on them. However, as the contact angle influences the dynamics coupling, it is of interest to investigate its influence on curve squeal.

The influence of the contact angle is studied in six squeal cases. The three one-point wheel/rail contact cases are analysed with  $\mu = 0.3$  and  $\mu = 0.6$  friction values. The lateral creepage value is set to  $\gamma_y = -0.01$ , and spin creepage is zero. A total of five seconds of rolling is simulated. In each squeal case, the contact angle is varied in the range  $0^\circ \leq \alpha_c \leq 10^\circ$  with  $\Delta\alpha_c = 1^\circ$ . Only positive contact angles are considered since negative angles are not expected due to wheel conicity. Study results are expressed with the lateral contact-force peak-2-peak amplitude  $F_y^{p2p}$ .

Figure 6.18 presents results for the -5 and -15 mm cases and 0.3 friction value. Cases with 0.6 friction did not lead to squeal in the cases mentioned above. Results of the -10 mm contact case, presented in Figure 6.19, show squeal occurring for both

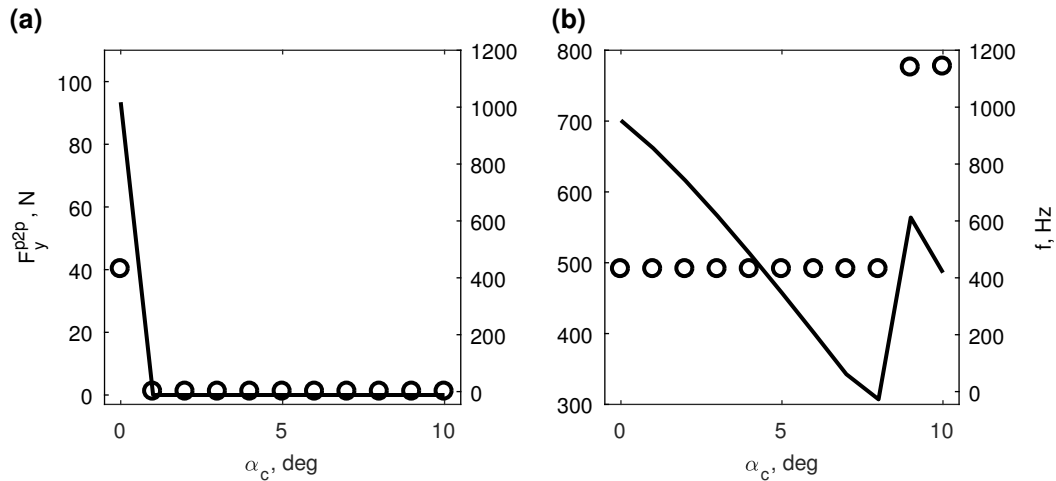


Figure 6.18: Results of the contact angle study for  $\gamma_y = -0.01$  and  $\mu = 0.3$ : (a)  $\Delta y^{WR} = -5$  mm contact case; (b)  $\Delta y^{WR} = -15$  mm contact case: (—) lateral contact force amplitude; (o) squeal frequency.

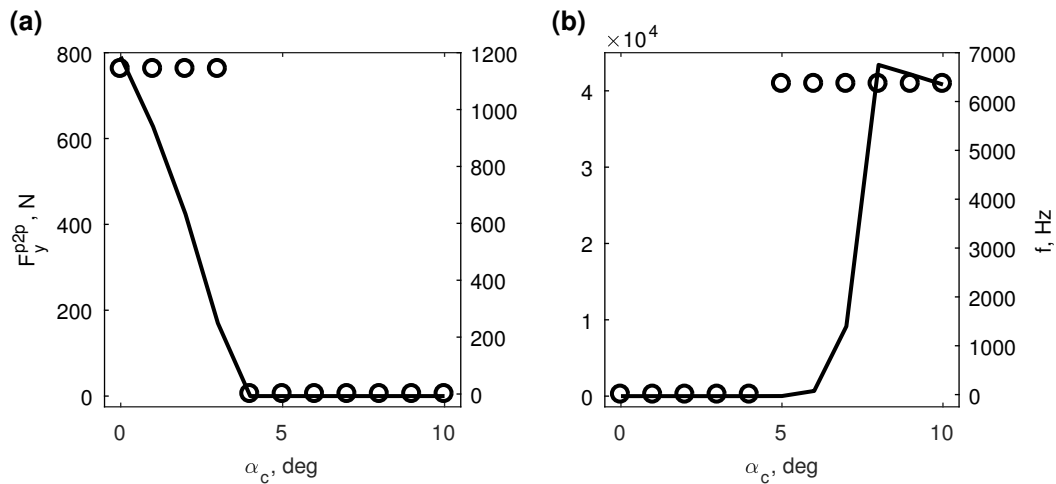


Figure 6.19: Results of the contact angle study for  $\gamma_y = -0.01$  and  $\Delta y^{WR} = -10$  mm contact case: (a) sub-case  $\mu = 0.3$ ; (b) sub-case  $\mu = 0.6$ : (—) lateral contact force amplitude; (o) squeal frequency.

friction values.

Study results show that the contact angle has a high, contact-case dependent influence on both the squeal amplitudes and the frequencies. A similar influence of the contact angle is observed in the -5 and -10 mm contact cases with 0.3 friction value, see Figures 6.18 (a) and 6.19 (a). Squeal amplitudes significantly decrease with increasing angle and, at a specific angle value, squeal disappears. The -5 mm contact case is very sensitive to the contact angle with squeal disappearing already at 1°. In comparison, squeal in the -10 mm case with 0.3 friction disappears at the angle value of 4°. Besides in amplitudes, the two contact cases differ in squeal

frequency. The axial  $(2, 0, a)$  mode at 429.9 Hz is excited in the -5 mm case, while in the -10 mm case the axial  $(3, 0, a)$  mode at 1143.2 Hz is excited. These squeal frequencies are in line with observations from the creepage/friction study of Section 6.1.

Contact case  $\Delta y^{WR} = -10$  mm with 0.6 friction, Figure 6.19 (b), shows a very different behaviour. Squeal does not develop at low contact angle values, but at  $\alpha_c = 5^\circ$  low-amplitude squeal is obtained. With increasing angle, the amplitude significantly increases and reaches a maximum at  $\alpha_c = 8^\circ$ . A further increase in the contact angle leads to a decrease in amplitudes. The squeal frequency corresponds to the  $(8, 0, a)$  wheel mode at 6315.8 Hz.

In the -15 mm contact case, Figure 6.18 (b), another interesting development is observed. As the angle increases, squeal changes frequency and amplitude but never disappears. Force-amplitudes decrease with increasing contact angle, but only if squeal remains at the same frequency. When squeal suddenly shifts from the 429.9 Hz to the 1143.2 Hz wheel mode (at  $\alpha_c = 9^\circ$ ), an increase in the lateral contact-force is observed. As the angle is increased further, amplitudes decrease, but squeal remains at the same, higher, frequency.

The contact angle and friction directly influence the dynamics-coupling mechanism by changing the relationship between the vertical and lateral forces in the system. The case at  $\Delta y^{WR} = -10$  mm and 0.6 friction is a vivid example of the combined influence that contact angle and friction can have on squeal. In that case, high friction and high contact angle lead to high-frequency and high-amplitude squeal. Squeal can also suddenly change frequency and amplitude, as in the contact case  $\Delta y^{WR} = -15$  mm in Figure 6.18 (b). Still, after a maximum or sudden jump occurs, amplitudes tend to decrease with increasing angle.

The -5 and -10 mm contact cases have a similar dynamic response. Contact points of the two cases are close, as shown in Figure 4.7. This closeness results in a relatively similar behaviour at the 0.3 friction case. In comparison, the -15 mm contact case is located further apart from the other contact locations. As a result, the dynamic response differs significantly. The different response leads to a different results behaviour. However, the presence of high friction influences the dynamics of the -10 mm case much stronger than other cases. Even if the present study is theoretical, results point to the nonlinear behaviour of curve squeal. Friction, contact angle and contact location all influence the wheel/rail system behaviour. It is, therefore, of particular importance to model all factors that influence the dynamics-coupling mechanism.

### 6.4.1 Combined influence of the contact angle and spin creepage

In the spin creepage and contact angle studies above, only one parameter was varied while others were kept constant. Such studies are suitable for determining the influence of a single parameter, but they do not reflect the real situation. As already mentioned, spin creepage and the contact angle are kinematically related. The

combined, simultaneous, influence of spin creepage and the contact angle on curve squeal is, therefore, investigated in this section. This investigation is only a step away from theoretical studies and does not reflect reality since the contact locations are not changed.

The analysed one-point contact cases are obtained for contact between the inner wheel and rail in a curve. The relationship between spin creepage and contact angle on the curve-inner wheel in steady-state curving is [9]:

$$\gamma_{\omega} = \frac{1}{R} \cos \alpha_c - \frac{1}{r_0} \sin \alpha_c. \quad (6.4)$$

The curve radius is  $R = 120$  m, and  $r_0 = 0.39$  m is the wheel nominal rolling radius. As in the contact angle study, the contact angle is varied in the range  $0^{\circ} \leq \alpha_c \leq 10^{\circ}$  with  $\Delta\alpha_c = 1^{\circ}$ . Spin creepage is the dependent variable calculated using Equation (6.4). Table 6.3 presents the values of spin creepage for defined contact angle values. The first value in the table, for zero angle, is the contribution due to the curve negotiation.

$\alpha_c, ^{\circ}$	0	1	2	3	4	5
$\gamma_{\omega}, \text{rad/m}$	0.008	-0.036	-0.081	-0.126	-0.17	-0.215
$\alpha_c, ^{\circ}$	6	7	8	9	10	
$\gamma_{\omega}, \text{rad/m}$	-0.259	-0.304	-0.348	-0.393	-0.437	

Table 6.3: Spin creepage values for different values of the contact angle.

In the combined study, the same six squeal cases used in the contact angle study of Section 6.4 are analysed. A total of eight seconds of rolling is simulated. Results are expressed with the lateral contact-force p2p amplitudes and the squeal frequency in Figures 6.20 to 6.22.

The presented results show that the contact angle has a dominant influence. This becomes apparent by comparing results of the combined study with results from the contact angle study. Figure 6.18 (a) and Figure 6.20 (a) show the same behaviour for the -5 mm contact case with 0.3 friction coefficient. The same behaviour is also observed for 0.6 friction: in both studies, squeal does not develop.

Results of the combined study in the -15 mm contact case with 0.3 friction show only slight differences compared to the angle-study results. This can be seen by comparing Figure 6.18 (b) with Figure 6.22 (a). The results behaviour in the two studies is very similar. In the combined study, squeal changes frequency at  $\alpha_c = 10^{\circ}$ , compared to  $9^{\circ}$  in the contact angle study. Amplitudes differ only slightly. Moreover, the influence of spin creepage can be observed as well. Part of the resulting curve in Figure 6.22 (a), before squeal changes frequency, resembles the shape of the resulting curve in Figure 6.16 (a).

High  $\mu = 0.6$  friction in the -15 mm case results in squeal at contact angle values  $\alpha_c \geq 8^{\circ}$ , as seen in Figure 6.22 (b). The  $(3, 0, a)$  wheel mode at 1143.2 Hz is excited. The contact angle study in the same contact case does not show such behaviour.

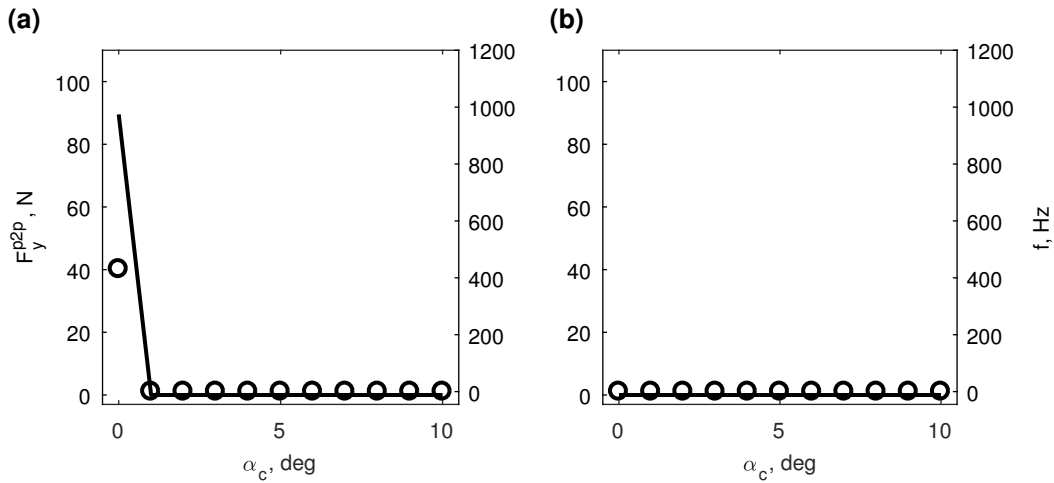


Figure 6.20: Results of the combined angle-spin study for the  $\Delta y^{\text{WR}} = -5$  mm contact case: (a) sub-case  $\mu = 0.3$ ; (b) sub-case  $\mu = 0.6$ : (—) lateral contact force amplitude; (o) squeal frequency.

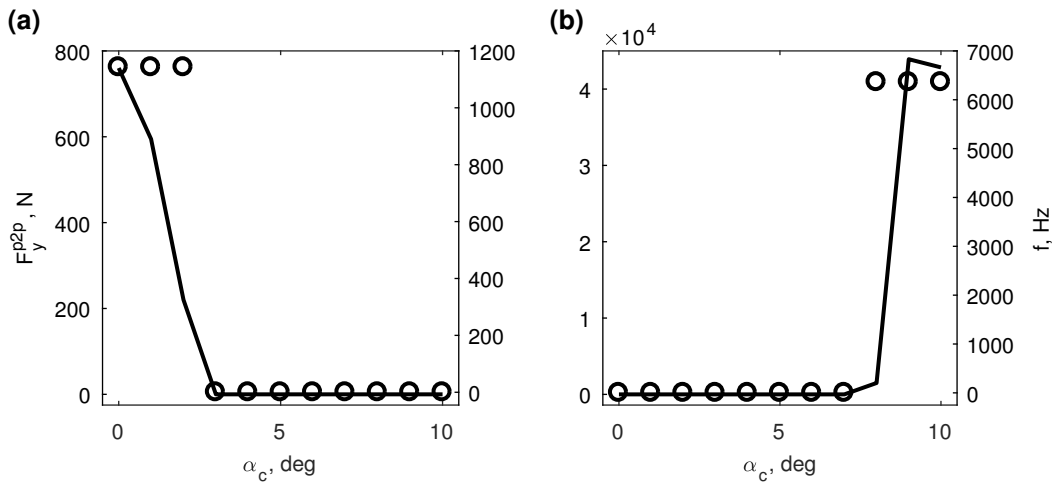


Figure 6.21: Results of the combined angle-spin study for the  $\Delta y^{\text{WR}} = -10$  mm contact case: (a) sub-case  $\mu = 0.3$ ; (b) sub-case  $\mu = 0.6$ : (—) lateral contact force amplitude; (o) squeal frequency.

Both the spin and the contact angle show a significant and simultaneous influence on squeal.

Similar to the other two contact cases, the combined-study results of the -10 mm contact case show a behaviour similar to the contact-angle study results. Figure 6.21 shows slightly lower contact-force amplitudes than in the contact-angle study, Figure 6.19. Additionally, squeal disappears at a lower angle value in the 0.3 friction case. In the case of 0.6 friction, squeal again develops at a high angle value ( $8^\circ$ ), and the presence of spin only delays squeal development.

Figure 6.23 presents a detail of the lateral contact force  $F_y$  and traction bound

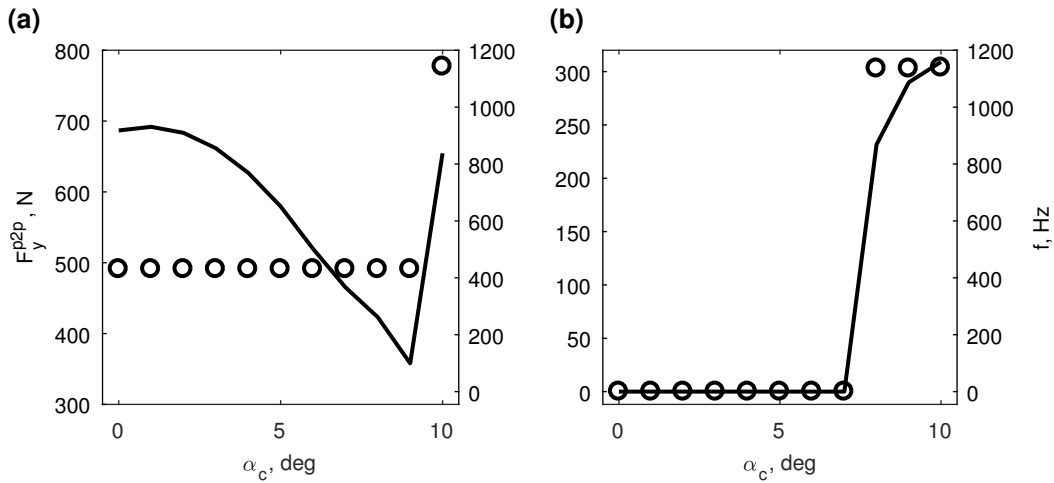


Figure 6.22: Results of the combined angle-spin study for the  $\Delta y^{\text{WR}} = -15$  mm contact case: (a) sub-case  $\mu = 0.3$ ; (b) sub-case  $\mu = 0.6$ : (—) lateral contact force amplitude; (o) squeal frequency.

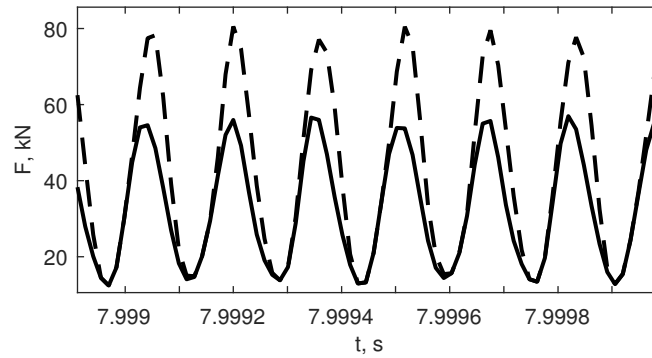


Figure 6.23: Detail of the lateral contact force time-history for the squeal case  $\Delta y^{\text{WR}} = -10$  mm,  $\mu = 0.6$ ,  $\alpha_c = 10^\circ$ ,  $\gamma_\omega = -0.437$  rad/m and  $\gamma_y = -0.01$ : (—) lateral contact force; (- -) friction force limit  $\mu F_z$ .

$\mu F_z$  time-history for the case  $\Delta y^{\text{WR}} = -10$  mm,  $\alpha_c = 10^\circ$ ,  $\mu = 0.6$  and  $\gamma_y = -0.01$ . Stick-slip is observed from the lateral force, which is not coincident with the traction bound throughout a period of oscillation. During the stick phase, the lateral contact force drops below the traction bound, whereas during the slip phase the relation  $F_y = \mu F_z$  holds. This squeal case was also analysed using Pieringer's detailed model [80, 81], which was extended to include contact angle effects. Curve squeal of the same frequency and similar amplitude was obtained. However, in the detailed model, squeal develops after 20 seconds of rolling. With the engineering model, it takes only four seconds of rolling simulation for squeal to develop. Further investigation is needed to understand the reasons behind this difference better.

The presented results show that spin creepage and contact angle in combination can significantly influence squeal occurrence and frequency. The influence of the

contact angle is dominant, which is somewhat unsurprising since the angle directly influences the dynamics coupling. Still, even spin can, besides amplitudes, influence squeal occurrence. An example of the spin-influence is the -15 mm contact case with  $\mu = 0.6$ , Figure 6.22 (b). This case is, however, specific due to significant values of the contact angle. In conclusion, it is important to consider both the influence of spin and contact angle. The contact angle is primarily important for the prediction of squeal occurrence, while spin is important in the prediction of squeal amplitudes. Still, their exact influence is unpredictable and case-dependent.

# Chapter 7

## Two-point wheel/rail contact results

---

In this chapter, a squeal case involving two-point wheel/rail contact is formulated and analysed. The two-point-contact case was defined in Section 4.1.3. Both the detailed and the engineering models for curve squeal are used to analyse the case. The models were extended to two-point contact, as described in Chapter 4 and in [123].

Parameters of the analysed squeal case are approximated since real or simulated parameters for the two-point-contact case are not available. This study aims at examining the development and complexity of squeal on curve-outer wheels in the presence of two-point wheel/rail contact. The results can also be looked upon as a validation of the engineering model.

Additionally, the two contact points of the analysed two-point-contact case are considered separately. Contact is assumed to occur only at one point. The aim is to determine the influence of modelling two contact points, their dynamic interplay and whether two-point contact can be simplified to one-point contact.

### 7.1 Two-point wheel/rail contact case parameters

Two-point wheel/rail contact is significantly more complex and requires more input parameters. These are defined for the two-point-contact case introduced in Section 4.1.3. The wheel profile is a new S1002 profile, while the rail is a worn UIC60 rail. Two-point contact occurs for the lateral wheelset displacement value of  $\Delta y^{WR} = -8$  mm. This case corresponds to contact between the outer wheel and rail in a curve.

The contact angles at the two contact points are significant and cannot be dis-

regarded, as was emphasised in Section 6.4. Due to high angle values, spin creepage is significant as well. Spin creepage on the curve-outer wheel/rail system during steady-state curving is determined from the contact angle as [9]:

$$\gamma_{\omega}^k = \frac{1}{R} \cos \alpha_c^k + \frac{1}{r_0} \sin \alpha_c^k, \quad k = 1, 2, \quad (7.1)$$

where index  $k$  denotes the contact point. Equations (6.4) and (7.1) differ in the sine term sign, which depends on whether the curve-outer or -inner wheel/rail system is considered. Additionally, the lateral creepages in the two contact points are dependent. Lateral creepage  $\gamma_y^2$  at *cp2* depends on lateral creepage  $\gamma_y^1$  at *cp1* and the contact angles  $\alpha_c^2$  according to [9]:

$$\gamma_y^2 = \frac{\gamma_y^1}{\cos \alpha_c^2}. \quad (7.2)$$

The cosine term  $\cos \alpha_c^1$ , which should appear in the numerator in Equation (7.2), is omitted. Namely, the contact angle at *cp1* is such that  $\cos \alpha_c^1 \approx 1$  and has a negligible influence on lateral creepage in *cp2*. Simulation parameters of the two-point-contact case are summarised in Table 7.1.

Parameter name	Symbol	Value
Normal distance <i>cp1-cp2</i>	$\delta_z$	$2 \cdot 10^{-5}$ m
Contact angle <i>cp1</i>	$\alpha_c^1$	8°
Contact angle <i>cp2</i>	$\alpha_c^2$	66.5°
Rolling velocity	$v$	50 km/h
Curve radius	$R$	120 m
Wheel rolling radius	$r_0$	0.39 m
Vertical wheel load	$F_{LZ}$	65 kN
Friction coefficient	$\mu^1, \mu^2$	0.35
Lateral creepage <i>cp1</i>	$\gamma_y^1$	0.0065
Lateral creepage <i>cp2</i>	$\gamma_y^2$	0.0163
Spin creepage <i>cp1</i>	$\gamma_{\omega}^1$	0.37 rad/m
Spin creepage <i>cp2</i>	$\gamma_{\omega}^2$	2.35 rad/m
Simulation time-step	$\Delta t$	$\Delta x/v = 36 \mu\text{s}$
Simulation end-time	$t_{end}$	1.5 s

Table 7.1: Two-point wheel/rail contact: squeal-case parameters.

Regularised friction curves used in the engineering model are determined with the procedure proposed in Section 4.3.6. Friction curves are determined individually for each contact point. Since the two contact points are not evenly loaded, the vertical load at each point was determined first. Then, the friction models were determined with the correct vertical load at each point.

Figure 7.1 shows the contact areas of contact points 1 and 2. These are used to evaluate the non-conformal contact assumption which was discussed in Section 3.2

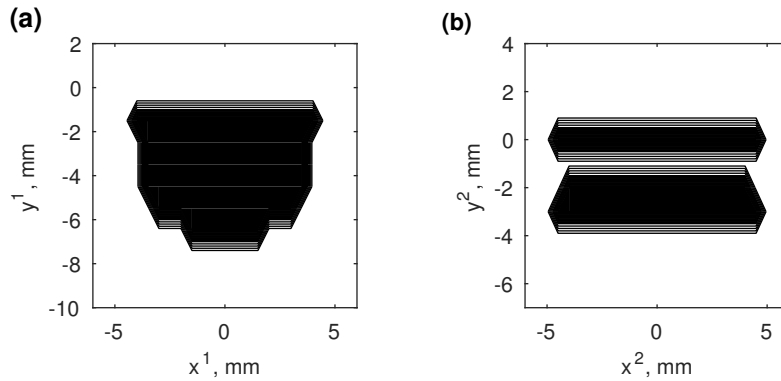


Figure 7.1: Shape and size of the contact area: (a) *cp1*; (b) *cp2*. Discontinuous edges are due to the resolution of the contact discretisation.

and used in Section 4.3.1. For the non-conformal contact assumption to be valid, the contact areas should be small compared to the characteristic dimensions of the wheel and rail near the contact points.

Contact at *cp1*, occurring between the wheel tread and rail head is non-conformal. The wheel and rail minimum radius of curvature at *cp1* ( $r_{min} = 0.3$  m) is large compared to the contact dimensions of  $\approx 10$  mm in Figure 7.1 (a). Contact at *cp2* occurs between the wheel flange and rail gauge corner, with dimensions of  $\approx 10$  mm along  $x^2$  and 5 mm along  $y^2$ , see Figure 7.1 (b). Contact *cp2* is located on the section of the wheel flange where the radius of curvature is large, which can be seen from Figure 4.9. On the rail, however, contact *cp2* is located on the rail gauge corner, where the radius of curvature is between 80 and 13 mm. This radius is comparable to the contact dimensions and may violate the non-conformal contact assumption. Still, according to Yan and Fischer [119], significant result deviations are not expected in this case. A discussion of Yan and Fischer's findings was given in Section 3.2. In line with these findings, it is safe to assume that contact at *cp2* can be analysed as non-conformal.

## 7.2 Results of the two-point wheel/rail contact case

Figure 7.2 presents results of the two-point-contact case with the lateral contact force time-histories. Results of the detailed model for squeal are presented in Figure 7.2 (a), while the engineering model results are presented in Figure 7.2 (b). Since two-point contact is considered, each plot contains two time-histories, one for each contact point. Squeal develops with significant amplitudes, and, in reality, this would be a disturbing squeal event.

During the first 4000 time steps (0.144 seconds), the wheel/rail contact is established by smoothly pressing the wheel against the rail. Simultaneously, creepages are increased from zero to their final value. This contact-initialisation procedure

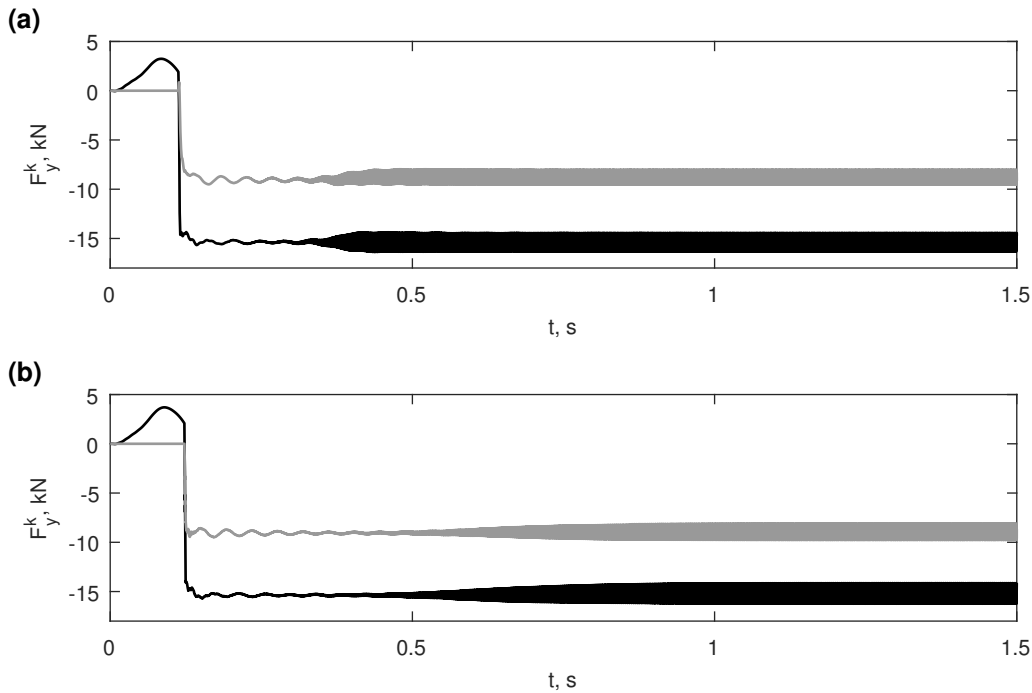


Figure 7.2: Lateral contact force time-history for the two-point-contact case: (a) detailed model; (b) engineering model: (— black) *cp1*; (— grey) *cp2*.

avoids a sudden impact between the wheel and the rail. Unphysical force impulses, which would be otherwise caused by a sudden increase of creepages, are also avoided. As assumed, contact point 1 makes initial contact, followed by contact at *cp2* at a later time. This is visible in Figure 7.2: when *cp2* comes into contact, a sudden drop in the lateral contact force in *cp1* occurs. Redistribution of the vertical load between the two contact points is the cause of this drop. As discussed in Section 4.1.3, the vertical load distribution is influenced by the normal distance  $\delta_z$ . The normal distance term was discussed in detail in Sections 4.1.3 and 4.3.2.

During the initialisation period, the lateral force  $F_y^1$  of *cp1* changes sign from positive to negative. The force is initially positive and increasing in value. Then, after reaching a maximum, it starts to decrease. The change in sign happens abruptly at the moment when *cp2* makes contact and is hastened by the load redistribution between the contact points. However, the load redistribution is not the real cause of the sign change since it is also found in the *cp1* one-point case in Figure 7.5 (a). This behaviour is instead attributed to the combined effect of the vertical force build-up, lateral creepage build-up and wheel/rail displacement during the initialisation period.

The build-up of the vertical force causes displacements that result in a non-zero lateral slip. The vertical force is, at 65 kN, high compared to the tangential force. Therefore, its gradient during the build-up is also high. The high force gradient leads to a significant gradient in the displacements and, ultimately, to a

high displacement-induced slip velocity<sup>1</sup>. Lateral creepage also gradually builds-up, but is lower in absolute value than the displacement-induced slip. The resultant slip velocity due to lateral creepage and displacement-induced slip is such that it leads to positive force. At a certain point in time, lateral creepage gets large enough to overcome the displacement-induced slip. Additionally, the displacement-induced slip decreases as the vertical force gets closer to its final value and its gradient decreases. Slip then changes direction and the force changes sign.

The reason why the force sign change occurs only at *cp1* lies in the combination of wheel asymmetry and high vertical load at *cp1*. The high vertical load at *cp1* causes, due to the wheel asymmetry, a significant lateral displacement at *cp1*. As a result, slip velocity values get high enough to overcome the lateral creepage during the contact initialisation. The sign change is not observed in *cp2*.

Figures 7.2 (a) and (b) reveal only minor differences between results of the detailed and the engineering model. The transient response in the initial 0.3 seconds is almost identical in both result sets. After that, results differ in the time it takes to reach steady-state squeal. Squeal develops faster in the detailed model, while the engineering model describes a longer and smoother build-up period.

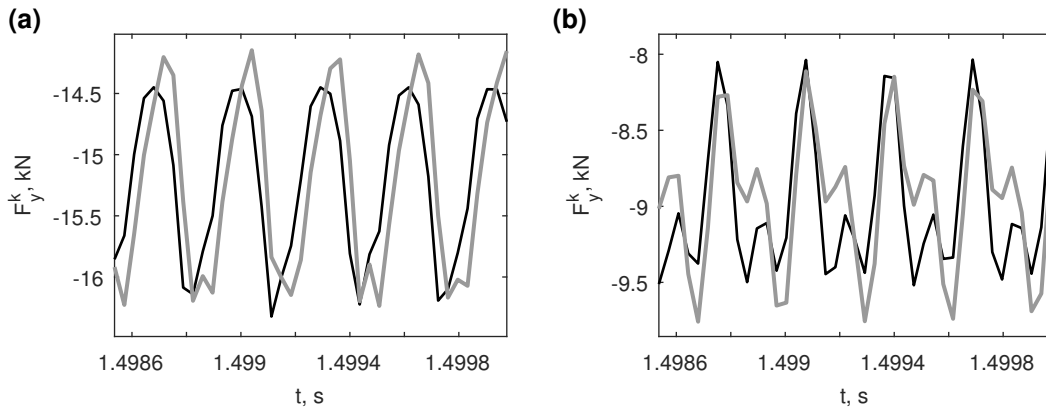


Figure 7.3: Lateral contact force time-history, detail of stick-slip: (a) *cp1*; (b) *cp2*: (— black) detailed model; (— grey) engineering model.

Figure 7.3 shows a detail of the lateral contact-force time history for the two contact points. The detail belongs to a steady-state section of the curves in Figure 7.2. Results of the detailed and engineering model are plotted against each other and show very good agreement. Small differences in the force amplitudes are noticed, but the frequency content and stick-slip details agree well. Stick-slip is observed in both contact points but is more pronounced in contact point *cp2*.

Table 7.2 summarises numerical results of the two-point-contact case. Lateral contact-force amplitudes  $F_y^{p2p,k}$ , the total radiated sound power from the wheel  $L_W^{tot}$  and the dominant frequency in the radiated sound  $f_{LW}^{max}$  are presented. The relative difference between force amplitudes of the detailed and engineering model is 11%.

<sup>1</sup>The vertical force causes tangential displacements in the contact due to (1) the non-zero contact angle and (2) the vertical-lateral coupling dynamics.

This difference is in line with the differences observed in the validation of the contact model in Section 5.2. The difference in the radiated sound power, which is more relevant for judging squeal severity, is 0.67 dB and is negligible. Table 7.2 and Figure 7.2 also show that the lateral contact-force amplitudes in the two points are comparable. The wheel is, therefore, strongly excited in both contact points.

Variable	Detailed model	Engineering model
$F_y^{p2p,1}$	1879.59 N	2092.73 N
$F_y^{p2p,2}$	1494.11 N	1664.36 N
$L_W^{tot}$	117.66 dB	118.33 dB
$f_{LW}^{max}$	3217.9 Hz	3216.2 Hz

Table 7.2: Numerical results of the two-point wheel/rail contact squeal case.

Figure 7.4 presents the radiated sound power spectrum. Again, good agreement between results of the two squeal models is found. Differences are noticed in regions with low power levels. However, the influence on the overall level is low, as seen from values in Table 7.2. The overall level is dominated by the highest peaks, which agree very well in both the detailed and engineering model spectra. Dominant sound peaks are located at 3217 Hz and 6434 Hz. As expected, the higher frequency peak corresponds to the second harmonic of the 3217 Hz peak.

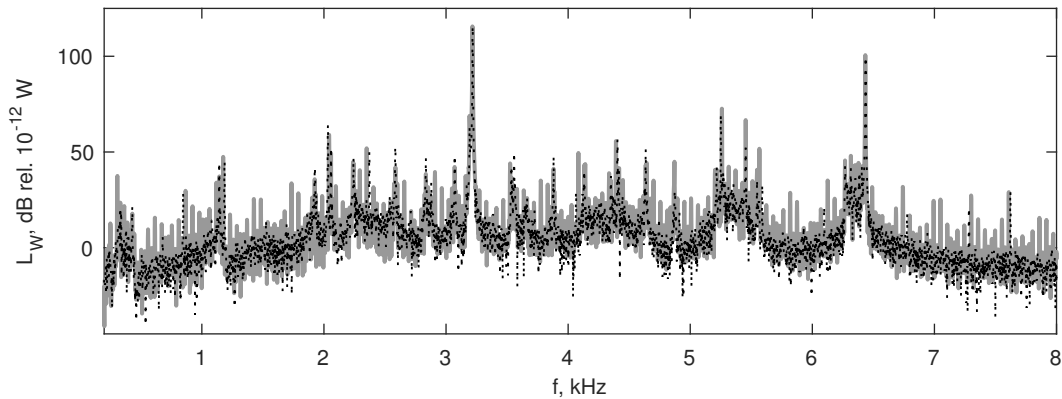


Figure 7.4: Radiated sound power spectrum of the two-point-contact case: (— black) detailed model; (— grey) engineering model.

Two wheel modes are present near the 3217 Hz frequency. One is the  $(5, 0, a)$  mode at 3070.8 Hz, and the other is mode  $(3, 1, a)$  at 3193 Hz. When either one of these modes is critically damped, squeal does not develop. Therefore, squeal in the analysed two-point-contact case is the result of the coupling of two wheel modes.

Curve squeal develops even if the normal distance is disregarded, i.e. set to zero ( $\delta_z = 0$ ). Squeal amplitudes are similar, and the main difference is in the lateral force mean value. The mean values of  $F_y^1$  and  $F_y^2$  are close, meaning that the vertical wheel load is distributed more evenly between the two points. Small variations in the normal distance are, therefore, not expected to influence squeal in this case.

### 7.3 Comparison to one-point wheel/rail contact results

In this section, the contact points of the two-point-contact case are evaluated separately. Each contact point is evaluated in a separate one-point wheel/rail contact case. This study aims at investigating the interaction between the two contact points and their importance for curve squeal. Additionally, the study also provides information about the possible simplification of a two-point-contact case to two one-point-contact cases.

Table 7.1 defines simulation parameters of the two one-point-contact cases. Squeal case parameters are the same as in the two-point-contact case: in the simulation of contact point  $k$ , parameters referring to that point are used. Since one-point contact is considered, the normal distance  $\delta_z$  is not used, and the vertical load  $F_{LZ}$  is the same in both contact cases. The cases are analysed with both squeal models.

Results of the one-point-contact cases are presented in Figure 7.5. Only results from the engineering model are shown since the detailed model gives the same results. The one-point-contact cases show remarkably different behaviour compared to the two-point-contact case. While in the two-point-contact case high-frequency squeal develops, in the one-point-contact cases squeal does not develop. The *cp2* case shows no unstable behaviour, but severe vibrations develop in the *cp1* case.

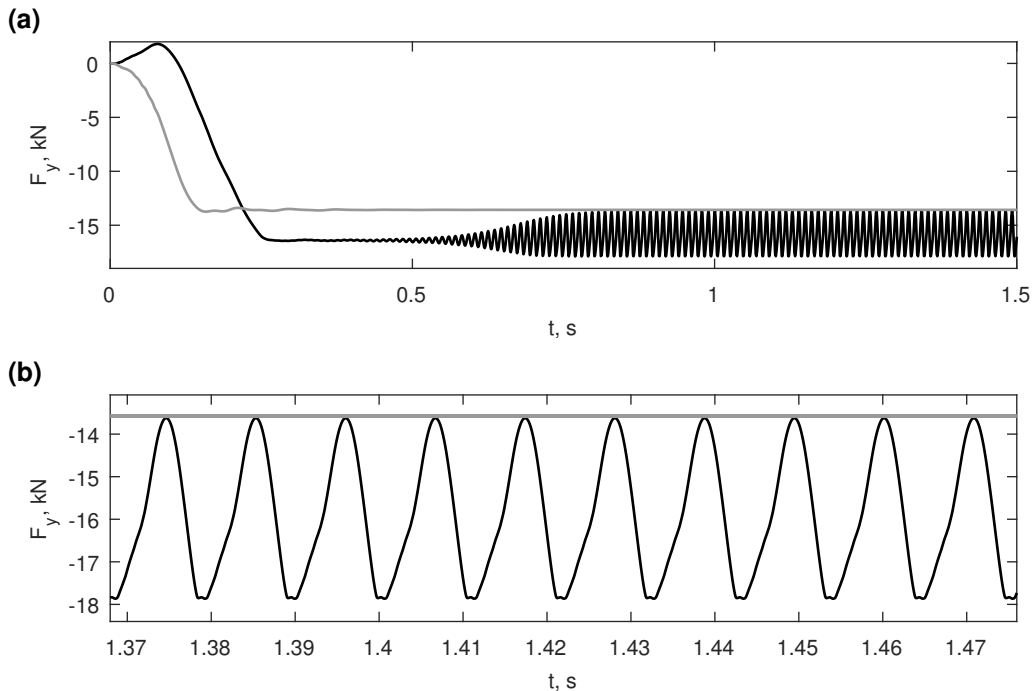


Figure 7.5: Lateral contact force time-history of the one-point wheel/rail contact cases: (a) complete time-history; (b) force time-history detail: (— black) case *cp1*; (— grey) case *cp2*.

The unstable behaviour obtained in the *cp1* one-point-contact case shows very high force amplitudes ( $\approx 4$  kN) with a frequency of 95 Hz. Similar oscillations were observed and discussed in Section 6.1.1. These are related to the primary vertical suspension of the wheelset and may be the same phenomenon observed in [63, 64].

## 7.4 Discussion

Results presented in Section 7.2 show that squeal is not limited to inner wheels in a curve, and can develop on outer wheels as well. In particular, the presence of two-point contact between wheel and rail can cause squeal. In the analysed two-point wheel/rail contact case, squeal develops with a sound power level of 118 dB. This sound power level is comparable with squeal on curve-inner wheels investigated in Section 6.1. The presented findings also support real observations of curve squeal on curve-outer wheels [26, 37, 97]. Curley et al. [26] observed during field tests that rail gauge face and gauge corner lubrication mitigated curve squeal. Lubrication in the two-point-contact case may influence the dynamic interaction of the two contact points and, therefore, mitigate squeal. To check this hypothesis simulations and detailed analyses of a real squeal case are required. Unfortunately, it is difficult and sometimes even impossible to gather all parameters required to completely define such a case.

Results of the detailed and the engineering model agree very well. Both models predict sound power levels that are very close in value. Differences in force amplitudes are also in line with the differences observed in the validation in Section 5.2. The engineering model, therefore, provides acceptable accuracy even in analyses of two-point-contact cases. Regarding computational efficiency, the engineering model is about three times faster than the detailed model. The speed of the engineering model makes it suitable for time-critical analyses and parameter studies. On the other hand, the detailed model is useful for detailed studies of processes in the contact area.

Squeal in the analysed two-point-contact case is the result of modes coupling. Two wheel modes with closely-spaced eigenfrequencies are needed to achieve sufficient dynamics coupling for squeal to occur. As soon as one of the two modes is damped out, squeal does not develop. Similar situations were already observed in [29, 34, 35, 37]. In [37], as much as three closely spaced modes had to be present for squeal to develop. The excited wheel modes are the  $(5, 0, a)$  and  $(3, 1, a)$  modes, which are both modes with dominant axial motion. This is in accordance with observations from the literature [100].

The two-point-contact case is compared to corresponding one-point-contact cases in Section 7.3. Results show that squeal in the two-point-contact case is caused by the dynamic interaction between the two contact points. When the contact points are considered independently, as one-point-contact cases with the same squeal case parameters, squeal does not develop.

In conclusion, the presented two-point-contact squeal case is a consequence of

---

two coupled wheel modes and the dynamic interaction of the two contact points. Due to the described case complexity, two-point-contact cases cannot be simplified to one-point-contact cases. It is, therefore, crucial that both contact points and their dynamic interaction are included and appropriately modelled.



# Chapter 8

## Conclusions and future work

---

### 8.1 Conclusions

In this thesis, a model for curve squeal formulated in the time domain has been presented. The model is suitable for use in engineering practice because it is computationally efficient and addresses a significant portion of the source-to-receiver chain. Curve squeal is analysed from its source to the radiated sound power.

The starting point of this thesis is the high-frequency wheel/rail interaction model developed by Pieringer [80, 81]. The central features of Pieringer's squeal model are the Green's functions approach and the use of Kalker's variational contact theory [55]. Green's functions enable the inclusion of any linear wheel and rail model. They also lead to faster time-domain computations than classical numerical integration techniques. Still, the computational cost associated with Kalker's variational theory is high. While faster than time-domain models based on the finite element method, Pieringer's model is still impractical for everyday engineering use. To make the model suitable for engineering practice several modifications and extensions are introduced.

The computational efficiency of the model is improved by exchanging Kalker's variational theory with a point-contact model for the tangential contact. The proposed model provides acceptable results, but with significant improvement in computational efficiency. The tangential point-contact model considers the contact variables globally. This global view is in contrast to Kalker's variational theory [55], which describes processes on the local contact level, i.e. on contact discretisation elements. Consequently, the Coulomb friction model, used by Kalker, describes friction between contact elements. The proposed point-contact model requires a friction model that defines friction properties of the complete contact. The global friction model, which is referred to as regularised friction, describes the transition from full-stick to full-slip contact conditions. This model is defined rigorously and is determined using Kalker's theory. The contact compliances are also defined on

the global level and are determined from the elastic half-space.

In its initial formulation, the tangential point-contact model is unable to evaluate cases with non-zero spin creepage. Therefore, a method for extending the point-contact model to cases with non-zero spin is proposed. Spin creepage is considered as a contact property and is included in the regularised friction model. In this way, the influence of spin on contact forces is accounted for beforehand and is not evaluated directly by the contact model.

The two models for curve squeal, the proposed engineering model and the detailed model [80, 81], are extended with three significant additions. Firstly, the influence of the contact angle is modelled. Secondly, the squeal models are extended to two-point wheel/rail contact cases. Lastly, the models are completed with a model for sound radiation from the railway wheel.

The first two extensions considerably improve the ability to evaluate realistic cases. The influence of more parameters on squeal occurrence and amplitudes can be studied. In particular, the extension to two-point wheel/rail contact enables the analysis of specific cases with curve squeal on outer wheels in curves. Scarce research on curve squeal in the presence of two-point contact is available in the literature. To the knowledge of the author, the model presented in this thesis is the first time-domain model for curve squeal that can consider two-point contact and covers a significant portion of the source-to-receiver chain.

The evaluation of radiated sound enables an informed and more objective judgement of squeal severity. It also provides a significant step towards modelling the complete source-to-receiver chain. In comparison, the force time-history, which is the initial output of the squeal models, does not give much information about noise levels. The implemented model is a simple and computationally efficient model originally developed by Thompson and Jones [102, 103, 104].

According to Knothe and Groß-Thebing [58], to model transient processes accurately, a contact model should be able to describe the change of contact variables in the contact area. The tangential point-contact model is unable to determine the spatial distribution of contact variables and is, therefore, not considered as transient. Another source of the model's steady-state nature is the formulation of the global friction model: regularised friction is determined so that it describes a steady-state transition from full-stick to full-slip contact conditions. Still, the validation of the point-contact model against Kalker's variational theory shows that the point-contact model can be used for transient problems under certain circumstances. A two-fold validation procedure is proposed to determine the applicability of a contact model for dynamic wheel/rail interaction modelling. Firstly, the model is validated independently with an imposed motion (stand-alone validation). Secondly, the model is validated with the system dynamics defining the input to the contact model (dynamic validation).

The stand-alone validation of the point-contact model against Kalker's variational theory shows significant differences already at 400 Hz. From that frequency on, the point-contact model cannot accurately describe transient processes. In contrast, the validation in dynamic conditions shows that the model gives acceptable

results up to at least 5 kHz. The engineering model for squeal is also able to predict squeal equally well as Pieringer's model [80, 81]. Validation results show that the system dynamics put significantly different demands on the contact model than the case with imposed motion. When the system dynamics are included, the contact model input is variable and depends on the system response and the contact forces. The imposed-motion case can be considered as a stiffer mathematical problem, not representative of squeal. In conclusion: the applicability of a contact model for dynamic wheel/rail interaction modelling should be determined in conditions that replicate the real application as closely as possible.

The validation of the extension to non-zero spin shows that differences between the extended engineering model and the detailed model are in line with deviations of the original model. Results indicate that the inclusion of the spin-creepage influence in the friction curve is a valid approach. Spin can, therefore, be considered as a contact property in curve squeal analyses. The friction curve may have the potential to include other data that is hard or nearly impossible to model. If measured friction curves are used, they could contain information about the contact area shape and size, pollution and other environmental factors, but also specific contact-kinematics related data.

A study of the influence of kinematic parameters and friction is performed using the proposed engineering model. The investigated kinematic parameters are lateral creepage and the wheel/rail lateral contact position. Both are related to the vehicle curving behaviour. Results show that the contact position, which influences the vertical-lateral coupling dynamics, is a critical parameter. It defines squeal frequency and severity and influences squeal occurrence. In one contact case, squeal developed even at low friction values. In such cases, friction modifiers are not expected to provide benefits. Instead, solutions have to be sought through improvements in the vehicle curving behaviour. Friction and lateral creepage define the input energy into the system and mostly influence squeal amplitudes. Their influence on squeal occurrence is contact-case dependent, and they, in combination, determine the tangential force-saturation point at which squeal may develop.

Since the wheel is the principal source of squeal, the influence of its modal damping on curve squeal is examined. Despite the somewhat limited study, interesting conclusions are drawn from the results. In the investigated cases, friction shows a strong influence on the number of wheel modes that are susceptible to squeal. In comparison, the influence of lateral creepage is lower. Still, in combination with high friction, high creepage can lead to more wheel modes becoming susceptible to squeal. From a mitigation perspective, it is easier to eliminate squeal in cases with low to moderate friction. The modal damping values required to eliminate squeal are, in the investigated cases, rather low. However, the wheel damping treatment should increase damping at all modes found susceptible to squeal in the considered case. If only the initially squealing wheel mode is damped, squeal may move to another mode with another frequency and amplitude. These findings partially explain why resilient wheels do not eliminate squeal in all cases [2].

Studies on spin creepage show that spin influences the squeal amplitudes by influ-

encing processes in the contact area. By changing spin creepage, squeal amplitudes change and squeal can even disappear. The spin value at which squeal disappears depends on the case under consideration. High values of spin can be considered as a disruption to the stick-slip process, thus not allowing the development of squeal. The contact angle shows a more complex influence on curve squeal. A change in the contact angle influences squeal amplitudes and, depending on the contact case, its occurrence. Moreover, in specific cases, squeal changes frequency, i.e. moves to another wheel mode. This change indicates that the contact angle influences the dynamics coupling.

Finally, results of the two-point wheel/rail contact case show the complexity of squeal. In line with field observations [26, 37, 97], squeal was obtained on the outer wheel in a curve. In the analysed case, curve squeal is the result of two wheel modes with closely spaced eigenfrequencies. The presence of the two modes is needed to achieve sufficient dynamics coupling for squeal to develop. The comparison to corresponding one-point-contact cases shows that squeal is caused by the dynamic interaction of the two contact points. The obtained squeal is, therefore, the result of a combination of the dynamic interplay of the two contact points and the presence of two closely spaced modes.

Regarding the modelling approach, results presented in this thesis show that all parameters influencing the dynamics coupling have to be considered in the model. Friction, the contact angle, contact position and the presence of two-point contact are the strongest identified influences on the dynamics-coupling mechanism. Finally, spin creepage should be considered for an accurate prediction of squeal amplitudes. Still, the influence of spin is mostly limited to cases with significant spin values.

## 8.2 Future work

Many questions remain open about the development of squeal and the required level of modelling detail. This thesis shows that a rather simple tangential contact model can provide satisfactory results. Still, many parameters that influence its precision need to be further investigated, and more parameters need to be included to broaden the model applicability.

Regarding the tangential point-contact model, directions of future work include its generalisation to cases with all three creepages (longitudinal, lateral and spin). Further investigations of the contact stiffness would be beneficial, especially if the contact model is extended to conformal contact. In that case, the elastic half-space assumption is invalid. The contact model has to be then modified to account for the different elastic behaviour of the contact. This extension would enable more accurate analyses of cases involving flange contact.

The proposed model for curve squeal does not account for longitudinal dynamics. Moreover, only cases with constant rolling velocity and contact position can be considered. While straightforward, the extension to longitudinal dynamics would enable for numerical investigations of the influence of longitudinal creepage and

longitudinal vehicle dynamics on curve squeal. Additionally, the implementation of a time-variable wheel/rail contact position and creepages would allow analyses of transient curving cases.

The proposed squeal model does not consider any variation of the contact variables caused by the wheel and rail irregularities and roughness. For example, an unsteady vertical contact force could be of particular importance for curve squeal. Such a vertical force could significantly influence the contact conditions and, consequently, squeal. Therefore, the extension of the model with an irregularity-induced time-variation of the contact forces is believed to be of high interest. This extension would enable studies that could significantly deepen the present understanding of curve squeal.

The distinction between local and global friction was made in this thesis. Lots of questions about both the local and global wheel/rail friction are still open. Whether Coulomb's friction accurately describes friction between contact particles can be put in doubt. Since even Kalker's model relies on a finite contact discretisation, it can be questioned whether a regularised friction curve should also be used in that model. Further research is, therefore, required to determine an appropriate level on which friction is to be defined. On the one hand, theoretical investigations about friction on the local level are needed. These could answer questions about the relationship between high-frequency phenomena and friction, which is sometimes questioned in the available literature. On the other hand, friction measurements could provide additional data about thermal, roughness and contamination effects on the global level.

Finally, the validation of the models against field or laboratory measurements should be carried out. This would enable the verification of the modelling approach and provide data for fine-tuning of the models. Of particular interest would be the use of measured friction curves in the engineering model and their influence on the simulated squeal.



# References

- [1] Burden of disease from environmental noise - Quantification of healthy life years lost in Europe. Technical report, WHO, 2011.
- [2] Railway noise Technical Measures Catalogue. Technical Report UIC003-01-04fe, UIC International Union of Railways, July 2013.
- [3] Annual European Union greenhouse gas inventory 1990–2015 and inventory report 2017. Technical Report 06/2017, European Environment Agency, May 2017.
- [4] ANSYS Mechanical Finite Element Analysis Software. ANSYS, Inc., <http://www.ansys.com/>, accessed December 2017.
- [5] Simpack Multi-Body Simulation Software, SIMULIA. Dassault Systèmes SIMULIA Corp., <http://www.simpack.com/>, accessed November 2017.
- [6] S. Alfi, S. Baro, R. Corradi, G. Squicciarini, D. J. Thompson, and M. Asplund. An investigation of the influence of wheel/rail contact conditions on curve squeal. In *Proceedings of INTER-NOISE 2016*, pages 6923–6930, Hamburg, Germany, 2016.
- [7] A. Alonso and J. G. Giménez. Tangential problem solution for non-elliptical contact areas with the FastSim algorithm. *Vehicle System Dynamics*, 45(4):341–357, 2007.
- [8] A. Alonso and J. G. Giménez. Non-steady state modelling of wheel-rail contact problem for the dynamics simulation of railway vehicles. *Vehicle System Dynamics*, 46(3):179–196, 2008.
- [9] E. Andersson, M. Berg, and S. Stichel. *Rail Vehicle Dynamics*. Division of Rail Vehicles, KTH, Stockholm, 2007.
- [10] P. Andersson. *Modelling Interfacial Details in Tyre/Road Contact - Adhesion Forces and Non-Linear Contact Stiffness*. PhD thesis, Department of Civil and Environmental Engineering, Chalmers University of Technology, Göteborg, Sweden, 2005.

- 
- [11] J. B. Ayasse and H. Chollet. Determination of the wheel rail contact patch in semi-Hertzian conditions. *Vehicle System Dynamics*, 43(3):161–172, 2005.
- [12] L. Baeza, F. J. Fuenmayor, J. Carballeira, and A. Roda. Influence of the wheel-rail contact instationary process on contact parameters. *Journal of Strain Analysis for Engineering Design*, 42:377–387, 2007.
- [13] M. L. Boas. *Mathematical Methods in the Physical Sciences*. John Wiley & Sons, third edition, 2006.
- [14] J. Boussinesq. *Application des Potentiels à l'Étude de l'Équilibre et du Mouvement des Solides Élastiques*. Gauthier-Villars, Paris, France, 1885.
- [15] H. Brick. *Application of the Boundary Element Method to combustion noise and half-space problems*. PhD thesis, Department of Civil and Environmental Engineering, Chalmers University of Technology, Göteborg, Sweden, 2009.
- [16] J. F. Brunel, P. Dufrenoy, M. Naït, J. L. Muñoz, and F. Demilly. Transient model for curve squeal noise. *Journal of Sound and Vibration*, 293:204–218, 2006.
- [17] F. W. Carter. On the Action of a Locomotive Driving Wheel. *Proceedings of the Royal Society of London. Series A*, 112(760):151–157, 1926.
- [18] V. Cerruti. *Mem. fis. mat.* Accademia dei Lincei, Roma, Italy, 1882.
- [19] G. X. Chen, Z. R. Zhou, H. Ouyang, X. S. Jin, M. H. Zhu, and Q. Y. Liu. A finite element study on rail corrugation based on saturated creep force-induced self-excited vibration of a wheelset-track system. *Journal of Sound and Vibration*, 329:4643–4655, 2010.
- [20] O. Chiello, J. B. Ayasse, N. Vincent, and J. R. Koch. Curve squeal of urban rolling stock—Part 3: Theoretical model. *Journal of Sound and Vibration*, 293:710–727, 2006.
- [21] A. Cigada, S. Manzoni, and M. Vanali. Vibro-acoustic characterization of railway wheels. *Applied Acoustics*, 69:530–545, 2008.
- [22] C. Collette. Importance of the wheel vertical dynamics in the squeal noise mechanism on a scaled test bench. *Shock and Vibration*, 19:145–153, 2012.
- [23] R. Corradi, P. Crosio, S. Manzoni, and G. Squicciarini. Experimental investigation on squeal noise in tramway sharp curves. In *Proceedings of the 8th International Conference on Structural Dynamics EURODYN 2011*, Leuven, Belgium, 2011.
- [24] D. G. Crighton, A. P. Dowling, J. E. F. Williams, M. A. Heckl, and F. A. Leppington. *Modern Methods in Analytical Acoustics: Lecture Notes*. Springer, 1996.

- [25] B. E. Croft. *The Development of Rail-head Acoustic Roughness*. PhD thesis, Institute of Sound and Vibration Research, University of Southampton, Southampton, United Kingdom, October 2009.
- [26] D. Curley, D. C. Anderson, J. Jiang, and D. Hanson. Field Trials of Gauge Face Lubrication and Top-of-Rail Friction Modification for Curve Noise Mitigation. In J. C. O. Nielsen, D. Anderson, P.-E. Gautier, M. Iida, J. T. Nelson, D. J. Thompson, T. Tielkes, D. A. Towers, and P. de Vos, editors, *Noise and Vibration Mitigation for Rail Transportation Systems: Proceedings of the 11th International Workshop on Railway Noise*, volume 126, pages 449–456. Springer, Berlin, Heidelberg, 2015.
- [27] F. G. de Beer, M. H. A. Janssens, and P. P. Koojiman. Squeal noise of rail-bound vehicles influenced by lateral contact position. *Journal of Sound and Vibration*, 267:497–507, 2003.
- [28] DEsolver. *GENSYS users manual*, 2009.
- [29] B. Ding, G. Squicciarini, and D. J. Thompson. Effects of rail dynamics and friction characteristics on curve squeal. *Journal of Physics: Conference Series*, 744(1), 2016.
- [30] D. T. Eadie, M. Santoro, and J. Kalousek. Railway noise and the effect of top of rail liquid friction modifiers: changes in sound and vibration spectral distributions in curves. *Wear*, 258:1148–1155, 2005.
- [31] D. T. Eadie, M. Santoro, and W. Powell. Local control of noise and vibration with KELTRACK friction modifier and Protectors trackside application: an integrated solution. *Journal of Sound and Vibration*, 267:761–772, 2003.
- [32] EC. EU transport in figures - statistical pocketbook 2016, 2016.
- [33] U. Fingberg. A model of wheel-rail squealing noise. *Journal of Sound and Vibration*, 143(3):365–377, 1990.
- [34] D. J. Fourie, P. J. Gräbe, P. S. Heyns, and R. D. Fröhling. Analysis of railway wheel squeal due to unsteady longitudinal creepage using the complex eigenvalue method. In *Proceedings of the 12th IWRN*, pages 36–45, Terrigal, Australia, 2016.
- [35] D. J. Fourie, P. J. Gräbe, P. S. Heyns, and R. D. Fröhling. Experimental characterisation of railway wheel squeal occurring in large-radius curves. *Proc. Inst. Mech. Eng., Part F: J. Rail and Rapid Transit*, 230:1561–1574, 2016.
- [36] J. G. Giménez, A. Alonso, and E. Gómez. Introduction of a friction coefficient dependent on the slip into the FastSim algorithm. *Vehicle System Dynamics*, 43(4):233–244, 2005.

- [37] C. Glocker, E. Cataldi-Spinola, and R. I. Leine. Curve squealing of trains: Measurement, modelling and simulation. *Journal of Sound and Vibration*, 324:365–386, 2009.
- [38] A. Gross-Thebing. Frequency-Dependent Creep Coefficients for Three-Dimensional Rolling Contact Problems. *Vehicle System Dynamics*, 18(6):359–374, 1989.
- [39] A. Guiral, A. Alonso, L. Baeza, and J. G. Giménez. Non-steady state modelling of wheel-rail contact problem. *Vehicle System Dynamics*, 51(1):91–108, 2013.
- [40] M. Heckl. Proposal for a railway simulation program. In *A Workshop on Rolling Noise Generation*, pages 128–148, Institut für Technische Akustik, Technische Universität Berlin, October 1989.
- [41] M. A. Heckl. Curve squeal of train wheels, part 2: which wheel modes are prone to squeal? *Journal of Sound and Vibration*, 229(3):695–707, 2000.
- [42] M. A. Heckl and I. D. Abrahams. Curve squeal of train wheels, part 1: mathematical model for its generation. *Journal of Sound and Vibration*, 229(3):669–693, 2000.
- [43] H. Hertz. Ueber die Berührung fester elastischer Körper. *Journal für reine und angewandte Mathematik*, 92:156–171, 1882.
- [44] N. Hoffmann, M. Fischer, R. Allgaier, and L. Gaul. A minimal model for studying properties of the mode-coupling type instability in friction induced oscillations. *Mechanics Research Communications*, 29:197–205, 2002.
- [45] S. S. Hsu, Z. Y. Huang, S. D. Iwnicki, D. C. J. C. Jones, G. Xie, and P. D. Allen. Experimental and theoretical investigation of railway curve squeal. *Proc. Inst. Mech. Eng., Part F: J. Rail and Rapid Transit*, 221:59–73, 2007.
- [46] Z. Y. Huang. *Theoretical Modelling of Railway Curve Squeal*. PhD thesis, ISVR, University of Southampton, Southampton, UK, 2007.
- [47] Z. Y. Huang, D. J. Thompson, and C. J. C. Jones. Squeal Prediction for a Bogied Vehicle in a Curve. In B. Schulte-Werning, D. J. Thompson, P.-E. Gautier, C. Hanson, B. Hemsworth, J. Nelson, T. Maeda, and P. de Vos, editors, *Noise and Vibration Mitigation for Rail Transportation Systems: Proceedings of the 9th International Workshop on Railway Noise*, volume 99, pages 313–319. Springer, Berlin, Heidelberg, 2008.
- [48] S. Iwnicki, S. Björklund, and R. Enblom. Wheel-rail contact mechanics. In R. Lewis and U. Olofsson, editors, *Wheel-Rail Interface Handbook*, chapter 3, pages 58–92. Woodhead Publishing, 2009.

- [49] J. Jiang, D. C. Anderson, and R. Dwight. The Mechanisms of Curve Squeal. In J. C. O. Nielsen, D. Anderson, P.-E. Gautier, M. Iida, J. T. Nelson, D. J. Thompson, T. Tielkes, D. A. Towers, and P. de Vos, editors, *Noise and Vibration Mitigation for Rail Transportation Systems: Proceedings of the 11th International Workshop on Railway Noise*, volume 126, pages 587–594. Springer, Berlin, Heidelberg, 2015.
- [50] J. Jiang, D. Hanson, and B. Dowell. Wheel Squeal: Insights from Wayside Condition Monitoring. In *Proceedings of the 12th IWRN*, pages 28–35, Terrigal, Australia, 2016.
- [51] K. L. Johnson. *Contact mechanics*. Cambridge University Press, 1985.
- [52] C. J. C. Jones and D. J. Thompson. Extended validation of a theoretical model for railway rolling noise using novel wheel and track designs. *Journal of Sound and Vibration*, 267(3):509–522, 2003.
- [53] J. J. Kalker. Survey of Wheel-Rail Rolling Contact Theory. *Vehicle System Dynamics*, 5:317–358, 1979.
- [54] J. J. Kalker. A Fast Algorithm for the Simplified Theory of Rolling Contact. *Vehicle System Dynamics*, 11:1–13, 1982.
- [55] J. J. Kalker. *Three-Dimensional Elastic Bodies in Rolling Contact*, volume 2 of *Solid mechanics and its applications*. Kluwer Academic Publishers, 1990.
- [56] J. J. Kalker. Wheel-rail rolling contact theory. *Wear*, 144:243–261, 1991.
- [57] K. Knothe and A. Gross-Thebing. Derivation of Frequency Dependent Creep Coefficients Based on an Elastic Half-Space Model. *Vehicle System Dynamics*, 15(3):133–153, 1986.
- [58] K. Knothe and A. Gross-Thebing. Short wavelength rail corrugation and non-steady state contact mechanics. *Vehicle System Dynamics*, 46(1-2):49–66, 2008.
- [59] K. Knothe, R. Wille, and B. W. Zastrau. Advanced Contact Mechanics - Road and Rail. *Vehicle System Dynamics*, 35(4-5):361–407, 2001.
- [60] J. R. Koch, N. Vincent, H. Chollet, and O. Chiello. Curve squeal of urban rolling stock—Part 2: Parametric study on a 1/4 scale test rig. *Journal of Sound and Vibration*, 293:701–709, 2006.
- [61] K. Kraft. Der Einfluß der Fahrgeschwindigkeit auf den Haftwert zwischen Rad und Scheine. *Archiv für Eisenbahntechnik*, 22:58–78, 1967.
- [62] W. Kropp. *Ein Modell zur Beschreibung des Rollgeräusches eines unprofiliereten Gürtelreifens auf rauher Strassenoberfläche*. PhD thesis, Fortschritt-Berichte Reihe 11, Nr 166, VDI Verlag, Düsseldorf, Germany, 1992.

- [63] B. Kurzeck. Combined friction induced oscillations of wheelset and track during the curving of metros and their influence on corrugation. *Wear*, 271:299–310, 2011.
- [64] B. Kurzeck and M. Hecht. Dynamic simulation of friction-induced vibrations in a light railway bogie while curving compared with measurement results. *Vehicle System Dynamics*, 48(sup1):121–138, 2010.
- [65] R. Lewis and U. Olofsson. Basic tribology of the wheel-rail contact. In R. Lewis and U. Olofsson, editors, *Wheel-Rail Interface Handbook*, chapter 2, pages 34–57. Woodhead Publishing, 2009.
- [66] X. Liu and P. A. Meehan. Wheel squeal noise: A simplified model to simulate the effect of rolling speed and angle of attack. *Journal of Sound and Vibration*, 338:184–198, 2015.
- [67] X. Liu and P. A. Meehan. Investigation of squeal noise under positive friction characteristics condition provided by friction modifiers. *Journal of Sound and Vibration*, 371:393–405, 2016.
- [68] G. Lundberg and H. Sjövall. Stress and deformation in elastic contacts. Göteborg, 1958.
- [69] P. A. Meehan and X. Liu. Prediction and Investigation of Wheel Squeal Amplitude. In *Proceedings of the 12th IWRN*, pages 434–443, Terrigal, Australia, 2016.
- [70] I. Merideño, J. Nieto, N. Gil-Negrete, A. Landaberea, and J. Iartza. Numerical vibro-acoustic analysis of railway wheels with and without damping solutions. *Noise Control Engineering Journal*, 60(4):458–472, 2012.
- [71] A. D. Monk-Steel and D. J. Thompson. Models for railway curve squeal noise. In *VIII International Conference on Recent Advances in Structural Dynamics*, Southampton, United Kingdom, 14-16 July 2003.
- [72] A. D. Monk-Steel, D. J. Thompson, F. G. de Beer, and M. H. A. Janssens. An investigation into the influence of longitudinal creepage on railway squeal noise due to lateral creepage. *Journal of Sound and Vibration*, 293:766–776, 2006.
- [73] C. M. Nilsson, C. J. C. Jones, D. J. Thompson, and J. Ryue. A waveguide finite element and boundary element approach to calculating the sound radiated by railway and tram rails. *Journal of Sound and Vibration*, 321:813–836, 2009.
- [74] A. Nordborg. Wheel/rail noise generation due to nonlinear effects and parametric excitation. *Journal of the Acoustical Society of America*, 111(4):1772–1781, 2002.

- [75] J. T. Oden and J. A. C. Martins. Models and computational methods for dynamic friction phenomena. *Computer Methods in Applied Mechanics and Engineering*, 52(1-3):527–634, 1985.
- [76] J. Oertli. Combatting curve squeal, phase II. Final report, UIC International Union of Railways, 2005.
- [77] E. Panulinova, S. Harabinova, and L. Argalasova. Tram Squealing Noise and Its Impact on Human Health. *Noise & Health*, 18:329–337, 2016.
- [78] B. Paul and J. Hashemi. Contact pressures on closely conforming elastic bodies. *Journal of Applied Mechanics*, 48(3):543–548, 1981.
- [79] F. J. Periard. *Wheel-Rail Noise Generation: Curve Squealing by Trams*. PhD thesis, Delft University of Technology, Delft, Netherlands, 1998.
- [80] A. Pieringer. *Time-domain modelling of high-frequency wheel/rail interaction*. PhD thesis, Department of Civil and Environmental Engineering, Chalmers University of Technology, Göteborg, Sweden, 2011.
- [81] A. Pieringer. A numerical investigation of curve squeal in the case of constant wheel/rail friction. *Journal of Sound and Vibration*, 333(18):4295–4313, 2014.
- [82] A. Pieringer, L. Baeza, and W. Kropp. Modelling of Railway Curve Squeal Including Effects of Wheel Rotation. In J. C. O. Nielsen, D. Anderson, P.-E. Gautier, M. Iida, J. T. Nelson, D. J. Thompson, T. Tielkes, D. A. Towers, and P. de Vos, editors, *Noise and Vibration Mitigation for Rail Transportation Systems: Proceedings of the 11th International Workshop on Railway Noise*, volume 126, pages 417–424. Springer, Berlin, Heidelberg, 2015.
- [83] A. Pieringer, W. Kropp, and D. J. Thompson. Investigation of the dynamic contact filter effect in vertical wheel/rail interaction using a 2D and a 3D non-Hertzian contact model. *Wear*, 271(1-2):328–338, 2011.
- [84] A. Pieringer, P. T. Torstensson, J. Giner, and L. Baeza. Investigation of railway curve squeal using a combination of frequency- and time-domain models. In *Proceedings of the 12th IWRN*, pages 444–451, Terrigal, Australia, 2016.
- [85] J. Piotrowski and H. Chollet. Wheel-rail contact models for vehicle system dynamics including multi-point contact. *Vehicle System Dynamics*, 43(6-7):455–483, 2005.
- [86] J. Piotrowski and W. Kik. A simplified model of wheel/rail contact mechanics for non-Hertzian problems and its application in rail vehicle dynamic simulations. *Vehicle System Dynamics*, 46(1-2):27–48, 2008.
- [87] O. Polach. Creep forces in simulations of traction vehicles running on adhesion limit. *Wear*, 258:992–1000, 2005.

- [88] W. J. Qian, G. X. Chen, H. Ouyang, M. H. Zhou, W. H. Zhang, and Z. R. Zhou. A transient dynamic study of the self-excited vibration of a railway wheel set-track system induced by saturated creep forces. *Vehicle System Dynamics*, 52(9):1115–1138, 2014.
- [89] P. J. Remington. Wheel/rail squeal and impact noise: What do we know? What we don't know? Where do we go from here? *Journal of Sound and Vibration*, 2(116):339–353, 1985.
- [90] M. J. Rudd. Wheel/rail noise - Part II: Wheel squeal. *Journal of Sound and Vibration*, 46(3):381–394, 1976.
- [91] E. Schneider and K. Popp. Noise generation in railway wheels due to rail-wheel contact forces. *Journal of Sound and Vibration*, 120(2):227–244, 1988.
- [92] S. Setsobhonkul and S. Kaewunruen. Life cycle analysis of railway noise and vibration mitigation methodologies with respect to curve squeal noises. In *Proceedings of INTER-NOISE 2016*, pages 4877–4886, Hamburg, Germany, 2016.
- [93] Z. Y. Shen, J. K. Hedrick, and J. A. Elkins. A Comparison of Alternative Creep Force Models for Rail Vehicle Dynamics Analysis. *Vehicle System Dynamics*, 12(1-3):79–83, 1983.
- [94] Z. Y. Shen and Z. Li. A fast non-steady state creep force model based on the simplified theory. *Wear*, 191:242–244, 1996.
- [95] J.-J. Sinou and L. Jézéquel. Mode coupling instability in friction-induced vibrations and its dependency on system parameters including damping. *European Journal of Mechanics A/Solids*, 26:106–122, 2007.
- [96] T. R. Spurr. A Theory of Brake Squeal. *Proc. Inst. Mech. Eng., Part D: J. Automob. Eng.*, pages 33–52, 1961.
- [97] G. Squicciarini, S. Usberti, D. J. Thompson, R. Corradi, and A. Barbera. Curve Squeal in the Presence of Two Wheel/Rail Contact Points. In J. C. O. Nielsen, D. Anderson, P.-E. Gautier, M. Iida, J. T. Nelson, D. J. Thompson, T. Tielkes, D. A. Towers, and P. de Vos, editors, *Noise and Vibration Mitigation for Rail Transportation Systems: Proceedings of the 11th International Workshop on Railway Noise*, volume 126, pages 603–610. Springer, Berlin, Heidelberg, 2015.
- [98] H. Stappenbeck. The curve noise of the tramway—possibilities of its suppression. *Journal of the Association of German Engineers*, 96(6):171–175, 1954.
- [99] D. J. Thompson. Wheel-Rail Noise Generation, Part II: Wheel Vibration. *Journal of Sound and Vibration*, 161(3):401–419, 1993.

- [100] D. J. Thompson. *Railway Noise and Vibration: Mechanisms, Modelling and Means of Control*. Elsevier, Oxford, UK, 2009.
- [101] D. J. Thompson and M. G. Dittich. Wheel response and radiation - laboratory measurements of five types of wheel and comparisons with theory. ORE Technical Document DT248 (C163), Utrecht, The Netherlands, June 1991.
- [102] D. J. Thompson, B. Hemsworth, and N. Vincent. Experimental validation of the TWINS prediction program for rolling noise, part 1: description of the model and method. *Journal of Sound and Vibration*, 193(1):123–135, 1996.
- [103] D. J. Thompson, M. H. A. Janssens, and F. G. de Beer. Track-Wheel Interaction Noise Software Theoretical Manual. TNO-report HAG-RPT-990211, TNO Institute of Applied Physics, November 1999.
- [104] D. J. Thompson and C. J. C. Jones. Sound radiation from a vibrating railway wheel. *Journal of Sound and Vibration*, 253(2):401–419, 2002.
- [105] D. J. Thompson, G. Squicciarini, and B. Ding. A state-of-the-art review of curve squeal noise: phenomena, mechanisms, modelling and mitigation. In *Proceedings of the 12th IWRN*, pages 1–27, Terrigal, Australia, 2016.
- [106] P. T. Torstensson, A. Pieringer, and L. Baeza. Towards a model for prediction of railway tread brake noise. In *The ISMA conference on noise and vibration engineering (ISMA 2014)*, pages 3543–3556, Leuven, Belgium, 2014.
- [107] M. Toward, G. Squicciarini, and D. J. Thompson. Reducing freight wagon noise at source. *International Railway Journal*, pages 47–49, March 2015.
- [108] C. J. M. van Ruiten. Mechanism of squeal noise generated by trams. *Journal of Sound and Vibration*, 120(2):245–253, 1988.
- [109] P. J. Vermeulen and K. L. Johnson. Contact of Nonspherical Elastic Bodies Transmitting Tangential Forces. *Transactions of the ASME, Journal of Applied Mechanics*, 31(E2):338–340, 1964.
- [110] N. Vincent, J. R. Koch, H. Chollet, and J. Y. Guerder. Curve squeal of urban rolling stock—Part 1: State of the art and field measurements. *Journal of Sound and Vibration*, 293:691–700, 2006.
- [111] E. A. H. Vollebregt. A Gauss-Siedel Type Solver for Special Convex Programs, with Application to Frictional Contact Mechanics. *Journal of Optimization Theory and Applications*, 87(1):47–67, 1995.
- [112] E. A. H. Vollebregt. User guide for CONTACT, Vollebregt & Kalker’s rolling and sliding contact model. Technical report, VORtech Computing, June 2012.
- [113] E. A. H. Vollebregt. Numerical modeling of measured railway creep versus creep-force curves with CONTACT. *Wear*, 314:87–95, 2014.

- [114] E. A. H. Vollebregt, J. J. Kalker, and H. X. Lin. A fast solver for normal and tangential contact mechanics in the half-space. *Transactions of Engineering Sciences*, 1:235–242, 1993.
- [115] E. A. H. Vollebregt and H. M. Schuttelaars. Quasi-static analysis of two-dimensional rolling contact with slip-velocity dependent friction. *Journal of Sound and Vibration*, 331:2141–2155, 2012.
- [116] E. A. H. Vollebregt and P. Wilders. FASTSIM2: a second-order accurate frictional rolling contact algorithm. *Computational Mechanics*, 47:105–116, 2011.
- [117] C. Wang, R. Dwight, W. Li, and J. Jiang. Prediction of curve squeal in the case of constant wheel rail friction coefficient. In *Proceedings of the 12th IWRN*, pages 428–433, Terrigal, Australia, 2016.
- [118] G. Xie, P. D. Allen, S. D. Iwnicki, A. Alonso, D. J. Thompson, C. J. C. Jones, and Z. Y. Huang. Introduction of falling friction coefficients into curving calculations introduction of falling friction coefficients into curving calculations for studying curve squeal noise. *Vehicle System Dynamics*, 44(sup 1):261–271, 2006.
- [119] W. Yan and D. Fischer. Applicability of the Hertz contact theory to rail-wheel contact problems. *Archive of Applied Mechanics*, 70(4):255–268, 2000.
- [120] Z. Yang, Z. Li, and R. Dollevoet. Numerical study on two-point contact by an explicit integration finite element method - A contribution to the modeling of flange squeal. In *Proceedings of the 10th International Conference on Contact Mechanics CM2015*, Colorado Springs, USA, 2015.
- [121] I. Zenzerovic, W. Kropp, and A. Pieringer. An engineering time-domain model for curve squeal: Tangential point-contact model and Green’s functions approach. *Journal of Sound and Vibration*, 376:149–165, 2016.
- [122] I. Zenzerovic, W. Kropp, and A. Pieringer. Influence of spin creepage and contact angle on curve squeal: a numerical approach. *Manuscript submitted for publication*, 2017.
- [123] I. Zenzerovic, W. Kropp, and A. Pieringer. Time-domain investigation of curve squeal in the presence of two wheel/rail contact points. *Manuscript submitted for publication*, 2017.
- [124] I. Zenzerovic, A. Pieringer, and W. Kropp. Towards an Engineering Model for Curve Squeal. In J. C. O. Nielsen, D. Anderson, P.-E. Gautier, M. Iida, J. T. Nelson, D. J. Thompson, T. Tielkes, D. A. Towers, and P. de Vos, editors, *Noise and Vibration Mitigation for Rail Transportation Systems: Proceedings of the 11th International Workshop on Railway Noise*, volume 126, pages 433–440. Springer, Berlin, Heidelberg, 2015.